2017

Chemical Sensing In Harsh Environments By Multivariate Optical Computing

Christopher Michael Jones
University of South Carolina

CHEMICAL SENSING IN HARSH ENVIRONMENTS BY MULTIVARIATE OPTICAL COMPUTING

by

Christopher Michael Jones

Bachelor of Science
University of South Carolina, 1996

Master of Science
University of Houston, 2000

Submitted in Partial Fulfillment of the Requirements

For the Degree of Doctor of Philosophy in

Chemistry

College of Arts and Sciences

University of South Carolina

2017

Accepted by:

Michael L. Myrick, Major Professor

Timothy Shaw, Committee Member

S. Michael Angel, Committee Member

John Rose, Committee Member

Cheryl L. Addy, Vice Provost and Dean of the Graduate School

DEDICATION

To my wife Angela and children Amanda, Tess and Sean who sacrificed more than I can ever express, to enable me to conduct this research and write this dissertation. Thank you, my gratitude is more than I can ever express.

ACKNOWLEDGEMENTS

In addition to my wife and children I would like to thank my parents, brother and sister, my wife's extended family (Stevenson's, Pasicatan's, Chapman's Browne's, Herty's, Martin's), most who live in my neighborhood. In many ways they have helped through these years as my family has sacrificed for me to attend graduate school, they have been there to help us and offered me encouragement.

I would like to thank Dr. Stephen Morgan, and Dr. William Egan (past Morgan Group). While I was undergraduate in chemistry, they introduced me to Chemometrics and intensified my interest in spectroscopy. It was Dr. Morgan who introduced me to Dr. Stanley Deming at the University of Houston where I attended graduate school, receiving my Masters of Science in Chemistry. I am indebted to Dr. Deming, my most active committee member, who both in the classroom and outside the classroom taught me my Chemometrics foundation.

I would like to thank my early professional mentors and friends Dr. Richard Drozd, Patrick Jacobs, Michael Dix. In my first professional job, they believed in me and encouraged my growth. Even at that early stage they had encouraged me to return to school and pursue a Doctor of Philosophy. They have each taught me lessons of life for which I am forever grateful.

I would like to thank my friends Ronald Cherry, Robert Engelman, and Mark Proett, who were also the mentors of my second job. They had directly encouraged me and supported my decision to finally return to graduate school.

I would like to thank Dr. Milos Milosevic Director of Technology at Halliburton, and Dr. Sriram Srinivasan Vice President of Technology at Halliburton, who enabled me to attend graduate school. They also, have allowed the collaboration between the University of South Carolina and Halliburton in order to conduct this research. I have truly enjoyed working with each of them, and consider them to be my latest mentors.

I would like to thank the current Myrick Group, Cameron Rekully, Stefan Faulkner, Elle Belliveau, and Ergun Kara for collaborations in various research activities over the past couple of years, and to Cameron and Stefan specifically for helping me with the seminars. I would specifically like to thank Dr. David Perkins, Dr. Megan Pearl (past Myrick Group), Dr. Bin Dai, Dr. James Price, Dr. Jian Li, Michael Pelletier, Dr. Jing Shen, Robert Atkinson, Darren Gascooke, and Tony van Zuilekom (Halliburton) with whom I most closely collaborated in this research.

I would like to thank Dr. Michael Myrick, the opportunity of my life. I have thoroughly enjoyed working with you and the entire group. I remember talking over lunch years ago excitedly discussing the potential I believed this technology held for harsh environments, and then a later lunch were we decided to pursue the graduate research formally. It has not been without challenges, but what has been accomplished is absolutely amazing.

ABSTRACT

Multivariate optical computing (MOC) is a compressive sensing technique for which an analyte concentration is detected in an interfering mixture by direct detector output. The detector measures the dot product of a linear regression vector with a sample spectrum, as an analog optical computation. The computation is accomplished with the multivariate optical element (MOE), to which the optical regression vector is encoded as a transmission pattern. As a spectrum of light emanates from a sample and passes through the MOE, the dot product naturally occurs when light strikes the detector. The MOC platform allows a simple, robust, and direct measurement of chemical properties. This work extends the MOC platform to high temperature, high pressure harsh environments and is tested with petroleum fluids in-situ within subterranean petroleum wells.

This work describes a unique experimental apparatus and method necessary to gather petroleum fluid reference spectra for petroleum at reservoir conditions. The instrument is capable of measuring the optical spectrum (long-wave ultraviolet through short-wave mid-infrared) of fluids from ambient up to 138 MPa (20,000 psia) and 422 K (300°F) using ~5 mL of fluid. The instrument is validated with ethane.

This work further describes new design and fabrication techniques necessary to enable a harsh environment single-core MOE. The entirely new MOE fabrication technology uses a highly customized ion-assisted electron-beam (e-beam) deposition system, with new processes control techniques. For methane, an analyte with relatively

low interference, the MOC sensor validates within 1% relative accuracy of a laboratory Fourier transform infrared (FTIR) spectrometer using partial least squares (PLS) regression.

Lastly this work describes a new MOC dual-core configuration, which is able to better mimic complex regression vector behavior relative to a single-core, thus enabling better analysis for analytes more highly interfered by complex petroleum fluid background. The regression vector is encoded as the linear combination of two MOE transmission patterns. Design considerations, the design workflow and fabrication methodology are described. High temperature and pressure laboratory and field validation is presented for methane with the single-core MOC sensor and methane and carbon dioxide for the dual-core MOC sensor.

TABLE OF CONTENTS

LIST OF TABLES

LIST OF FIGURES

CHAPTER 1

INTRODUCTION

1.1 THE PETROLEUM INDUSTRY

The petroleum industry is estimated at 4.46 trillion United States dollars (USD) value as of August 2017, as the composite market cap of 1,618 publically traded companies tracked worldwide by the *Financial Times*.(1) This estimation does not consider private companies and national oil companies (NOCs) such as Saudi Aramco, and Kuwait Oil Company. The 2016 Oil and gas sector revenues, as tracked for the largest 45 publically traded petroleum companies of the *Fortune Global 500*, have a combined total revenue of 3.3 trillion USD, a number that excludes the NOCs and smaller independent producers with revenue less than 22 billion USD annually.(2) With the organization of the petroleum exporting countries (OPEC), accounting for a majority of the world's national oil company production, the OPEC market share of 40% (3) can be used to estimate revenue of 2.2 trillion USD for national oil companies bringing the global petroleum industry estimate 5.5 trillion USD revenue. The oil industry produced an average 95 million barrel production of oil per day in 2015, with transportation sector accounting 60% of the consumption and gas, industrial consumption and chemical production accounting for the balance (3). During the year 2016 gasoline traded for a global average of 1.4 USD based on the NasDaq commodity exchange (4) thereby accounting for about 1.2 trillion USD of annual revenue in 2016 for the oil and gas industry. Therefore the majority of revenue can be attributed to the gas, industrial and

chemical sector. Petroleum is in high demand with this demand expected to grow until 2040 as a moderate projection.(3) To meet this demand, approximately 2100 drilling rigs are in operation for the year 2017 vs 1600 drilling rigs from 2016.(5) Costs for deep water offshore wells can exceed 1 million USD/ Day with total well costs above 100 million USD/ Day.(6) Two thirds of the wells drilled use formation evaluation services which includes in-situ formation testing fluid analysis and sampling services. The same report shows the strongest need for technology improvement, as determined by 278 oilfield operator corporate responses, is improved sensor resolution with 25%, sensor innovation with 15%, and reliability improvement with 12% as the number one driver, with no remaining category receiving above %7.(7)

1.2 PETROLEUM FRACTIONS AND COMPOSITION

Petroleum is a geological fluid mixture that can contain of thousands of hydrocarbon and non-hydrocarbon components.(8-13) The fluid may either be in the liquid or gas state at reservoir conditions. Hydrocarbon components only contain the atoms of carbon and hydrogen, where as non-hydrocarbon components may be organics that contain other atoms known as heteroatoms, or inorganic components. The most common heteroatoms are nitrogen, sulfur, and oxygen, although phosphorus, and the transition metals nickel and vanadium, iron and copper, can be found to a lesser extent. (12,14-15) The carbon dioxide, nitrogen, hydrogen sulfide are the typical inorganic non-hydrocarbon gas components associated with petroleum.(10,12) Within the petroleum industry, the carbon number is the common nomenclature for groups of molecular components with the same number carbon atoms.(8,12) Molecular groups are designated as CN where N is the integer that designates the total number of carbons in the

molecule. Therefore C1, C2, and C3 are exactly methane, ethane, and propane, but C4 refers to normal butane, and isobutene, C5 refers to all isomers of molecules containing 5 carbon atoms and so on.

Petroleum is formed from the thermogenic cracking of buried detrital biomass, of primarily plankton sources.(10,16) The buried biomass first fuses under temperature and pressure, and then at higher temperatures ultimately cleaves by a first order decomposition reaction forming smaller organic components. The progressive cracking of organic matter into subsequently smaller compounds leads to a characteristic exponential decay (log linear) distribution as a function of carbon number.(8,10,14,17-23) Hydrocarbon components include the hydrocarbon gases methane, ethane, propane and the isomers of butane and pentane. Hydrocarbon gases are defined as components that are thermodynamically stable as a pure state in the gas phase at stock tank conditions, namely 60F (15.5C) and 14.7 psi (1.01 bar).(8-9) Methane is the primary hydrocarbon gas and at stock tank conditions is usually greater than 70% of the hydrocarbon gas phase volume, and frequently about 80% to 85%.(9,24-25) Non hydrocarbon gases commonly found in petroleum are primarily carbon dioxide, nitrogen, and hydrogen sulfide. Carbon dioxide varies greatly in abundance within petroleum gas and can typically account for trace concentration to 5% by volume of the produced fluid stock tank gas phase, but can be a majority of the gas phase reaching 10% to 90%.(9,26) Nitrogen, when present is usually found in concentration of less than 1% by volume at stock tank conditions. Hydrogen Sulfide, when present is usually found in concentration of less than 1% by volume of petroleum at stock tank conditions. Typically, the majority of petroleum gas is composed of methane and carbon dioxide.(8-9)

Components with 6 or more carbon atoms (C6+) are the liquid fraction.(8-9) The C6+ petroleum fraction is divided into four common sub fractions of hydrocarbons and non-hydrocarbons. The hydrocarbon fractions include the C6+ saturates fraction and C6+ aromatics fraction. The non-hydrocarbon fractions include the C6+ resins fraction and the C6+ asphaltenes fraction. The resins and aromatics fraction increase the solubility of asphaltenes in solution.(10,27-29) High concentrations of the saturates fraction, hydrocarbon gas, and especially carbon dioxide, destabilize the asphaltene fraction and favor asphaltene precipitation. A decrease in pressure also destabilizes the asphaltene fraction.(28-31) The non-hydrocarbon fractions are characterized by molecules that contain functional groups with atoms other than hydrogen and carbon and are known as heteroatoms. The non-hydrocarbon C6+ resins and C6+ asphaltenes fractions generally contain nitrogen, sulfur and oxygen which give the fractions an electrically polar charge.(10,32)

Petroleum is generally classified into five reservoir fluid types including black oils, volatile oils, gas condensates, wet gas, and dry gas. Gas vs oil is defined by phase behavior with respect to reservoir conditions, with oil as liquid being contained in a reservoir at a temperature lower than the critical point of the petroleum fluid, and gas being contained in a reservoir at a temperature higher than the critical point. The liquid oil will bubble a lower density gas from a denser liquid phase upon the reduction of pressure. Black oils have a gas to oil ratio (GOR) less than 1,700 scf/bbl and may further be divided into sub classifications of heavy oils, medium oils and light oils. The sub classifications of black oils are based on American Petroleum Institute (API) gravity, a quantity inversely proportional to the specific gravity (SG) of the C6+ fraction liquid

oil, as measured at the stock tank conditions of 14.7 psi and 60F. The API gravity is calculated from the specific gravity by Equation 1.1. For the black oils, the heavy oils are of API gravity less than 22.5, medium oils are between 22.5 and 30 API gravity, and light oils are greater than 30 and usually less than 40 API gravity. Volatile oils have a GOR greater than 1,700 scf/bbl, and typically less than 3500 scf/bbl with an API gravity typically between 30 and 45. Condensates are gas mixtures that precipitate dew with a reduction of pressure at reservoir temperature. Condensates are typically of GOR greater than 3,500 scf/bbl and between 35 and 50 API gravity. No phase segregation occurs for wet or dry gas as a reduction of pressure from reservoir pressure to stock tank pressure, however, a wet gas precipitates a dew upon temperature reduction to stock tank temperature, were as dry gas does not precipitate any liquid upon temperature or pressure reduction from reservoir conditions to stock tank conditions.(9)

$$API = \frac{141.5}{SG} - 131.5 \qquad 1.1$$

1.3 DRILLING

Petroleum wells are drilled with a specialized bit used to grind rock and sediment into chips called cuttings. The bit is located at the end of a specialized pipe called a drill string. Specialized sections of the drill string close to the bit known as drill collars can provide control steering control, drilling measurements, rock formation measurements, power, and telemetry. The grinding action can be provided either by rotation of the drill string, or direct hydraulic power to the bit supplied by a drilling fluid. The wells start with a vertical section of at least a few hundred feet, but may deviate to any angle including horizontal. Wells may be split into multiple branches known as sidetracks. Horizontal production branches are known as multi-laterals.(6) Petroleum wells have

been drilled to greater than 7700 meters vertical depth in up ultra-deep water of 3174 meters of water (33), although the deepest wells have been drilled to more than 12,200 depth (34). The thermal and pressure gradients of the wells can routinely provide hostel pressures and temperatures of 20,000 psi and 400 F respectively, although temperatures and pressures as high as 35,000 psi and 500 F respectively not uncommon.(35)

1.3.1 Drilling Fluid

The drilling fluid, sometimes called a mud, is a fluid containing a high concentration of solid clay particles. The drilling fluid circulates through the center of the drill string pipe, out the bit, and back to surface through the annular space between the drill string and the well. This drilling fluid, called a mud, has a liquid portion that may be aqueous, organic, or an emulsified mixture of aqueous and organic components. The drilling fluid serves multiple purposes. The drilling fluid provides an overbalance pressure to seal the formation and prevent formation fluid influx. The hydrostatic pressure provided by the mud also prevents the newly drilled and unprotected wellbore from collapsing. The drilling fluid lubricates the drill string, and the bit. The drilling fluid also cools the bit. As the drilling fluid circulates to the surface it carries the sediment and rock cuttings to the surface.(6,36) Also the drilling fluid is designed to mitigate the presence of hydrogen sulfide, and carbon dioxide for safety, and to mitigate corrosion.(37-38) The maximum extent to which a well section may be drilled is determined by the drilling fluid weight, although other factors may limit the well section extent. Specifically, the hydrostatic pressure at the top of the section must be high enough to prevent formation fluid influx, and hence blowouts, while remaining below the fracture pressure of the formation near the bottom of the drilled section, a scenario that

can also cause a blowout. The drilling mud places a hydrostatic pressure on the rock formation as it is drilled, and maintains that pressure until the section is cemented and cased.(6)

1.3.2 Invasion

Because the mud is weighted to provide a hydrostatic pressure on the formation as to keep the formation fluids from invading the wellbore, there is a net driving force for liquid filtrate to enter the formation. Clay particles which build on the surface of the well into a filter cake, compresses over time to form a low permeability barrier which prevents further loss of fluid into the formation.(39) Therefore, as a result of the drilling process a near wellbore invaded zone of drilling fluid filtrate if formed. Typically this zone extends from 8 to 32 inches.(40) The organic components of a drilling fluid can be petroleum distillation fractions such as diesel or mineral oil, or synthetic components such as olefins, esters, or ketones.(36,41-42) For oil (organic) based mud, OBM, the filtrate is highly miscible with petroleum formation fluid, and as such there is no laboratory technique to exclusively separate them without disturbing the inherent petroleum composition.(43)

The invasion process, as shown in Figure 1.2, has been commonly described as piston displacement.(39-40,44-48) Piston displacement is the common invasion model used for simulations, although other models if invasion have been proposed.(49-54) Figure 1.2 is an illustration showing a cylindrical section of a generic, fluid containing formation, centered on a wellbore. The mud filtrate invasion displaces the formation fluid, much like a plug, from the near wellbore region. As shown in Figure 1.2, three zones around the wellbore form: 1) The flushed zone of only drilling fluid filtrate; 2) The

transition zone comprising an composition intermediate to that of the filtrate and formation fluid; and 3) The uninvaded zone containing the native formation fluid. Together the flushed zone and transition zone comprise an invaded zone. All three zones are observed by formation probing sensors including resistivity sensors, nuclear sensors, acoustic sensors, and NMR sensors.(39)

1.3.3 Formation Evaluation

The hydrostatic mud column pressure is specifically designed to contain a formation fluid within the rock formation.(6,36) Therefore, evidence of petroleum within a zone is suppressed and not obvious without closer inspection of the formation. It is surprisingly easy to drill through a potential petroleum reservoir, and never determine its existence, only to discover the bypassed pay decades later upon re-evaluation of the formation log data.(55) In fact, the metadata results for the search of "bypassed pay" in the OnePetro petroleum industry database operated by the Society of Petroleum Engineers returned 1255 articles, suggesting that the occurrence of "bypassed pay" is painfully common.(56) To find a petroleum reservoir within a well, the well must be evaluated by sensors specifically for the presence, nature and quality of liquid or gas petroleum. Also, the formation is evaluated for rock properties indicative of reservoir quality. Methods of evaluation include wireline and or logging while drilling sensing, surface data logging, fluid and core sample evaluation, and well testing. The formation evaluation is conducted on the open hole prior to casing and cementing a well section.(6,57-58)

Surface data logging, attempts to measure the change in drilling fluid properties upon return to the surface from the drill bit, and is hence also called mudlogging. As the

cuttings are carried to the surface and depressurize, the formation fluid contained within the cuttings evolves into the drilling fluid as mud gas.(59-60) Mud gas is analyzed at the surface on the drilling rig platform, by gas chromatography and spectroscopic equipment. Mud gas analysis provides a qualitative gas distribution but not reservoir fluid concentration.(61) However, the gas distribution and isotopic content can indicate the presence and nature of formation fluids. Also, the evaluation of the rock cuttings can also provide some formation properties.(59-60) Unfortunately the exact location of a petroleum occurrence is not known with high resolution as the cuttings and fluid churn in transit to the surface.(6,62)

Wireline and Logging While Drilling (LWD) sensor evaluation can provide a more accurate location of formation and fluid properties along the wellbore.(6, 57-68) For a wireline evaluation, sensors are lowered into the well along a wireline cable that provides telemetry and power. The sensors probe the formation from a distance. The electrical wireline cable provides direct kilowatt range power with up to megabit speed telemetry for in-situ sensors.(6,58,63) LWD logging places the sensors in specialized drill pipe sections called collars, which are just behind the drill bit, as part of the bottom hole assembly (BHA).(6,58) Although wired pipe for LWD telemetry and power does exist, it is far more common for those sensors to be powered by battery or generated power from hydraulic drilling, with surface telemetry provided by mud pulses at about 20 bits per second.(6,64) The conventional wireline and LWD sensors look into the formation using electromagnetic technology, nuclear physics technology, acoustic technology, and magnetic resonance imaging technology. The conventional logging sensors provide some rock and rock and formation fluid information which is

unfortunately convoluted. To provide pure rock and fluid information, the formation fluid responses and rock responses must not only deconvoluted, but also the effects of the near wellbore drilling fluid filtrate invasion, and the wellbore drilling fluid influence subtracted from the logging responses.(58) None the less, in combination with surface data logging, the information provided by conventional wireline logging can identify zones of interest for well testing and sampling.(6,57,61)

Well testing is the only logging technology that provides conclusive evidence for the presence of petroleum deposits within a reservoir zone and the dynamic production potential of that petroleum.(6) Additionally, the formation fluid properties are provided in real time which is critical information for safely addressing issues encountered during well construction.(6,65-66) Well testing includes wireline and LWD formation testing, and drill stem well testing. In well testing, fluid is withdrawn from the formation and analyzed separate from the rock formation and well bore drilling fluid. Formation pressure and production rates are measured as a function of pressure.(6,58,65-66)

A drill stem test produces fluid to surface through specialized pipe or tubing. Drill stem testing places a temporary production apparatus in a well to produce large quantities of petroleum reservoir fluid to the surface. At a surface a gas separator removes the dissolved gas from the liquid oil in a controlled depressurization. The production rate of oil and gas from a reservoir section is monitored at surface.(6,8) The liquid oil and flashed gas are sampled separately and analyzed in a laboratory.(8) The test is usually conducted for days to weeks at considerable expense, but conclusively provides production potential of a reservoir section, reservoir extent, rock permeability, formation pressure and fluid samples clean of drilling fluid filtrate invasion.(6,67-68) The fluid,

however, is an average of the produced zone which can span multiple compartments and any compositional grading that often occurs within a reservoir section is not preserved.(10,30,65) Unfortunately, the fluid recovered at surface is depressurized and phase segregated, which can alter the fluid properties, especially with respect to asphaltene precipitation.(10,30,65,69) The cost is substantial and fluid disposal is of great concern; hence well testing is not always practical, especially in deep wells, highly gas charged systems and unconsolidated formations.(67,70-71)

In many cases, drill stem well testing has given way to formation testing which extends a rubber pad against the formation to make hydraulic contact, measure the formation pressure, and withdraw fluid using a mechanical pump. The fluid can be sampled under pressure and returned to surface using a pressure compensating chamber.(67-68,70) Rock cores can be cut either with a specialized drill bit on the drill string, or a wireline device which is often run with the formation testing equipment. The cores can be tested in a laboratory for mechanical rock properties, and fluids withdrawn and analyzed.(6,36)

1.3.4 Casing and Completions

Each section of a well is cased with a metal pipe to provide fluid isolation and cemented to provide reinforced well strength and bonding of the casing with the formation. A well section is usually immediately cased and cemented after formation evaluation both for safety reasons, and to meet the drilling schedule. Each subsequent section is drilled with a smaller bit, forming a smaller wellbore. The casing is lowered into the well and either hung into position as a liner, or from surface as a pipe casing. Cement is pumped through the casing and pushed into the annular space behind the

casing with a displacement fluid. The casing and cement are selected based on pressure, environmental and chemical considerations with corrosion and gas content of primary concern, and hence early fluid analysis is important. After the well has been drilled to the terminal depth, the well is either cemented and abandoned if purely an exploration well, or completed if a production well. A well may be temporarily decommissioned if to be completed and produced at a later date.(6)

To complete the well, explosive charges are lowered into position and discharged, in the presence of a completion fluid, to perforate the casing and cementing within an identified production zone. A completion string which may consist of packers and production tubulars can be lowered into the well to produce from multiple reservoirs which can be commingled and separate tubulars to zones which may not be commingled. Production may also take place directly through suitable casing if separate production strings are not necessary. The completion design is primarily dependent on the reservoir pressure as well as fluid compatibility. High quality fluid analysis is required to understand which zones may be commingled. The fluid analysis results regarding the corrosive nature of the production fluid is a primary concern in selecting completion designs. The top side facilities, which separate the gas from oil, must be designed for the proper gas to oil (GOR) as based on the fluid analysis. Additionally, the top side facilities must also be designed specifically for the chemical corrosiveness of the production fluid, including scrubbers to prepare the fluid for transport.(6)

1.4 FORMATION TESTING AND SAMPLING

Wireline or LWD formation testing provides petroleum asset evaluation and risk reduction information for field development. The analysis of open hole formation fluid

samples, acquired in the oil well at the reservoir, are a primary means to provide the fluid properties necessary to simulate production strategies, design completions, design large capital investment surface facilities, anticipate any flow assurance production issues and associated operational expenses, and ultimately make the financial decision as to whether an asset should be developed.(65-66,75) However, the utility of the samples acquired is only discovered after laboratory analysis. After a delay of transport, the laboratory analysis often takes weeks to months. Unfortunately, as formation testing is often the last activity prior to casing and cementing a zone, only one opportunity is available to acquire these open hole samples, and that opportunity is not afforded the benefit of a second chance to mitigate poorly acquired samples.(66,73-74)

Accurate compositional measurements of a reservoir petroleum fluid is necessary to ensure a well is safely drilled, to identify a new discovery, to evaluate the production potential and value of that discovery, to optimize the capital investment required to the produce petroleum, and to design a field management system for multiple reservoirs in a field.(66) There are three primary methods are used to obtain chemical information of a petroleum fluid contained in a reservoir, mud gas analysis, drill stem tests, and bottom hole sampling by formation testing. Mud gas analysis is qualitative, and drill stem tests are often unfeasible.(61,67,69,75) Bottom hole sampling acquires samples directly from a reservoir with a device lowered along the electrical wireline cable. The device has pumps designed to extract petroleum from a precise location along the wellbore and place that sample into a pressurized container which is then sent to a laboratory for analysis.(8,65-66) Typically on a single wireline sampling run, only 3 to 9, 1000 ml samples can be collected, although in special circumstances more samples or larger

samples can be collected.(76-77) Based on 10 case studies, 64 samples, with 16 wells and 117 pressure tests for 3 wells, an average formation tester sampling run takes 14.1 hours for an average 4 samples per well and average pressure test takes 0.36 hours for an average 39 pressure tests per well.(78-87) Therefore the average formation test pressure and sampling run, including trip and set time, takes 70.4 hours or almost 3 days. To acquire 3, 6, and 9 samples on a formation testing run it would take 56, 99 and 141 hours on average respectively by those statistics. LWD formation testing and sampling operationally has a similar duration to that of wireline formation testing with estimates of 4 to 7 days, however, LWD formation testers must stay in hole typically from 120 to 396 hours (5 to 16.5 days) for the entire drilling of a well section.(88) It is clear that formation testing fluid analysis sensors must operate days and survive weeks without service in harsh environment conditions.

The laboratory analysis of fluids can be performed in as little as 3 weeks but can also take months, and the transport and a lead time can be weeks to months before sample analysis can even begin.(73,89) Because samples can be taken at multiple locations along a single reservoir, the samples are more representative of the reservoir geometry than with mud gas analysis, or drill stem test samples.(60-61,65) If the samples are kept above reservoir pressure, the samples are not irreversibly altered. Usually, by the time a laboratory analysis is performed, the well section from which samples were acquired, has been shut in cased and cemented, and often, the drilling rig moved to another location. The laboratory analysis reveals the quality of the sample and hence their usefulness.(73-74) Unfortunately, as formation testing is often the last activity prior to casing and cementing a zone, only one opportunity is available to acquire samples, and that

opportunity is not afforded the benefit of a laboratory analysis to mitigate poorly acquired samples, or if those samples were not acquired from the best locations. Therefore some level of analysis is required in real time to assess the suitability and utility of samples prior to acquisition downhole. That fluid analysis may also be used to augment the laboratory data acquired from the samples at sparse locations.(90-91) For this reason, both physical and chemical fluid property sensors exist in formation testers. Fluid temperature and pressure, resistivity, capacitance, density, viscosity, bubble point, compressibility, index of refraction, speed of sound, and compositional sensors are routinely employed to monitor the properties of fluids during a formation pumpout.(66,72,76-77) A formation pumpout is the process of mechanically withdrawing large volumes of fluid from the formation with a formation tester in order to flush the near wellbore region clean from invasion of drilling fluid filtrate. Usually between 100 L and 600 L are withdrawn. Figure 1.3 shows a simulation of the fluid withdrawn from formation during a two endmember pumpout. Multi-endmember pumpouts are possible if the fluid is withdrawn from a transition zone containing oil and water, or if the filtrate invasion is an emulsion of oil and water. The two endmember pumpout considered here is specifically for petroleum based drilling fluid filtrate and miscible oil based drilling fluid filtrate invasion. The formation fluid grades monotonically asymptotically from high contamination at early time lower contamination at later time after an initial breakthrough of formation fluid.

Figure 1.4 shows a diagram of a formation tester, containing the Multivariate Optical Computing (MOC) sensor, the topic of this study. From top to bottom, the formation tester contains an electric power and telemetry section. This section converts

high voltage 60 Hz alternating current (880 V) to low voltage 60 Hz alternating current 220 V and 20 V direct current. The telemetry sub sends up to 1.2 Mbit/s, and receives 200 Kbit/s with ASDL protocol. The hydraulic power section converts electrical power to hydraulic power to be used throughout the formation tester for mechanical action. The dual probe section hydraulically sets up to two donut shaped pads against the formation like suction cups with 4,000 psi of pressure, balanced opposite by two hydraulic rams. The probe section also contains a Pressure Volume Temperature (PVT) test cylinder to monitor the bubble point and compressibility of the fluid withdrawn. The quartz gauge section accurately reads the pressure of the fluid to +/- 0.1 psi. The flushing pump section contains a hydraulically powered reciprocating pump with speeds operational between 2 ml/s and 40 ml/s. The pump withdraws fluid from the formation through the probe into through the tool sections and with exit to the wellbore through the last sample chamber section. The densitometer section accurately records the fluid density to +/- 0.01 g/cc, with a precision of 0.001 g/cc. This section also contains a capacitance sensor and resistivity sensor. The MOC sensor is an optical sensor capable of detecting methane and carbon dioxide as the subject of this work. The sample chamber holder switches the fluid from the wellbore exit path into any sample chamber. Up to 5 sample chamber sections may be stacked, although 1 to 3 are most common due to weight and length constraints. The spacer contains a series of retractable thermometers for measuring wellbore temperature, but also a shock absorber to minimize impact during descent. The ram is wider than the spacer, and spherical in shape with the intention of preventing sticking on an uneven wellbore surface during decent. The tool sections can be arranged in multiple ways with the power and telemetry section at the top, and the spacer

and ram section at the bottom. The hydraulic power section must be co-located with the probe section opposite of the flushing pump. The direction of pumping may either be up or down. The probe section starts the formation flow line and the sample chamber sections must terminate the formation flow line.

Three critical questions define the success of any open hole sampling program. Specifically: Where to sample?; When to sample?; and How to sample?(92-93) Samples must be gathered from the best locations along the wellbore such that fluid trends can be adequately defined. Reservoir fluids must be sampled at the optimal time during the formation fluid cleanup pumpout at a point for which the contamination is sufficiently low as to achieve the goals of sampling. Lastly, the samples must be acquired in such a way as to ensure they are representative aliquots of the formation fluid, and are maintained as such in transit from the down hole reservoir to the laboratory.(92)

1.4.1 Where to Sample?

Reservoir compartmentalization and fluid column compositional grading within a reservoir compartment are the two primary defining factors in assessment of sampling location.(66,72,90-91,94-99) However, it is the fluid analysis from the samples that will ultimately confirm compartmentalization and compositional grading.(73,94) Therefore, it is generally desirable to obtain at least one sample from every reservoir compartment, and up to three samples from reservoirs which exhibit sufficient compositional grading. (73,94,100) Conventional wireline log data and formation pressure test data can provide some compartment information, but little compositional grading information.(94,101) Fluid properties, including methane carbon dioxide and asphaltene concentration, provide the most direct assessment for both compartmentalization and compositional

grading.(66,73,90-91,94-99,101) Significant advancement has been made toward using downhole fluid analysis data for the purpose of determining sampling location and for augmenting laboratory sample analysis for final compartmentalization and compositional grading assessment. Compartmentalization and compositional grading assessment has been assigned geochemically, statistically, and by thermodynamic principals governed by cubic equations of state utilizing fluid composition as determined in laboratory studies and in situ on formation testers.(61,90,94,102-105)

1.4.2 When to Sample?

Samples need to be of sufficient quality to be representative of reservoir fluid properties. Those samples must be acquired with sufficiently low filtrate invasion contamination. In acquiring a bottom hole sample it is the goal to collect a sample with sufficiently low contamination in as short a time as is possible. Multiple sensors for down hole fluid sensors exist to assess contamination level, however, including methane concentration and GOR. It is desirable to acquire a sample as soon as it can be determined with certainty that the contamination is below a threshold required for the series of laboratory analysis.(25,72,106) Generally, 5% contamination is sufficiently low contamination for most medium and light oil analysis although 10% to 15% can be acceptable for some applications.(73,107-108) Volatile oils and condensates phase envelop is highly influenced by slight contamination and as such less than 3% to 1% contamination respectively is often desirable.(66,73,107)

Various schemes have been proposed for real time downhole contamination assessment including, trend fitting (72), endmember fingerprinting (94), and equation of state deconvolution (102). Fingerprinting methods have been difficult to apply generally

and ubiquitously. Equation of state methods have required more, high quality input than is generally available downhole. To date the most common comercial means of real time contamination assessment is asymptotic trend fitting as shown in Equation 1.2.(65,93,109) Trend fitting relies on two basic assumptions: 1) That as the instantaneous pumpout fluid, monotonically grades with volume pumped, from filtrate to formation fluid, a pure formation fluid is asymptotically approached, and 2) that the pumpout gradation follows a strict analytical form that may be sufficiently fit as to determine the asymptote endmembers.(53,109-110) Equation 1.2 shows an asymptotic equation derived by Hammond(109) for a hemispherical formation tester probe in a homogeneous isotropic reservoir rock with respect to permeability and porosity. Other equations have been derived for anisotropic media and other probe configurations.(111-112) For Equation 1.2 the values S_M, S_A, and S_S are the signals, at the monitor time, asymptote at infinite time and start time respectively. The volume, V, at start time is not zero, but rather the volume required to pump in order to clear the flushed zone and first observe filtrate at the formation testing sensor. The value of 2/3 was derived for a circular probe of negligible size compared to the wellbore radius, and γ is constant dependent on the formation and fluid properties such that the denominator of Equation 1.2 at the start time is unity. For trend fitting, a single sensor parameter, linear with contamination, such as density, methane concentration, asphaltene concentration is required.(113-114) Contamination is calculated as the percentage of the monitor signal value to asymptote value difference relative to the starting value asymptote difference shown in Equation 1.3 where C% is the contamination percent.(114) To apply an of the trend fitting, equation of

state, or statistical methods of contamination estimation, accurate, high resolution fluid measurements with respect to fluid contrast are required.(102,115-116)

$$S_M = S_A + \frac{S_S - S_A}{\gamma V^{\frac{2}{3}}} \quad 1.2$$

$$C\% = \frac{\lfloor S_M - S_A \rfloor}{\lceil S_S - S_A \rceil} \times 100 \quad 1.3$$

Often the starting value for the monitor signal is not observed and is extrapolated with some uncertainty. Therefore a third assumption is often imposed, that the starting monitor value for mud filtrate properties is known. Such is the case with methane and asphaltenes that are assumed to be zero concentration at pumpout start. Because mud filtrate depressurizes at the surface, any filtrate which permeates into the formation ideally contains no methane. Also any asphaltenes that do contaminate the drilling mud, usually flocculate and hence do not enter the formation but rather cling to the mud cake on the wellbore surface. Usually either methane or asphaltenes can provide a good contrast for asymptotic fitting. Petroleum samples with high methane have low asphaltene concentrations and samples with high asphaltene concentration have low methane concentration. Therefore methane and asphaltene concentrations are primary signals for trend fitting. Also, asphaltene gradient, and GOR gradients as a function of reservoir depth can constrain the ending asymptote for a pumpout, with methane and carbon dioxide accounting for a majority of the GOR gas.(25,53,72-73,75,106)

1.4.3 How to Sample?

For a sample to be useful in petroleum asset assessment, it must be representative of the reservoir fluid from which it was aliquoted.(73) Of concern are phase changes which can fractionate either heavier components from a bulk fluid, or gas components

from a bulk fluid.(8) Fluid chemical measurements can provide information about potential sample fractionation issues while sampling.(66,91,94-95,97) For gas condensates, it is very common to fractionate a liquid portion from a bulk gas. However, fractionation of light components relative to heavy components can naturally take due to differences in mobility, not unlike with the effect of chromatography.(10,25,117-118) Therefore to ensure a sample is not fractionated as withdrawn from the formation, methane can be a useful fluid component to monitor.(93) Also, the caustic and reactive nature of the near wellbore drilling fluid filtrate can fractionate acetic components of a petroleum sample.(37-38,73) Therefore acetic components of the petroleum fluid such as carbon dioxide may also be useful to monitor in order to ensure a representative fluid sample.

It is desirable that the sample be acquired with enough pressure as to ensure preservation of single phase with regards to a gas/ liquid phase envelop and asphaltene phase envelop.(30,119) Pressure, preservation of samples receives the greatest amount of attention with regards to fractionation issues. The asphaltene phase envelop is complicated with pressure effects, temperature effects, and compositional effects.(11) It has been shown, that once asphaltenes precipitate from solution, it is not always favorable for them to attain their reservoir state even when the sample is reintroduced to reservoir temperature and pressure.(27-28,31,119-120) Also if precipitation of asphaltenes occurs in the reservoir, an unrepresentative sample may be acquired devoid of those asphaltene species.(31,119) Therefore it is important to ensure the asphaltenes do not precipitate in the first place.(92,119,121)

1.5 Laboratory Analytical Techniques

After acquired, open hole samples are brought to surface, samples that are not acquired in Department of Transportation (DOT) certified sample containers are transferred into certified shipping sample cylinders. This process dictates a single phase transfer above reservoir temperature and pressure.(77,100,119,122-123) Although not prevalent, during the transfer, some sample may be aliquoted and analyzed at the well site.(73,123-125) Wellsite analysis is usually limited to a volumetric flash in which the sample is immediately lowered from reservoir temperature and pressure to stock tank temperature and pressure. The gas and liquid phases immediately separate and the volumes are measured. The ratio of gas to liquid is reported as the GOR. A subsample of the gas fraction is usually measured in a gas chromatograph with a thermal conductivity detector (GC-TCD) composition, and a liquid subsample is measured by gas chromatography with a flame ionization detector (GC-FID) for composition. Up to the C10 components, individual species may or may not be reported, but above C10 individual components are rarely reported. Carbon numbers are reported as a plus fraction of usually 10 to 30. A stock tank condition density is usually measured for the liquid fraction. The gas and liquid compositions are re-combined mathematically using the molecular weight estimated from the compositional analysis, density of the liquid fraction and the measured flashed volume, as the reservoir fluid composition.(8,12,73,123,125-128)

The DOT certified shipping sample cylinder is sent to a laboratory for analysis. It is standard for the DOT certified cylinder to contain a mixing ball to aid in sample restoration, by mixing, once it is received at the laboratory.(77) During transit if the

sample was in an airplane cargo hold, the sample may have been exposed to temperatures well below freezing. Otherwise the samples were at least exposed to the environmental temperatures during transit, which may also be below freezing. In some circumstances, the temperature of exposure may lower the pressure in the cylinder below the cylinder compensation system's ability to keep the sample above a multiphase envelope. The sample is therefore restored to reservoir conditions, over the course of 1 to 3 days, but sometimes up to 1 week. Standard restoration consists of heating the sample back to reservoir temperature, maintaining pressure at reservoir pressure, and mixing the sample cylinder by rocking it back and forth with the mixing ball providing agitation.(8,69,77,124) Once recombined, the flash and compositional measurements are made as described above. However, in the laboratory, is also standard laboratory practice to measure the molecular weight of the liquid fraction by freezing point depression as opposed to estimation by composition. Also it is standard practice to measure the density of the gas fraction in order to calculate the molecular weight of the gas fraction. The density of the liquid fraction is measured as before. Chemical analysis for geochemistry, oil fingerprinting and biomarker analysis such as two dimensional Gas Chromatography (GC X GC), gas chromatography with a mass spectrometry detector (GC-MS), Fourier transform ion cyclotron resonance mass spectrometry (FT-ICR MS), and Isotope Ratio Mass Spectrometry (IRMS).(10,12,129)

To determine the composition and physical properties of the pure reservoir fluid, acquired with formation testers, it is necessary to provide a good estimate of the concentration of drilling fluid filtrate, and back out that effect.(130-131) The drilling fluid filtrate is usually estimated using either the skimming method or the subtraction

method.(17,23) Both methods assume that the natural logarithm, of the mole fraction, of a true reservoir fluid composition, is linear with respect to carbon number. Because the drilling fluid distribution is usually Gaussian or Lorentzian and specific to a narrow carbon number range of approximately C12 to C22, any deviation above the log linear trend in this range is assumed to be due to drilling fluid filtrate. If a sample of the mud is available, the filtrate can be obtained by filtering in a high pressure filter device known as a mud press, or centrifuged. The composition of the filtrate may be measured by GC-FID and then the exact distribution subtracted from the reservoir fluid to obtain the best log linear fit across the filtrate carbon number range with respect to the remaining reservoir fluid distribution. If a mud sample is not available, then the distribution may be estimated by the skimming method. The skimming method assumes the distribution of components above the log linear trend is the same as the distribution for the drilling fluid filtrate. The distribution may further be constrained by either a Gaussian or Lorentzian distribution. The resultant estimation of the profile is normalized to 100% composition, and the subtraction method described above applied. The applicability of the method depends both on the accuracy of the mud filtrate distribution and on the applicability of the log linear assumption. The applicability of the log linear distribution may be poor for oils altered by multiple reservoir charges, water washing, secondary migration due to leaky reservoir seals, immature oils that have not fully reached a log linear distribution, or biodegradation. The accuracy of the method further depends on the accuracy of the analysis.(17,23,130-131)

The accuracy of the OBM filtrate contamination estimation methods have been the subject of multiple studies.(13,17-18,23,74,105) In round robin studies, it was

determined that for a standard fluid of known composition, with known filtrate added, laboratories were surprisingly inconsistent in providing contamination estimates. About for over 25 laboratory participants, 20% of the laboratories estimated the contamination reasonably well within 5% relative of the true value. An additional 20% estimated the contamination with a relative accuracy of between 5% and 15%. The remaining 60% of the laboratories estimated the contamination worse than 20% with the global average at 20% relative accuracy for contamination determination.(74) In general multiple laboratory studies have found determination of petroleum properties including contamination level to be accurate within 10% to 15%. (13,17,23,74,105) The laboratory may in some cases measure the contamination by means of standard addition when a sufficient drilling fluid filtrate quantity is obtained. The method is however more time consuming and therefore less frequently used. For standard addition, mud filtrate is spiked into the dead oil or live fluid sample. Physical properties of the mixture are monitored and subsequently extrapolated to that of the pure formation fluid with the contamination level calculated therein. If the contamination level is determined for the dead oil, then either equation of state, or mass balance is used to relate the contamination level to that of the live oil.(73,132-133)

It is common to measure the liquid fraction for saturates fraction concentration, aromatics fraction concentration, resins fraction concentration and asphaltenes fraction concentration by liquid chromatography and asphaltene precipitation, collectively known as a SARA analysis.(10,12,134) Bulk property live oil phase behavior testing is also usually conducted. The asphaltene phase envelop, wax phase envelop, and gas-liquid phase envelop are commonly measured. PVT production testing experiments may also

be conducted such as constant composition expansion, differential liberation and constant volume depletion may also be performed. These tests mimic an idealized production for the fluid and the behavior of that fluid over the lifetime of production.(8,13,17,73-74,89,105,123,125,127-128,135-136) The results are used to tune the equation of state models for reservoir production simulations and provide a more realistic estimation of recoverable fluids and production rates for production scenarios that are combinations of the idealized proxies. Each of the PVT production experiments may also measure composition of the segregated fluid in order to tune the simulators to the compositional trajectory of the reservoir fluid throughout the lifetime of production.(135,137-140) Throughout all PVT production experiments, the viscosity of the resultant liquid and gas phase are measured. Flow assurance testing, for fluid compatibility, corrosion, and scaling may also be conducted.(26,29,31,120,134,141-148) Enhanced oil recovery testing may also be conducted to monitor the fluid behavior with respect to carbon dioxide or methane gas floods, water floods or chemical floods.(31,149-156)

1.6 Forward

Petroleum wells are extreme environments with both high temperature and high pressure.(35) The petroleum industry requires ever more reliable and higher resolution sensors, with new analysis capabilities to meet the challenges of the large number of new wells being drilled.(5,7) Specifically methane and carbon dioxide are of interest because together they together compose a majority of the petroleum dissolved gas and provide critical information for drilling and exploration activities.(8-9) Accurate measurements these components can help ensure a well is safely drilled, to identify a new discovery, to evaluate the production potential and value of that discovery, to optimize the capital

investment required to the produce petroleum, and to design a field management system for multiple reservoirs in a field. Further, measurement of these components can help identify the best location along a wellbore from which to acquire reservoir fluid samples, identify how to acquire these samples and minimize the drilling fluid filtrate of these samples.(66)

It is the goal of this work to develop Multivariate Optical Computing (MOC) technology for the purpose of harsh environment in-situ sensing of formation fluid in petroleum wells during formation testing activities. MOC sensors have been shown to provide comparable results to that of conventional laboratory based spectroscopic analysis using multivariate regression. The following chapters discuss the advancements necessary to develop new MOC sensor capability and the subsequent validations of these sensors including in-situ petroleum well field trials. Chapter 2 describes new experimental equipment and methods necessary to acquire the reference optical data required at harsh environment conditions. Chapter 3 describes new high temperature design and fabrication technology, validated with a methane MOC sensor using laboratory data and field data. Chapter 4 describes a new dual core configuration for MOC sensing that improves accuracy and sensitivity compared to previous configurations for methane. Chapter 4 also extends harsh environment optical sensing in petroleum wells to the mid infrared for the first time, thereby enabling carbon dioxide detection. The methane and carbon dioxide MOC sensors are validated with both laboratory and field data.

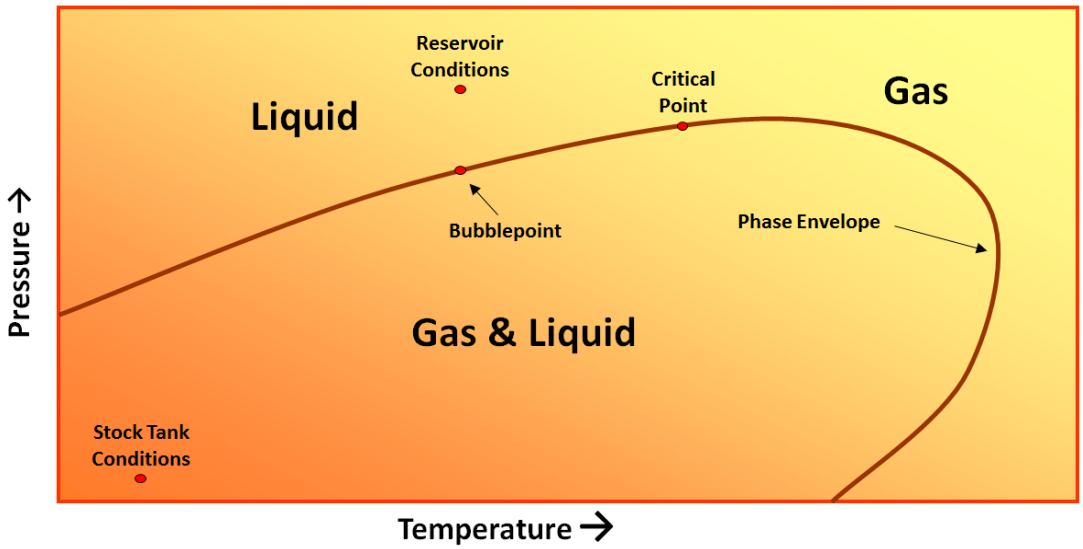

Figure 1.1 Shown is an illustration of a generic petroleum fluid phase diagram. The phase envelop is the typical shape of petroleum fluids. The phase envelope separates the single phase fluid region of liquid or gas outside the envelope from the two fluid phase region of liquid and gas inside the envelope. The critical point which lies along the phase envelope separates gas at higher temperature from liquid at lower temperature. The bubble point is defined as the point at which as less dense gas first bubbles from the liquid oil at reservoir temperature.(9)

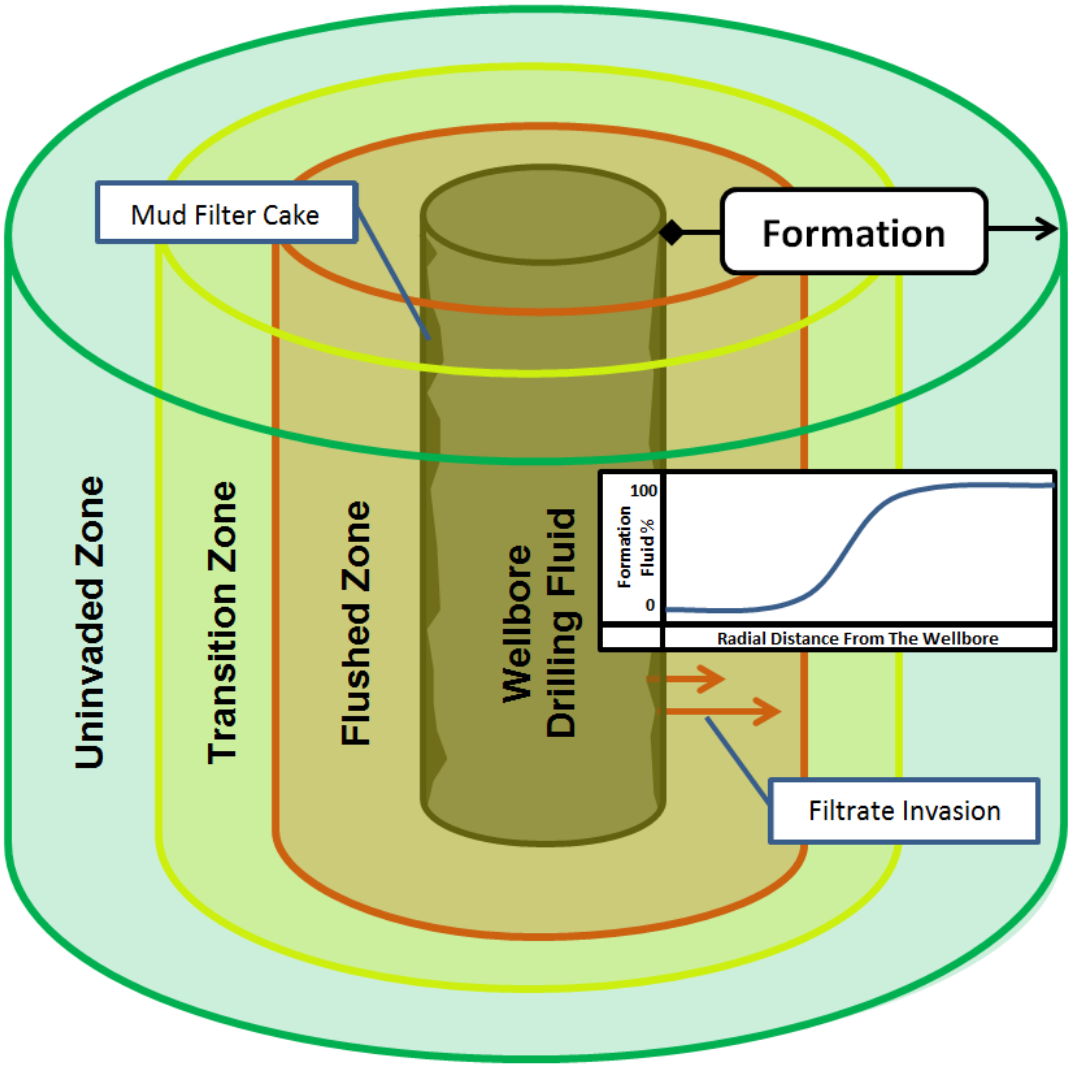

Figure 1.2 Shown is an illustration of a cylindrical section of a fluid saturated formation centered on a wellbore containing drilling fluid filtrate. Filtrate invasion is driven into the formation, displacing the formation fluid in a near wellbore region. The invasion rate is proportional over burden pressure, and inversely proportional to the thickness of the mud filter cake. Filtrate invasion profiles have been modeled by finite element simulation.(50-53) The transition shown by the imbedded graph is a generic illustration of the typical formation fluid profile throughout the three zones which have been described. The imbedded graph is aligned with the radial zones in the illustration grading from 0% formation fluid in the near wellbore region to 100% formation fluid in distal to the wellbore in the uninvaded zone.

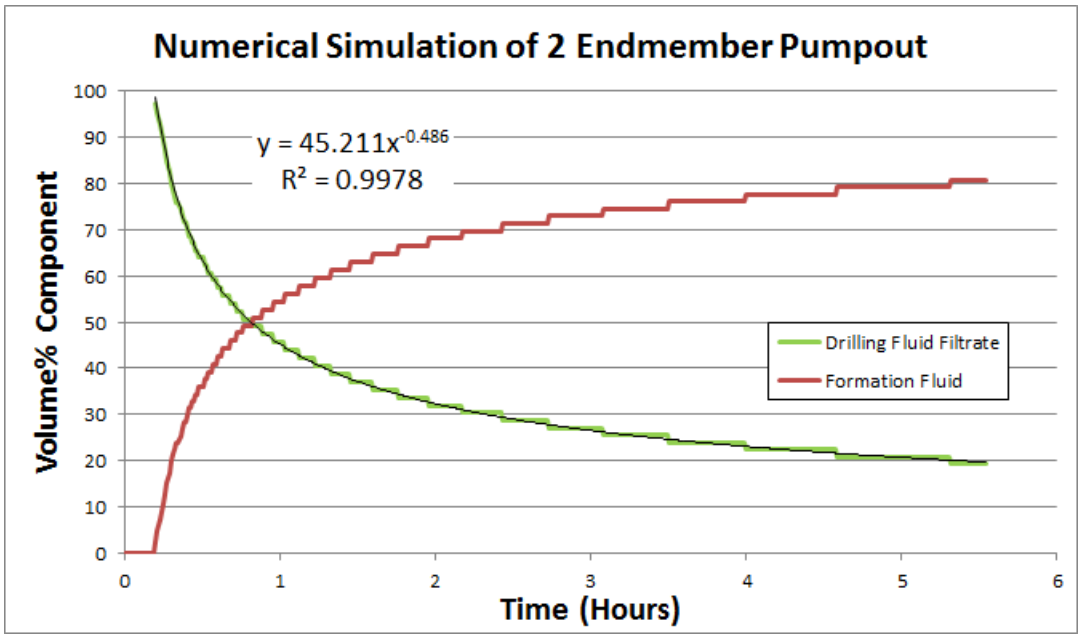

Figure 1.3 A numerical simulation of a formation pumpout assuming a 16 inch radial invasion depth of filtrate with an additional 16 inch radial linear graded convectively mixed transition zone with a formation fluid, homogeneous and isotropic permeability and 0.25 porosity, rate limited by a pumping speed of 40cc/min with a Lamar flow velocity profile.

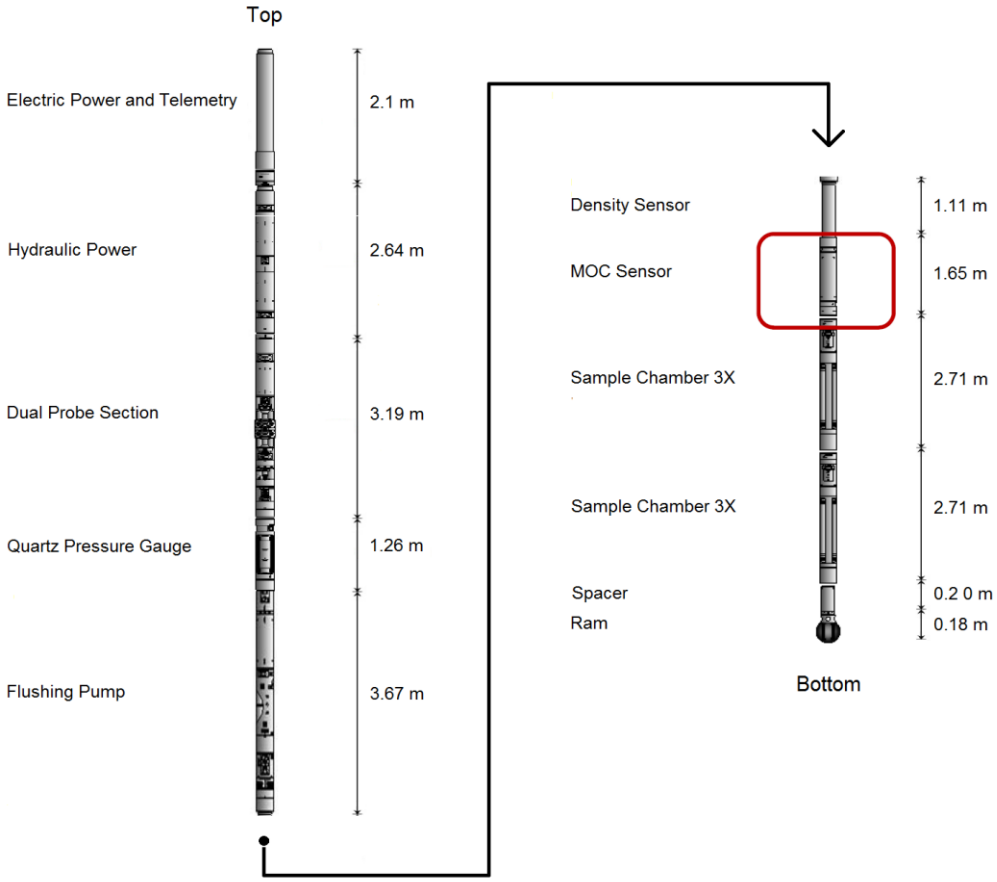

Figure 1.4 A diagram of a formation tester, containing the Multivariate Optical Computing (MOC) sensor, the topic of this study. From top to bottom, the formation tester contains an electric power and telemetry section, supplying power to the formation tester and telemetry to and from the surface. The hydraulic power section converts electrical power to hydraulic power to be used throughout the formation tester for mechanical action. The dual probe section uses up to two pads to make a hydraulic seal with the formation and contains a hydraulically powered Pressure Volume Temperature (PVT) test cylinder. The quartz gauge section the pressure of the fluid to +/- 0.1 psi. The flushing pump section contains a hydraulically powered reciprocating pump with speeds operational between 2 ml/s and 40 ml/s. The densitometer section accurately records the fluid density to +/- 0.01 g/cc 95% confidence, with a resolution of 0.001 g/cc. This section also contains a capacitance sensor and resistivity sensor. The MOC sensor is an optical sensor capable of detecting methane and carbon dioxide as the subject of this work. The sample chamber holder switches the fluid from the wellbore exit path into any sample chamber. The spacer contains a series of retractable thermometers for measuring wellbore temperature, but also a shock absorber to minimize impact during descent. The ram is wider than the spacer, and spherical in shape with the intention of preventing sticking on an uneven wellbore surface during decent.

REFERENCES

1. Thomson Reuters. Oil & Gas, 2017. Financial Times: Sectors and Industries. HYPERLINK "https://markets.ft.com/data/sectors/Oil-and-Gas" https://markets.ft.com/data/sectors/Oil-and-Gas (accessed August 29th, 2017).

2. Elam, D.; Altschuler, R.; Lyons, C.; Smyth, K.; Dan, Z.; Varghese, S.; Mosaic, L. S. Fortune Global 500 , 2017. Fortune. HYPERLINK "http://fortune.com/global500" http://fortune.com/global500 (accessed August 29, 2017).

3. Conti, J.; Holtberg, P.; Diefenderfer, J.; LaRose, A.; Turnure, J. T.; Westfall, L. *International Energy Outlook 2016 With Projections to 2040;* United States Government; United States Department of Energy: Washington D. C., 2016.

4. CME Group. Latest Price & Chart for Gasoline. HYPERLINK "http://www.nasdaq.com/markets/gas.aspx?timeframe=2y" http://www.nasdaq.com/markets/gas.aspx?timeframe=2y (accessed August 30th, 2017).

5. Baker Hughes. Rig Count Overview & Summary Count. HYPERLINK "http://phx.corporate-ir.net/phoenix.zhtml?c=79687&p=irol-rigcountsoverview" http://phx.corporate-ir.net/phoenix.zhtml?c=79687&p=irol-rigcountsoverview (accessed August 30, 2017).

6. Devereux, S. *Drilling Technology in Nontechnical Language, 2nd Edition,* 2nd ed.; PennWell: Tulsa, Oklahoma, 2012.

7. Kimberlite. *Formation Evaluation Supplier Performance & Competitive Positioning Report;* Kimberlite International Oilfield Research: Spring, TX , 2016.

8. Pedersen, K. . a. P. L. C. P. *Phase Behavior of Petroleum Reservoir Fluids;* CRC: Boca Raton, 2007.

9. Dandekar, A. Y. *Petroleum Reservoir Rock and Fluid Properties;* Taylor & Francis Group, CRC Press : Boca Raton, 2006.

10. Hunt, J. *Petroleum Geochemistry and Geology, 2nd Ed.;* W. H. Freeman and Company: New York, 1996.

11. McCain Jr., W. D. *The Properties of Petroleum Fluids, 2nd Ed.;* Pennwell Books: Tulsa OK, 1990.

12. Rodgers, R. P.; McKenna, A. M. Petroleum Analysis. *Analytical Chemistry* **2011,** *83* (12), 4665–4687.

13. Morris, C. W.; Sonnier, B. Evaluation of Reservoir Fluids Using Formation Tester Tool Samples. *International Arctic Technology Conference*, Anchorage, Alaska, 1991.

14. Tissot, B. P.; Welte, D. H. *Petroleum Formation and Occurrence;* Springer-Verl: Berlin, 1984.

15. Boduszynski, M. M. Composition of heavy petroleums. 1. Molecular weight, hydrogen deficiency, and heteroatom concentration as a function of atmospheric equivalent boiling point up to 1400.degree.F (760.degree.C). *Energy and Fuels* **1987,** *1* (1), 2–11.

16. Peters, K. E. . M. J. M. *The biomarker guide: Interpreting molecular fossils in petroleum and ancient sediments;* Prentice Hall: Englewood Cliffs, NJ, 1993.

17. Gozalpour, F.; Danesh, A.; Tehrani, D.-H.; Todd, A. C.; Tohidi, B. Predicting Reservoir Fluid Phase and Volumetric Behaviour from Samples Contaminated with Oil-Based Mud. *SPE Reservoir Evaluation & Engineering* **2002,** *5* (3), 197 - 205.

18. Austad, T.; Isom, T. P. Compositional and PVT properties of reservoir fluids contaminated by drilling fluid filtrate. *Journal of Petroleum Science and Engineering* **2001,** *30* (3), 213-244.

19. Braun, R. L.; Burnham, A. K. A new method for kinetic analysis of source rocks:Analysis of chemical reaction kinetics using a distribution of activation energies and simpler models. *Energy and Fuels* **1987,** *1* (2), 296-298.

20. Ungerer, P.; Pelet, R. Extrapolation of the kinetics of oil and gas formation from laboratory experiments to sedimentary basins. *Nature* **1987,** *327,* 52 - 54.

21. Behar, F.; Vandenbroucke, M.; Tang, Y.; Marquis, F.; Espitalie, J. Thermal cracking of kerogen in open and closed systems: determination of kinetic parameters and stoichiometric coefficients for oil and gas generation. *Organic Geochemistry* **1997,** *26* (5), 321-339.

22. Paso, K. G.; Fogler, H. S. Influence of n-Paraffin Composition on the Aging of Wax-Oil Gel Deposits. *AIChE Journal* **2003,** *49* (12), 3241-3252.

23. Zuo, J. Y.; Gisolf, A.; Pfeiffer, T.; Achourov, V.; Chen, L.; Mullins, O. C.; Edmundson, S.; Partouche, A. Advances in Quantification of Miscible Contamination in Hydrocarbon and Water Samples From Downhole to Surface Laboratories. *SPWLA 58th Annual Logging Symposium*, Oklahoma City, Oklahoma, 2017; pp SPWLA-2017-EE.

24. Mullins, O. C.; Daigle, T.; Crowell, C.; Groenzin, H.; Joshi, N. B. Gas-Oil Ratio of Live Crude Oils Determined by Near-Infrared Spectroscopy. *Applied Spectroscopy*

2001, *55* (2), 197-201.

25. Mullins, O. . B. G. . C. M. . T. T. a. K. K. DOWNHOLE DETERMINATION OF GOR ON SINGLE-PHASE FLUIDS BY OPTICAL SPECTROSCOPY. *SPWLA 42 "d Annual Logging Symposium,* Houston, 2001.

26. Sun, R.; Li, C.; Yu, S.; Wang, S.; Sun, O.; Liu, E. Hydrate Formation Conditions of Natural Gas with High Content of Carbon Dioxide and the Calculation Model. *International Oil and Gas Conference and Exhibition in China*, Beijing, China , 2010; pp SPE-131812-MS.

27. Aske, N.; Kallevik, H.; Johnsen, E. E.; Johan, S. Asphaltene Aggregation from Crude Oils and Model Systems Studied by High-Pressure NIR Spectroscopy. *Energy and Fuels* **2002,** *16* (5), 1287-1295.

28. Peramanu, S.; Singh, C.; Agrawala, M.; Yarranton, H. W. Investigation on the Reversibility of Asphaltene Precipitation. *Fuel and Energy* **2001,** *15* (4), 910-917.

29. Wiehe, I. A. Asphaltene Solubility and Fluid Compatibility. *Energy and Fuels* **2012,** *26* (27), 4004−4016.

30. Gonzalez, D.; Francisco, V.; Hirasaki, G.; Chapman, W. Modeling Study of CO2-Induced Asphaltene Precipitation. *Energy and Fuels* **2008,** *22* (2), 757-762.

31. Sarma, K. H. Can We Ignore Asphaltene in a Gas Injection Project for LIght-Oils? *SPE International Improved Oil Recovery Conference in Asia Pacific*, Kuala Lumpur, Malaysia, 2003; pp SPE-84877-MS.

32. Mitra-Kirtley, S.; Mullins, O.; van Elp, J.; George, S.; Chen, J.; Cramer, S. Determination of the Nitrogen Chemical Structures in Petroleum Asphaltenes Using XANES Spectroscopy. *Journal of the American Chemical Society* **1993,** *115* (1), 252-258.

33. Indunker, J.; ChandraSekhar, S.; Dotiwala, F.; Singh, J.; Shedde, P. Reaching India's Deepest Target Depth in World Deepest Water Depth Environment - A Success Story. *International Petroleum Technology Conference*, Doha, Qatar, 2015.

34. James, R. W.; Pastusek, P. E.; Kuhn, G. R.; Andreev, A.; Bailey, J. R.; Wang, L. Successful Optimization Strategies Combine to Deliver Significant Performance Boost at the Edge of the ERD Envelope, Sakhalin Island, Russia. *IADC/SPE Drilling Conference and Exhibition*, San Diego, California, 2012; pp SPE-150959-MS.

35. Belani, A.; Orr, S. A Systematic Approach to Hostile Environments. *Journal of Petroleum Technology* **2008,** *60* (7), 34 - 39.

36. Burke, C. J.; Veil, J. A. SYNTHETIC-BASED DRILLING FLUIDS HAVE MANY ENVIRONMENTAL PLUSES. *Oil and Gas Journal* **1995,** *93* (48), 59-64.

37. Harrison, J. R.; Stansbury, M.; Patel, J.; Cross, A. T.; Kilburn, M. Novel Lime-Free Drilling Fluid System Applied Successfully in Gulf of Thailand. *SPE/IADC Drilling Conference*, Amsterdam, NE, 1999; pp SPE-52817-MS.

38. Garcia, J. M.; Lordo, S. A. CHEMISTRY AND IMPACTS OF Chemistry And Impacts Of Commonly Used Amine-Based H2S Scavengers On Crude Unit Towers And Overheads. *NACE International Conference and Expo: Corrosion*, Nashville, Tennessee, 2007; pp NACE-07571.

39. Allen, D.; Auzerais, F.; Dussan, E.; Goode, P.; Ramakrishnan, T. S.; Schwartz, L.; Wilkinson, D.; Fordham, E.; Hammond, P.; Williams, R. Invasion Revisited. *Oilfield Review* **1991,** *3* (3), 10-23.

40. Phelps, G. D. Computation of Mud Filtrate Invasion Profiles. *The Journal of Canadian Petroleum Technology* **1995,** *34* (1).

41. Bloys, B.; Davis, N.; Smolen, B.; Bailey, L.; Houwen, O.; Reid, P.; Sherwood, J.; Fraser, L.; Hodder, M.; Montrouge, F. Designing and managing drilling fluid. *Oilfield Review* **1994,** *6* (2), 33-43.

42. Growcock, F. B.; Patel, A. D. The Revolution in Non-Aqueous Drilling Fluids. *AADE National Tecnical Conference and Exhibition*, Houston, TX, 2011; pp 1-8.

43. Hadibeik, H.; Kwabi, E.; Torres-Verdin, C.; Sepehrnoori, K. Miscibility Effects of Oil-Base Mud and In-Situ Gas on Conventional Well Logs. *SPWLA 54th Annual Logging Symposium*, New Orleans, Louisiana, 2013; pp SPWLA-2013-EEEE.

44. Donaldson, E. C.; Chernoglazov, V. Characterization of drilling mud fluid invasion. *Journal of Petroleum Science and Engineering* **1987,** *1* (1), 3-13.

45. Lane, S. H. Numerical Simulation of Mud Filtrate Invasion and Dissipation. *SPWLA 34th Annual Logging Symposium*, Calgary, Alberta, 1993; pp SPWLA-1993-D.

46. Civan, F. A Multi-Phase Mud Filtrate Invasion and Wellbore Filter Cake. *SPE International Petroleum Conference & Exhibition*, Veracruz, Mexico, 1994; pp SPE-28709-MS.

47. Riazi, R. M. A new method for experimental measurement of diffusion coefficients in reservoir fluids. *Journal of Petroleum Science and Engineering* **1996,** *14* (3), 235-250.

48. Malik, M. . B. D. B. . E. H. . T.-V. C. Numerical Investigation of Oil - Base-Mud Contamination in Condensates: From Cleanup to Sample Quality. *SPE Annual Technical Conference and Exhibition*, New Orleans, Louisiana, 2009; p SPE

124371.

49. Peeters, M.; Allen, D.; Gomes, R.; Kristiansen, J. I. Invasion In Space And Time. *SPWLA 40th Annual Logging Symposium*, Oslo, Norway, 1999; pp SPWLA-1999-A.

50. Wu, J.; Torres-Verdin, C.; Sepehrnoori, K.; Delshad, M. Numerical Simulation of Mud Filtrate Invasion in Deviated Wells. *Annual Technical Conference and Exhibition*, New Orleans, Louisiana, 2001; pp SPE-71739-MS.

51. Wu, J. . T.-V. C. . S. K. . P. M. A. The Influence of Water-Base Mud Properties and Petrophysical Parameters on Mudcake Growth, Filtrate Invasion, and Formation Pressure. *Petrophysics* **2005,** *46* (1), 14-32.

52. Malik, M.; Torres-Verdín, C.; Sepehrnoori, K. Axially symmetric compositional simulation of formation tester measurements. *Journal of Petroleum Science and Engineering* **2007,** *59* (3), 333–349.

53. Angeles, R.; Torres-Verdin, C.; Malik, M. PREDICTION OF FORMATION-TESTER FLUID-SAMPLE QUALITY IN HIGHLY-DEVIATED WELLS. *SPWLA 49th Annual Logging Symposium*, Austin, Texas, 2008; pp SPWLA-2008-SS.

54. Malik, M. . T.-V. C. . S. K. . J. R. . W. P. . M. O. C. . E. H. . D. B. . H. M. Comparison of Wireline Formation-Tester Sampling with Focused and Conventional Probes in the Presence of Oil-Base Mud-Filtrate Invasion. *Petrophysics* **2009,** *50* (5).

55. Howard, A. The Challenge of Locating Maximum Bypassed Pay. *Journal of Petroleum Technology* **2006,** *58* (9), 38 - 40.

56. Society of Petroleum Engineers. Search results: Your search for bypassed pay has returned 1,255 results. HYPERLINK "https://www.onepetro.org/search?q=bypassed+pay" https://www.onepetro.org/search?q=bypassed+pay (accessed September 15th, 2007).

57. Timur, A. Open Hole Well Logging. *International Petroleum Exhibition and Technical Symposium*, Beijing, China, 1982; pp 639-374.

58. Ellis, D. V.; Singer, J. M. *Well logging for Earth Scientists, 2nd Ed.;* Springer: Dordrecht, 2008.

59. Aarrestad, T. V.; Tapper, R. Use Of Mud Logging Data In Drilling Performance Analysis. *Offshore Europe*, Aberdeen, United Kingdom, 1989; pp SPE-19243-MS.

60. Jurcic, H.; Maretic, S.; Cogelja, Z. Petrophysical Parameters Evaluation in Unconventional Reservoirs by Well Logging and Mud Logging Data Interactive

Correlation Method. *SPE/EAGE European Unconventional Resources Conference and Exhibition*, Vienna, Austria, 2012; pp SPE-150961-MS.

61. Kyi, K. K.; Lynn, C. S.; Haddad, S.; Chouya, S.; Wa, W. W.; Gligorijevic, A. Integration of Downhole Fluid Analysis and Advanced Mud Gas Logging Reduces Uncertainty in Reservoir Evaluation. *International Petroleum Technology Conference*, Doha, Qatar, 2014; pp IPTC-17485-MS.

62. Kyllingstad, A.; Horpestad, J. L.; Klakegg, S.; Kristiansen, A.; Aadnoy, B. S. Factors Limiting the Quantitative Use of Mud-Logging Data. *SPE Asia Pacific Oil and Gas Conference*, Singapore, 1993; pp SPE-25319-MS.

63. Liyanage, M.; Tulett, J.; Endo, T.; Saito, A.; Yamamoto, H.; Imai, R. Evolution of Wireline Telemetry and Its Impact on Formation Evaluation. *22nd Formation Evaluation Symposium of Japan*, Chiba, Japan, 2016; pp SPWLA-JFES-2016-A.

64. Bybee, K. High-Speed Wired-Drillstring Telemetry. *Journal of Petroleum Technology* **2008,** *60* (12), 76 - 78, 12.

65. Hashem, M.; McHardy, A.; Wynne, M.; Pool, W.; Viets, T.; Keuser, C.; Eriksen, K. O. Formation Pressure While Drilling, Wireline Formation Testing, And Fluid Sampling In a High Pressure/High Temperature Exploration Well Using Oil Based Mud: A Case History 1. *Petrophysics* **2007,** *48* (4), 258-270.

66. Elshahawi, H.; Hashem, M. N.; McKinney, D.; Ardila, M.; Ayan, C. The Power of Real-Time Monitoring and Interpretation in Wireline Formation Testing–Case Studies. *SPE Reservoir Evaluation and Engineering* **2007,** *10* (3), 241–250.

67. Ramaswami, S. R.; Elshahawi, H.; El-Battawy, A. Integration of Wireline Formation Testing and Well Testing Evaluation--An Example From the Caspian. *SPE Reservoir Evaluation and Engineering* **2012,** *15* (3), 300 - 313.

68. Coelho, D. A. C.; de Camargo, C.; Kato, E. T.; Legrand, V. M. Utilizing Mini-DST for Formation Evaluation. *SPE Latin American and Caribbean Petroleum Engineering*, Rio de Janeiro, Brazil, 2005; pp SPE-94963-MS.

69. Michaels, J.; Moody, M.; Shwe, T. Wireline Fluid Sampling. *SPE Annual Technical Conference and Exhibition*, Dallas, Texas , 1995; pp SPE-30610-MS.

70. Uwaga, A.; Bardal, D.; Ward, C.; Trim, M. Mini-DST in a Gas Reservoir: Issues, Challenges and Benefits. *SPE Nigeria Annual International Conference and Exhibition*, Lagos, Nigeria , 2014; pp SPE-172421-MS.

71. Whittle, T. M.; Lee, J.; Gringarten, A. C. Will Wireline Formation Tests Replace Well Tests? *SPE Annual Technical Conference and Exhibition*, Denver, Colorado, 2003; pp SPE-84086-MS.

72. Dong, C.; O'Keefe, M.; Elshahawi, H.; Hashem, M.; Williams, S.; Stensland, D.; Hegeman, P.; Vasques, R.; Terabayashi, T.; Mullins, O.; Donzier, E. New downhole-fluid-analysis tool for improved reservoir characterization. *SPE Reservoir Evaluation and Engineering* **2008,** *11* (6), 1107-1116.

73. Hy-Billiot, J.; Bickert, J.; Montel, F.; Segalini, G. Getting the Best From Formation Tester Sampling. *SPE Annual Technical Conference and Exhibition*, San Antonio, TX, 2002; pp SPE-77771-MS.

74. Stephen, A. G.; Bergman, D. F.; Dodd, T.; Kriel, W. PVT Data Quality: Round Robin Results. *SPE Annual Technical Conference and Exhibition*, Denver, Colorado, 2008; pp SPE-116162-MS.

75. American Petroleum Institute. *API Recommended Practice 44: Sampling Petroleum Reservoir Fluids, second edition;* Orginization; American Petroleum Institute: Washington, DC, 2003.

76. Badry, R.; Head, E.; Morris, C.; Traboulay, I. New Wireline Formation Tester Techniques And Applications. *SPWLA 34th Annual Logging Symposium*, Calgary, Alberta, 1993; pp SPWLA-1993-ZZ.

77. Proett, M. A.; Gilbert, G. N.; Chin, W. C.; Monroe Jr, M. L. New Wireline Formation Testing Tool With Advanced Sampling Technology. *SPE Reservoir Evaluation and Engineering* **2001,** *4* (2), 76 - 87.

78. Schlumberger. *Test, Sample and Analyze in Extremely Harsh H2S and CO2 Environments; Case study: Schlumberger tests hazardous sour gas well for ADNOC and ConocoPhillips;* Corporate; Schlumberger: Houston, TX, 2011.

79. Halliburton. *Halliburton helped clients obtain clean samples in deepwater Gulf of Mexico; A Case Study: Fluid sampling from unconsolidated formations;* Corporate; Halliburton: Houston, TX, 2012.

80. Schlumberger. *Eni Australia Achieves Reservoir Fluid Sampling and Analysis Objectives in 347-degF Well:Case Study: SCAR sampling enables collection of contaminat-free, single-phase reservoir fluids with 7.5 days of downhole exposure time and 100% success rate;* Corporate; Schlumberger: Houston, TX, 2014.

81. Schlumberger. *Successful Permeability Measurement and Fluid Sampling in 0.1mD/cP Mobility, Deepwater Angola; Case Study: Saturn 3D radial probe performs IPTTs and collects fluid from a tight sand where conventional probes are ineffective;* Corporate; Schlumberger: Houston, TX, 2014.

82. Schlumberger. *Quicksilver Probe Focused Extraction increases Fluid Sample Purity by >60%; Case Study: Novel Probe design slashes fluid aquisition time and contamination levels in the Gulf of Mexico;* Corporate; Schlumberger: Houston, TX,

2014.

83. Schlumberger. *High-Quality Pressure Data, Sample Collection, and Formation Testing in Wide Permeability Range; Case Study: Saturn 3D radial probe collects low-contamination samples in OBM and Conducts good pressure transient and vertical inteference tests, Norwegian Se;* Corporate; Schlumberger: Houston, TX, 2014.

84. Schlumberger. *Saturn 9-in Probe Samples Near-Saturation Hydrocarbon in an Unconsolidated Laminated GOM Reservoir; Case Study: Ultralow contamination single-phase samples aquired in one-fifth the time compared with conventional single-probe sampling;* Corporate; Schlumberger: Houston, TX, 2015.

85. Halliburton. *Two large-scale deepwater projects successfully launched using Halliburton's advanced technology and top service delivery; Case Study: Halliburton saves time and money in deepwater southeast Asia;* Corporate; Halliburton: Houston, TX, 2015.

86. Baker Hughes. *FTeX Service Aquired Pressure Data in Widely variable Formation Permeability, Saved 20 Hours Rig Time;* Corporate; Baker Hughes: Houston, TX, 2016.

87. Baker Hughes. *FTex Service Successfully Mapped the Pressure Profile in Chalk;* Corporate; Baker Hughes: Houston, TX, 2016.

88. Djefel, M.; Tigre Maia, C. R. S.; Proett, M. A.; Eyuboglu, A. S.; Naupari, C. E.; Beck, G. Potential Economic Value-Added Model Using Formation Sampling-While-Drilling in Development Fields. *SPE Latin American and Caribbean Petroleum Engineering* , Lima, Peru, 2010; pp SPE-138956-MS.

89. Freyss, H.; Guieze, P.; Varotsis, N.; Khakoo, A.; Lestelle, K.; Simper, D. PVT Analysis for Oil Reservoirs. *The Technical Review* **1989,** *37* (1), 4-15.

90. Elshahawi, H.; Venkataramanan, L.; McKinney, D.; Flannery, M.; Mullins, O. C.; Hashem, M. Combining Continuous Fluid Typing Wireline Formaion Testers, and Geochemical Measurments for an Improved Understanding of Reservoir Architecture. *SPE Reservoir Evaluation and Engineering* **2008,** *11* (1), 27 - 40.

91. Venkataramanan, L.; Elshahawi, H.; McKinney, D.; Flannery, M.; Hashem, M.; Mullins, O. C. Downhole Fluid Analysis and Fluid Comparison Algorithm as an Aid to Reservoir Characterization. *SPE Asia Pacific Oil & Gas Conference and Exhibition*, Adelaide, Australia, 2006; pp SPE-100937-MS.

92. Ahmed, K.; Hassan, F.; Taqi, F.; Ahmad, F.; Pearl, M.; Jones, C.; Vasquez, R.; Zuilekom, A. v.; Pelletier, M. Real-Time Downhole Fluid Analysis and Sampling with a New Optical Composition Analysis Sensor: A Case Study from Kuwait Heavy Oil Formation. *SPE International Heavy Oil Conference and Exhibition*,

Mangaf, Kuwait, 2016; pp SPE-184112-MS.

93. Dai, B.; Jones, C. M.; Van Zuilekom, T. A New Multisensor Approach to Downhole Sample Filtrate Measurement With a Wireline Formation Tester. *SPWLA 58th Annual Logging Symposium*, Oklahoma City, Oklahoma, 2017; pp SPWLA-2017-HHHH.

94. Venkataramanan, L.; Weinheber, P.; Mullins, O. C.; Andrews, A. B.; Gustavson, G. Pressure Gradients and Fluid Analysis as an Aid to Determining Reservoir Compartmentalization. Society of Petrophysicists and Well-Log Analysts. *SPWLA 47th Annual Logging Symposium*, Veracruz, Mexico, 2006; pp SPWLA-2006-S.

95. Dong, C.; Elshahawi, H.; Mullins, O. C.; Venkatramanan, L.; Hows, M. P.; McKinney, D. E.; Flannery, M.; Hashem, M. N. Improved Interpretation of Reservoir Architecture and Fluid Contacts through the Integration of Downhole Fluid Analysis with Geochemical and Mud Gas Analyses. *Asia Pacific Oil and Gas Conference and Exhibition*, Jakarta, Indonesia, 2007; pp SPE-109683-MS.

96. Mullins, O. C.; Zuo, J. Y.; Freed, D. E.; Mishra, V. K.; Gisolf, A.; Elshahawi, H.; Cribbs, M. E. Downhole Fluid Analysis Coupled With Novel Asphaltene Science For Reservoir Evaluation. *SPWLA 51st Annual Logging Symposium*, 2010; pp SPWLA-2010-32770.

97. Zuo, J. Y.; Zhang, D.; Dubost, F. X.; Dong, C.; Mullins, O.; O' Keefe, M.; Betancourt, S. Equation-of-State-Based Downhole Fluid Characterization. *SPE Journal* **2016,** *16* (1), 115 - 124.

98. Zuo, J. Y.; Mullins, O. C.; Elshahawi, H.; Ramaswami, S.; Dong, C.; Dumont, H.; Zhang, D.; Ruiz-Morales, Y. Advanced Reservoir Evaluation Using Downhole Fluid Analysis and Asphaltene Flory-Huggins-Zuo EoS. *North Africa Technical Conference and Exhibition*, Cairo, Egypt , 2013; pp SPE-164596-MS.

99. Mullins, O. C.; Zuo, J. Y.; Wang, K.; Hammond, P. S.; De Santo, I.; Dumont, H.; Mishra, V. K.; Chen, L.; Pomerantz, A. E.; Dong, C.; Elshahawi, H.; Seifert, D. J. The Dynamics of Reservoir Fluids and their Substantial Systematic Variations. *Petrophysics* **2014,** *55* (2), 96-112.

100. American Petroleum Institute. *Sampling Petroleum Reservoir Fluids, second edition;* API: Washington, DC, 2003.

101. Smalley, P. C.; Hale, N. A. Early Identification of Reservoir Compartmentalization by Combining a Range of Conventional and Novel Data Types. *SPE Formation Evaluation 11* (3), 163 - 170.

102. Zuo, J. Y. . Z. D. . D. F. X. . D. C. . M. O. . K. M. . &. B. S. EOS Based Downhole Fluid Characterization. *SPE Annual Technical Conference and Exhibition*, Denver,

Colorado, 2008; pp SPE-114702-MS.

103. Andrews, A. B.; Schneider, M. H.; Canas, J.; Freitas, E.; Song, Y.; Mullins, O. C. Fluorescence Methods for Downhole Fluid Analysis of Heavy Oil Emulsions. *Journal of Dispersion Science and Technology* **2008,** *29* (2), 171-183.

104. Jones, C. . D. B. . C. D. . H. T. . P. M. . &. G. D. Measurement and use of Formation Fluid, Saturate, and Aromatic Content, With Wireline Formation Testers. *SPWLA 56th Annual Logging Symposium*, Long Beach, California, 2015.

105. Jones, C. M.; van Zuilekom, T.; Iskander, F. How Accurate Is Enhanced Optical Fluid Analysis Compared to Lab PVT Measurements? *SPWLA 57th Annual Logging Symposium*, Reykjavik, Iceland , 2016; pp SPWLA-2016-JJJ.

106. Jones, C.; Gao, L.; Perkins, D.; Chen, D.; Gascook, D. Field Test of the Integrated Computational Elements: A New Optical Sensor for Downhole Fluid Analysis. *SPWLA 54th Annual Logging Symposium*, New Orleans, Louisiana, 2013; pp SPWLA-2013-YY.

107. Dong, C.; Hegeman, P. S.; Carnegie, A. J. G.; Elshahawi, H. Downhole Measurement of Methane Content and GOR in Formation Fluid Samples. *SPE Reservoir Evaluation and Engineering* **2006,** *9* (1), 7 - 14.

108. Wilmot, S. C. Techniques To Improve The Quality Of Wireline Oil Samples In Wells Drilled With Oil Base Mud. *SPWLA 41st Annual Logging Symposium*, Dallas, Texas, 2000; pp SPWLA-2000-T.

109. Hammond, P. S. One- and two-phase flow during fluid sampling by a wireline tool. *Transport in Porous Media* **1991,** *6* (3), 299-330.

110. Mullins, O. C.; Schroer, J. Real-Time Determination of Filtrate Contamination During Openhole Wireline Sampling by Optical Spectroscopy. *SPE Annual Technical Conference and Exhibition*, Dallas, Texas, 2000; pp SPE-63071-MS.

111. Eyuboglu, S.; Gao, L.; Pelletier, M.; van Zuilekom, T.; Proett, M. A New Real-Time Contamination Method That Combines Multiple Sensor Technologies. *SPWLA 52nd Annual Logging Symposium*, Colorado Springs, Colorado, 2011; pp SPWLA-2011-GGG.

112. Pineda, W.; Gozalpour, F.; Hagshenas, M. Effective Method for Monitoring Oil Based Mud Contamination in Wireline Formation Testers Sampling. *SPE Annual Technical Conference and Exhibition*, Houston, Texas, 2015; pp SPE-175116-MS.

113. Felling, M. M.; Morris, C. W. Characterization of In-Situ Fluid Responses by Use of Optical Fluid Analysis. *SPE Reservoir Evaluation and Engineering* **1998,** *1* (4), 297-302.

114. Akkurt, R.; Proett, M. CONTAMINATION ESTIMATION USING FLUID ANALYSIS MODELS. WO2005065277, July 21, 2005.

115. Zuo, J. Y.; Gisolf, A.; Dumont, H.; Dubost, F.; Pfeiffer, T.; Wang, K.; Mishra, V. K.; Chen, L.; Mullins, C.; Gemelli, S. A Breakthrough in Accurate Downhole Fluid Sample Contamination Prediction in Real Time. *Petrophysics* **2015,** *56* (3), 251 - 265.

116. Alpak, F. O.; Elshahawi, H.; Hashem, M. N.; Mullins, O. C. Compositional Modeling of Oil-Based-Mud-Filtrate Cleanup During Wireline Formation Tester Sampling. *SPE Reservoir Evaluation & Engineering* **2008,** *11* (2), 219 - 232.

117. Larter, S. R.; Aplin, A. C.; Corbett, P. W. M.; Ementon, N.; Chen, M.; Taylor, P. N. Reservoir Geochemistry: A Link Between Reservoir Geology and Engineering? *SPE Reservoir Engineering* **1997,** *12* (1), 12 - 17.

118. Jones, C.; Dai, B.; Chen, D.; He, T.; Pelletier, M.; Gascooke, D. Measurement and use of Formation Fluid, Saturate, and Aromatic Content, With Wireline Formation Testers. *SPWLA 56th Annual Symposium*, Long Beach, 2015; pp SPWLA-2015-EE.

119. Jamaluddin, A. K. M.; Ross, B.; Calder, D.; J. Brown, D.; Hashem, M. Single-Phase Bottomhole Sampling Technology. *Journal of Canadian Petroleum Technology* **2002,** *41* (7), 25-30.

120. Kallevik, H.; Kvalheim, O. M.; Sjoblom, J. Quantitative Determination of Asphaltenes and Resins in Solution by Means of Near-Infrared Spectroscopy. Correlations to Emulsion Stability. *Journal of Colloid and Interface Science* **2000,** *255* (5), 494–504.

121. Michaels, J.; Moody, M.; Shwe, T. Advances In Wireline Formation Testing. *SPWLA 36th Annual Logging Symposium*, Houston, Texas, 1995; pp SPWLA-1995-BBB.

122. Pop, J. J.; Villareal, S.; Bernard, F.; Baxter, M.; Hakam, A.; Firth, A.; Megat, A.; Fey, S.; Haq, S.; Vahi, N. Sampling While Drilling: An Emerging Technology. *SPE Reservoir Evaluation and Engineering* **2014,** *17* (2), 128 - 140.

123. Khan, I. A.; McAndrews, K.; Jose, J.; Jamaluddin, A. K. M.; Chetri, H. Reservoir Fluid Analysis Using PVT Express. *Abu Dhabi International Petroleum Exhibition and Conference*, Abu Dhabi, UAE, 2006; pp SPE-101219-MS.

124. Williams; M., J. Getting the Best Out of Fluid Samples. *Journal of Petroleum Technology* **1994,** *46* (9), 752 - 752.

125. Ceyhan, A. G.; Cronin, B. Early Determination Of Pvt Data And Integration With Formation Testing Information To Reduce The Petrophysical Uncertainties In West Africa: Part-2. *SPWLA 46th Annual Logging Symposium*, Orleans, Louisiana , 2005;

pp SPWLA-2005-N.

126. Varotsis, N.; Guleze, P. On-Site Reservoir Fluid Properties Evaluation. *Journal of Petroleum Technology* **1990,** *42* (8), 1,046 - 1,052.

127. Sun, C.-Y.; Liu, H.; Yan, K.-L.; Ma, Q.-L. L. C.-J.; Xiao, X.-J.; Wang, H.-Y.; Zheng, X.-T.; Li, S. Experiments and Modeling of Volumetric Properties and Phase Behavior for Condensate Gas under Ultra-High-Pressure Conditions. *Industrial Engineering and Chemistry Research* **2012,** *50* (19), 6916–6925.

128. Samaniego-V., F.; Bashbush, B. J. L.; Leon, G. A.; Mazariegos, U. C.; Corona, B. A.; Castillo, P. P. F. On the Validation of PVT Compositional Laboratory Experiments. *SPE Annual Technical Conference and Exhibition*, Houston, Texas; pp SPE-91505-MS.

129. Riazi, M. R. *Characterization and Properties of Petroleum Fractions 1st ed;* American Society for Testing and Materials International: West Conshohocken, PA, 2005.

130. MacMillan, D. J.; Ginley, G. M.; Dembicki Jr., H. How to Obtain Reservoir Fluid Properties from an Oil Sample Contaminated with Synthetic Drilling Mud. *SPE Annual Technical Conference and Exhibition*, San Antonio, Texas, 1997; pp SPE-38852-MS.

131. Sah, P.; Gurdial, G.; Pedersen, K.; Izwan Deraman, H.; Ramli, F. Equation-of-State Modeling for Reservoir-Fluid Samples Contaminated By Oil-Based Drilling Mud Using Contaminated-Fluid Pressure/Volume/Temperature Data. *SPE Reservoir Evaluation and Engineering* **2012,** *15* (2), 139 - 149.

132. Thomas, F. B.; Shtepani, E.; Adams, M. E.; Bennion, D. B. Deconvolution of Drilling Fluid-Contaminated Oil Samples. *Journal of Canadian Petroleum Technology* **2005,** *44* (6), 28-35.

133. Sharaf, M. A.; Ilman, D. L.; Kowalski, B. R. *Chemometrics;* Wiley: New York, 1986; Vol. 82.

134. Tharanivasan, A. K.; Svrcek, W. Y.; Yarranton, H. W.; Taylor, S. D.; Merino-Garcia, D.; Rahimi, P. M. Measurement and Modeling of Asphaltene Precipitation from Crude Oil Blends. *Energy and Fuels* **2009,** *23* (8), 3971–3980.

135. Gaganis, V.; Varotsis, N.; Nighswander, J.; Birkett, G. P. Monitoring PVT Properties Derivatives Ensures Physically Sound Tuned EOS Behaviour Over The Entire Operating Conditions Range. *SPE Europec/EAGE Annual Conference*, Madrid, Spain , 2005; pp SPE-94211-MS.

136. Jacoby, R.; Yarborough, L. PVT Measurements on Petroleum Reservoir Fluids and

Their Uses. *Industrial and Engineering Chemistry* **1967,** *59* (10), 48–62.

137. Collins, D. A.; Nghiem, L. X.; Li, Y.-K.; Grabonstotter, J. E. An Efficient Approach to Adaptive- Implicit Compositional Simulation With an Equation of State. *SPE Reservoir Engineering* **1992,** *7* (2), 259 - 264.

138. Peng, W.; Pope, G. A. Proper Use of Equations of State for Compositional Reservoir Simulation. *Journal of Petroleum Technology* **2001,** *53* (7), 74-81.

139. Webb, S. J.; Revus, D.; Myhre, A. M.; Goodwin, N. H.; Dunlop, N.; Heritage, J. Rapid Model Updating with Right-Time Data - Ensuring Models Remain Evergreen for Improved Reservoir Management. *Intelligent Energy Conference and Exhibition*, Amsterdam, The Netherlands, 2008; pp SPE-112246-MS.

140. Wei, Y.; Chen, Z. J.; Satyro, M.; Dong, C. C.; Deng, H. Compositional Simulation Using an Advanced Peng-Robinson Equation of State. *SPE Reservoir Simulation Symposium*, The Woodlands, Texas, 2011; pp SPE-141898-MS.

141. Abouie, ; Korrani, K. N.; Shirdel, ; Sepehrnoori, K. Comprehensive Modeling of Scale Deposition by Use of a Coupled Geochemical and Compositional Wellbore Simulator. Society of Petroleum Engineers. *SPE Journal* **2017,** *22* (4).

142. Tjomsland, T.; Grotle, N. M.; Vikane, O. Scale Control Strategy and Economical Consequences of Scale at Veslefrikk. *International Symposium on Oilfield Scale*, Aberdeen, United Kingdom, 2001; pp SPE-68308-MS.

143. Tjomsland, T.; Sæten, J. O.; Olav, V.; Michael, Z. Veslefrikk Scale Control Strategy and Economic Implications: Revisited 7 years later - did we improve? *SPE International Oilfield Scale Conference*, 2008; pp SPE-114086-MS.

144. NACE International. *Corrosion of Oil-and Gas-Well Equipment;* American Petroleum Institute: Dallas, TX, USA, 1958.

145. Bonis, M. R.; Crolet, J. L. Why So Low Free Acetic Acid Thresholds, in Sweet Corrosion at Low PCO2? *Corrosion*, Houston, 2005; pp NACE-05272.

146. Perez, T. E. Corrosion in the Oil and Gas Industry: An Increasing Challenge for Materials. *The Journal of The Minerals, Metals and Materials Society* **2013,** *65* (8).

147. Popoola, L. T.; Grema, S. A.; Latinwo, G. ; Gutti, B.; Balogun, S. A. Corrosion problems during oil and gas production and its mitigation. *International Journal of Industrial Chemistry* **2013,** *4* (35).

148. Zerpa, L. E.; Salager, J.-L.; Koh, C. A.; Sloan, E. D.; Sum, A. K. Surface Chemistry and Gas Hydrates in Flow Assurance. *Industrial and Engineering Chemistry Research* **2011,** *50* (1), 188–197.

149. Kaminsky, R. D.; Wattenbarger, R. C.; Szafranski, R. C.; Coutee, A. Guidelines for Polymer Flooding Evaluation and Development. *International Petroleum Technology Conference*, Dubai, U.A.E., 2007; pp IPTC-11200-MS.

150. Ravagnani , A. T. F. S.; Ligero, S. B.; Suslick, S. B. CO2 sequestration through enhanced oil recovery in a mature oil field. *Journal of Petroleum Science and Engineering* **2009,** *65* (3), 129-138.

151. Shaw, J.; Bachu, S. Screening, Evaluation, and Ranking of Oil Reservoirs Suitable for CO2-Flood EOR and Carbon Dioxide Sequestration. *Journal of Canadian Petroleum Technology* **2002,** *41* (9), 51-61.

152. Taber, J. J.; Martin, F. D.; Seright, R. S. EOR Screening Criteria Revisited - Part 1: Introduction to Screening Criteria and Enhanced Recovery Field Projects. *SPE Reservoir Engineering* **1997,** *12* (3), 189 - 198.

153. Thomas, S. Enhanced Oil Recovery – An Overview. *Oil & Gas Science and Technology* **2008,** *63* (1), 9-19.

154. Flaaten, A.; Nguyen, Q. P.; Pope, G. A.; Zhang, J. A Systematic Laboratory Approach to Low-Cost, High-Performance Chemical Flooding. *SPE Symposium on Improved Oil Recovery*, Tulsa, Oklahoma, 2008; pp SPE-113469-MS.

155. Ali, S. M. F.; Thomas, S. The Promise And Problems of Enhanced Oil Recovery Methods. *Journal of Canadian Petroleum Technology* **1997,** *35* (7), 57-63.

156. Gutierrez, D.; Skoreyko, F.; Moore, R. G.; Mehta, S. A.; Ursenbach, M. G. The Challenge of Predicting Field Performance of Air Injection Projects Based on Laboratory and Numerical Modelling. *Journal of Canadian Petroleum Technology* **2009,** *48* (4), 23 - 33.

CHAPTER 2

A SMALL-VOLUME PVTX SYSTEM FOR SPECTROSCOPIC CALIBRATION OF DOWNHOLE OPTICAL SENSORS

2.1 INTRODUCTION

The chemical and physical properties of fluids in a petroleum reservoir are highly variable and directly affect their commercial value.(1-8) Traditionally, fluid samples are recovered and analyzed in a laboratory. However, the time, expense, and tendency of samples to change after sampling by means of phase separation, precipitation, loss of volatiles, etc. make it desirable to determine at least some of the fluid properties *in situ* through instruments located directly in the reservoir formation.(9,10) Some important reservoir fluid properties are physical in nature— temperature, pressure, density, viscosity, radiation, resistivity, etc., for which *in situ* sensors already exist.(10-12) Other important properties, such as component concentrations, require measurement of fluid chemical properties. Data providing chemical composition are vital for determining the nature of a reservoir, govern the techniques needed to recover its contents, and help establish whether it can be economically produced. *In situ* instruments for some aspects of downhole chemical analysis currently exist.(13-17)

Vibrational spectroscopy offers a possible approach to the *in situ* measurement of many chemical properties of fluids.(8,9,18-21 and references therein) Near-infrared (NIR) and mid-infrared (MIR) absorption and Raman spectroscopy have all been used

successfully to determine fluid compositions in industrial, agricultural and medical applications, and a number of companies exist that exploit these vibrational spectroscopy tools for chemical analysis.(22-36) Colorimetry and ultraviolet- (UV-) visible electronic spectroscopy have also been shown to enable the study of molecules with conjugated π electronic systems, such as asphaltenes, dissolved in a fluid.(37-44)

For many years, the environmental challenges of downhole measurements delayed the introduction of these spectroscopic methods for the analysis of reservoir fluids, but the introduction of miniaturized spectroscopy tools and novel methods in the past two decades enable the design and construction of instruments suited to these harsh environments. Indeed, at least one commercial vibrational spectroscopy-based instrument now exists for limited *in situ* measurement of reservoir fluids, along with other instruments measuring fluorescence and color.(14,15,44)

In most cases, the important chemical constituents are not sufficiently unique in their structure and bonding to give rise to unique vibrational absorption or Raman bands, and there are few examples of isolated spectral features that can be unambiguously assigned to a single constituent. Fluorescence and UV-visible spectra are likewise constrained by broad features and spectral overlap. In such cases, multivariate calibration approaches for separating the spectral contributions of important species, such as alkanes, from interfering species are required.(45-50) Although these mathematical methods are powerful, multivariate approaches to measurement (such as partial least squares, PLS) require the user to model a data set created from calibration samples that span the range of the compositional and physical variations expected in actual downhole formation fluids. Such calibrations can perform poorly for many reasons, some of which lead to

obvious low quality of the calibration during modeling. More troublesome are flaws in the calibration arising from a poorly chosen calibration set that can be undetected throughout modeling and only be revealed during use. Covariance of the analyte with another fluid component, for instance, can lead to deceptively good models that pass criteria for calibration and validation but perform poorly if field samples do not show the same covariance. Similarly, failure to study samples under an appropriate range of temperature and pressure conditions would limit the usefulness of any sensors based on those calibration data.(50-52)

The most practical path to creating an adequate data set for exploring the variability of actual reservoir fluids begins with available samples of "dead" fluids (crude oils). Dead (crude) oils are samples of crude oil from most of the volatiles have escaped. Volatiles are components that have sufficient vapor pressure to significantly liberate from the crude oil liquid at stock tank conditions, 60F and 14.7 psi, such as carbon dioxide, methane, ethane, propane, butane, and pentane. This is in contrast to native live fluids (crude oils) which are obtained directly from the reservoir at temperature and pressure, and maintained at pressures above the bubble point, the pressure at which volatiles begin to escape from the liquid for a given temperature. These native live oil samples are very rare compared to the abundance of dead oil samples, but dead oil samples usually are available only in small volumes ie less than 50ml. The dead oils may be reconstituted as live oil by injecting with volatiles to varying degrees or by mixing live oils with other dead oil samples. The mixture is then spectroscopically explored through a range of pressure, density, and temperature (P-ρ-T) conditions. A number of such dead fluids would need to be studied in this way to span the range of reservoir fluid types. However,

collections of reservoir fluids spanning the necessary range of types are rare and valuable commodities because each sample has been obtained at significant cost in time, effort, and capital. If such collections exist in a laboratory, they are precious resources and only a limited amount of each sample is available. Thus, any instrument capable of creating samples that could form an adequate spectral database needs to work with small quantities of the base oils.

Conventional instrumentation capable of controlling and independently varying the pressure, volume, temperature, and composition of reservoir fluids and their simulants already exists, with the resultant data enabling equation of state (EOS) modeling.(53-67) This instrumentation has the ability to inject gas or liquid components and dynamically mix the resultant composition by circulation both to achieve homogenization of a single phase, or multiphase constitutions. While these larger volume petroleum PVTX can be adapted for spectral analysis, the sample volume necessary (typically 50 mL or more) makes their use impractical for creating a full spectral database, due to the low availability of samples. A previous system reported for spectral analysis as a function of (P-ρ-T) used a single fluid composition for live oils, with no dynamic mixing; no information on the system volume was given.(48, 49) Very small volume spectroscopic cells are common for high pressure, high temperature work.(68-71) These cells could be used for the analysis of live oil fluids at single composition conditions, but the availability of live oils is low. High pressure laboratory spectroscopic systems are not usually designed for independent pressure, volume, temperature and compositional (liquid and gas injection) controlled variation, and also most do not have active circulation and shear mixing for rapid petroleum reconstitution. It is the subject of this

work that integrates two small volume spectroscopic cells, to a new small volume PVTX system to overcome these existing limitations.

This report presents a small-volume pressure-volume-temperature-composition (miniature PVTX) system designed specifically for building a high-quality, variation-rich, broad-spectrum database sufficient for developing models for spectroscopic measurements of chemical constituents in downhole fluids. This system differs from traditional PVTX instruments by using an additive approach (i.e., adding constituents to a base) to creating specific sample compositions rather than subtractive approaches (e.g., allowing volatiles to off-gas). To conserve valuable starting materials, the mass required to charge the system is ≤ 5.5 grams of base oil under the highest density conditions. The system operates between ambient temperature and 450 K (350°F), and over pressures ranging from 1 to 138 MPa (150 to 20,000 psia). Phase data, density, and optical spectra from 400 nm (25 000 cm^{-1}) to 5000 nm (2000 cm^{-1}) for oil samples or from 200 nm (50 000 cm^{-1}) to 5000 nm (2000 cm^{-1}) for gas and condensate samples, are collected continuously on a dynamically-mixed sample. Oil samples contain resin and asphaltene components, not present in gas or condensate samples, which react in the presence of ultraviolet light, and therefore the ultraviolet lamp is turned off during oil experiments.

The construction, operation, and minimum accuracy of the chemical compositions of the system are discussed, and the accuracy and stability of density determinations are also presented. Finally, the spectroscopy of a pure fluid, ethane, is shown after normalizing to the pressure, temperature-dependent optical pathlength, and the measured density to illustrate that even pure fluids exhibit changes to their optical spectra in response to excursions of temperature and pressure, which affects multivariate

calibrations unless spectral data are measured under realistic conditions. Strengths and assignments of weak ethane transitions are provided based on data acquired using this instrument.

2.2 EXPERIMENTAL

In association with the experimental operation of the apparatus, as will be discussed in subsequent sections, EOS modeling is used, and requires some brief introduction. The EOS form used for oil and other liquid data is the Peng-Robinson cubic EOS by Equation 2.1. (72)

$$P = \left(\frac{RT}{V_m - b_{PR}}\right) - \left(\frac{a_{PR}(T)}{V_m(V_m + b_{PR}) + b_{PR}(V_m - b_{PR})}\right); \quad 2.1a$$

$$a_{PR}(T) = 0.45724\left(\frac{R^2T_C^2}{P_C}\right)\left(1 + k\left(1 - \sqrt{\frac{T}{T_C}}\right)\right)^2; \quad 2.1b$$

$$k_{PR} = 0.37464 + 1.5422\omega - 0.26922\omega^2; \quad 2.1c$$

$$b_{PR} = 0.07780\frac{RT_C}{P_C}; \quad 2.1d$$

In Equation 2.1 P is the system pressure, V_m is the molar volume, R is the universal gas constant, T is the absolute temperature, b_{PR} is a constant related to the irreducible volume of the molar quantity of substance, and a_{PR} is a temperature dependent value describing the attractive forces of molecules. Both a_{PR} and b_{PR} can be related to the critical temperature T_c, and critical pressure P_c through Equations 2.1b, and 2.1d respectively. The temperature dependent value a_{PR} is further related to the acentric factor ω, by Equation 2.1c, which describes the deviation of molecular behavior from a hard sphere by the constant k_{PR}.

The EOS form used for gas data is the SRK cubic EOS shown by Equation 2.2. (73)

$$P = \left(\frac{RT}{V_m - b_{SRK}}\right) - \left(\frac{a_{SRK}(T)}{V_m(V_m + b_{SRK})}\right); \quad 2.2a$$

$$a_{SRK}(T) = 0.4274\left(\frac{R^2T_C^2}{P_C}\right)\left(1 + k_{SRK}\left(1 - \sqrt{\frac{T}{T_C}}\right)\right)^2; \quad 2.2b$$

$$k_{SRK} = 0.480 + 1.57\omega - 1.76\omega^2 \quad 2.2c$$

$$b_{SRK} = 0.08664\frac{RT_C}{P_C} \quad 2.2d$$

In Equation 2.2 the parameters P, T, R, V_m, and ω have the same meaning as that of Equation 2.1, and the same values. The parameters a_{SRK} , b_{SRK}, and k_{SRK} have the same meaning as a_{PR}, b_{PR} and k_{PR} respectively as in Equation 2.1 but are calculated in Equation 2.2 with different functional constants, and therefore have different values.

A schematic of the system is shown in Figure 1.2. As shown, Valves v1 to v7 are pneumatically controlled valves supplied from Swagelok (Part No. SS-T2-C1VFS1-D; Solon, OH). Valves v8, v10 to v11, and v14 to v17 are supplied from Vindum Engineering (Part No. CV-520A-SS; San Ramon, CA). Valves v9, v12 to v13, and v18 to v19 are supplied from High Pressure Equipment Company HIP (Part No. 15-15AF1; Erie, PA). All internal metal surfaces in Figure 1.2 are coated with a few micrometer layer thin film of Sulfinert® by Restek (110 Benner Circle, Bellefonte, PA 16823) to improve measurement low levels of polar and nonpolar compounds, especially traces of hydrogen sulfide, organosulfur and mercury compounds.

In Figure 1.2, C1 represents a methane sample loop with a volume of 2 cm^3; C2 represents an ethane sample loop with a volume of 1 cm^3; CO2 represents a carbon dioxide sample loop with a volume of 0.5 cm^3; C3 represents a propane sample loop with a volume of 1 cm^3; and NGL represents a natural gas liquids sample loop of 0.25 cm^3. When necessary, these loops are filled through the valves on their left by means of appropriate gas regulators (represented by the letter R) that are attached to cylinders or containers of the respective volatiles (not shown). Pressure gauges (P) monitor the fill pressure, and the appropriate EOS can be used to determine the amount of each volatile being loaded into the sample loops before injection, if desired, by solving Equation 2.2 for molar volume, based on the load temperature and pressure. The sample loop volume is then divided by the molar volume to obtain the amount of volatile added. In practice, the procedure used for most simple volatiles injection does not use these sample loops; this is described in more detail in the section on injection of volatiles. Valve v7 connects to a vent or vacuum line.

Measurement of mass is performed with an analytical balance model XS1003S from Mettler Toledo (CH-8606 Greifensee, Switerzland) with a maximum capacity of 1010 g and repeatability of +/-0.8 mg.

The densitometer (D) is an Anton Paar densitometer (Model No. DMA HPM; Österreich, Austria), which is used to measure the density of the fluids in real time. In the early phase of work on the instrument, EOS modeling was used as a substitute for the densitometer. The densitometer provides a well-calibrated, independent measurement that supplements EOS modeling. Specifically, the molar volume calculated by either the EOS of Equation 2.1 or 2.2 is inversely proportional to the density measured with respect to

the molecular weight of the volatile. The molar volume may therefore be directly measured with the densitometer, in addition to that calculated by the EOS.

Temperature and pressure of the recirculating fluids are measured with a Paine Electronics temperature and pressure gauge (Part No. 211-37-990-01; East Wenatchee, WA; PT1). The pressure sensor is temperature compensated with an internal thermistor. The calibration is completed every 60-90 days per manufacture recommended scheduled maintenance. The calibration is conducted with a dead weight system. The bounds of the 95% confidence interval from ambient to 137.9 MPa (20,000 psi) for all measurements across the range are .097(+/- 14 psi). The pressure sensor precision is determined as +/- 3 psi 95% confidence over the full pressure range.

One dual chamber Quizix pump from Chandler Engineering (Model 6125; Broken Arrow, OK) provides pressurization and a means to mix the fluid samples in the oven (Q1 and Q2). H1 to H3 and SC are custom-built piston accumulators designed to enable long-term, reliable operation at high temperatures and pressures. Q1 and Q2 control piston accumulators H1 and H2 respectively. H3 and SC hydraulic pumps are pressurized by a Teledyne Isco pump (Model No. 100DM; Lincoln, NE). A particulate filter (F) is installed in the system to protect the accumulators from debris. It is custom-manufactured from a Swagelok union with stainless steel screens added. SC which is used to inject liquids into the measurement system shown in Figure 1.2 has an empty weight of 806 g and a capacity of 20ml.

EC is a laboratory oven from Sun Electronic Systems, Inc. (Model No. EC12; Titusville, FL) used to provide temperature control of the fluids under study. SI is a six-

port injection valve from Valco Instruments Company, Inc. (Part No. C72U-1696E; Houston, TX) used to add small amounts of fluids to the sample system.

Two optical cells are used in the instrument, O1 for NIR and MIR transmission measurements and O2 for UV-visible spectroscopy. The cells were built by Phoenix Instruments (Part No. HB-3WC-20K-2; Splendora, TX). In each case, light from a commercial spectrometer is coupled to a fiber optic bundle routed into the oven containing the small-volume optical PVTX system. A cross-section of these optical cells is provided in Figure 2.2.

For the infrared transmission cell, the fiber optic bundles contain seven 1/2-mm diameter chalcogenide infrared (CIR) As_2S_3 fibers (High Tech Photonics, Oviedo, FL); the bundles are either 1 or 2 m in length. The primary pressure-containing windows are made of sapphire and are 1/8-in. diameter and 5/8-in. thickness, providing a nominal 1-mm pathlength for normal use. The pathlength of the windows is adjustable to approximately 100mm, but must be set and fixed prior to an experimental run. The thermal expansion of the pathlength at ambient pressure is calculated from the coefficients of thermal expansion of the materials and the structure of the cell. The pressure-induced expansion of the pathlength in the infrared cell at ambient temperature was determined with a micrometer. Both sets of data were fit to the following equation:

$$d(mm) = 0.8801 + 0.000402065 \text{ X } T\ (°K) + 0.00060493 \text{ X } P\ (MPa) \qquad 2.3$$

For the visible transmission cell, the fiber bundles were composed of low-OH silica fibers (CeramOptec, East Longmeadow, MA) with lengths of 2 m.

Not shown in Figure 1.2 are the Fourier transform infrared (FTIR) and UV-visible spectrometers that are fiber coupled to transmission cells O1 and O2.

The FTIR is a Bruker TENSOR 27 system equipped with a liquid N_2-cooled mercury, cadmium, telluride (MCT) broadband detector, a NIR source, and modified right-side external fiber optic coupling module. The spectral range is 350 to 11 000 cm^{-1} and maximum resolution is 1 cm^{-1}. An OPUS FTIR data collection program was used to operate the spectrometer and parse spectra data. The FTIR spectrometer is coupled to the optical cell (O1 in Figure 1.2).

The UV-visible spectrometer is an Ocean Optics HR2000+ high-resolution spectrometer and a balanced deuterium tungsten source (180 to 1700 nm). The detector's range is 200 to 1100 nm. The optical resolution is ~0.5 nm full width at half maximum (FWHM), and the integration time ranges from 1 millisecond to 65 seconds, with shorter integration times used for very transparent samples, and longer integration times for low-transparency samples. SpectraSuite® spectroscopy operating software is used to operate the UV-visible spectrometer. The UV-visible spectrometer is coupled to the optical cell (O2 in Figure 1.2).

A Norhof liquid N_2-microdosing system is connected to the FTIR liquid N_2-cooled MIR detector to keep the detector cool through one complete experiment (usually one week) without manually loading liquid N_2.

2.2.1 Software

A custom program written in the LabVIEW (National Instruments, Inc., Austin, TX) programming environment is used to control and operate the state of the PVT system. This program provides measurement of pressure, volume, temperature, and density. OPUS software (Bruker Corporation, Billerica, MA) was used to operate the FTIR and was automated with the aid of the Windows® interface language WinBatch®

(Wilson WindowWare, Inc., Seattle, WA). After every 8 hours of operation, a WinBatch program written in-house closes the OPUS program, restarts the FTIR, and restarts the OPUS FTIR control program to record a preset number of spectra under experimental conditions.

2.2.2 Operation

The system described in Figure 1.2 is operated by (a) initially charging the system with an oil, (b) making optical transmission measurements of each oil composition through a range of pressures and temperatures, (c) systematically modifying the composition of the oil in the system by adding either volatile components or small amounts of nonvolatile components, and (d) analyzing the oil composition after the experimental cycle is complete to confirm the performance of the system.

2.2.3 Initial charge of a dead oil

The following procedure assumes that the system begins clean (see section J. Cleaning the system), all hydraulic lines are attached except those between valve v13 and v19 (Figure 1.2; all following references to components use notations from Figure 1.2), and all pistons are in their top, lowest volume, positions, with the exception of the Isco (I) pump, which needs at least 15 cc of working volume for charging the system.

Before fluids are added to the recirculation loop, transmission measurements of the empty optical cells are recorded to serve as a baseline.

The volume within the closed portion circulation loop system shown in Figure 1.2 can be measured by density, for a known internal mass, or by the difference of the Quizix pump barrel positions, Q1 and Q2. The Quizix 6125 pump is a volumetrically metered syringe pump designed to deliver continuous flow by a oscillating two barrel system in

increments as low as 0.0000034 ml/motor step, a barrel capacity of 125 mL and a double barrel delivered volume accuracy of 0.1% across temperature and pressure specification range of up to 285^{o}C (545^{o}F) and 137.9 MPa (20,000 psi). However, the single barrel, the constant pressure, constant temperature injection accuracy has been measured to better than 0.001 mL for a 5 mL injection volume with water by the precision balance. Over the PVTX system operational range, the relative volume of the two quizzes barrels Q1, and Q2 can be used to determine the system volume by difference. For a 25 stroke average the accuracy volume measurement by Q1 and Q2 difference has been determined as 0.01 ml, using the known density of 5 g of water as in internal standard. The Anton Paar Density Meter has a precision of better than 0.0001g/cc and allows the internal volume of the system to be tracked based the injected mass. Comparison between the density method of volume measurement and the differential piston positon method of internal can be used to detect leaks. Piston stick slip can be monitored based on the pressure readout of each Quizix barrel. The differential piston position volume measurement can be affected by piston stick and slip. The stick and slip pressure is typically is typically 50-75 psi collectively for all pistons in the system, but grows as the piston seals age. The pistons seals are maintained when the slip stick pressure reaches 150 psi. The stick slip can affect the differential barrel volume calculation based on the compressibility of the fluid in the system. Therefore the differential barrel positon volume calculation is averaged to reduce the impact of this effect.

A cylindrical stainless steel cell (SC) with a maximum fluid volume approximately twice that of the oil to be added, and having a piston and male threads at the top and bottom for connecting to valves, is preset with the piston held by friction at

the mid-point of the cylinder. Approximately 7to 10 mL of generic dead crude oil (i.e., containing no volatiles) sample, under study, is added to the cell; this volume and piston setting provides extra space in the cell so that when heated, space exists for expansion. The components between Valve v13 and Pump I are then assembled in sequence and in a manner (see below) to eliminate air spaces in this section, so that when the tubing is attached to v13, the only air space is between the end of the tubing and the valve seat in v13. This unfilled space is no larger than approximately 0.05 mL. This assembly is weighed to the nearest milligram before attachment and then connected to Valve v13.

Using vacuum lines attached to Valves v7 and v9, the system is evacuated down to Valve v13. When Valve v13 is opened, Pump I forces the dead oil sample into the recirculation system inside Oven EC. This is performed in steps to measure the volume of small sections of the recirculation loop and also to reduce the size of the expansion steps to minimize phase separations during loading. While oil is gradually being injected, a section-by-section leak test of the instrument is performed. The entire process for loading the initial dead oil is described in more detail in the following paragraphs.

With Valve v19 open and Valve v13 closed, Pump I is pressurized to ~20.7 MPa (3,000 psia) to establish pressure up to Valve v13. Sample Cylinder SC is then heated to injection temperature, which is currently set to 339 K (150°F) to keep the system in liquid phase during injection. During this interval, Pumps Q1 and Q2 are pressurized to 3.4 MPa (500 psia) to hold the Hydraulic Pumps H1 and H2 in place at the top of their range.

Valve v13 is then opened to fill the tubing section between Valves v13 and v12. The volume required to fill the section of tubing up to Valve v12 is measured using the displacement of Pump I, set to maintain ~20.7 MPa (3,000 psia).

After a period of time for stabilization, Valve v12 is opened and the volume required to fill the recirculation unit out to Valves v10 and v11 at ~20.7 MPa (3,000 psia) is measured using displacement on Pump I.

Pumps Q1 and Q2 are then pressurized to approximately ~24.1 MPa (3,500 psia) to hold the pistons at the tops of their ranges during loading. Valve v10 is switched to fill the line to the left recirculating Hydraulic Pump H1; the volume fill for this section is measured by displacement at Pump I. Valve v10 is then switched to fill the line through Densitometer D up to Valve v11. Valve v11 is then opened to fill to the right recirculating Hydraulic Pump H2. Volumes for each step are measured by displacement on Pump I.

The next step in the procedure is adding equal amounts of oil into Pumps H1 and H2. Pumps Q1 and Q2 are reduced in pressure to ~20.7 MPa (3,000 psia), and under isobaric conditions, Pumps H1 and H2 are filled equally until approximately 1.5 to 2 mL of oil is added, as measured by Pump I, half in each recirculating pump. The recirculating system should now be up to an approximately 5.5 mL volume, as measured by Pump I. During operation, Pumps H1 and H2 are operated in tandem with Valves v10 and v11 to recirculate fluids until both are nearly filled by the addition of more oils or volatiles, at which time the system volume reaches ~9 mL.

After this initial filling operation, Valve v12 is closed. The pressure setpoint of Pump I is reduced to 0.7 MPa (100 psia), and Valve v13 is then closed. The pressure at

Pump I is then reduced to ambient. Valves v18 and v19 around Sample Cell SC are closed, and the tube at Valve v13 is disconnected. The hydraulic line is disconnected from Valve v19, and dry air is blown into the orifice of Valve v19 until all water has evaporated from the connection. Sample Cell SC is reweighed to estimate the total mass of oil injected, after correction for line volumes. A second estimation of mass in the circulation loop is provided by the density of the fluid at temperature and pressure, as measured by D, and the volume of injected fluid, as measured by Pump I. The actual mass of oil injected can vary a few milligrams because of the small air gap in the original connection at Valve v13, which itself was compressed in the original pressurization of the injection system. The typical mass of oil injected at this stage is in the range of 5.5 mL, making this error in the range generally less than 0.02%.

2.2.4 Initial charge of a "live" oil

For a live oil (an oil containing significant volatiles), the control point for weighing is no longer the connection to Valve v13, but the connection at v18 of the same tube. The line connecting Valves v13 and v18 is evacuated, and the injection pressure is changed from 20.7 MPa (3,000 psia) to well above the known bubble point pressure, as modeled by the Peng-Robinson EOS of Equation 2.1, of the oil at 339 K (150°F) plus 6.9 MPa (1,000 psia) to ensure the sample does not undergo phase separation in the sample cell. The loading procedure for the sample cell also differs because the sample has to be charged under conditions to maintain single-phase behavior. This is a separate operation not covered by the current experimental discussion but can be performed by anyone with a working knowledge of PVT laboratory practice. The fluid sample is injected in a similar manner, section by section, as described in the initial charge of a dead oil

procedure, until the pistons at H1 and H2 are encountered. H1 and H2 are backed with sufficient pressure to maintain a minimum volume configuration during injection. Valves v10 and v11 are operated in a manner to introduce the fluid in the direction of the arrows in Figure 1.2. The line after Valve v8 can be backed with a needle valve (not shown) and released to vent directly. The fluid is then flushed through Valve v8 with the needle valve in a small orifice position, such that Pump I can maintain the fluid in the system above the bubble point. After the system has been flushed, typically 3X the system volume, v8 is closed. Valve v10 can then be opened to H1 with sufficient pressure to keep the fluid in the system above the bubble point. Pistons H1 and H2 are now withdrawn to introduce ~5.5 mL of sample into the recirculation loop. The mass of introduced fluid is measured by the injected volume corrected for the flush volume and line volume, as measured by Pump I, and the density of the injected fluid.

2.2.5 Measurements on a single fluid composition

After the recirculation loop has been filled using the previous procedures, laboratory measurements typically begin at the injection pressure of ~20.7 MPa (3,000 psia) and the lowest planned test temperature. The typical measurement protocol is described as follows.

The recirculation loop extends from H1 to H2 and includes the section with Optical Cells O1 and O2, the pressure and temperature measurement unit PT1, and the section with Densitometer D. Pumps Q1 and Q2 are used to transfer as much volume from Hydraulic Pumps H1 and H2 as possible into H1, leaving H2 at its maximum position. Valves v10 and v11 are switched so that H1 can transfer fluid under isothermal and isobaric conditions by means of the optical cells to H2. Along this line, the fluid

passes through a narrow capillary "stinger" located in PT1 to aid in mixing. The stinger applies shear for mixing and also occupies some of the otherwise dead volume, converting the internal volume of PT1 into swept volume.

When H2 is filled and H1 emptied, Valves v10 and v11 are switched and the fluid is transferred back under isobaric and isothermal conditions by means of the densitometer line. This process of transferring from H1 to H2 and back is repeated, with mixing at the stinger during each left-to-right transfer of the oil until mixing is complete. A well-mixed oil is characterized by constant density measured at D and constant spectroscopic data measured at O1 and O2. The Peng-Robinson EOS of Equation 2.1 is used to target single phase conditions with respect to the gas/ liquid phase envelop, however, initially as local bubbles dissolve into solution, density and optical variation may be high. The concentration of free gas decreases as the bubbles from injected gas dissolve and the densitometer and optical data variation decreases substantially. Multiphase conditions can still exist with respect to solid asphaltene particulates, and aqueous phase. Usually the optical signals are more sensitive to solid and aqueous multiphase phase variation than the density signals. Multiphase gas-liquid systems have substantial density and optical signal variation as compared to single phase and homogeneous systems, because the multiphase oil-gas systems never completely homogeneously mix. Therefore free gas can usually be detected as an indication that the system bubble point has been crossed. Also the decrease in variation is indicative that free gas is reducing and the volatile components have been dissolved into a single phase. After it is believed that the system has reached single phase conditions for a system above the expected bubble point, the circulation can be stopped and the multiphase conditions confirmed. If multiphase

conditions still exist, there will be density driven gas gravity segregation in the optical cells and density sensor which is easily detected.

Once density and spectroscopic data indicate the system has reached a well-mixed equilibrium state under isothermal conditions and at ~20.7 MPa (3,000 psia) for 15 to 30 minutes, the mixing is paused for 15 minutes to collect density and stagnant fluid optical spectroscopy data while avoiding artifacts resulting from fluid pumping/pressure transients. These data are considered the most appropriate and highest quality for the particular pressure, temperature, and density of the equilibrated system. During the static time of spectroscopic collection, if a multiphase condition unexpectedly exists it will be detected.

After these characteristic data are acquired, the pressure is increased by an increment (often ~20.7 MPa) using Pumps Q1 and Q2. The decrease in system volume is measured, the density measured, and spectroscopy again recorded.

Increments of ~20.7 MPa in pressure are added until reaching the maximum pressure for the test parameters, usually up to ~80 MPa (12,000 psia), although the system can reach 138 MPa (20,000 psia). Density, volume change, and spectroscopy are recorded for both dynamic and stagnant fluids, with the stagnant fluid measurements considered characteristic, as described previously, and the dynamic measurements being used for confirmation of the system operation and troubleshooting, as necessary.

Once the maximum pressure designated for the test sequence has been reached and data recorded, the pressure is reduced in increments, retracing the original pressure steps back to ~20.7 MPa (3,000 psia), with data again recorded at each step.

At this point, the temperature of the system is increased by an increment (often ~28.7 K or 50^{o}F) and allowed to equilibrate while the oil system is continuously mixed under isobaric conditions. The equilibration time is again determined by stabilization of the system density and optical spectroscopy. At the new temperature, the pressure cycle is repeated.

After each pressure cycle, the temperature of the system is increased by an increment and the pressure cycle repeated. At each step in each pressure cycle, data are recorded for density and volume change, and the optical spectroscopy of the system is measured.

Once the highest temperature is reached, Valve v11 is closed to isolate the optical train, densitometer, and H1. Pump Q1 is slowly withdrawn to measure the pressure-density curve for the fluid. If the fluid is a dead oil, a compressibility curve is obtained. If volatiles are present, a compressibility curve above the bubble point, and the pressure for that bubble point, is initially provided. Bubble point pressure is both detected by the appearance of lower-pressure bubbles in the fluid by the densitometer as the fluid circulates and by an inflection point on the compressibility curve. A phase envelope—the bubble point as a function of temperature and pressure—can be measured by detecting the bubble point as the system cools from the highest temperature back to the injection temperature, as controlled by an automated routine. As bubble point information is measured, the Peng-Robinson EOS may be tuned to provide a more accurate bubble point expectation at the next temperature.

2.2.6 Adding volatiles to a fluid

After a full set of experiments on a single fluid composition, the composition can be changed by adding volatiles. A set of six valves connected in series allows volatiles to be added into an external hydraulic pump in preparation for injection. The volatiles illustrated in Figure 1.2, in order, are methane (C1), ethane (C2), carbon dioxide (CO_2), propane (C3), and natural gas liquids (NGL), with NGL being last in the series toward the hydraulic pump. The final valve, after the NGL valve, connects to a vacuum for emptying the lines before additions. The natural gas liquid contains multiple hydrocarbon volatiles. The primary purpose is to allow the injection multiple hydrocarbon components primarily with molecular weights higher than that of propane, although the mixture does contain some ethane and propane. The actual standard used is BU34.2X1ZCAS from Praxair (11425 W. Little York Road; Houston, TX 77041) containing a balance of Propane 37.8 mol%, Ethane 12.2 mol%, Butane 34.2 mol%, Pentane 8.4 mol%, Hexane 4.9 mol%, Heptane 1.6 mol%,Octane 0.9 mol%, as a liquid blend certified standard grade. For the following discussion, methane, ethane, and carbon dioxide data are modeled by an SRK EOS whereas propane and NGL are modeled by the Peng-Robinson EOS.

In preparation for volatiles injection, the recirculation system temperature is allowed to cool to the initial test temperature. While that is occurring, the volatiles are readied for injection.

Beginning with the sample preparation system evacuated and isolated from the recirculation line by Valve v8, one of the volatiles valves is opened to fill the line. Pump I, by means of Valve v16, is used to draw a volume of gas into Pump H3. The gas in

Pump H3 is isolated by Valve v9 and then compressed under isothermal conditions to map the pressure as a function of volume change, based on the volume change at Pump I. For single-component gases, the compressibility factor is directly taken into account, and for a gas mixture, the EOS estimates the compressibility factor. From these measurements, the number of moles of gas in the cylinder of Pump H3 is determined. At this point, external Hydraulic Pump I is used to compress the gas until the pressure equals the pressure in the closed recirculation loop of the system. Valves v8 and v9 are switched to connect Pump H3 with the recirculation loop. Then, Pumps I, Q1, and Q2 are used to transfer a volume of the gas through a narrow capillary line into the recirculation loop. Q1 and Q2 are driven at a constant rate, and isobaric conditions are maintained by setting Pump I to constant pressure. The volume of gas transferred out of the external hydraulic pump is approximately 0.75 mL, as measured by Q1 and Q2 during addition. One method to measure gas addition is determining the volume change at H3 as measured by the volume change at Pump I. A better measure of the gas volume injected is obtained by repeating the pressure volume scan using Pump I and determining the number of moles injected by the difference. After equilibration in the recirculation loop, the volume change in the recirculation loop can again be measured, and because of volume changes associated with mixing, it is usually significantly less than 0.75 mL. Using the measured change in density and change in volume of the fluid in the circulation loop, a third estimate of gas injected into the system can be obtained.

When NGL or propane is to be transferred, the procedure is slightly different. For large-volume additions, approximately 15 mL of liquid is transferred into H3 under 20.7 MPa (3,000 psia) pressure, and the known density and volume change at H3 are used to

determine how much is charged. Transfer is again isobaric at the test pressure to add approximately a 0.75 mL volume before significant mixing, as measured by H1 and H2.

For small-volume additions of NGL or propane, the liquid is captured in sample injection loops between Valves v5 and v6 for NGL or between v4 and v5 for propane. In such cases, the number of moles of propane or NGL transferred is known from the volume of the sample loop. These liquids are then swept into H3 with an addition of a volatile gas (such as methane), and the pressure in H3 is kept low to maintain the compressibility factor close to unity. Propane and NGL are in a gas phase in H3, so at that point, the addition is performed under the same isobaric conditions as for volatiles.

2.2.7 Adding nonvolatile liquids to the fluid

To modify the base fluid, it is often desirable to mix it with portions of another liquid having a different composition. A high-performance liquid chromatography (HPLC) switching valve, SI, with a sample loop can be used for this purpose. It is placed in line between Pump H3 and Valve v9 above the pump. The sample loop can be loaded, providing a known small volume of the liquid (water or oil). A volatile gas is loaded into the pump, and the number of moles of gas is determined by pressure and volume measurements. The gas is pressurized for transfer as described previously, but the HPLC valve is switched to place the new liquid into the line before transfer. The transfer of gas then drives the new liquid with it into the recirculation loop. The gas volume injected needs to be reduced by the volume of liquid that was injected in the transfer loop. Larger amounts of a nonvolatile liquid can be added to the system according to the initial charge of a dead oil procedure and added mass determined as stated previously.

2.2.8 Analysis after testing

At the end of a full testing procedure, the composition of the fluid in the recirculation loop should be known. To confirm the composition, Pumps H1 and H2 are used to transfer a volume of fluid into a reservoir situated at the same location as SC was originally. The transferred volume is usually through a needle valve (not shown) to keep the contents within the circulation system above the bubble point. The replacement for SC is weighed beforehand and again after filling. The pressure and gas of the reservoir contents are lowered, and the contents are separated and isolated. The mass of the liquid fraction is measured in the reservoir, providing the weight of the gas by difference. The gas-to-oil ratio (GOR) can be calculated as a fluid property of interest.

HPLC Agilent (5301 Stevens Creek Blvd.; Santa Clara, CA 95051) 7890 is used to determine the saturates, aromatics, resins C6+ liquid fractions of petroleum samples, and asphaltenes C6+ liquid fraction are measured gravimetrically after precipitation with pentane. An Agilent 7890 GC with Agilent J&W DB-1 capillary column is used to determine the composition of liquid and gas components in the fluid. These values are usually within 2% or less of the expected compositions. Given the uncertainty in the compositional analysis, a test within 2% is considered validation of the expected composition. Trending in the deviations, or a large deviation, is considered an indication that wear on the hydraulic pistons is causing a loss of volatiles or some other problem occurred with the apparatus. Data from a run with significant deviations at the end measurement are considered untrustworthy, and maintenance is performed on the apparatus before it is repeated. Data from a run that tests within 2% of the expected

composition at the end is assumed to be characteristic of the calculated compositions throughout the measurement set.

2.2.9 Miscellaneous procedures

In the event that the volume of the recirculating fluid becomes sufficiently large that both H1 and H2 are forced to the ends of their range and cannot circulate the fluid any longer, fluid is withdrawn from the recirculation loop using the same procedure for a post-test analysis. Additional nonvolatile liquid or volatile gas can be subsequently added.

2.2.10 Cleaning the system

After an experimental run has been completed, the oil is ejected from the system through valves 12, 13, and 18 with cylinder SC removed. Pistons H1 and H2 are pushed to their maximum extent in order to push as much fluid from the system as is possible. Generally, because the fluid under analysis contains dissolved gas under pressure, when the pressure is released by opening valve 18, the bulk of the fluid naturally expels. Cylinder H3 is loaded with approximately 20 mL of toluene for flushing. Approximately 5 to 7 mL of toluene is loaded into the system by cylinder H3 with valve 12 closed, and circulated with cylinders H1 and H2 in tandem with valves 10 and 11 at approximately 200 psi and room temperature. Dry pressurized nitrogen is connected to valve 8 and used to push the toluene out of the system at 200 psi through valve 18. The toluene injection, rinse, and ejection with nitrogen is repeated until the ejected toluene is clear and contains no visible. This usually takes no more than one additional H3 loading of toluene for a total of 6 rinses. After the final rinse, valves 8 and 18 are closed and the system

temperature is increased to 394K (250^{o}F). The entire system is pulled under vacuum until a stable pressure of less than 300 milli-Torr is achieved to ensure the system is dry.

2.2.11 Data processing

NIR and MIR spectra collected on the optical-PVT system's FTIR spectrometer are linear in wavenumbers, from 10 000 to 1500 cm^{-1}, and normally set to a resolution of 32 cm^{-1} for a total of 551 spectral channels, although 1 cm^{-1} resolutions are possible. A total of 64 spectral scans is averaged to generate a single recorded spectrum. Typically, one averaged spectrum is recorded every 15 seconds, and 50 of these averaged spectra are collected for one temperature-pressure combination. Averaged spectra are filtered for Type II outliers (i.e., outliers caused by sample composition) (74) and then averaged for a global signal-to-noise ratio (SNR) of approximately 10,000:1.

Data are originally saved in OPUS format but subsequently converted to an ASCII XY format readable by other programs for further analysis. Wavenumbers and absorption values ten digits beyond the decimal point were retained for precision in these text documents. File header information (filename, date, time, and resolution) in the OPUS format files was read using in-house MATLAB® code and used to match the date and time of each FTIR file to a sequence of events file (SOE) for pressure, temperature, component concentrations, etc.

When the TENSOR 27 is set to record spectral data from 10 000 to 1500 cm^{-1}, it actually records data from 9982.5 to 1496.6 cm^{-1} (1001.7495 to 6679 nm), thereby defining the spectral range typically used. During acquisition, the data are linear in wavenumber, so they are interpolated onto an axis that is linear in wavelength from 1001.7495 to 6679 nm in 2048 channels using the MATLAB function interp1 with either

the shape-preserving cubic Hermite polynomial interpolation option “pchip” or with simple linear interpolation if the data are particularly noisy.

UV-visible spectra collected on the optical-PVT system’s Ocean Optics spectrometer are reported by the manufacturer to be linear in wavelength from 188 to 1100 nm, with a spectral resolution of 0.5 nm. The spectral range is divided into 2048 wavelength channels. The integration time varies from milliseconds to seconds, depending on the fluid, with short integration times for highly transparent fluids. Hundreds or thousands of samples are averaged to generate a single spectrum. Regardless of the integration time, a combination of integration time and numbers of samples averaged is chosen so that the UV-visible spectra are recorded at the same rate as the FTIR spectra (i.e., one spectrum every 15 seconds). Data are stored in a readable format, and each spectrum is matched to system conditions by the nearest time in the SOE file.

For each set of experiments, a large number of single-beam spectra of the empty transmission cell (under vacuum) are measured the same way the sample spectra are recorded and averaged to form a background measurement. Because of the higher refractive index of most fluids compared to air, reflection losses at the interface between the sapphire windows and the sample are usually reduced for an oil spectrum compared to the spectrum of the empty cell. As a result, the actual transmission of the filled cell can be higher than for the empty cell when the sample exhibits low absorption. To correct for this factor, the fluid FTIR single-beam transmission spectra are linearly normalized to span the intensity range between zero and that of the empty cell FTIR single-beam spectra, with the fit performed over the oil baseline window region. Under the assumption that there are regions of near 100% transmission in the oil spectrum in the

1000 to 1600 nm spectral window, this provides an approximate correction for the difference in reflection losses and also removes a constant offset in regions of high oil absorption resulting from stray light and other effects. In some instances, usually for very dark oils with high asphaltene content, the high transmission assumption is known to be invalid. In these cases, the asphaltene absorption tail is partially compensated by a correction that is exponential in wavenumbers before air normalization.

Once transmission is computed as described, absorption is calculated from it as the decadic logarithm of the reciprocal of transmission at each wavelength.

2.3 RESULTS AND DISCUSSION

2.3.1 Isothermal/isobaric/isochoric stability

A full pressure cycle from ~20.7 MPa (3,000 psia) to maximum and back requires between two and several hours, depending on how much recirculation is necessary to equilibrate the system. Single-component fluids require little time in recirculation because no mixing is necessary. Figure 2.3 shows a continuous measurement of pressure and density as a function of time during a pressure cycle for pure ethane, with the time recorded at approximately 15 second intervals. The response time for the sensors is considerably shorter than the time between data recordings. The temperature during this run averaged 336.64 ±0.08 K (the uncertainty is the sample standard deviation, with a maximum recorded temperature of 336.93 K and a minimum of 336.34 K).

The data shown in Figure 2.3A illustrate a cycle in which the pressure is nominally held at ~21 MPa (3,000 psia), then cycled to nominal values of ~41 MPa (6,000 psia), ~55.2 MPa (8,000 psia), ~69 MPa (10,000 psia), ~76 MPa (11,000 psi), ~62

MPa (9,000 psia), ~41 MPa (6,000 psia), and ~21 MPa (3,000 psia). The average measured pressure across the entire time of a set point for each stage was 21.78 ±0.23 MPa (3,159 ±33 psia), 41.53 ±0.21 MPa (6,024 ±30 psia); 55.10 ±0.08 MPa (7,992 ±12 psia); 68.81 ±0.09 MPa (9,980 ±13 psia); 76.43 ±0.11 MPa (11,085 ±16 psia); 62.40 ±0.12 MPa (9,050 ±18 psia); 41.91 ±0.24 MPa (6,078 ±35 psia); and 21.93 ±0.25 MPa (3,181 ± 36 psia) where the standard deviation associated with each measurement is indicative of the system stability.

Figure 2.3 shows that the pressures are not held fully constant under most conditions but are gradually drifting (usually rising). This can occur because the pressure setpoint is set by the pumps and reflects the pressure set only up to the hydraulic pumps; the internal pressure in the system apparently provides a small contribution with no external effects. This slow drift does not cause significant performance issues under most circumstances because the time at each stage is relatively short and the drift is relatively slow—approximately 0.05 MPa/minute. The accuracy with which the nominal pressures are achieved is likewise not perfect—the average pressure achieved is 0.2 ±0.5 MPa higher than the target setpoint pressures; again, the setpoint accuracy of the pressure generators is not a critical factor because the pressure, temperature, and density of the fluid are measured precisely inside the recirculation loop in real time.

The temperature is maintained within relatively tight limits using a feedback control on the oven; the largest temperature fluctuations occur when the pressure is increased or decreased suddenly. When this occurs at a pressure step, the temperature of the fluid increases during compression and decreases during expansion because the fluid behaves adiabatically to instantaneous changes. Temperature fluctuations are minimized

by having a large surface interface between the fluid and its containment and also by changing pressure more gradually. The largest temperature fluctuations during the collection of the data in Figure 2.3A are no more than 0.2 K in either direction.

Figure 2.3B shows the measured density during the experimental cycle shown in Figure 2.3A. The density measurement is significantly noisier than either the temperature or pressure measurements. Over the range of pressures in Figure 2.4, the noise in the density measurements does not significantly change for pure ethane. At the highest pressures shown in Figure 2.3A, there is little drift in pressure or temperature; the changes are small, especially relative to the absolute pressure, and the fluid is significantly less compressible. Therefore, variabilities in density measurements under this condition can be used as a measurement of their simple repeatability. The density recorded during the highest pressure step was 0.483 ±0.008 g/mL, so this sample standard deviation is used as a measurement of the inherent precision of individual density measurements for most of the fluids of concern. An alternate view of the same data is computing the difference between points separated in time and then calculating the variability in the differences. This removes variability caused by slow changes in the environment, and the residual variability square root is expected to be two greater than for the individual measurements. The variability between the difference of adjacent points is 0.0117, also providing an estimate of the single-point sample standard deviation of 0.008 g/mL. Because of the relatively high variability of the individual density measurements and their lack of correlation with one another, points can be averaged together to obtain improved precision. In general, spectral data and (P-ρ-T) data are

averaged over the approximately isobaric plateaus in compression/expansion cycles once the fluid is considered well mixed to provide higher precision.

2.3.2 Accuracy of (P-ρ-T) data

Figure 2.4 shows data for a study of ethane recorded using the small-volume optical PVTX system with the SRK EOS isotherm curves for ethane at the same temperature as calculated by Equation 2.2 for an acentric (ω) factor of 0.098 (3217), critical temperature of 305.322 K, and critical pressure of 4.8722 MPa.(75) All temperatures studied are above the critical point, so the fluid is always in a single phase. Each curve was recorded as described previously under approximately isothermal conditions (temperatures were stable within 0.5 K).

In 2006, Buckner and Wagner (76) surveyed the available data for EOS modeling of ethane as part of a collaborative effort between the National Institutes of Standards and Technology in Boulder, Colorado and Ruhr University in Bochum, Germany. Their survey provided a crucial assessment of the data sets in terms of their precision and quality. The pressure, temperature, and density range over which the optical PVT system described in Figure 1.2 records spectroscopic data overlaps some of the values of significant references in that survey. Buckner and Wagner ranked literature data into three groups. Of these, Group 1 was rated the most important for characterizing the properties of ethane. These most important references provided the highest-quality data for the particular pressure and temperature conditions, as well as providing a wide range of conditions. Group 2 data were deficient in some way relative to Group 1 but were considered valuable for certain purposes. Group 3 data were largely unimportant for quantitative modeling, having been superseded by data in Groups 1 and 2. Of the

references they provide, only Claus et al. (77) are listed in the Group 1 class and also overlap some of the data in the current study. Their data overlap all of the temperatures presented in Figure 2.4 for ethane but only at the lowest pressures shown.

Because (77) does not provide data at the exact pressure and temperature conditions recorded in this study, an interpolation procedure was used to estimate equivalent values. In the first step, density was plotted versus pressure for all temperature values provided (77) that bracket the current experimental temperatures. A high-order polynomial (generally, 7^{th} order) that fit the data well was calculated and used to estimate densities at the exact pressures recorded in this study at all relevant temperatures in (77). Afterward, the density estimates were plotted compared to the relevant temperatures, forming a separate density versus temperature plot for each experimental pressure. In each case, the density versus temperature plot fit well with a line, which was used to estimate densities consistent with (77) for the temperatures and pressures recorded experimentally. Only three points of overlap exist between the current study's data and those of (77); for these data points, recorded densities in this study were, on average, 0.8 ±2.7% higher than the values in (77).

Byun et al. (78) are in Group 2 data sets for ethane because their reported densities are not considered as accurate as data sets in Group 1; however, their data overlap 12 ethane measurements for the current study. Interpolating the data in (78) using the procedure described previously provides estimates for all 12 current experimental conditions at the two higher temperatures but none of the six lower temperature conditions. For these 12 data points, densities derived from (78) were 3.9 ±1.3% higher than current data. Data from (78) and (77) overlap one another for two of the current

study conditions—the lowest pressure measurements at the two higher temperatures. For these two points, Group 2 (78) values are 4.2 and 4.1% higher than those of Group 1 (77). This suggests that current density measurements exhibit more scatter but tend toward the same mean values as those of the high-precision data of (77).

Additional data were obtained for methane but are not discussed here. In 1991, Setzman and Wagner (79) surveyed available data for methane and in 2001 (80) repeated, at higher precision, a set of data that overlaps three of the current study's methane (P-ρ-T) values at pressures up to 13 MPa and a temperature of 389.7 K. At the time these data were collected, the current *in situ* densitometer had not yet been built and densities were calculated by EOS modeling using the program PVTsim (Calsep A/S, Kongens Lyngby, Denmark). The EOS estimates of density for methane were determined to deviate from measurements in (80) by -1.0 ±1.1%. Overall, the *in situ* densitometer is considered an accurate indicator of actual density because it agrees well with the best quality literature data and EOS modeling.

2.3.3 Spectroscopy as a function of (P-*ρ*-*T*)

Most measurements of chemical composition using spectroscopy occur under conditions that are nearly isothermal, isobaric, and isochoric. The purpose of the small-volume optical PVTX instrument is to enable simultaneous spectroscopic and PVT measurements of an in situ reconstituted and or perturbed petroleum chemical composition under widely varying conditions of temperature, density, and pressure.

A variety of effects in the vibrational spectrum of a fluid result from varying (P-ρ-T) factors that have nothing to do with composition, or X. These effects include changes in peak intensities, changes in peak positions, and changes in peak width.(81, 82) The

causes underlying these effects are many fold and include refractive index changes with density (83-87) based on the Onsager model of electric moments in polarizable media (88); changes in intramolecular bond lengths resulting from attractive and repulsive forces with the surroundings, leading to changes in force constants (89-93); corresponding changes in intermolecular interactions, resulting in changes to acoustic and far-infrared modes that couple with MIR modes (81, 91, 94); collisional broadening or collapse of rotational fine structure as a result of increasing intermolecular interactions (87); changes in coupling between modes by means of Fermi resonance as the frequencies of vibrations shift differently as a function of pressure (82, 94-96); dipole-dipole coupling that changes with density (96-97); changes in stability of isomers caused by packing effects at higher densities (98-103); collision-induced absorption and other changes to wavefunctions, and thus to transition strengths, arising from perturbations by adjacent molecules (104); competition between repulsive interactions that tend to broaden the linewidths of transitions with increasing density, and forces that vary slowly with position that act the opposite (105); temperature-dependent continuum equilibrium properties of the surroundings (106-110); and non-equilibrium properties of the ensemble of absorbing molecules with their surroundings that affect both frequencies and intensities (111). In systems where there are strong associations, such as hydrogen bonding, the effects are even more extreme.(112-114)

In addition to these more exotic explanations for temperature and pressure dependence of the infrared spectrum, there is the well-known appearance of "hot bands" in the infrared spectrum whose strength depends on thermal population of excited vibrational levels.(115) Because ethane has a low-frequency torsional motion with a

transition energy of less than 300 cm^{-1}, a number of different state assignments can be made for each of the fundamental and overtone/combination/difference bands observed for ethane. In most cases, this would give rise to a set of absorptions at each band position, spaced closely and probably not observable separately under condensed phase isothermal/isobaric conditions but that could give rise to temperature dependence in the optical spectrum.

The different explanations offered for the observed infrared and Raman spectroscopy of molecules as a function of temperature and pressure are made more complicated because the various mechanisms have generally been invoked to explain a single aspect of observation. For instance, broadening and lineshape changes are the main focus of explanations related to collisional broadening and dephasing. A number of these reports deal with frequency shifts, and yet another portion deal with changes to intensities. What is clear is that multiple mechanisms can be in operation for any given molecule under a given set of conditions and that mechanisms invoked to explain one effect might also be invoked for another, whether or not this has yet been published in the scientific literature.

What is also clear is that a lack of knowledge of the actual spectroscopic behavior of a chemical system could cause serious problems with any analytical application of MIR, NIR, or Raman spectroscopy under conditions of widely varying temperature and pressure. In short, any analytical application using vibrational spectroscopy in dense media needs data from the actual chemical system under the actual conditions of measurement, because it is practically impossible to accurately anticipate the consequences of changing conditions.

This is illustrated in a small portion of the NIR spectrum, including the first overtone of the C-H stretching vibrations of ethane in Figure 2.5. These data were all acquired at the same temperature but at different pressures and have been normalized for density recorded by the *in situ* densitometer and the pressure-dependent pathlength using Equation 3. In general, absorption bands tend to remain at the same strength or decrease in intensity with increasing pressure, and each band can exhibit different behaviors. This is the case in Figure 2.5, in which the band centered at 5797 cm^{-1} loses intensity with increasing pressure faster than the larger band next to it. In addition, while the spectrum in the region of 5620 to 5950 cm^{-1} is dominated by what appear to be three bands, the difference spectrum shows at least five, with peak maxima at different wavelengths than those observed in the individual spectra, suggesting that the original spectrum is considerably more complex that it first appears. Little frequency shifting is obvious in these spectra, but some broadening of the band centered near 5910 cm^{-1} is evident.

Figure 2.6 shows a different portion of the transmission spectrum of ethane and how changes in temperature under isobaric conditions, as well as changes in pressure under isothermal conditions, affect the spectrum. Shown in the top of the figure is the spectrum of ethane in the 3550 to 4750 cm^{-1} region under conditions of 362 K (mid-range temperature) and ~62.6 MPa (mid-range pressure).

These conditions were selected because spectral data were recorded for a range of pressures within a fraction of a degree K and for three different temperatures within 0.2 MPa of one another. The bottom part of the figure shows the difference spectrum between the 388 and 337 K spectrums at ~62.6 MPa (blue) and between the 21.2 MPa and 82.5 MPa spectrum at 362 K. In each case, the normalized and corrected spectrum at

higher density is subtracted from the normalized and corrected spectrum at lower density. A negative peak in the difference corresponds to a band whose normalized intensity increases with increasing density, while a positive peak is one whose normalized intensity decreases with increasing density.

Although some similarities are present in the features of these different spectra as the density changes, distinct differences exist as well. Many of the same maxima and minima appear in each curve, with differing magnitudes. The absolute differences between the two curves are not directly comparable because an error of 1 to 2% in the correction factors can cause the two curves to almost overlap in some regions, and it is believed that this is the level of accuracy of the current densitometer. Nevertheless, if the same mechanisms were at work, one would expect to see upward and downward peaks coinciding in both of the curves. Many of the peaks show such behavior, albeit with inconsistent magnitude, but one that is distinctly different is in the region of 4255 cm^{-1}, where there is an apparent significant difference in the behavior of a band that is not simply a function of density. It was noted that changes resulting from a ~60 MPa change in pressure are of the same general magnitude as those resulting from a 50 K change in temperature.

2.3.4 Molar absorption coefficients

In addition to observing changes in the optical spectrum with pressure, volume, temperature, and composition, the direct measurement of density permits an approximate estimation of molar absorption coefficients and integrated molar absorption coefficients for pure or mixed fluids as a function of wavelength/energy. The best means of performing this calculation would be to compute the change in absorption with

pathlength (not with concentration, because that would change the density and lead to a change in the spectrum). Because the pathlength is not variable, the simpler, if less accurate, approach is taken of estimating from a single measurement using the Beer-Lambert law. The result for ethane is shown in Figure 2.7 given the known pathlength (from Equation 2.3) and density of the fluid (measured).

These molar absorption coefficients can be integrated over a particular band or group of bands to estimate the total transition strength of a particular infrared transition. In the simplest calculation, used here, the band integrated molar absorption coefficient is calculated as the sum of the pathlength and concentration normalized absorption spectrum over a the wavelengths for particular band. For comparison to literature, the log base 10 absorption molar absorption constant multiplied by 2.303 for consistency with the natural log base absorption units, A_j, for transition j, used by references (116-122), although, a more detailed calculation (116) corrects for multiple reflections that vary with wavelength, this correction is not performed here. Two additional forms of the integrated molar absorptivity that have the same units (typically km/mol) are found in literature. These additional forms are denoted as B_j and C_j but that are smaller than A_j by approximately one (B_j) or two (C_j) orders of magnitude for absorption bands for a typical organic liquid. The form A_j, which is commonly estimated by many computational chemistry programs and which is also typical of many reports in the chemical literature and is adopted here. Reports from the quantitative radiometry community more typically address one of the latter forms of total oscillator strength. The computation of B_j and C_j depend on calculation of real and imaginary refractive indexes for a fluid, which is not measured in the current work, followed by an assumption of a polarizability model; the

relation between the three measures is described in (117). The estimation of the integrated molar absorption coefficients for this work are complicated by the overlap of adjacent bands at the current pressures, leading to significant uncertainty for a single band. Also, the estimation of the molar absorption coefficient lacks of reflectance corrections and the lack of Kramers-Kronig analysis, and current uncertainties baseline subtraction further increase the uncertainty in molar absorption coefficients. That, in combination with the significant band overlap the molar absorption coefficients (A_j) provided here are estimated to have an accuracy of no better than ±50%.

Infrared molar absorption coefficients for fundamental vibrational modes are considerably smaller than those of electronic transitions, and values below 200 M^{-1} cm^{-1} are typical. Values of A_j for fundamental transitions are typically less than 1000 km/mol and often less than 100 km/mol for hydrocarbons (118). The coefficients shown in Figure 2.7 are considerably smaller, as are the integrated band areas that come from them. The only fundamentals shown in Figure 2.7 are those of the C-H stretching region (just above 3300 nm) extending above the plot off scale; all other transitions here are combination bands (overtones being forbidden in this symmetry group).

Table I provides a series of MIR and NIR absorption band centers observed in dense ethane fluid under the conditions in Figure 2.7, augmented by literature frequencies of the fundamentals and their symmetries. Hansen and Dennison (119), Shimanouchi (120), and Person and Zerbi (121) provide estimates of all 12 fundamental frequencies of ethane in the D_{3d} point group classification. These sources number the fundamentals differently and provide slightly different values of their frequencies. Here, the more standard numbering system of Shimanouchi (120) is followed to make symmetry

assignments for combination bands, and the frequencies themselves are a mix of those from Shimanouchi (120) and Person and Zerbi (121) that is currently accepted by the National Institute of Standards and Technology chemistry resource website.

Because the more intense combinations are expected to be those involving no more than two quanta of excitation, assignments are made to as many of the stronger observed combination bands as possible. Efforts were made to estimate the integrated absorption strength of each band for all recorded absorption bands because they contribute to the optical density of ethane under these conditions in the MIR and NIR spectral windows. Strengths of the five fundamental infrared-allowed transitions were not measured here but were taken from Nyquist et al. (122) with an appropriate conversion from log base 10 absorption units to natural log base absorption units. Based on these values, the strongest combination bands measured are ~3% as strong as the strongest fundamental in the ethane spectrum, with the smallest observed bands being more than two orders of magnitude weaker.

2.3.5 Multicomponent mixtures

Methyl mercaptan has been selected as a proxy for the study of mercaptans in natural gas. To study trace trace concentrations of methyl mercaptan in hydrocarbon gas, the windows of the UV-Vis cell were reset almost to maximum extent at 8.89cm. Figure 2.8 shows a binary mixture of 200 ppmV methyl mercaptan in methane from 200 nm to 300 nm . The data is acquired with a compression ratio of over twenty one times from an ambient pressure of 0.097 MPa (14.07 psi) to 2.069 MPa (300 psi) and an ambient temperature of 295.7K. The peak position is determined by a local second order polynomial fit over a centered 2.72 nm window to the 4 spectra as 204.52 nm +/- 0.08

nm to one standard deviation which agrees with well with literature reports of 204.0 nm (123) conducted at .0146 MPa (7.65 Torr) to 0.0780 MPa (601.1 Torr). The absorption cross section calculated for the current work at 0.097 MPa using a log base 10 absorption unit of 0.199 abs is $9.54X10^{-18}$ cm^2/molecule after converting to the natural log base which is in good agreement with the literature reported value of $8.49X10^{-18}$ cm^2/molecule.

A typical live crude oil was loaded according to experimental procedure and measured, with the visible-mid infrared spectrum shown in Figure 1.2. The normalized composition for the live oil measured as: methane 8.74 wt%, ethane 4.45 wt%, propane 2.61 wt% combined butane and pentane of 4.14 wt% remaining saturates C6+ fraction 53.53 wt%, aromatics C6+ fraction 15.03 wt%, resins C6+ fraction wt% 5.98 and asphaltenes C6+ fraction 5.37wt% with a density of 0.6753 at 82.76 MPa and 394K and bubble point of 980scf/bbl. The Peng-Robinson EOS predicts a GOR of 1058 scf/bbl, density of 0.6816 g/cc and bubble point of 19.82 MPa (2875 psi) at the same conditions. Estimation of bubble point was important to determine that the sample would be single phase above 20.69 MPa (3000 psi) the typical start pressure in this experimental run at the highest temperature of 394K. The critical temperature for this fluid was predicted as 616K (650F), so the sample was liquid phase for all experimentation. Care was taken for the lowest pressure experimentation of 20.69 MPa since the Peng-Robinson EOS predicted bubble point was very close to this start pressure. During experimentation the bubble point was measured as 17.59 MPa (2550 psi) for 394 F.

The spectrum of Figure 2.9 demonstrates a typical live oil measurement spectrum in the system at 1mm pathlength. The pathlength of 1mm provides sufficient

transmission light for measurements above approximately 500 nm , with the exception of the fundamental CH stretch centered just below 3400 nm. For this setup, the limit of absorbance measurements in the visible was just below 3 abs, and in the near and mid infrared just below 2.5 abs. The spectrum shows a highly overlapping set of peaks without much individual resolution of the various classes of molecules present, and shows that a multivariate calibration technique may be necessary to extract chemical information. The ν3 carbon dioxide overtone band with a center at 4257 nm (2349 cm^{-1}), (124), is observed without much interference from other species, however, the P and R branch have largely merged due to peak broadening at these pressures.

2.4 CONCLUSION

The small-volume PVTX system for broad-band spectral calibration studies presented here was found to have a volume near 5.5 mL, up to a maximum volume near 9 mL. It provides the ability to charge dead oils with volatiles and to make oil mixtures, while recording spectral data continuously covering the entire spectral range between 400 nm (25 000 cm^{-1}) and 5000 nm (2000 cm^{-1}) for oils, or between 200 nm (50 000 cm^{-1}) and 5000 nm (2000 cm^{-1}) for gas and condensate samples, while varying the pressure and temperature systematically over the pressure range of 0 to 138 MPa and at temperatures between room temperature and 422 K. Comparisons of density measured as a function of pressure and temperature with the best available literature values for a single-component fluid provides a mean error of zero, within experimental certainty. The spectra from this tool are suited to chemometric analysis and physico-chemical measurements.

Table 2.1 Fundamentals and observed combination bands of ethane from Figure 2.7.[a]

ν (/cm)	λ (nm)	Assignment	Symmetry	A_j (km/mol)
2954	…	ν_1	A_{1g}	…
1388	…	ν_2	A_{1g}	…
995	…	ν_3	A_{1g}	…
289	…	ν_4	A_{1u}	…
2896	…	ν_5	A_{2u}	47.8
1379	…	ν_6	A_{2u}	4.0
2969	…	ν_7	E_g	…
1468	…	ν_8	E_g	…
1190	…	ν_9	E_g	…
2985	…	ν_{10}	E_u	123.2
1469	…	ν_{11}	E_u	13.4
822	…	ν_{12}	E_u	6.1
2005	4988	$\nu_9 + \nu_{12}$	$E_g \times E_u$	0.14
2221	4502	$\nu_2 + \nu_{12}$	E_u	0.37
2359	4239	$\nu_3 + \nu_6$	A_{2u}	1.1
2655	3766	$\nu_9 + \nu_{11}$	$E_g \times E_u$	1.4
2769	3611	$\nu_2 + \nu_6$	A_{2u}	2.8
3225	3101	$\nu_4 + \nu_7$	E_u	1.9
3395	2946	…	…	0.14
3645	2743	…	…	0.07
3763	2657	$\nu_7 + \nu_{12}$	$E_g \times E_u$	1.1
3935	2541	…	…	0.35
4106	2435	$\nu_5 + \nu_9$	E_u	3.3
4139	2416	$\nu_9 + \nu_{10}$	$E_g \times E_u$	2.6
4338	2305	$\nu_6 + \nu_7$	E_u	3.5
4396	2275	$\nu_2 + \nu_{10}$	E_u	2.7
4621	2164	…	…	0.12
4737	2111	…	…	0.05
4952	2019	…	…	0.18
5262	1900	…	…	0.05
5341	1872	…	…	0.02
5437	1839	…	…	0.05
5546	1803	…	…	0.07
5685	1759	…	…	0.23
5800	1724	$\nu_1 + \nu_5$	A_{2u}	0.69
5909	1692	$\nu_1 + \nu_{10}$ or $\nu_5 + \nu_{10}$	E_u	1.1
6972	1434	…	…	0.14
7209	1387	…	…	0.32
8440	1185	…	…	0.30

[a]Frequencies have been converted to wavenumbers; numbering of fundamentals follows Shimanouchi (*1*) (120). Assignments of the

combination bands are given where possible. Combinations that involve more than two vibrations are not assigned. The overall symmetry of assigned combinations is provided for the D_{3d} point group. An estimate of the integrated molar absorptivity from the spectrum converted to units of km/mole is provided. Values for fundamentals were taken from (*2*) (122).

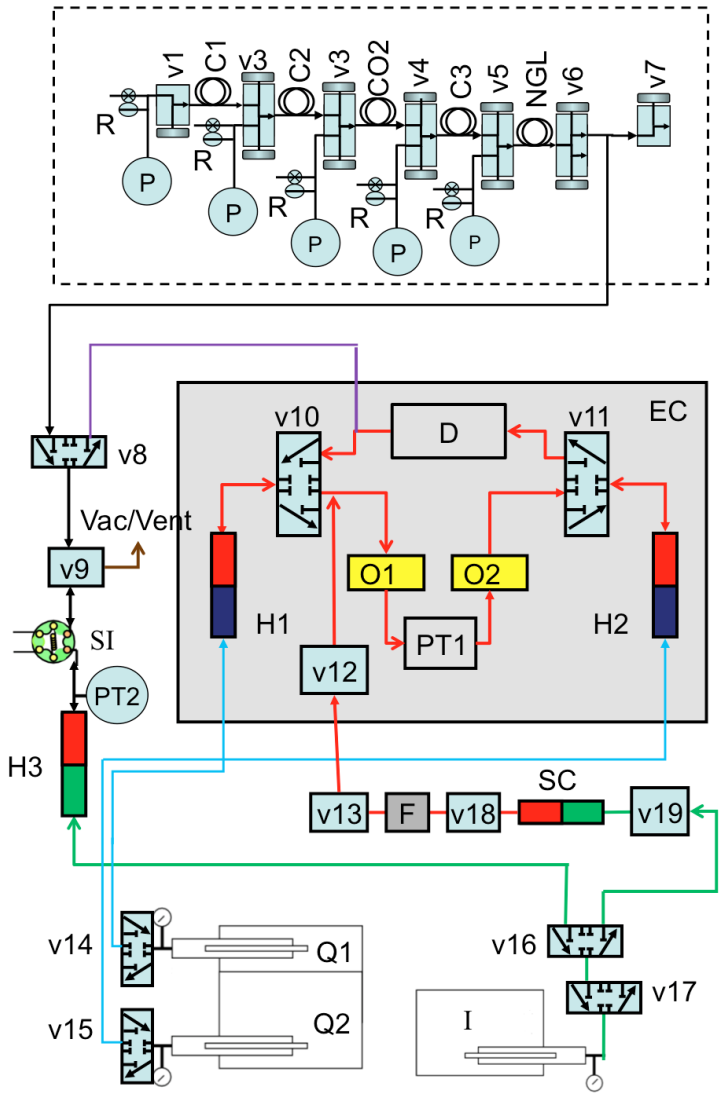

Figure 2.1 Schematic. The top section is used to prepare injections of volatiles. The center section is the main section of the PVTX instrument housed in an oven. The lower right portion of the instrument is used to prepare and inject nonvolatiles and to extract samples for analysis. Valves are labeled v1 to v19; I is a pump driving hydraulic sample injection pumps H3 and SC; Q1 and Q2 are pumps driving hydraulic recirculating pumps H1 and H2, respectively; F is a particulate filter for injected oils; SI is a sample-injection valve; D is a densitometer; PT1 is a pressure and temperature gauge; EC is an oven enclosing the temperature-regulated portion of the instrument; O1 and O2 are fiber-coupled optical cells for FTIR and UV-visible spectroscopy, respectively; C1, C2, CO2, C3, and NGL represent sample loops that can be loaded with volatiles for preparing injections. All Rs represent gas regulators for the respective volatiles, and all Ps represent pressure gauges for the volatiles. See the text for details.

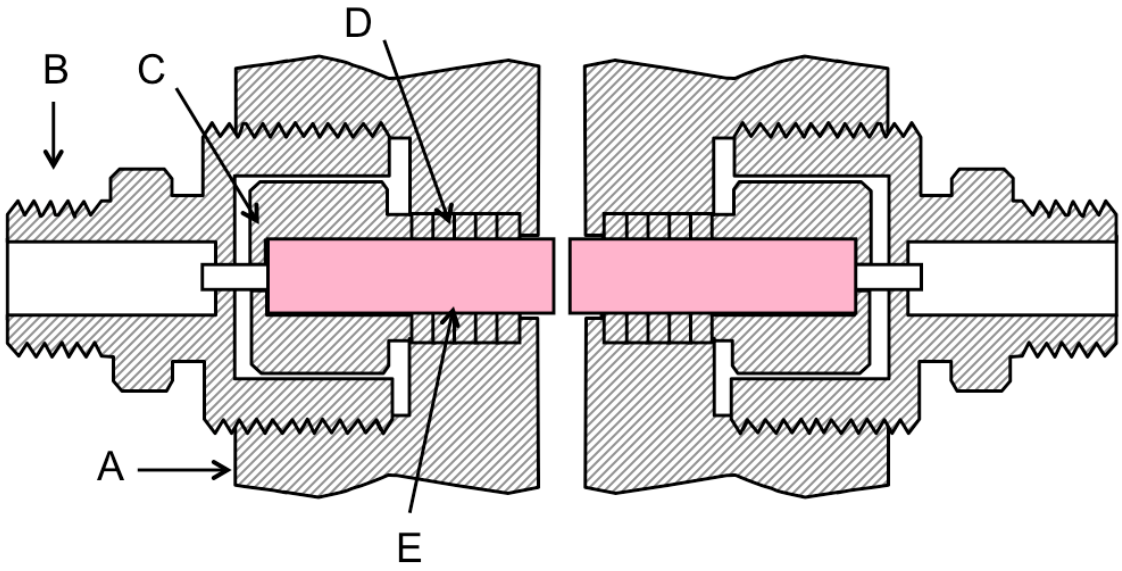

Figure 2.2 Optical cell sketch. The stainless steel cell (A) is constructed to couple to a SMA fiber connector (B). The light is coupled to a 1/8-in. sapphire rod (E) that is held in place with a custom bushing (C) and seal (D). Each sapphire rod extends into the flow path and is set to provide a 1-mm optical pathlength.

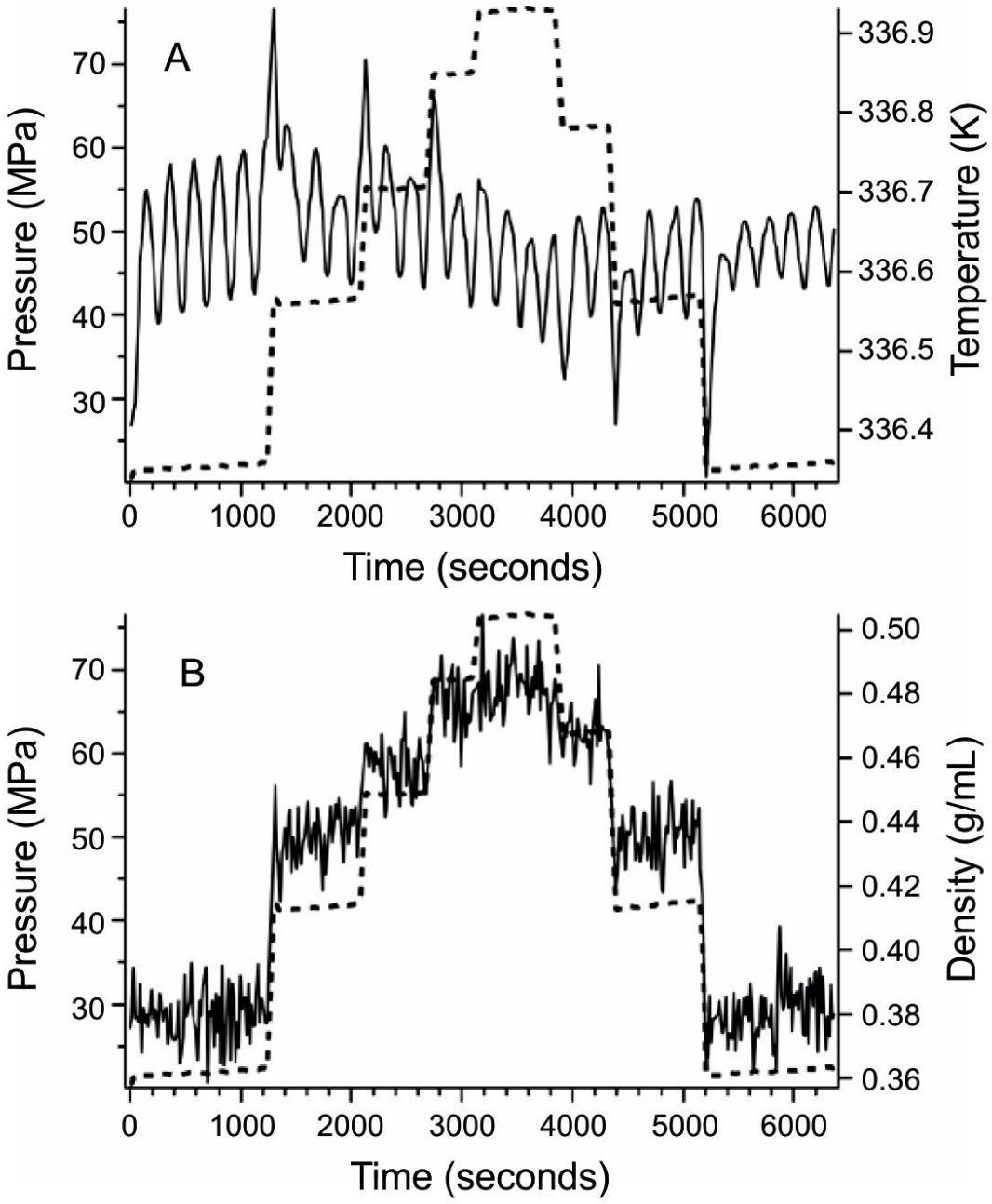

Figure 2.3 Pressure, temperature, and density measurements for a typical isothermal compression/decompression cycle for ethane: (A) measured pressure (dashed line, left axis) during cycle and measured pressure (solid line, right axis). Regular temperature fluctuations result from the reversals of the mixing pumps. Spikes in the instantaneous temperature occur at each step of compression/decompression, but all within approximately 0.5 K of the setpoint. Spectroscopic measurements are made after settling; (B) density (solid line, right axis) during the same cycle as measured by the *in situ* densitometer. Correspondence between these measurements and literature are described in the text.

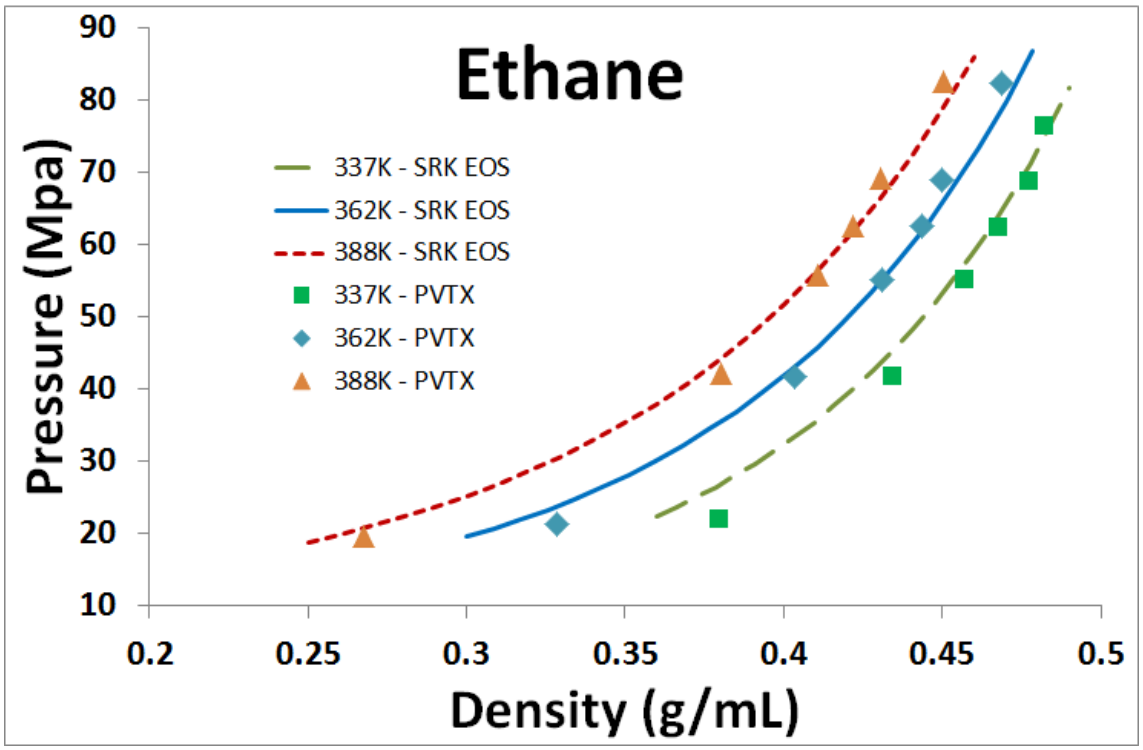

Figure 2.4 Measured density and pressure (PVTX) of ethane under isothermal conditions with the calculated pressure (SRK EOS) for a given density at the same isothermal conditions.

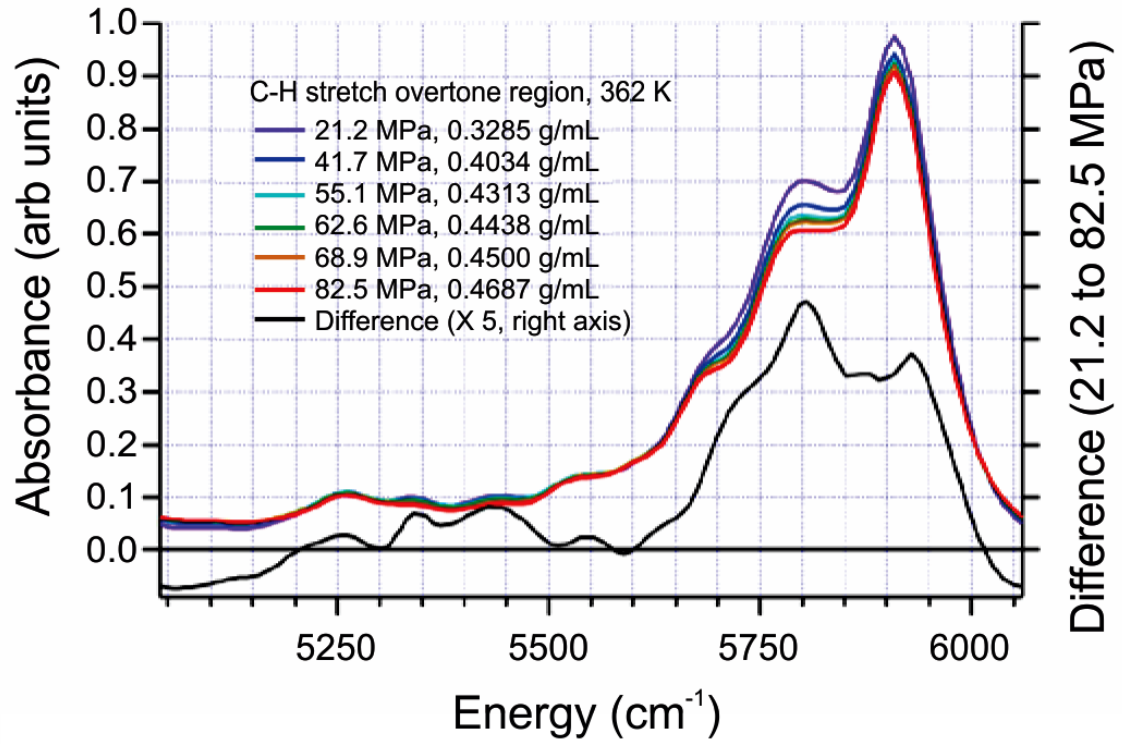

Figure 2.5 Ethane absorption spectra in the NIR region between 5040 to 6060 cm^{-1} (1650 to 1850 nm) under isothermal conditions at 362 K for a range of pressures. Colored curves correspond to the left axis and have been compensated for the density and pathlength changes as a function of pressure and then scaled together for illustrative purposes. The black curve represents the difference between the lowest and highest pressure conditions. Again, in arbitrary units, the zero for this curve is the black horizontal line. Arbitrary scales on the left and right have the same range but different zeros; the black curve has been multiplied by a factor of five for clarity.

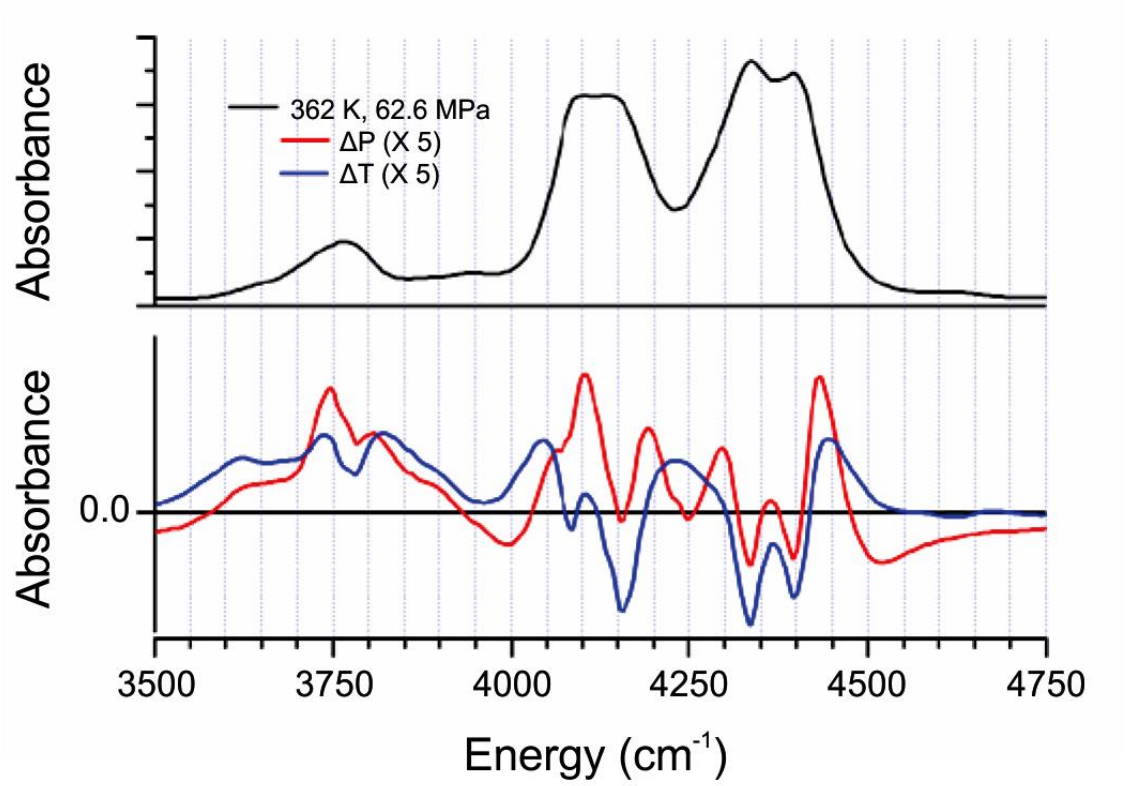

Figure 2.6 Ethane spectra respond differently to changes in temperature and pressure. The top curve is the absorption spectrum (corrected for density and pathlength) at a particular temperature and pressure in the strongest part of the NIR spectrum. The colored curves represent changes in absorption in this spectral window when the temperature or pressure vary around this condition. Both difference curves are between the lower and higher density conditions. The red curve represents the change in absorption with pressure, calculated as the difference between a low (21.2 MPa) and high (82.5 MPa) pressure spectrum. The blue curve represents the difference between a high (388 K) and low (337 K) temperature spectrum. The blue and red curves lie on the same arbitrary axis, with the zero difference line shown as a horizontal black line. The colored curves are each multiplied by five to show them on the same axis range as the upper curve.

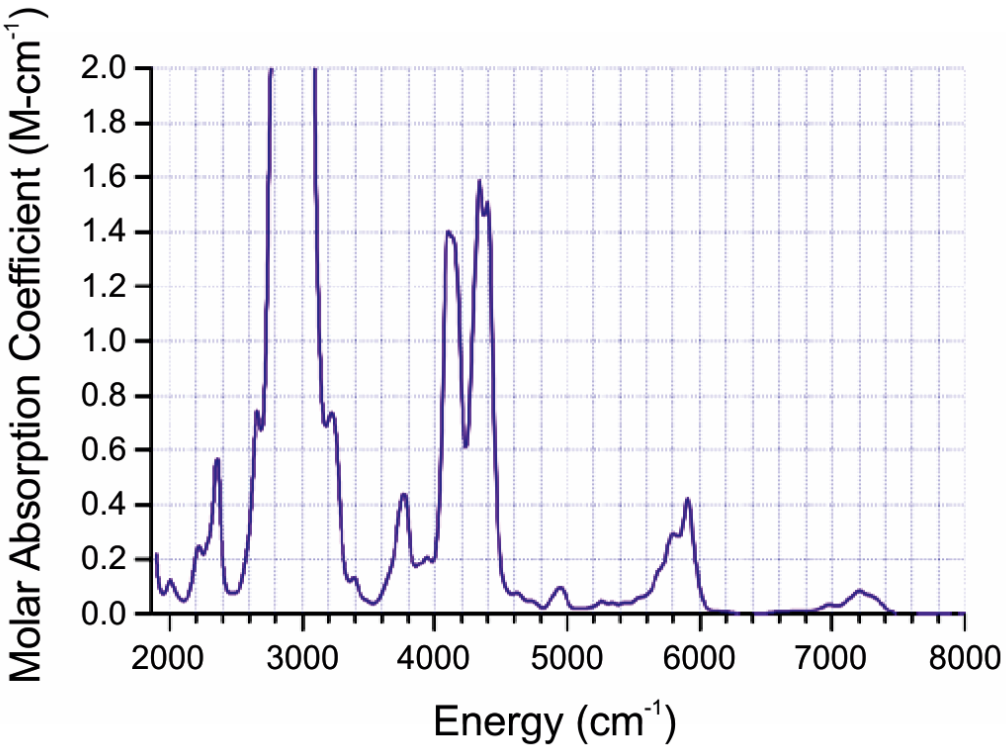

Figure 2.7 Ethane molar absorption coefficient in the C-H stretching fundamental absorption region near 3000 cm^{-1} out to the short-wave NIR. The fundamental absorptions themselves are too strong to be measured in this spectrum because of the relatively long pathlength. All of the stronger bands here have been assigned as either fundamentals (off scale) or combination bands of ethane in Table 2.1.

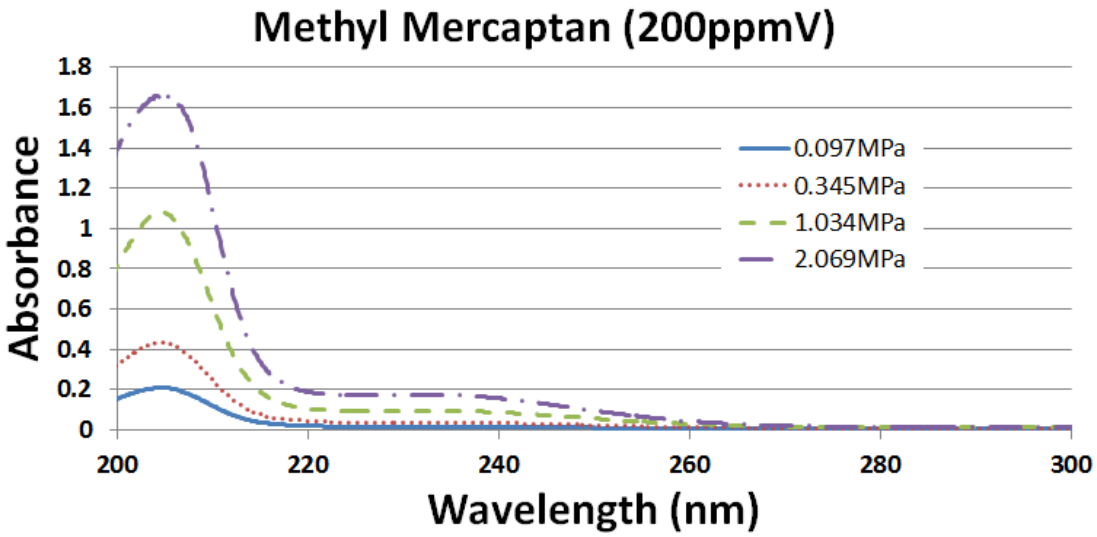

Figure 2.8 200 parts per million by volume (ppmV) methyl mercaptan (methanethiol) in a balance of methane as a function of pressure at 8.89cm pathlength.

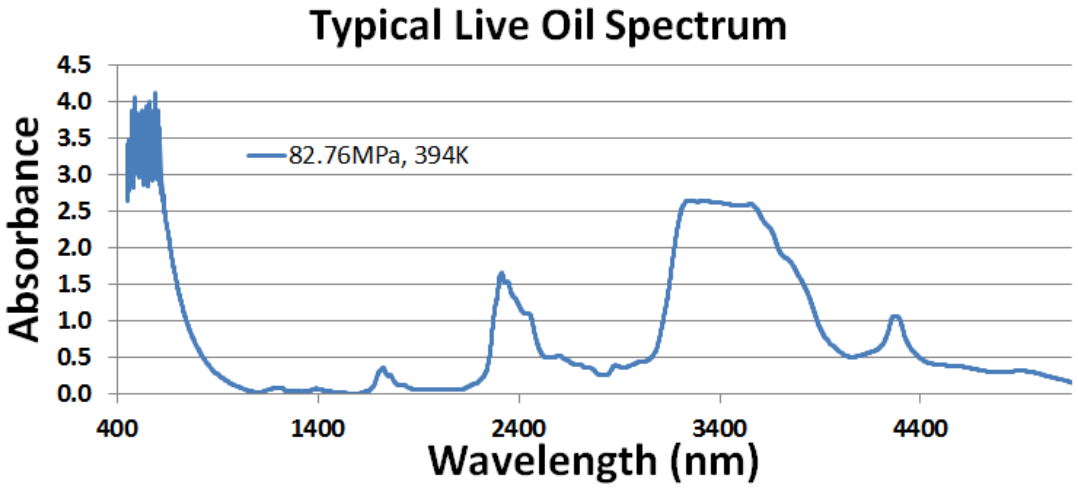

Figure 2.9 A typical live oil spectrum shown from 450 nm in the visible to 5000 nm in the mid infrared acquired at a pressure of 82.76 MPa and 394K 1mm pathlength. Absorbance limit for the visible spectrometer is above 3 abs and for the FTIR spectrometer above 2.5 abs.

REFERENCES

1. McCain Jr., W. D. *The Properties of Petroleum Fluids, 2nd Ed.;* Pennwell Books: Tulsa OK, 1990.

2. Groenzin, H.; Mullins, O. C. Asphaltene Molecular Size and Structure. *Journal of Physical Chemistry A* **1999,** *103* (50), 11237–11245.

3. Petroleum Society of CIM. *Determination of Oil and Gas Reserves,* 1st ed.; Petroleum Society of the Canadian Institute of Mining, Metallurgy and Petroleum: Altona, MB Canada, 1994; Vol. 1, p 41.

4. Boduszynski, M. M. Composition of heavy petroleums. 1. Molecular weight, hydrogen deficiency, and heteroatom concentration as a function of atmospheric equivalent boiling point up to 1400.degree.F (760.degree.C). *Energy and Fuels* **1987,** *1* (1), 2–11.

5. Fox, J. N.; Martiniuk, C. D. Reservoir Characteristics And Petroleum Potential of the Bakken Formation, Southwestern Manitoba. *Journal of Canadian Petroleum Technology* **1994,** *33* (8), 19-27.

6. Coto, B.; Martos, C.; Espada, J. J.; Robustillo, M. D.; Peña, J. L. Analysis of paraffin precipitation from petroleum mixtures by means of DSC: Iterative procedure considering solid–liquid equilibrium equations. *Fuel* **2010,** *89* (5), 1087-1094.

7. Fernandez-Lima, F. A.; Becker, C.; McKenna, A. M.; Rodgers, R. P.; Marshall, A. G.; Russell, D. H. Petroleum Crude Oil Characterization by IMS-MS and FTICR MS. *Analytical Chemistry* **2009,** *81* (24), 9941–9947.

8. Mullins, O.; Daigle, T.; Crowell, C.; Groenzin, H. Gas-Oil Ratio of Live Crude Oils Determined by Near-Infrared Spectroscopy. *Applied Spectroscopy* **2001,** *55* (2), 197-201.

9. Mullins, O. C. Methods and apparatus for determining gas-oil ratio in a geological formation through the use of spectroscopy. 5,939,717, August 17th, 1999.

10. Hashem, M.; McHardy, A.; Wynne, M.; Pool, W.; Viets, T.; Keuser, C.; Eriksen, K. O. Formation Pressure While Drilling, Wireline Formation Testing, And Fluid Sampling In a High Pressure/High Temperature Exploration Well Using Oil Based Mud: A Case History1. *Petrophysics* **2007,** *48* (4), 258-270.

11. Exploration, C. s. d. l. r. e. d. l. p. d. p. e. d. g. n. C. *Wireline Logging Tool Catalog: Publications de la Chambre syndicale de la recherche et de la production du pétrole et du gaz naturel;* Technip, 1984.

12. Ellis, D. V.; Singer, J. M. *Well logging for Earth Scientists, 2nd Ed.,* 2nd ed.; Springer: Dordrecht, 2008.

13. Crombie, A.; Halford, F.; Hashem, M.; McNeil, R.; Thomas, E.; Melbourne, G.; Mullins, O. Innovations in Wireline Fluid Sampling. *Oilfield Review* **1998,** *10* (3), 26-41.

14. Andrews, A.; Schneider, M.; Canas, J.; Freitas, E.; Song, Y.; Mullins, O. Fluorescence Methods for Downhole Fluid Analysis of Heavy Oil Emulsions. *Journal of Dispersion Science and Technology* **2008,** *29* (2), 171-183.

15. Dong, C.; O'Keefe, M.; Elshahawi, H.; Hashem, M.; Williams, S.; Stensland, D.; Hegeman, P.; Vasques, R.; Terabayashi, T.; Mullins, O.; Donzier, E. New downhole-fluid-analysis tool for improved reservoir characterization. *SPE Reservoir Evaluation and Engineering* **2008,** *11* (6), 1107-1116.

16. Mullins, O.; Rodgers, R.; Weinheber, P.; Klein, G.; Venkataramanan, L.; Andrews, A.; Marshal, A. Oil Reservoir Characterization via Crude Oil Analysis by Downhole Fluid Analysis in Oil Wells with Visible−Near-Infrared Spectroscopy and by Laboratory Analysis with Electrospray Ionization Fourier Transform Ion Cyclotron Resonance Mass Spectrometry. *Energy and Fuels* **2006,** *20* (6), 2448-2456.

17. Mullins, O. C.; Joshi, N. B.; Groenzin, H.; Daigle, T.; Crowell, C.; Joseph, M. T.; Jamaluddin, A. Linearity of Near-Infrared Spectra of Alkanes. *Applied Spectroscopy* **2000,** *54* (4), 624-629.

18. Honigs, D. E. Near Infrared Analysis. *Instrumentation Science and Technology* **1985,** *14* (1), 1-62.

19. Janata, J. Chemical sensors. *Analytical Chemistry* **1992,** *64* (12), 196–219R.

20. Rabkin, Y. M. Technological Innovation in Science: The Adoption of Infrared Spectroscopy by Chemists. *Isis* **1987,** *78* (1), 31-54.

21. Workman, J. .; Veltkamp, D. J.; Doherty, S.; Anderson, B. B.; Creasy, K. E.; Koch, M.; Tatera, J. F.; Robinson, A. L.; Bond, L.; Burgess, L. W.; Bokerman, G. N.; Ullman, A. H.; Darsey, G. P.; Mozayeni, F.; Bamberger, J. A. Process Analytical Chemistry. *Analytical Chemistry* **1999,** *71* (12), 121–180R.

22. Watari, M. Applications of near-infrared spectroscopy to process analysis using fourier transform spectrometer. *Optical Review* **2010,** *17* (3), 317–322.

23. Sulub, Y.; LoBrutto, R.; Vivilecchia, R.; Wabuyele, B. W. Content uniformity determination of pharmaceutical tablets using five near-infrared reflectance spectrometers: A process analytical technology (PAT) approach using robust multivariate calibration transfer algorithms. *Analytica Chimica Acta* **2008,** *611* (2),

143-150.

24. Bamford, D. J.; Cook, D. J.; Sharpe, S. J.; Van Pelt, A. D. Widely tunable rapid-scanning mid-infrared laser spectrometer for industrial gas process stream analysis. *Applied Optics* **2007,** *46* (19), 3958-3968.

25. Fayolle, P.; Picque, D.; Corrieu, G. On-line monitoring of fermentation processes by a new remote dispersive middle-infrared spectrometer. *Food Control* **2000,** *11* (4), 291-296.

26. Martin, R. L.; Thomas, B. W. Infrared Gas Analyzer for Butane Splitter Control. *Industrial and Engineering Chemistry* **1954,** *46* (7), 1393–1396.

27. Simonsen, D. R.; Crouch, H. W. Monitoring of Solvent-Air Mixtures with Infrared Analyzers. *Industrial and Engineering Chemistry* **1957,** *49* (10), 1741–1743.

28. Barnes, R.; Liddel, U.; Williams, V. Synthetic Rubber, A Spectroscopic Method for Analysis and Control. *Industrial and Engineering Chemistry* **1943,** *15* (8), 83–90.

29. Barnes, R. *Spectroscopy in Science and Industry: Proceedings of the Fifth Summer Conference on Spectroscopy and its Applications, Massachusetts;* John Wiley and Sons: New York, 1938; pp 71-75.

30. Barr, E. S. Men and milestones in optics. VI: The rise of infrared spectroscopy in the U.S.A. to World War II. *Applied Optics* **1976,** *15* (7), 1707-1721.

31. Deinum, H. W.; Rietveld, B. J. Some experiments with the Baird associates infra-red gas analyser. *Recueil des Travaux Chimiques des Pays-Bas Journal of the Royal Netherlands Chemical Society* **1948,** *67* (9), 725–736.

32. Biggs, D. A. Milk Analysis with the Infrared Milk Analyzer. *Journal of Dairy Science* **1967,** *50* (5), 799–803.

33. van de Voort, F. R. Evaluation of MIlkoscan 104 Infrared Milk Analyser. *Journal of the Association of Official Analytical Chemists* **1980,** *63* (5), 973-980.

34. Lawson, D.; Samanta, S.; Magee, P. T.; Gregonis, D. E. Stability and long-term durability of raman spectroscopy. *Journal of Clinical Monitoring* **1993,** *9* (4), 241–251.

35. Everall, N.; Owen, H.; Slater, J. Performance Analysis of an Integrated Process Raman Analyzer Using a Multiplexed Transmission Holographic Grating, CCD Detection, and Confocal Fiber-Optic Sampling. *Applied Spectroscopy* **1995,** *49* (5), 610-615.

36. Freeman, J. J.; Fisher, D. O.; Gervasio, G. J. FT-Raman On-Line Analysis of PCI3

Reactor Material. *Applied Spectroscopy* **1993,** *47* (8), 1115-1122.

37. Lykken, L.; Treseder, R. S.; Zahn, V. Colorimetric Determination of Phenols. Application to Petroleum and Allied Products. *Industrial and Engineering Chemistry Analytical Edition* **1946,** *18* (2), 103–109.

38. Mullins, O. C.; Mitra-Kirtley, S.; Zhu, Y. The Electronic Absorption Edge of Petroleum. *Applied Spectroscopy* **1992,** *46* (9), 1405-1411.

39. Mullins, O. C.; Zhu, Y. First Observation of the Urbach Tail in a Multicomponent Organic System. *Applied Spectroscopy* **1992,** *46* (2), 354-356.

40. Deutsch, K.; Kühn, H.-J.; Polzin, M.; Deutsch, I.; Grunow, S.; Stöcker, J. Aromatic Structure Type Analysis of Hydrotreated Petroleum Fractions by U.V.-Spectroscopy. *Journal für Praktische Chemie* **1987,** *329* (4), 681-698.

41. Ramaswamy, V. Applications of ultraviolet spectroscopy in the analysis of petroleum constituents. *Journal of Scientific and Industrial Research* **1981,** *40,* 584 - 5595.

42. Schmidt, V. H. UV- und NIR-Absorptionsspektroskopie fur die Analyses von Aromatengemischen. *Erdoel, Kohle, Erdgas, Petrochem* **1968,** *21* (6), 334-340.

43. Schmidt, V. H. Die quantitative UV-spektrometrische Analyse von Gemishen hochisedender Aromaten. *Erdoel, Kohle, Erdgas, Petrochem* **1966,** *19* (4), 275-278.

44. Badry, R.; Fincher, D.; Mullins, O.; Schroeder, B.; Smits, T. Downhole Optical Analysis of Formation Fluids. *Oilfield Review* **1994,** *6* (1), 21-28.

45. Abbas, O.; Dupuy, N.; Rebufa, C.; Vrielynck, L.; Kister, J.; Permanyer, A. Prediction of source rock origin by chemometric analysis of fourier transform infrared-attenuated total reflectance spectra of oil petroleum: evaluation of aliphatic and aromatic fractions by self-modeling mixture analysis. *Applied Spectrosctroscopy* **2006,** *60* (3), 304-314.

46. De Peinder, P.; Petrauskas, D. D.; Singelenberg, F.; Salvatori, F.; Visser, T.; Soulimani, F.; Weckhuysen, B. M. Prediction of Long and Short Residue Properties of Crude Oils from Their Infrared and Near-Infrared Spectra. *Applied Spectroscopy* **2008,** *62,* 414-422.

47. Satya, S.; Roehner, R. M.; Deo, M. D.; Hanson, F. V. Estimation of properties of crude oil residual fractions using chemometrics. *Energy and Fuels* **2007,** *21* (2), 998-1005.

48. Van Agthoven, M. A.; Fujisawa, G.; Rabbito, P.; Mullins, O. C. Near-Infrared Spectral Analysis of Gas Mixtures. *Applied Spectroscopy* **2002,** *56* (5), 593–598.

49. Fujisawa, G.; Van Agthoven, M. A.; Jenet, F.; Rabbito, P. A.; Mullins, O. C. Near-infrared compositional analysis of gas and condensate reservoir fluids at elevated pressures and temperatures. *Applied Spectroscopy* **2002,** *56* (12).

50. Malinowski, E. R. *Factor Analysis in Chemistry, 2nd ed.;* Wiley-Interscience: New York, 1991.

51. Norris, K. H.; Ritchie, G. E. Assuring specificity for a multivariate near-infrared (NIR) calibration: The example of the Chambersburg Shoot-out 2002 data set. *Journal of Pharmaceutical and Biomedical Analysis* **2008,** *48* (3), 1037-1041.

52. Næs, T.; Isaksson, T. Locally Weighted Regression in Diffuse Near-Infrared Transmittance Spectroscopy. *Applied Spectroscopy* **1992,** *46* (1), 34-43.

53. Zhuan, W.; Kiran, E. An automated high pressure PVT apparatus for continuous recording of density and isothermal compressibility of fluids. *Review of Scientific Instruments* **1996,** *67* (1), 244-250.

54. Kamimura, T.; Iso, A.; Y. Higashi, A.; Uematsu, M.; Watanabe, K. Apparatus for measurements of PVT properties and their derivatives for fluids and fluid mixtures with a metal bellows as a variable-volume vessel. *Review of Scientific Instruments* **1989,** *60* (9), 3055-3061.

55. Linsky, D.; Sengers, L. J. M. H.; Davis, H. A. Semiautomated PVT facility for fluids and fluid mixtures. *Review of Scientific Instruments* **1987,** *58* (5), 817-821.

56. Seitz, J. C.; Blencoe, J. G.; Joyce, D. B.; Bodnar, R. J. Volumetric properties of CO2-CH4-N2 fluids at 200°C and 1000 bars: A comparison of equations of state and experimental data. *Geochimica et Cosmochimica Acta* **1994,** *58* (3), 1065-1071.

57. Kiran, E.; Sen, Y. L. High-pressure viscosity and density of n-alkanes. *International Journal of Thermophysics* **1992,** *13* (6), 411–442.

58. Babb Jr., S. E.; Scott, G. J.; Epp, C. D.; Robertson, S. L. Apparatus for PVT Measurements of Gases to 10 Kilobars. *Review of Scientific Instruments* **1969,** *40* (5), 670-675.

59. Tekáč, V.; Cibulka, I.; Holub, R. PVT properties of liquids and liquid mixtures: a review of the experimental methods and the literature data. *Fluid Phase Equilibria* **1984,** *19* (1), 33-149.

60. Kennedy, G. C. Pressure-volume-temperature relations in water at elevated temperatures and pressures. *American Journal of Science* **1950,** *248* (8), 540-564.

61. Van Nieuwenburg, C. J.; Blumendal, H. The isotherms of water from 350-480° c and for pressures up to 600 kg/cm2. *Recueil des Travaux Chimiques des Pays-Bas*

1932, *15* (8), 707–811.

62. Tammann, G.; Ruhenbeck, A. Die spezifischen Volumen des Wassers zwischen 20° und 650°, die des Äthyläthers und des Äthylalkohols zwischen 20° und 400° bei Drucken von 1-2500 kg/cm2. *Annalen der Physik* **1932,** *405* (1), 63–79.

63. Jacoby, R.; Yarborough, L. PVT Measurements on Petroleum Reservoir Fluids and Their Uses. *Industrial and Engineering Chemistry* **1967,** *59* (10), 48–62.

64. Bridgman, P. W. The Volume of Eighteen Liquids as a Function of Pressure and Temperature. *Proceedings of the American Academy of Arts and Sciences* **1931,** *66* (5), 185-233.

65. Francis, A. W. Pressure-temperature-density relations of pure liquids. *Chemical Engineering Science* **1959,** *10* (1), 37-46.

66. Rahman, S.; Barrufet, M. A. A new technique for simultaneous measurement of PVT and phase equilibria properties of fluids at high temperatures and pressures. *Journal of Petroleum Science and Engineering* **1995,** *14* (1), 25-34.

67. Funke, M.; Kleinrahm, R.; Wagner, W. Measurement and correlation of the (p, ρ, T) relation of ethane II. Saturated-liquid and saturated-vapour densities and vapour pressures along the entire coexistence curve. *The Journal of Chemical Thermodynamics* **2002,** *34* (12).

68. Tapavicza, V. . B. M. . F. E. U. . High-Pressure Infrared Cell for Kinetic Investigations to 3 kbar and 300 °C. *High Temperatures-High Pressures* **1975,** *7* (5), 535-538.

69. Brantley, N. H. . K. S. G. . E. C. A. . In situ FTIR measurement of carbon dioxide sorption into poly(ethylene terephthalate) at elevated pressures. *Jorunal of Applied Polymer Science* **2000,** *77* (4), 764-775.

70. Dowy, S. . B. A. . R.-L. K. . L. A. Laser analyses of mixture formation and the influence of solute on particle precipitation in the SAS process. *The Journal of Supercritical Fluids* **2009,** *50* (3), 265-275.

71. Braeur, A. *Supercritical Science Technology Series Volume 7: In Situ Spectroscopic Techniques at High Pressure;* Elsevier: Amsterdam, Netherlands, 2015.

72. Peng, D. Y. . a. R. D. B. A New Two-Constant Equation of State. *Industrial and Engineering Chemistry Fundamentals* **1976,** *15* (59), 59-64.

73. Soave, G. Equilibrium Constants from a Modified Redlich-Kwong Equation of State. *Chemical Engineering Science* **1972,** *27* (6), 1197-1203.

74. Muirhead, C. R. Distinguishing outlier types in time series. *Journal of the Royal Statistical Society, Series B* **1986,** *48* (1), 39-47.

75. Pedersen, K. . a. P. L. C. P. *Phase Behavior of Petroleum Reservoir Fluids;* CRC Press: Boca Raton, 2007.

76. Bucker, D.; W. Wagner, D. A Reference Equation of State for the Thermodynamic Properties of Ethane for Temperatures from the Melting Line to 675 K and Pressures up to 900 MPa. *Journal of Physical and Chemical Reference Data* **2006,** *35* (1), 205-266.

77. Claus, P.; Kleinrahm, R.; Wagner, W. Measurements of the (p,ρ,T) relation of ethylene, ethane, and sulphur hexafluoride in the temperature range from 235 K to 520 K at pressures up to 30 MPa using an accurate single-sinker densimeter. *The Journal of Chemical Thermodynamics* **2003,** *35* (1), 159-175.

78. Byun, H.-S.; DiNoia, T. P.; McHugh, M. A. High-Pressure Densities of Ethane, Pentane, Pentane-d12, 25.5 wt Ethane in Pentane-d12, 2.4 wt Deuterated Poly(ethylene-co-butene) (PEB) in Ethane, 5.3 wt Hydrogenated PEB in Pentane, 5.1 wt Hydrogenated PEB in Pentane-d12, and 4.9 wt Hydrogenated PEB. *Journal of Chemical and Engineering Data* **2000,** *45* (5), 810–814.

79. Setzmann, U.; Wagner, W. A New Equation of State and Tables of Thermodynamic Properties for Methane Covering the Range from the Melting Line to 625 K at Pressures up to 100 MPa. *Journal of Physical and Chemical Reference Data* **1991,** *20* (6), 1061-1155.

80. Klimeck, J.; Kleinrahm, R.; Wagner, W.. Measurements of the(p,ρ,T) relation of methane and carbon dioxide in the temperature range 240 K to 520 K at pressures up to 30 MPa using a new accurate single-sinker densimeter. *The Journal of Chemical Thermodynamics* **2001,** *33* (3), 251-267.

81. Sherman, W. F.; Wilkinson, G. R. Raman and infrared studies of crystals at variable pressure and temperature. In *Advances in Infrared and Raman Spectroscopy;* Clark, R. J. H., Hester, R. E., Eds.; JohnWiley and Sons: New York, 1980; Chapter 4, Vol. 6, pp 206–220.

82. Sherman, W. F. Vibrational spectroscopy under high pressure. *Bulletin de la Societe Chimique de France: Partie 2, Chimie moléculaire, organique et biologique* **1982,** *49* (11), 347-369.

83. Welsh, H. L.; Sandiford, P. J. The Absolute Intensity of the ν4 Infrared Absorption Band of Methane and Its Enhancement by Nitrogen at High Pressures. *The Journal of Chemical Physics* **1952,** *20* (10), 1646-1647.

84. Welsh, H. L.; Sandiford, P. J. The Absolute Intensity of the ν4 Infrared Absorption Band of Methane and Its Enhancement by Nitrogen at High Pressures. *The Journal*

of Chemical Physics **1952,** *20* (10), 1646-1647.

85. Polo, S. R.; Wilson, M. K. Infrared Intensities in Liquid and Gas Phases. *The Journal of Chemical Physics* **1955,** *23* (12), 2376-2377.

86. Jaffe, J. H.; Kimel, S. Infrared Intensities in Liquids. *The Journal of Chemical Physics* **1956,** *25* (2), 374-375.

87. Blitz, J. P.; Yonker, C. R.; Smith, R. D. Infrared spectroscopic studies of supercritical fluid solutions. *The Journal of Physical Chemistry* **1989,** *93* (18), 6661–6665.

88. Onsager, L. Electric Moments of Molecules in Liquids. *Journal of the American Chemical Society* **1936,** *58* (8).

89. Badger, R. M. A Relation Between Internuclear Distances and Bond Force Constants. *The Journal of Chemical Physics* **1934,** *2* (3), 128-131.

90. Badger, R. M. The Relation Between the Internuclear Distances and Force Constants of Molecules and Its Application to Polyatomic Molecules. *The Journal of Chemical Physics* **1935,** *3* (11), 710-714.

91. Zallen, R. Pressure-Raman effects and vibrational scaling laws in molecular crystals: S8 and As2S3. *Physical Review B: Condensed Matter* **1947,** *9* (10), 4485-4496.

92. Wu, Y. H.; Shimizu, H. High-pressure Raman study of liquid and crystalline CH3F up to 12 GPa. *The Journal of Chemical Physics* **1995,** *102* (3), 1157-1163.

93. Hansen, S. B.; Berg, R. W.; Stenby, E. H. Raman Spectroscopic Studies of Methane—Ethane Mixtures as a Function of Pressure. *Applied Spectroscopy* **2001,** *55* (6).

94. Sherman, W. F.; Smulovitch, P. P. Pressure-Scanned Fermi Resonance in the Spectrum of NH4+ Isolated in CsBr. *The Journal of Chemical Physics* **1970,** *52* (10), 5187-5193.

95. Lewis, S.; Sherman, W. F. Pressure-scanned Fermi resonances in the vibrational spectra of the sulphate ion. *Spectrochimica Acta Part A: Molecular Spectroscopy* **1979,** *35* (6), 613-624.

96. Schindler, W.; Zerda, T. W.; Jonas, J. High pressure Raman study of intermolecular interactions and Fermi resonance in liquid ethylene carbonate. *The Journal of Chemical Physics* **1984,** *81* (10), 4306-4313.

97. Schindler, W.; Sharko, P. T.; Jonas, J. Raman study of pressure effects on frequencies and isotropic line shapes in liquid acetone. *The Journal of Chemical*

Physics **1982,** *76* (6), 3493-3496.

98. Brasch, J. W. High-Pressure Effects on Organic Liquids. II. Infrared Spectra and P—V—T Relationships of Rotational Isomers of Some Halogenated Ethanes. *The Journal of Chemical Physics* **1965,** *43* (10), 3473-3476.

99. Pratt, L. R.; Hsu, C. S.; Chandler, D. Statistical mechanics of small chain molecules in liquids. I. Effects of liquid packing on conformational structures. *The Journal of Chemical Physics* **1978,** *68* (9), 4202-4212.

100. Ikawa, S.; Whalley, E. Effect of pressure on molecular conformations. V. The internal rotation angle of 1,2-dichloroethane by infrared spectroscopy. *The Journal of Chemical Physics* **1984,** *81* (4), 1620-1625.

101. Sim, P. G.; Klug, D. D.; Ikawa, S.; Whalley, E. Effect of Pressure on the Structure of Molicules. *Journal de Physique Colloques* **1984,** *45* (C8).

102. Katō, M.; Taniguchi, Y. High pressure study on molecular conformational equilibria of n-pentane. *The Journal of Chemical Physics* **1991,** *94* (6), 4440-4445.

103. Yamaguchi, M.; Serafin, S. V.; Morton, T. H.; Chronister, E. L. Infrared Absorption Studies of n-Heptane under High Pressure. *The Journal of Physical Chemistry B* **2003,** *107* (12), 2815-2821.

104. Crawford, M. F.; Welsh, H. L.; Locke, J. L. Infra-Red Absorption of Oxygen and Nitrogen Induced by Intermolecular Forces. *Physical Review* **1949,** *75* (10), 1607-1607.

105. Schweizer, K. S.; Chandler, D. Vibrational dephasing and frequency shifts of polyatomic molecules in solution. *The Journal of Chemical Physics* **1982,** *76* (5), 2296-2314.

106. Slowinski, E. J.; Claver, G. C. On the Temperature Dependence of the Intensity of Infrared Absorption Bands of Liquids. *Journal of the Optical Society of America* **1955,** *45* (5), 396-397.

107. Zabiyakin, Y. E.; Bakhshiev, N. G. EFFECT OF TEMPERATURE ON THE WIDTH OF THE INFRARED ABSORPTION BANDS OF ORGANIC LIQUIDS. *Optics and Spectroscopy* **1968,** *24* (6), 539--540.

108. George, W. O.; Hassid, D. V.; Maddams, W. F. Variation of the intensity of infrared bands of chloroform and acetone with temperature. *Journal of the Chemical Society, Perkin Transactions 2* **1973,** No. 7, 957-960.

109. Buckingham, A. D. Solvent effects in infra-red spectroscopy. *Proceedings of the Royal Society of London. Series A. Mathematical and Physical Sciences* **1958,** *248*

(1253), 169-182.

110. Ackels, L.; Stawski, P.; Amunson, K. E.; Kubelka, J. On the temperature dependence of amide I intensities of peptides in solution. *Vibrational Spectroscopy* **2009,** *50* (1), 2-9.

111. Cappelli, C.; Corni, S.; Cammi, R.; Mennucci, B.; Tomasi, J. Nonequilibrium formulation of infrared frequencies and intensities in solution: Analytical evaluation within the polarizable continuum model. *The Journal of Chemical Physics* **2000,** *113* (24), 11270-11279.

112. Tassaing, T.; Danten, Y.; Besnard, M. Infrared spectroscopic study of hydrogen-bonding in water at high temperature and pressure. *Journal of Molecular Liquids* **2002,** *101* (1), 149-158.

113. Jin, Y.; Ikawa, S.-i. Near-infrared spectroscopic study of water at high temperatures and pressures. *The Journal of Chemical Physics* **2003,** *19* (3), 12432-12438.

114. Ratcliffe, C. I.; Irish, D. E. Vibrational spectral studies of solutions at elevated temperatures and pressures. 5. Raman studies of liquid water up to 300.degree.C. *The Journal of Physical Chemistry* **1982,** *86* (25), 4897-4905.

115. Herzberg, G. Molecular Spectra and Molecular Structure: Infrared and Raman Spectra of Polyatomic Molecules. Van Nostrand: New York, 1945; Vol. 2, pp 266–269.

116. Bertie, J. E.; Zhang, S. L.; Keefe, C. D. Measurement and use of absolute infrared absorption intensities of neat liquids. *Vibrational Spectroscopy* **1995,** *8* (2), 215-229.

117. Bertie, J. E.; Zhang, S. L.; Eysel, H. H.; Baluja, S.; Ahmed, M. K. Infrared Intensities of Liquids XI: Infrared Refractive Indices from 8000 to 2 cm−1, Absolute Integrated Intensities, and Dipole Moment Derivatives of Methanol at 25°C. *Applied Spectroscopy* **1993,** *47* (8), 1100-1114.

118. Bishop, D. M.; Cheung, L. M. Vibrational Contributions to Molecular Dipole Polarizabilities. *Journal of Physical and Chemical Reference Data* **1982,** *11* (1), 119-133.

119. Hansen, G. E.; Dennison, D. M. The Potential Constants of Ethane. *The Journal of Chemical Physics* **1952,** *20* (2), 313-326.

120. Shimanouchi, T. Tables of Molecular Vibrational Frequencies Consolidated Table. In *National Standard Reference Data Series 39;* National Bureauof Standards: Washington, D.C., 1972; Vol. 1, p 92.

121. Person, W. B.; Zerbi, G. *Vibrational intensities in infrared and Raman*

spectroscopy; Elsevier Scientific Pub. Co.: New York, 1982; Vol. 20.

122. Nyquist, I. M.; Mills, I. M.; Person, W. B.; Crawford, B. Ethane-d6, Vibrational Intensities. VII. Ethane and. *The Journal of Chemical Physics* **1957,** *26* (3), 552-558.

123. Vaghjiani, G. L. CH3SH ultraviolet absorption cross sections in the region 192.5-309.5 nm and photodecomposition at 222 and 193 nm and 296 K. *The Journal of Chemical Physics* **1993,** *99* (8), 5936-5943.

124. H. M. Hcise, D. Infrared spectra of gases. In *Infrared and Raman Spectroscopy: Methods and Applications;* Schrader, Bernhard, Eds.; VCH Verlagsgescllschaft: Weinheim, 1995; p 264.

CHAPTER 3

IN-SITU METHANE DETERMINATION IN PETROLEUM AT HIGH TEMPERATURES AND PRESSURES WITH MULTIVARIATE OPTICAL COMPUTING

3.1 INTRODUCTION

Accurate compositional measurements of reservoir petroleum fluid are necessary for various exploration and production activities, such as ensuring a well is safely drilled, identifying new discoveries, evaluating the production potential and value of such discoveries, optimizing the capital investment for production, and designing a field management system across multiple wells.(1-3) To determine the petroleum fluid composition in a newly drilled well, samples are typically acquired from within that well at high temperature and pressure using a wireline formation tester (WFT).(1-13) The WFT is lowered into the well using an electrical wireline cable, and it physically extracts fluid, by means of a mechanical pump, from the rock formation to capture that fluid in pressurized sample chambers. The pumping action reduces near-wellbore drilling fluid filtrate contamination, which invades the rock as a result of the drilling process. Sufficient pumping time is necessary to acquire a pristine formation fluid sample with little miscible filtrate contamination. WFT sampling is often the last activity before sealing that section of the well with cemented metal casing. A laboratory analysis is usually completed 2 weeks to 1 year after the samples are acquired and the well section

has been sealed.(1,3,11,14) By the time the laboratory has established the quality and usefulness of the samples, it is not possible to acquire additional samples even if they are determined to be of insufficient quality to assess exploration and production activities. As such, a basic level of real-time in-situ analysis is necessary to ensure the sample quality for laboratory analysis. Additionally, this basic level of fluid analysis provides immediate information for real-time decisions and also advanced planning before the full laboratory analysis is available. Because a WFT can only acquire a limited number of samples, it is important to collect samples from the locations that best represent the fluid in all reservoir compartments. It is important to ensure that those samples are of low contamination and represent the formation fluid from which they were collected. Lastly, it is important to ensure that the sample integrity is maintained until laboratory analysis is performed. The dissolved methane gas concentration in the petroleum fluid is used to address these concerns.(1,3,15,16)

Various extreme environment sensors are used to measure physical and chemical fluid properties in-situ. Typical physical property fluid measurements include density, speed of sound, capacitance, resistivity, index of refraction, compressibility, and bubble point pressure.(3,17) Chemical fluid composition has been measured using filter spectrometers or combination of filter and grating spectrometers.(2,8,16,18) Filter spectrometers have been shown to measure dissolved methane with an accuracy of 0.0235 g/cc (15); when combined with a temperature-compensated grating spectrometer measurement, this accuracy can improve to 0.0139 g/cc.(2,6) Various laboratory studies have shown dissolved methane measurement accuracy in the range of 0.007 to 0.01 g/cc in high-temperature and pressure crude oil with FTIR spectrometers operating at room-

temperature and pressure conditions.(9, 20-22) Unlike these laboratory FTIR spectrometers, in-situ instruments operate in extreme oil well environments and therefore do not achieve the same accuracy. Narrow band pass filter spectrometers are rugged but lack resolution and wideband coverage. Grating spectrometers have improved resolution but are restricted over relatively narrow regions and require temperature compensation.(2) Our laboratory has been developing new approaches to in-situ instruments that hold the potential for performance approaching that of the laboratory measurement. Specifically, MOC has been shown to enable compositional optical analysis in complex interfering mixtures with similar accuracy to that of laboratory optical instruments.(23-26) In the present manuscript, we discuss the application of MOC in the high-temperature environments of subterranean petroleum reservoirs for measuring petroleum compositions with the accuracy and sensitivities more similar to those of a laboratory FTIR. We report validated field dissolved methane accuracies of 0.0089 g/cc over a concentration range of 0 to 0.229 g/cc methane using the MOC approach with an instrument operating between 65 to 121°C compared to an independent PLS validation of 0.0086 g/cc for a laboratory instrument at room temperature over a concentration range of 0 to 0.1729 g/cc.

3.2 THEORY

3.2.1 Multivariate calibration and regression

Multivariate regression, in contrast to univariate regression, uses multiple sensor channel measurements to estimate sample characteristics. Multivariate regression is often used for the analysis of complex mixtures.(26-28) A multivariate model can successfully mitigate the effects of interference for which there is a lack of analyte specificity at a

given signal channel. Interference is a signal or signal effect from a source other than the analyte.(29-30) For the near-infrared (NIR) or mid-infrared (MIR) optical spectra of complex mixtures, the analyte absorption signal at any channel is rarely interference free.(30-31) Figure 3.1 shows a set of spectra for a light crude oil that illustrates this point. At no position within this wavelength range is the absorption signal from a single component isolated. For univariate and classical least squares regression, interference is explicitly corrected, but for multivariate regression techniques, the interference correction is implicated to that regression.(28) For multivariate regression to implicitly correct interference for a new sample that is not part of that calibration set, the calibration set needs to be sufficiently designed with linearly independent, representative concentrations of the analyte and interfering species.(28,31-32) The crude oil in Figure 3.1 is a simple light oil with an American Petroleum Institute (API) weight of 40 and does not contain the complex resins and asphaltenes fractions of heavier (i.e., lower API weight) oils. Because of the natural variation of crude oil samples, in which many chemical species are present, significant diversity of interference exists. However, the optical spectroscopy of a complex interfering matrix, including that of crude oils, is often successfully used to analyze component concentrations through multivariate techniques.(26-28,33-46)

A multivariate model correlates a set of sample characteristics to a set of sensor measurement observations for a given set of samples by the process of calibration. Equation 3.1 shows a linear model, where y is the sample characteristic, X is the sensor response matrix calibration set, B is the array of model parameters, and e is the residual error of the model. For a linear model, all parameters coefficients are first-order linear with respect to the analyte concentration. The discussion herein is limited to the

characteristic of a chemical analyte concentration in a mixture. The model is used to estimate characteristics for new samples that are not in the calibration set.(29) The inverse least squares solution, which is commonly used to determine the coefficients array B, is determined by minimizing the square of the error from Equation 3.1 to obtain Equation 3.2. The coefficients are then used to predict analyte concentration estimates $\hat{y}$ with a new set of sample measurements. Equation 3.3 makes this prediction as the dot product of the sample response matrix S with the parameter array transposed B^T. In this paper, the convention is for observations to be in columns and samples in rows of X and S.(29) The set of coefficients for the linear model B is called a regression vector, X is the calibration matrix, and S is a response matrix of new samples not contained in the set of X. The regression vector as determined by Equation 3.2 implicitly corrects the interference signal for the concentration estimates of Equation 3.3, provided that the types and nature of the interference and level of interference for the unknown sample are similar to those of the calibration set.(34,37)

$$y=XB+e \tag{3.1}$$

$$B=(X^{*}X)^{-1}X^{T}y \tag{3.2}$$

$$B^{T}S=\hat{y} \tag{3.3}$$

Optical spectroscopy methods are convenient for analyzing the chemical and physical properties of materials by multivariate regression.(27-28,30-31,33-45,48) Sensors making use of optical analysis are rapid, nonintrusive, and nondestructive. The analyte concentration can be estimated using optical transmission measurements. Optical intensity, I_0, attenuates as the light traverses a sample of path length l by an analyte-specific attenuation constant ε for a concentration C to emanate resultant single-beam

intensity I according to Equation 3.4, the well-known Beer-Lambert law.(28,49) The linear form is expressed for absorption, A, calculated by Equation 3.5 from the initial intensity I_0 and resultant intensity I, to yield Equation 3.6. In this paper, the absorption A follows the logarithm base 10 convention, as opposed to the natural logarithm convention. Equation 3.6 conveniently relates the composite absorption of a sample mixture at each wavelength λ to the sum effect of all species, within the mixture, that have attenuation at that wavelength. Using the vector notation form of Equation 3.6 as Equation 3.7, it is evident that the absorption spectrum $\vec{A}$ satisfies the conditions of Equation 3.1 and each finite wavelength channel fills the columns of X (and S) for i sample rows. As Equation 3.7 takes the same form as Equation 3.1, Equation 3.2 can be used to estimate a set of regression coefficients B for a calibration set of absorbance spectra X.(27-28,49)

$$I = I_0 e^{\varepsilon l C} \tag{3.4}$$

$$A = -LOG_{10}(T);\ T = I/I_0 \tag{3.5}$$

$$A_{i\lambda} = \sum_{i=1}^{i=p} \varepsilon_{i\lambda} l C_i \tag{3.6}$$

$$\vec{A}_i = (\vec{\varepsilon}_i l) C_i \tag{3.7}$$

For a large set of highly correlated channels, as is often the case with NIR data, the response matrix of Equation 3.2 can be poorly conditioned for inversion.(34) Rotation of the correlated variables to a set of orthogonal latent variables by means such as principal component analysis (PCA) overcomes this difficulty.(27) A principal component (PC) scores matrix is constructed as a linear combination of the original response matrix by projecting the responses for each sample onto a new set of orthogonal axis dimensions (i.e., PCs). The PC axis is constructed such that each PC is orthogonal

and captures the largest residual variation within the dataset not described by previous (lower-order) PCs.(50) The PC dimensions capture the internal correlation of the dataset, and the reduced dimensionality of new orthogonal variable scores is well-conditioned for inversion. A linear dot product regression vector in the original response variable space can be constructed from the PC scores coefficients and the PC eigenvectors as a principal component regression (PCR) to the analyte.(27) PLS is another eigenvector calibration technique of reduced dimensionality. PLS also designs a linear dot product regression vector, but each successive eigenvector is constrained to capture the maximum variation for the reference analyte concentration from the calibration matrix.(27) Although the PCR and PLS regression vectors are constructed from different rotations of the calibration matrix, the performance is often similar, even over a broad range of conditions, but PLS generally requires fewer eigenvector latent variable levels.(28) In fact, many algorithms, linear and nonlinear, can be used to construct a linear dot product regression vector of similar performance.(31)

3.2.2 Multivariate optical computing

MOC is a multivariate linear regression technique that performs an analog dot product calculation, in the optical domain, between a linear regression vector and the inherent optical intensity spectrum of light emanating from a sample. The regression vector shape is encoded as a transmission pattern for one or more optical elements. MOC most typically uses an MOE, which is constructed as an interference filter. Laminated, thin film layers of two materials with different refractive indexes (R_i) are deposited on a substrate. Here, R_i is used to denote the complex refractive index (index of refraction) as opposed to the real part n vs. the imaginary part ik for $R_i = n + ik$. The goal of calibration is to encode a

regression vector as a transmission profile using a thin film stack design. A specifically designed thin layer stack can sufficiently match a regression vector shape. The MOE regression vector can either be predetermined—for instance, by PCR or PLS—or directly designed to a calibration set.(25) As spectral light passes through the MOE, the Hadamard vector product, an element-by-element multiplication, of the sample intensity spectrum with the MOE naturally occurs. The Hadamard vector product is followed by a summation of all light wavelengths by a detector, thereby completing the dot product. Therefore, the resultant detector signal is proportional to the analyte concentration for which the regression vector was designed plus a sample-dependent offset.(24) The sample-dependent offset can be subtracted either by use of light reflected from the element, a reference spectral signal, or a secondary spectral element.(23,51) MOEs operate on the intensity spectrum emanating from a sample as described in Equation 3.4, not the linear absorbance form of the Beer-Lambert law from Equation 3.5. Therefore, the MOE does not strictly operate on signals linear with the analyte concentration. However, it has been shown that higher-order linear models can model some nonlinearity.(51-55) As such, MOEs operating on single-beam intensity transmittance can still provide a reasonable measurement, as long as they can reproduce a higher-order regression vector.

A regression vector calibrated to correct interference has both positive and negative coefficients. For the dot product regression, assuming a positively correlated analyte and interference signal, positive regression coefficients sum the analyte signal, whereas negative coefficients subtract interference.(31,47,56-57) An optical element that encodes a transmission pattern innately has only positive coefficients with respect to a

detector sum, giving rise to the sample-dependent offset. For a perfectly designed regression vector, a sample with no interference would have no offset, whereas a sample with interference would have a positive offset. Various MOE configurations have been described to allow a positive and negative coefficient solution, thereby subtracting the sample-dependent offset, including the single-element beam splitter design (23) and the dual- element positive-negative fixed lobe design.(51) In both configurations, to describe positive and negative coefficients for an all optical regression, the difference between at least two signals is necessary. The dual-MOE design encodes the positive coefficients of a regression vector into one element and the negative lobes into another. Light passing through the elements either strikes two dedicated detectors or a single multiplex detector. This requirement constrains the MOE design; specifically, the transmission has to be zero where the complimentary element has a nonzero coefficient contribution. This constraint often proves difficult to fabricate for complex regression vector designs and can lead to low overall transmission intensity. The beam splitter arrangement overcomes this limitation by using the transmission vs. reflection signals of a single element as measured by a set of detectors. However, in practice, the 45° configuration can be difficult to implement. Although an angle-tolerant MOE design technique has been demonstrated (58), an angle dependency of the transmission pattern combined with a temperature dependency of the transmission pattern is a complex and difficult interaction for which to design a stable transmission pattern. Therefore, a different option for sample-dependent offset correction has been chosen.

This work adapts the uses of a perpendicular MOE configuration similar to that described for imaging MOE applications.(59) In this configuration, an MOE regression

vector pattern is encoded as a single element transmission pattern and designed against a second reference channel. However, in this work, the reference channel is a band pass filter and the MOE signal is measured in combination with a band pass filter of identical design on a different detector of the same design. In this configuration, the band pass transmission T_{BP} serves as a baseline vector that, when scaled by α_0 and subtracted from the MOE transmission T_{MOE}, allows for positive and negative regression coefficients as elements of B, as shown in Equation 3.8. The magnitude of the MOE is scaled by α_1 to the regression vector. The band pass also isolates a suitable optical region for calibration.

$$B = \alpha_1 T_{MOE} - \alpha_0 T_{BP} \tag{3.8}$$

The ideal shape of a reference band pass channel would be a "top hat," with 100% transmission in the spectral region of interest and 0% transmission elsewhere. However, a band pass of this nature is unattainable. Figure 3.2 shows a typical commercial band pass transmission function in black with an ideal top hat band pass. The ideal profile is unattainable because an actual band pass is a compromise of shape, transmittance, range, and complexity of design. Although the shape of an actual band pass filter is not ideal, the convoluted regression vector design can be compensated by the MOE thin layer stack design. Herein, it is understood that the MOE transmission refers to the band pass convoluted MOE transmission regression vector.

Equation 3.9 shows the operation of a regression vector B as an MOE on the single-beam intensity spectra S for prediction of the analyte concentration $\hat{y}$. Figure 3.3 illustrates the physical application of Equation 3.9. From a spectral library, a linear optical regression vector pattern is designed and encoded as an MOE using an interference pattern. When light passes through a sample, it acquires the spectral

fingerprint of the sample. The application of the regression vector, *B*, is physically accomplished by measuring the detector signal of light passed through the convoluted MOE and measuring the detector signal of light passed through the reference band pass. It is the scaled difference between these two detector channels that provides the estimation of the analyte concentration.

$$\hat{y}=BS=\alpha_1 T_{MOE}S-\alpha_0 T_{BP}S \qquad 3.9$$

Signal intensity variations unrelated to the analyte concentration can introduce a bias in the measurement. Such variations can be a result of light source intensity variations, detector sensitivity variations, or white light Mie scattering within the sample causing neutral density variation. Reflectance spectra that commonly experience neutral density fluctuations are normalized to unit intensity and then regressed to provide analyte concentration estimations.(60-62) Normalizing to unit intensity preserves the spectral shape. Linear calibrations are then developed from a normalized calibration set X_N to provide a set of linear model parameter estimates B_N. A similar technique called pseudo normalization (51) and norm-1 normalization (59) has been described for use with MOC. In this work, the sum of the detector signals through the band pass is used for signal normalization (Equation 3.10). Thus, the regression vector B_N yields the concentration of the analyte, with constant offset α_0, when operating on a normalized spectrum, as shown in Equation 3.11.

$$S/(T_{BP}S)=S_N \qquad 3.10$$

$$\hat{y}=B_N S_N=\alpha_1 T_{MOE}S_N-\alpha_0 \qquad 3.11$$

3.3 EXPERIMENTAL

For this study, 2,582 spectra are collected for petroleum fluids recombined with gas using a small optical pressure, volume, temperature, x-composition (PVTX) system. The experimental system and operation have been described.(63) The spectra are collected at 65.5, 93.3, and 121.1°C and at 20.684, 41.369, 62.053, and 82.727 MPa, which spans the pressure and temperature range for the intended MOC system use. The spectra include more than 167 different base petroleum fluids initially containing no dissolved gas. The base fluid is then recombined with different concentrations of gas components, with subsequent spectral collection at the temperature-pressure combination points. The gas components include methane, ethane, propane, and carbon dioxide reconstituted to match the composition of typical reservoir fluids. The natural span of typical petroleum compositions is determined using a global petroleum fluid properties database containing more than 14,000 sample compositions (Geomark Research, Houston, Texas). For this study, the petroleum base fluids are limited to medium oils, defined as 20 to 30 API weight, and light oils, defined as 30 to 40 API weight. The recombined GOR is limited to a typical medium oil range through condensate range, typically 100 to 25,000 scf/bbl, respectively. Heavy oil samples with weight less than 20 API and petroleum gas samples are excluded from the current study. The spectra are screened for outliers,(64) with 47 removed, and then subsampled to ensure an evenly distributed concentration range for methane and interferences and to reduce the processing power required for nonlinear optimization. The methane design relies on 721 spectra; an additional 314 spectra within this range are held out for independent validation testing. The independent validation spectra all reside within the compositional

range of the design samples. Table 3.1 shows he composition range for all fluids used in the design and validation.

3.3.1 Custom band pass design

To increase the accuracy and sensitivity of the MOE, it is necessary to restrict the optical computation to a specific wavelength region and truncate unwanted spectral contributions. This is achieved by using a separate band pass filter along the MOE optical path. Although a commercially available band pass filter could be used, this practice has several disadvantages. Batch-to-batch nonuniformity of the band pass transmission profile is difficult to control and characterize and therefore offers a degree of uncertainty when designing the MOE. Only the available stock can be used for MOC. While there is considerable choice for band pass wavelength regions, it is highly unlikely for an available band pass region to identically match the optimum region for a given MOE. Commercial band pass filters are usually designed and fabricated to operate at room temperature and not at the broad high-temperature range of petroleum oil wells. These disadvantages can be mitigated by design and fabrication of a custom band pass filter. Fortunately, because such band pass filters are thin film multilayer stack designs, their design and fabrication follows procedures similar to those for MOE fabrication. As a further advantage, the band pass can be directly integrated into the optical path by depositing the MOE onto the backside of the custom band pass filter. Backside deposition of the MOE can also improve total optical throughput, as an air gap is eliminated from between the MOE and band pass filter. Therefore, it is preferable to customize a band pass filter designed specifically to optimize the MOE performance and operate under high-temperature downhole conditions.

The design of a custom band pass filter begins by selecting the working wavelength range for an MOC sensor using the full wavelength range single-beam transmission data. It is assumed that a wavelength range that is optimal for a PLS regression will be optimal for an MOE because both regression vectors operate on the same inherent spectral information content. Limitations to this assumption could be that the PLS and MOE regression vectors are applied to different sensors: FTIR vs. MOC, respectively. The validation of this assumption is not the subject of this investigation but has provided sufficient results to date.

A PLS with leave-one-out cross-validation(27-28) is conducted over the widest candidate wavelength range for consideration. The cross-validation sets the PLS maximum level (ML) of eigenvectors from which to construct the model. If the cross-validated value is greater than 7, then the ML holds to 7, as it is our experience that a single MOE system typically can only replicate the performance of a five- to seven-level PLS model. Once the ML is determined, an in-house algorithm constructs the series of truncated wavelength range local PLS models to no more than the ML. The local PLS model is cross-validated to a new level equal to or less than the ML. For each local PLS model, the standard error of prediction (SEP) is calculated by leave-one-out cross-validation. The truncation procedure follows in small wavelength increments, typically 5 to 20 nm each for NIR data. All continuous combinations for wavelength increments of 5 to 20 nm, from the beginning wavelength to ending wavelength, are tested.

Although the wavelength range can be automatically selected, a color map of SEP is helpful to inspect search results. Figure 3.4 shows the results of a search algorithm held to an ML of 7 for methane using the calibration spectra in this study. SEP correlates from

blue to red such that the darker the blue, the better the SEP, and the darker the red, the worse the SEP. Low SEP is one consideration for wavelength region selection, but as a practical issue, the tolerance of MOE fabrication needs to be considered. It is best to identify a sufficiently wide region of good SEP to provide the MOE a large tolerance for design and fabrication. In Figure 3.4, two distinct regions of acceptable SEP are prevalent. The first extends from 1400 to 1700 nm. Unfortunately, outside this region, the SEP decays rapidly. The region from 1500 to 2500 nm shows a wide region of good SEP. The beginning and ending wavelengths have a tolerance of approximately +/- 200 nm. This second region provides a good tolerance for custom band pass and MOE design and fabrication.

The custom band pass is designed and fabricated in the same manner as a shape-matched MOE, which is described in greater detail later in this work. However, the exact shape of the custom band pass filter is less important for that of an MOE than that for generic use. The important characteristics of a custom band pass filter for MOE use include isolation of the spectral region, high transmission of the isolated spectral region, good out-of-band intensity rejection outside the isolated spectral region, good temperature stability, and low undulation at the top position. The sharpness of the cut on and cut off are less important for the custom band pass than is typical for a commercial multipurpose band pass filter. This is because the MOE design can compensate the composite transmission profile. Additionally, it is only important to constrain the out-of-band transmission to low values over the intense regions of the MOC sensor light source, whereas a commercial band pass usually typically rejects out-of-band light over a larger region so that the commercial band pass can be used for a generic light source. The total

out-of-band intensity is constrained to better than one thousandth of the total in-band intensity for the light source of the MOC sensor. A top hat transmission design, such as in Figure 3.2, is used to select the region of interest. A band pass is designed to that function with a limit of 30 layers and 6 μm thickness. From various design options, a new compromised top hat target is selected with relaxed transmission throughput. The exact position and sharpness of the cut on and cut off wavelengths are relaxed if a high MOE SEP wavelength region of broad wavelength tolerance has been selected. The top portion of the band pass can also be weighted to limit the undulation.

3.3.2 Multivariate optical element design

The fabrication of an MOE proceeds by depositing alternating thin layers of nominally transparent material, with index of refraction contrast, on a substrate. The thickness and complex index of refraction for all layers define the transmission profile. The complex index of refraction is expressed with *n* as the real part and *k* as the imaginary part. For MOC, calibration is the process of stack recipe design, such that an optical element transmission profile forms a scaled dot product regression vector for single-beam intensity spectra.(25) To design a regression vector for an MOC sensor, a sample calibration spectra set is transformed to the single-beam intensity spectra sensor domain. Radiometric data are measured for representative MOC optical components. The single-beam intensity sensor spectra are calculated as the Hadamard product of the light source; optical components, including the custom band pass filter; detector response vector; and the calibration set fractional transmittance spectra. Lastly, spectra are pre-processed by band pass normalization. For simplicity, this is called the virtual sensor (VS) calibration set, as it represents the ideal response of a sensor if the detector in a

sensor were to measure the spectral profile of all samples. The MOE stack design is evolved using a quasi-Newtonian nonlinear optimization routine to either a predetermined shape or as a direct design to a calibration dataset.(25)

A set of optimized candidate stack designs are evolved from a large set of random seed stacks. For the direct design approach, the quasi-Newtonian nonlinear optimization routine identifies the local minima of a merit function such that the VS detector response, convoluted with the transmission function T_{opt}, is linear with analyte concentration y. The merit function used for direct design is that of Equation 3.12. The MOE seed design is projected against the spectral dataset for a given temperature. Specifically, the dot product is calculated between the MOE transmission profile and the VS to find the simulated detector response. The merit-based optimization routine then iteratively changes the layer thicknesses to achieve a new step in the design process, yielding a new MOE transmission spectrum. At each temperature t, the scalar dot product of the transmission function $\hat{T}_t$ with the normalized calibration set X_N is calculated as a simulated detector response. The coefficients α_1 and α_0, of a first-order polynomial, are established between the simulated detector response and the calibration reference analyte concentration values y. Equation 3.12b is then used to predict the analyte concentration estimation $\hat{y}_t$. Equation 3.12 calculates the optimized transmission as the arguments of minima (argmin) for the temperature-dependent squared standard error of calibration (SEC^2). That is, each local minimum is evolved to provide the best temperature performance. Additionally, the reference spectra, X_{Nt}, are matched to the same temperature increments for which the spectra, $\hat{T}_t$, are calculated. Therefore, the optimized

transmission functions T_{opt} are designed for the best temperature performance over that temperature range.

$$T_{opt} = \text{argmin} \frac{\sum_{t_L}^{t_H} \left(\| y - \hat{y}_T \| \right)}{n} \quad 3.12a$$

$$\hat{y}_t = \alpha_1 \left(\hat{T}_t \cdot X_{Nt} \right) + \alpha_0 \quad 3.12b$$

Alternatively, the stack design can be optimized using the merit function of Equation 3.12, such that the transmission function, T_{opt}, of the stack correlates to the predetermined regression vector shape *B* or that of a custom band pass. Equation 3.13 calculates the optimized transmission as the arguments of minima (argmin) for the mean square error (MSE) between the regression vector shape and the temperature-dependent scaled transmission function. Therefore, the resultant optimized transmission function is evolved to retain the best fixed shape over a temperature range. The transmission function, $\hat{T}_t$, is scaled to the regression vector, *B*, by a first-order parameter α_1 and offset α_0 using Equation 3.13b, yielding the estimate of $\hat{B}_t$ at every iteration.

$$T_{opt} = \text{argmin} \frac{\sum_{t_L}^{t_H} \left(\| B - \hat{B}_t \| \right)}{n} \quad 3.13a$$

$$\hat{B}_T = \alpha_1 \left(\hat{T}_t \right) + \alpha_0 \quad 3.13b$$

The slope α_1 is inversely proportional to the sensitivity of a given design. That is, the smaller the α_1, the less amplification is required for the transmission function to scale to the regression vector. The offset α_0 and scalar α_1 for both Equations 3.12b and 3.13b are determined for each step of the iteration for the optimization, but at each iteration step, are held temperature invariant. At each temperature of each iteration step, an in-house routine solves Abele's matrix formalism for the propagation of electromagnetic waves through an alternating layer dielectric medium.(25) The formalism is used to

calculate the total transmission and reflection profile for the evolving stack design as a function of the light's wavelength, angle, and ensemble of all layer complex indexes of refraction and thicknesses.(65) The thin film materials' optical properties then need to be characterized as a function of temperature, *t*, so that the transmission function can also be calculated as a function of temperature. The fit parameter, SEC^2 for Equation 3.12 and MSE for Equation 3.13, is calculated as the average of a series of predetermined temperatures from a low temperature, t_L, and high temperature, t_H, for *n* temperatures. For the current study, t_L is 65.5°C, t_H is 121.1°C, and *n* is 3 with an intermediate of 93.3°C.

The optimization routine is terminated when the resulting regression vector produces a minimum in the objective function or when a maximum number of iterations, typically 5,000, has been reached. Designs that do not converge are discarded. To ensure that a sufficient design has been determined, a large number of candidate designs is produced. A sufficient design is one that has a prediction error close to the PLS solution, that can be easily fabricated, is tolerant to the temperature variation, and has sufficient sensitivity for use.

The MOE regression vectors are not constructed as a combination of orthogonal eigenvectors, as is PLS, and therefore cannot be constrained to a maximum level. There is no control for how many inherent latent variables are captured by an MOE regression vector, nor is it practical to cross-validate the evolutionary design because the held out samples would be optimized with subsequent iterations. It is the experimental design that protects the MOE design against overfitting. The experimental design needs to be not only of sufficient rank to validate the MOE model but also sufficiently large to prevent

overfitting. Validation of the MOE regression vectors should be conducted with an independent validation set that is not used to construct the MOE regression vector.

For some calibration sets, MOEs designed to the merit function of Equation 3.12 can lead to model overfit. In these circumstances, direct shape matching of an MOE to a predetermined and cross-validated regression vector using the merit function of Equation 3.13a provides a more robust MOC. Unfortunately, direct shape matching of complex regression vectors, such as in Figure 3.10, is difficult because an interference pattern produced is usually reminiscent of a collection of Gaussian peaks, as illustrated in Figure 3.6. Obtaining a good SEC through shape matching usually requires a larger number of layers than for a similar SEC of a direct design MOE. Because it is difficult to exactly match a predetermined regression vector, after a good approximate match is determined, that design is relaxed slightly with a direct match to SEC^2 by use of Equation 3.12. Unfortunately, the directly matched complex shapes are usually of lower transmission than those of direct design MOEs and therefore lower sensitivity for comparable SEC. For this reason, direct optimization of an MOE is preferred to shape matching unless overfitting is a concern.

To select among the many candidate designs, the in-house automated algorithm, fabrication suite, has been developed. The fabrication suite simulates the tolerance to fabrication for each of the candidate designs and the resultant performance for the MOC VS. Although the designs are constructed considering temperature, it is important to evaluate temperature stability with respect to imperfect fabrication and characteristic sensor noise. The outline of the algorithm is as follows:

1) High-SEC (or MSE) designs are automatically discarded above a threshold.

2) Low-sensitivity designs (large α_1) are automatically discarded below a threshold.

3) The remaining designs are screened for fabrication tolerance.

   a. The thicknesses of the designed layers are all simultaneously shifted by the same fraction, with SEC (or MSE) calculated as the average for a set of 10 perturbations. The set is selected according to a predetermined limit by the tolerance of the fabrications system's uniformity. High-average SEC (or MSE) designs are discarded above the threshold.

   b. The thicknesses of the designed layers are individually shifted by a different fraction, with SEC (or MSE) calculated as the average for 25 iterations. The fraction is selected according to normal random distribution based on the fabrication system's deposition thickness control. High-average SEC (or MSE) designs are discarded above the threshold.

4) Average SEC (or MSE) is calculated across *n* temperatures for each of the remaining perturbed layer sets of Step 3.

5) For the remaining designs, noise is added according to an MOC characterized signal-to-noise ratio (SNR) for 100 iterations using a normal random distribution.

Each step is designed to remove unsuited designs efficiently, with the easiest calculations removing designs for consideration from later, more computationally intensive calculations. Each subsequent step operates on each of the perturbations for

each of the surviving designs from the previous step. The threshold SEC is usually two times the PLS SEC. Likewise, the sensitivity threshold of Step 2) is usually set to three times the PLS sensitivity. The PLS sensitivity is described later in this document. The signal-to-noise characterization for an MOC sensor has been performed for approximately 85 MOC sensors. The lower 95% confidence level is used as the SNR limit, SNR=500, such that any MOE fabricated will be robust for a fleet of MOC sensors. The designs are ranked according to SEC, with the top candidates viewed for inspection compared to a reference PLS regression vector for final selection. For shape matching a custom band pass filter, Step 5) is eliminated.

3.3.3 Ion-assisted e-beam fabrication system

The selected MOE is fabricated using a custom ion-assisted e-beam vacuum deposition process described previously.(66) The ion-assisted e-beam vacuum deposition system was built by Denton Vacuum LLC. This tool uses electromagnetically focused high-energy electrons to evaporate a target's atomic species. The ion-assisted beams then help focus and densify the vapor atomic species onto the MOE substrates, which are borosilicate glass in the current study. Four substrate holders, 13 inches in diameter, are mounted in the chamber in a planetary configuration that rotates about the chamber azimuthal axis, which is 16 inches in diameter, as well as the substrate holder axis. This dual-rotation planetary configuration allows for highly reproducible, uniform film deposition for all MOE products. Figure 3.5 shows a top-down illustration of this configuration. Each substrate holder accommodates 66 MOE substrates of 25.4 mm or 6 mm and a 3 inch glass witness sample for optical monitoring.

To monitor the deposition process in-situ, the chamber is also equipped with a suite of analytical tools. Rate control and physical thickness monitoring is supplied by an Inficon IC6 crystal sensor deposition controller slaved to the main control system for recipe downloads and active feedback. Each e-beam gun has its own crystal sensor head unit. A Newport single-wavelength optical monitor system is also employed for deposition rate control. Both of these in-situ tools are coupled with the e-beam gun to provide real-time feedback for endpoint detection. A VIS-NIR spectroscopic ellipsometer (J.A. Woollam, Lincoln, Nebraska) is mounted to the chamber windows with a fixed 70° angle of incidence and can be used to measure the film thicknesses and optical constants after the thin films are deposited. NIR and MIR transmission spectrometers (Newport, Irvine, California) are mounted to the chamber at normal incidence and can also be relied upon for measuring the transmission response of the fabricated MOE, as well as the individual film layer thicknesses.

The temperature of the deposition system can be changed from ambient to greater than 230°C. Typical silicon (Si)/silicon dioxide (SiO_2) fabrication occurs at 200°C, with optical monitoring at various temperature increments, usually of 27.8°C, from ambient to 176.7°C. This allows temperature-dependent characterization of both the transmission profile of MOEs under fabrication and the optical constants to be determined at increments throughout the deposition process. Characterization and re-optimization of remaining layers is crucial for MOE performance of the target shape.(23-24,67) Because of the temperature dependency of the index of refraction and material thermal expansion, the transmission profile of the optical element changes with temperature. It is therefore important to re-optimize the remaining layers based on measurements and

characterization across the intended temperature range for MOC sensor use. As many as five materials can be located in one of five protected pockets within the deposition system, such that only a single material is exposed during e-beam vaporization. For the current study, Si and SiO_2 are loaded as the deposition materials, although aluminum dioxide and titanium dioxide were present.

The ion source is used during the deposition process to create high-density films with high *n* and highly repeatable *n* and *k*, which is important for creating layers with good optical contrast. The high-density film also reduces moisture and porosity for films. These properties are crucial for the MOE to work successfully in a downhole environment at high temperature. This film stack profile, along with each layer's material optical properties, *n* and *k*, is used to determine a transmission spectrum profile. The advanced in-situ characterization available in the fabrication system allows for the characterization of the material optical properties over a broad range of high temperatures. It is important that the material properties used in the design process be similar to those used during MOE fabrication to allow for real-time re-optimization.

The speed of the ion-assisted e-beam deposition system is faster than that of the previously reported magnetron sputtering systems.(23) Speed is an advantage in MOE fabrication because of the drift rate of the optical constants for the materials being deposited. Although the layer stack is re-optimized in real time during deposition, optical constants that drift quickly during the process of MOE fabrication can make designs under fabrication difficult to re-optimize. In the current system, approximately 1 μm is deposited per hour with an accuracy of +/- 1 nm. With 1 hour of re-optimization between layers, a complete fabrication can be completed in one 24 hour period. The uniformity is

also 1 nm thick, which corresponds to the wavelength uniformity for transmission features of better than +/- 7 nm for typical MOE designs.

To establish the wavelength uniformity for features of a typical double-sided MOE design, for which the MOE is deposited on the backside of a custom band pass filter, a complex, 13 layer, 6.1 μm thick design is selected for fabrication (Table 3.2). Twenty custom band pass filter substrates, 25.4 mm in diameter, are placed in the chamber for MOE fabrication on the reverse side, followed by twenty custom band pass filter substrates, 6 mm in diameter, in the chamber for MOE fabrication on the reverse side. Figure 3.6 shows the measured transmission of a single fabricated MOE from each batch. Note that the real-time re-optimization during design fabrication converges to slightly different shapes. In fact, different batches typically do not converge to exactly the same shape, even when using the same initial design because of imperfections in the deposition process followed by re-optimization. Even though the shapes are different, the re-optimization can recover the designs to nearly the same target SEC. The five peaks between 1600 and 2300 nm are used to calculate the peak position distribution for each. Table 3.3 shows the peak position and standard deviation for each batch. For both the 25.4 mm MOE and the 6 mm MOE, the standard deviation increases as a function of wavelength. The 6 mm fabricated batch shows slightly better uniformity than the 25.4 mm fabricated batch.

3.3.4 MOE fabrication

A PLS model is constructed using VS single-beam transmission data to the analyte methane using the wavelength range from 1200 to 3000 nm. The leave-one-out cross-validation shown in Figure 3.7 suggests that perhaps as many as 19 latent variables

are significant; however, improvement is marginal from Level 7 to Level 19. Additionally, as suggested previously, it is difficult for an MOE to replicate the performance of a PLS model with more than seven levels. Therefore, seven levels is selected as the maximum amount for the custom band pass filter wavelength range search. The overall SEP performance for the full wavelength range PLS is 0.00782 g/cc by root mean square error of cross-validation (RMSECV). The independent validation using the held out 314 spectra not used in the PLS regression vector calculates a SEP of 0.0086g/cc methane. Figure 3.4 shows the results of the truncated wavelength range analysis. The range from 1600 to 2400 nm was selected because it has a good SEP and provides good tolerance for MOE design. Next, a simple top hat design profile is constructed that restricts transmission intensity to one thousandth of the contribution from outside of this wavelength region. A top value of 80% transmission is selected within this wavelength window. The custom band pass is designed to the top hat using the random seed quasi-Newtonian method and the merit function of Equation 3.13. The layer thickness is restricted to less than 6 μm and 30 layers. Designs are eliminated and sorted using the fabrication suite. Remaining designs are selected manually to identify a good candidate of low undulation in the top portion. Although the optimal region is determined to be from 1600 to 2400 nm, the lower range is extended slightly, with a more gradual rise to peak transmission.

The resulting film stack consists of 16 layers of alternating Si and SiO_2 on a BK7 substrate (Table 3.2). The Si and SiO_2 layers are deposited by means of ion-assisted e-beam evaporation at a pressure of 1E-4 Torr and temperature of 200°C. Optimization of the ion-assisted process variables allows for densely packed films that are invariant to

moisture absorption and temperature-induced changes in the optical properties. This is evident from Figure 8, which demonstrates the final resultant spectra collected from two different samples at room temperature (20°C) and 120°C. After the deposition of each individual layer, the process is paused such that in-situ transmission spectra and spectroscopic ellipsometry data can be acquired. Data analysis of the multiple spectra sets allows precise characterization of the materials' optical constants and deposited thickness. These data are then implemented back into the film stack design and held constant while the remaining layers are subsequently optimized to provide an in-situ re-optimization process that precisely accounts for any deviations in the fabrication process from the intended design. Although the fabricated transmission function of Figure 3.8 deviates from the ideal top hat design, the design is re-optimized during fabrication to the top hat function, not the design.

After radiometric measurement of the band pass filter at all temperature increments, the MOE is designed. The single-beam spectra are convolved with the radiometric contributions from each optical component in the MOC platform, including the lamp emission profile, sapphire sampling windows, and the custom band pass filter, providing the VS calibration set. Figure 3.9 shows the resulting VS spectra after convolution. A PLS analysis is performed for the convoluted spectra of Figure 3.9, which determined 0.007755 g/cc SEP using leave-one-out cross-validation. The regression vector is constructed using five levels, which is two less than the broad-range PLS with marginally better performance. The PLS SEP establishes a lower limit for the expectation of the MOE candidate design performance. Comparison of the SEP helps select an MOE candidate design close to a global optimum. In the event that the dataset is not adequately

defined and/or has insufficient rank, the PLS analysis would yield a poor SEP by cross-validation. In such an event, the calibration set and the experimental design need to be evaluated. Figure 3.10 shows the five-level PLS regression vector. Note that while absorption positively correlates with analyte concentration, transmission negatively correlates with analyte concentration. Therefore, the strong negative PLS regression vector features are important for analyte detection. Careful inspection of the regression vector in Figure 3.10 identifies important spectral regions between 1600 to 1800 nm and 2000 to 2200 nm. It is expected that these spectral regions are also significant features in a robust MOE design.

Figure 3.11 shows the results of an MOE design search initialized for methane with an initial 200 randomly seeded designs. The MOE thickness was restricted to 6 μm and total number of layers to 16. The objective function for the optimization routine was SEC^2 by means of Equation 3.12. Nearly 75% of the designs converge to an SEC better than 0.02 g/cc, which is better than 12% of the calibration design range. All initial 200 random designs have an SEC better than 0.035 g/cc or 20% of the methane calibration range, thus confirming the optimization routine converges to a local minimum. Both SEC and sensitivity are criteria for optimal design selection. The lower the SEC, the more accurate the predictive performance for a given MOE. Sensitivity is inversely related to the regression coefficient α_1 from Equation 3.12. Sensitivity impacts performance of an MOC sensor with respect to noise and drift. Designs with smaller values for α_1 are more robust with respect to noise. The fabrication suite selection process suggests Design A, indicated by the black X in Figure 3.11, is the best design for use with the MOC sensor among these MOE candidate designs. In Figure 3.11, the red X shows Design B, which

has a similar SEC but more than 6.5 times lower sensitivity. Figure 3.12 shows the calculated transmission at 121.1°C for Designs A and B. MOE sensitivity is related to the total amount of analyte-specific light reaching the detector. In this regard, designs with larger transmission are typically of greater sensitivity. Note that Design B is of substantially lower transmission and thereby restricts the total light throughput for the MOC sensor relative to Design A, illustrating this point. With such small overall transmission intensity, not much light would contribute to interrogating the sample, and one could expect the MOC sensor performance to suffer significantly. The evolution of this design to a small overall transmission intensity is then compensated by the model applying a large (α_1 = 52) regression coefficient. The optimal design with a small regression coefficient (α_1 = 8) has a large overall intensity and would therefore contribute significant light throughput for interacting with the sample spectrum. Given designs of similar SEC values, it is intuitive that the design with the better sensitivity be chosen for implementation into the MOC system. Complicating the choice among the designs, Figure 3.11 shows designs with better SEC and others with better sensitivity. The design selection method implemented with the fabrication suite identifies Design A from this pool of 200 designs as the best compromise for the characterized noise level of the existing MOC system. For comparison, if the PLS regression vector of Figure 3.10 is scaled as an MOE transmission function from 0 transmission at the minimum to a maximum transmission of 1, the α_1 is 9.6, which is 20% less sensitive than Design A. In addition, the PLS regression vector has a 23% better SEP than the SEC of Design A. Therefore, the selected design is sufficiently near the PLS optimum, and additional randomly seeded designs need not be considered.

The resulting film stack of Design A consists of five layers of alternating Si and SiO_2 on a BK7 substrate (Table 3.2). The Si and SiO_2 layers are deposited by means of ion-assisted e-beam evaporation, as described previously. Figure 3.13 shows the design MOE match to the fabricated MOE. As previously, after the deposition of each individual layer, the process is paused and optical data acquired such that the precise characterization of the materials' optical constants and deposited thickness can be measured. However, unlike the shape matching re-optimization, the direct MOE process re-optimizes the additional layers directly to the SEC. For this reason, the final shape can deviate from that of the initial design. In fact, as each fabrication has unique stack errors, and each fabrication re-optimizes with unique optical constants, an identical transmission shape is not fabricated between two batch runs. The SEC re-optimization produces final fabricated MOEs with better SEC performance than shape re-optimization to the initial design. Additionally, final temperature stability and sensitivity of the fabricated design generally do not deviate significantly from the original specifications, even with the slight shape drift. The fabricated MOEs verified with an average 0.0109 g/cc methane concentration SEC +/- 0.0006 g/cc to one standard deviation for the batch of 10 MOEs, as calculated by projection vs. the spectral design set. The sensitivity was slightly better than that of the target deign, with an α_1 value fabricated as 7.16 +/- 0.23 to one standard deviation vs. the target value of 8.

3.3.5 Validation

For validation, the methane MOE and band pass reference are placed into multiple identical MOC systems. The MOC sensor for which the MOE is designed has been described previously.(19-22,68-69) A 5 watt tungsten halogen lamp powered at 1.8

watts is focused by a gold-coated parabolic reflector through a 1 mm sample gap. The high-pressure windows are 9.5 mm diameter sapphire with a 6 mm clear aperture and length of 12.7 mm. A 6 RPM rotating carousel carries an inner and outer circumference of 20 paired positions for an MOE and corresponding band pass reference channel. The light emanating from the sapphire sample cell is split and passed through the MOE and band pass reference along separate paths and subsequently focused to a pair of balanced dual-channel thermopile detectors by means of gold-coated off-axis parabolic mirrors. The total distance from filament to detector is less than 33 mm.

For the laboratory validation, a set of MOC sensors containing MOEs for the methane analyte are placed in an oven and attached to a hydraulic pump to provide conditions similar to that of a fluid in a subterranean petroleum well at 65.6 to 121°C and 20.68 to 82.74 MPa. The validation setup is similar to that described previously (63) However, in the current validation, the optical cell and spectrometer described in (63) are removed from the system, with the MOC sensor instead plumbed into the validation system. For the laboratory validation experiment, the MOC system detector is wired to a commercial National Instruments (Austin, Texas) USB data acquisition board for digital records. A custom in-house built driver board supplies power to the light source, detector amplifier, and motor. Fluids were prepared by a third-party vendor (Westport Technology Center International, Houston, Texas) and subsequently injected into the validation system using procedures described previously.(63)

The laboratory validation was conducted in three phases using three different sensors, all containing the same methane MOE design. In Table 3.4, the sensor number specifies a different physical sensor, whereas the series number specifies the carousel

configuration of sensor. The global oil library (GOL) consists of dead oils (i.e., fluids containing no volatile gas components) that are reconstituted to live oil (LO) (i.e., fluids with dissolved gas under pressure) conditions, and also the LOs were sampled from petroleum reservoirs. Both GOL and LO samples were analyzed by gas chromatography for reference.(63) The different sensor configurations contain additional MOEs for different analytes with each series increase, but each also contains the original MOE methane design. With the exception of the carousel configuration, the MOC optical train and sensor electronics are of the same design among sensors and sensor series.

Field validations for the MOC sensor were conducted. A total of two sensors were used to determine the methane concentration of fluid contained within four different oil wells (Table 3.5). The oilwell conditions varied from 37.8 to 80°C and 16.55 to 34.47 MPa. The sensors were placed in a 120.65 mm (4 3/4 inch) outer diameter pressure housing with temperature-robust electronics and lowered into the petroleum wells while mechanically, electrically, and hydraulically connected to four different WFTs for each test. Each WFT contained a mechanical hydraulic pump that collected fluid from the petroleum-bearing rock formation. The pumpouts lasted from 1 to 4.5 hours, depending on the formation properties. The fluid was passed along a flow line from the wellbore rock formation interface, through the pressure sealing pad, past a hydraulic pump, through the MOC sensor, and then past a check valve into the wellbore. After the sample was considered sufficiently clean from drilling fluid filtrate contamination, a portion of the flow was diverted into a pressure-compensated sample chamber and brought to surface. The contents of the collected sample were analyzed by gas chromatography and compared to readings from the MOC sensor received during pumpout. Table 3.5 shows

the results. The direct readings of the detector signal are used to calculate methane concentration without temperature correction, or temperature based calibration. All live oils and field samples were analyzed in a blind fashion with results provided to a third party before receiving reference values.

3.4 RESULTS AND DISCUSSION

Figure 3.14 shows an SEC comparison of the measured vs. predicted concentration between the theoretical performance of Design A and the PLS model. The MOE performance is similar to the PLS regression, slightly outperforming the MOE regression. Broadly, the individual samples appear to project with a similar structure as the PLS and MOE regression. A primary difference between the MOE vs. PLS regression vector performance is the system for which each regression vector is developed. The MOE is developed for a compact, multitemperature, high-pressure sensor, whereas the PLS regression vector is developed for comparatively large FTIR operating at a stable room temperature with a liquid-nitrogen-cooled MCT detector. Although the PLS regression vector is developed using fluid spectra across a temperature range from 65.5 to 121.1°C, the MOE needs to operate with a lower SNR and larger temperature variation. Therefore, during the MOE design, the optical regression vector is intentionally developed for petroleum well in-situ use across this same temperature range. This is achieved by pairing the temperature-dependent transmission spectrum, as dictated by the temperature-dependent materials' optical constants, with the fluid spectrum of the same temperature. For the example illustrated in Figure 3.13, the MOE design is plotted for a temperature of 121.1°C. Typically, higher temperatures tends to red-shift interference filter-based transmission spectra, such as the MOE optical regression vector. The shift

causes a degradation of regression performance if this is not considered during the design evolution. By forcing the evolution of a multitemperature MOE design, the performance of a single-temperature MOE design is never quite achieved; however, performance is stable over the multiple temperatures. At a given temperature over the design range, the MOE regression profile compensates to best match the corresponding temperature-specific spectra.

Figure 3.15 shows the effect of a multitemperature compensated design vs. a single-temperature design. Beginning with the same 200 initial random seed designs, single-temperature MOE designs are optimized using Equation 3.12 but with the number of temperatures, n, as only one such that the high temperature and low temperature, t_H and t_L, are both 121.1°C. The multitemperature designs are optimized using Equation 3.12 with the number of temperatures, n, set to three—specifically, 65.5, 93.3, and 121.1°C. The single-temperature designs, as a population, achieve better single-temperature SEC than the multitemperature designs, having both better SEC, on average, and a tighter distribution of SEC. In fact, the single-temperature optimized designs achieve an SEC more similar to that of the PLS regression vector. However, when the single-temperature design transmissions are re-calculated with the temperature-dependent material optical properties and compared to the same fluid calibration set, a significant degradation in performance is observed. This illustrates the necessity to design MOEs with respect to the temperature range of intended use.

3.4.1 Laboratory and field validation

Table 3.4 shows results for the laboratory blind validation of the MOE-based MOC sensor. The root mean square (RMS) accuracy across all sensors and fluids from

Table 3.4 is 0.00937 g/cc methane, which is similar to the typical design limit of MOEs from Figure 3.11 and slightly better than that predicted for Design A (0.0101 g/cc methane). Samples LO190821 and LO197188 were replicate samples as aliquots of the same oil. The standard deviation of the replicate samples was 0.00106 g/cc, demonstrating the resolution of a same sample measurement with the same MOC sensor. The standard deviation of the set of four samples at a concentration of 0.08 g/cc methane is 0.00232 g/cc methane, demonstrating the precision of a single MOC sensor in multiple fluids. Samples LO246541-A and LO246541-B were aliquots of the same sample measured using two different MOC sensors. The standard deviation of these samples is 0.00443 g/cc methane, demonstrating the precision of a single sample across multiple MOC sensors.

Table 3.5 shows the field validation results for two different MOC sensors.(68,70) Samples 1, 3, and 4 are from the same well, while Samples 2, 5, and 6 are each from different wells; Samples 1 through 4 are light oils, and Samples 5 and 6 are gas. Although this MOE was not specifically designed for gas, the results are surprisingly consistent for gas. This might be a result of the stronger signal and lower interference for gas samples relative to oil samples. Specifically, the gas samples are, on average, 96% methane. The total RMS error between the field measurements and laboratory measurements for all samples in Table 3.5 is 0.00748 g/cc methane. The RMS error of Oil Sample 1 is 0.00904 g/cc methane, which is closer to the design SEC. Again, the RMS error is slightly smaller than that of the design.

Figure 17 shows the combined dataset of the laboratory validation and the field validation. The global RMS accuracy across the laboratory validations and field test is

0.0089 g/cc methane concentration. The combined range of validation is from 0 to 0.229 g/cc methane, which is a larger range than that of the 0.002 to 0.1729 g/cc calibration range used for the MOE design. Additionally the combined dataset spans five MOC sensors, albeit with the same MOE design. The validated MOC performance is similar to the independent PLS validation of 0.0086 g/cc.

It is worth noting that an optimal candidate design was very simple with only 5 layers with an average thickness of 688 nm. This MOE was chosen as having the best SEC after Fabrication Suite screened the potential candidates. In fact the designs with the top 10 SEC had an average of 6.8 layers with 842 nm thickness. In comparison, the best 10 SEC candidate designs without regards to ease of fabrication were on average 12.5 layers of 404 nm average thickness. In addition the designs that were easiest to fabricate were tested by edging the layer uniformity criteria up until only 10 designs remained. These designs that are considered most able to be fabricated had an average of only 4.8 layers with an average of 823 nm thickness. All considered designs from all three groups were of SEC better than 10% of the calibration range. There are two potential advantages of fewer layers and thicker layers. First, more layers are more opportunities for fabrication mistakes to take place. Second, thinner layers are affected more by a fabrication error than thicker layers. Temperature robustness likely has an innate tendency to drive the MOE design toward fewer layers of greater thickness as broader regression features will be less likely to be affected by thermally induced wavelength shifts. Alternatively more layers allow narrower and more complex transmission features. MOE regression vector design is then a compromise between the competing criteria of accuracy driving more and thinner layers verses fabricatibility and

temperature performance driving fewer and thicker layers. The overall thickness of the designs are limited to 6000 nm in order to ensure stability with respect to temperature cycling induced delamination, but the optimal design did not even use this maximum allowed thickness with a total thickness of 4873 nm.

It is interesting to note that the design used for uniformity test was performed using a methane MOE design. The design was chosen because it had sharp features thereby making identification of the wavelength position easy to identify and because it was particularly difficult to fabricate which would test wavelength uniformity for a relatively difficult design. Although the fabricated MOEs were never intended for use, every attempt was made to re-optimize the fabrication to the best possible SEC. The design SEC for the MOE was 0.0088 g/cc methane. However, the calculated SEC for the batch of fabricated 25.4 mm MOE cores was .037 +/- .005 g/cc methane, and for the 6 mm cores was .039 +/- .005 g/cc methane. Each reported batch performance distribution is to one standard deviation, suggesting that calculated performance of the two sets of MOEs is not significantly different for a two tailed distribution with rejection probability of 0.05. In comparison, the distribution for the batch performance was +/- 0.0006 g/cc methane for the best candidate methane design of this study, 8 times better than the MOE fabricated for the uniformity test. With two separate fabrication batches of the same performance, it can be argued that either performance was not the product of a bad fabrication, but rather a product of the limit of the fabrication uniformity. Clearly this design was not easily fabricated, as evidenced by its removal with the fabrication suite simulation and the design characteristics of 13 layers of 469 nm thickness. Lastly it is worth noting that the peak positions are displaced for the two runs in order from lowest

wavelength to highest wavelength by 11.2 nm, 14.1 nm, 17.4 nm, 12.1 nm, and 16.4 nm with the 25.4 mm MOEs shifted to longer wavelengths. This shift is likely not the result of fabrication errors, but rather a consequence of the real time re-optimization. As the deposition process stacks errors, the recovery process as governed by the real time re-optimization never quite recovers the exact same design. However, usually, the SEC can be recovered within the limit of the fabrication capability as evidenced by this example.

It is interesting that for the past 15 years since the inception refining an MOE design by nonlinear optimization to a random layer initialization, no other method of MOE design has been found to be more effective. Past initialization searches within this laboratory have utilized 5,000 to 20,000 random seeds. As such, a search of only 200 random initializations for an optimization routine may seem small and insufficient to fully map a 16 variable multi-dimensional MOE regression vector design space. However, designing the MOE to be temperature invariant in response requires considerably more iterations to converge than problems that do not consider temperature invariance. The using the same 200 random initializations the routine which did not consider temperature required only required a few hours to complete for the entire set, whereas the design that did consider temperature required a couple of days to complete. In actuality, we are not trying to fully map the design space, but rather only find a sufficient that can be fabricated with good accuracy and good sensitivity.

The MOE regression SEP performance of 0.0089 g/cc methane is very similar to the PLS SEP regression performance of 0.0086 g/cc methane. None the less, it is of interest to determine if the MOE performance is significantly different from that of a PLS regression. The confidence 95% interval of the single MOE regression vector can be

estimated based on a leave one 16 validation points. The MOE regression vector was determined to be 0.0089 g/cc +/- .0005 g/cc methane to the 95% confidence interval for 15 degrees of freedom. To determine if this MOE SEP performance was within the distribution of PLS performance, the distribution was estimated by an iterative hold out procedure. The dataset was divided 40,000 times, iteratively such that randomly 1/3 of the data was held out for validation, and a PLS regression 5 level PLS regression vector developed with the remaining 2/3 data. The mean performance of regression vectors calculated was 0.0086 +/- 0.0008 g/cc methane to the 95% confidence interval. The MOE regression performance lies well within the distribution of PLS, and cannot be rejected as an outlier. Therefore, performance of the MOE regression vector and is not significantly different from the performance of 5 level PLS regression as designed to this dataset.

It is important to note that the PLS regression vector is not necessarily the best MOE core. In fact this has been observed with the design of other PLS regression vectors for other analytes in which the sensitivity of is lower by nearly a factor of two compared to a MOE regression vector of similar SEC. The PLS regression vector is designed to FTIR dataset to be applied to future samples collected on the FTIR spectrometer. Although the ICE core is designed to the FTIR dataset, it is not to be applied to that dataset, but rather to be applied to the MOC sensor. Any FTIR spectrometer has nuances and artifacts unique to that instrument and likely not relevant to the MOC sensor. A PLS regression vector designed on an instrument, and applied to the same instrument inherently mitigates these effects. An MOE is not an FTIR and inherently can't reproduce these artifacts. Therefore, when the MOE regression vector is

applied against the FTIR dataset, the performance is underestimated as it is penalized by the inability to mitigate these artifacts. However, because the MOC sensor does not contain these artifacts, the validated performance is usually better than expected. This has been observed repeatedly with MOC systems in our laboratory, and in some instances, the validated MOE performance is better than that obtained with the PLS regression vector.

Not all error of calibration, SEC or validation SEP, is due to the performance of the regression vector, or the instrument. Some of the error is due to reference value. For reconstituted samples, this error is low, since methane is accurately added by pressure to a cylinder and the liquid is volumetrically measured with a metering pump. The ability to add pressure can be measured within +/- 0.1 psi to one standard deviation using a quartz gauge, and the ability to measure liquid volume is accurate to within +/- 0.1 ml to one standard deviation. Fluids were reconstituted with 200 ml of liquid, and final density measured to +/- 0.0001 g/cc to one standard deviation with an in situ densitometer. Using a Monte Carlo simulation for the API gravity, and reservoir fluid density measurements of the calibration set, it is likely that the fluids were reconstituted to better than +/- 0.00005 g/cc methane to one standard deviation for the reference fluids including the reconstructed live oils of the validation study. Using the reconstituted samples as a reference, it has further been shown that methane may be measured in the live sample to better than 4.6% relative accuracy to one standard deviation. This value is taken to be the accuracy for which methane may be measured in 4 field samples of oil. The 4 field samples of oil, Field 1 through Field 4, can provide a reference of about +/- 0.002 g/cc to one standard deviation. The field gas samples are directly measured on a gas

chromatograph with a relative accuracy of 0.5 mol%. The field gas samples were contained approximately 95% methane with the balance primarily ethane and only trace higher hydrocarbons. The samples Field 4 and Field 5 are known to accuracy of +/- 0.001 g/cc methane and +/- 0.0008 g/cc methane respectively. Therefore, the composite contribution of validation uncertainty across all 16 samples due to the reference values is approximately +/- 0.001 g/cc methane to one standard deviation.

3.5 CONCLUSION

Analyte measurement in a complex mixture using MOC by the MOE method is similar in performance to an FTIR instrument in the laboratory using a PLS regression vector. Surprisingly, this is accurate even when the MOC sensor operates at a broad range of high temperatures representative of petroleum reservoirs. This success is achieved as a result of both design and fabrication. The MOE needs to be designed for high temperatures considering both the fluid and MOE spectral changes with temperature. During design, it is not necessary to exhaustively map the MOE transmission design space, but a sufficient mapping leads to a good understanding of the performance expectations of MOEs. Even if the fabrication suite slightly overestimates the validated RMS performance, this is preferable to ensure a robust design is selected for MOC sensor use. The simulated response of the MOEs using the fabrication suite also helps select a design capable of fabrication that will perform well in real-world conditions. Equally important to the design and selection of an MOE for broad-range high-temperature use is the fabrication of the optical component. The ion-assisted e-beam deposition system described here allows real-time in-situ monitoring of the complex index of refraction for materials deposited. In conjunction with the transmission function, this allows re-

optimization of the MOE to account for deposition and modeling imperfections. The re-optimization is successful, in part, because the optical constants and transmission function are determined in-situ at the temperatures which the MOE has been designed and will be used. Additionally, the optical constants drift slightly in the time period over which deposition occurs. The high-temperature ion-assisted deposition provides low moisture, low porosity, and a highly dense medium, which are important for high-temperature use. The fabrication consistency of the MOEs across the five MOC sensors likely enhanced the performance consistency. The current technique represents a significant improvement for the measurement of chemical compositions in high-temperature, high-pressure petroleum wells.

Table 3.1: The composition range of recombined components into petroleum fluid base oils. The GOR shows the relative concentration of recombined fluids to the petroleum base.

	Minimum	**Maximum**
Temp. (°C)	65.5	121.1
Pressure (MPa)	20.684	82.727
Methane (g/cc)	0.002	0.1729
Ethane (g/cc)	0	0.0882
Propane (g/cc)	0	0.071
CO2 (g/cc)	0	0.1211
GOR (scf/bbl)	76	22851

Table 3.2: Shown are the thin layer stack recipes for the designs discussed. Each row shows the thickness of the thin film for the material shown in the last column. The first column shows the layer number with the first layer being deposited directly onto the substrate and the last layer for that design exposed to air. The second column "MOE Design (nm)" shows the recipe for the fabricated methane MOE. The third column, "Alternate Design (nm) shows a design that was not chosen for fabrication, but rather listed for comparison to the selected design due to the good SEC but very low sensitivity. The fifth column shows the bandpass filter fabricated in this study. The fifth column, "Uniformity Test Design (nm)", is an MOE chosen for sharp easy to measure features but difficult to fabricate so that an upper boundary of wavelength fabrication tolerance can be established.

Layer	Design A (nm)	Design B (nm)	Band Pass (nm)	Uniformity Test (nm)	Material
1	406.4	703.8	38.7	412.4	Si
2	1232.4	262.7	133.2	536.2	SiO_2
3	514.7	566.9	53.7	188.8	Si
4	1059.0	150.0	632.8	663.5	SiO_2
5	225.6	203.4	217.8	264.1	Si
6	—	130.1	542.2	564.5	SiO_2
7	—	452.0	207.5	240.6	Si
8	—	392.5	532.8	667.7	SiO_2
9	—	392.5	210.0	85.3	Si
10	—	741.3	651.7	716.6	SiO_2
11	—	627.9	37.8	720.2	Si
12	—	602.8	792.1	469.5	SiO_2
13	—	409.5	28.2	572.7	Si
14	—	435.3	831.2	—	SiO_2
15	—	—	26.9	—	Si
16	—	—	356.9	—	SiO_2
Total	4873.4	6070.7	5254.8	6102.1	

Table 3.3: The results of the MOE fabrication system uniformity test. Twenty MOEs were fabricated on substrates for each of the 6 mm substrates and 25.4 mm substrates. The standard deviation for each peak of the each batch is calculated. The mean position difference for each peak is also calculated for the 25.4 mm substrate to the 6 mm substrate.

	6 mm Substrate		**25.4 mm Substrate**		
	Mean Position	**Standard Deviation**	**Mean Position**	**Standard Deviation**	**Position Difference**
Peak 1	1641.6	4.9	1652.8	5.4	11.2
Peak 2	1689.2	4.4	1703.3	6.5	14.1
Peak 3	1827.4	5.4	1844.8	6.5	17.4
Peak 4	1935.4	5.9	1947.5	5.9	12.1
Peak 5	2160.2	6.6	2176.6	8.0	16.4
Mean	—	5.44	—	6.46	14.24

Table 3.4: Laboratory validation work for MOC Sensor Series 1, 2, and 3. All measurements presented are acquired at 93.3°C and 40.369 MPa. The reference values are reconstituted with methane to known concentrations with an uncertainty of approximately +/- 0.00005 g/cc methane. Live oil samples labeled LO were run as blind validation.

MOC Sensor	Sample	Laboratory	MOC Sensor
Sensor 2 Series 100	GOL13	0	0.008
Sensor 2 Series 100	GOL33	0	0.002
Sensor 2 Series 100	LO190821	0.08	0.0946
Sensor 2 Series 100	LO197188	0.08	0.0931
Sensor 2 Series 100	LO192809	0.08	0.091
Sensor 2 Series 100	LO196726	0.06	0.0503
Sensor 2 Series 100	LO192795	0.04	0.0328
Sensor 2 Series 100	GOL34	0.08	0.0893
Sensor 3 Series 200	LO246541-A	0.104	0.09573
Sensor 4 Series 300	LO246541-B	0.104	0.102

Table 3.5: Results for the field test of MOC sensors using the methane MOEs. Samples 1-4 are oil samples with reference accuracy of approximately +/- 0.002 g/cc methane to one standard deviation. Samples 5-6 are gas samples with reference accuracy of approximately +/- 0.001 g/cc methane. All samples were run as blind validation.

MOC Sensor	Sample No.	Laboratory	MOC Sensor
Sensor 5 Series 200	Sample 1	0.046	0.050
Sensor 5 Series 200	Sample 2	0.055	0.041
Sensor 5 Series 200	Sample 3	0.036	0.045
Sensor 5 Series 200	Sample 4	0.042	0.036
Sensor 1 Series 100	Sample 5	0.229	0.236
Sensor 1 Series 100	Sample 6	0.170	0.167

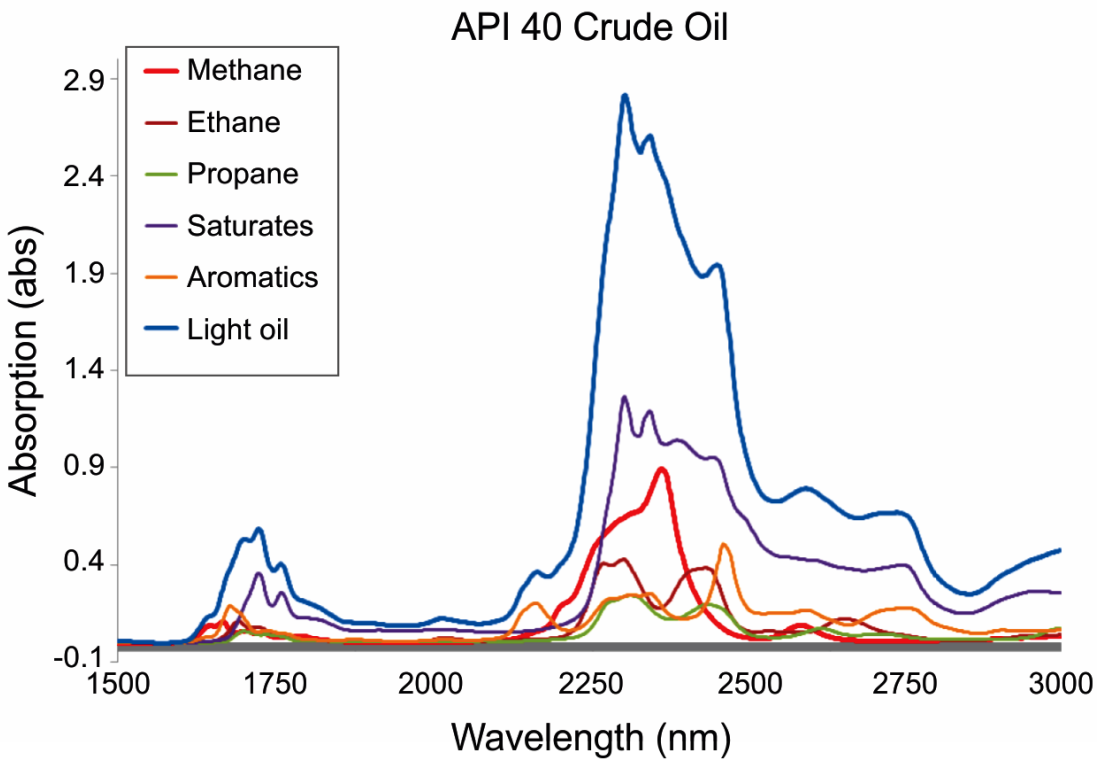

Figure 3.1: Pure component spectra and API 40 crude oil at a gas-to-oil ratio (GOR) of 1600 scf/bbl (standard cubic feet per barrel of liquid) light crude oil acquired at 41.369 MPa and 121.1°C.

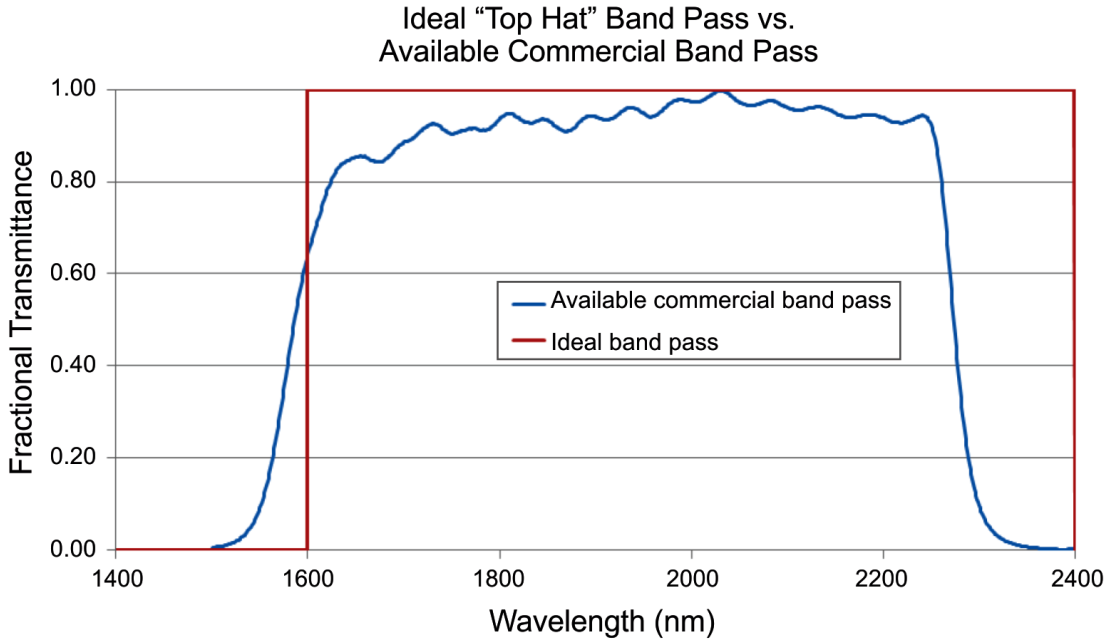

Figure 3.2: Custom band pass filter vs. an ideal top hat baseline offset. The deviation from an ideal reference is compensated by the MOE design.

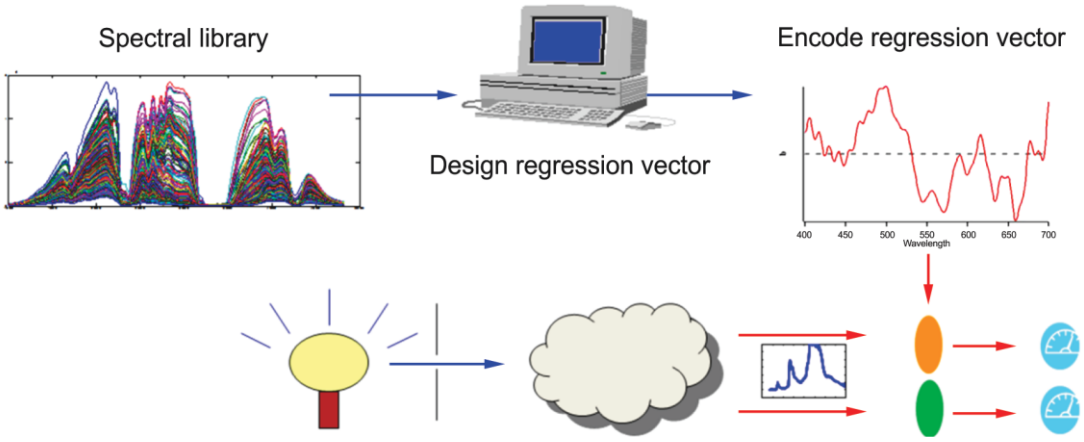

Figure 3.3: The MOE reference configuration. A regression vector is designed from a spectral library and encoded as the transmission function for an MOE (shown in orange). As light (blue arrow) passes through an unknown sample, represented by the cloud, the resultant light (red arrows) passes through the MOE and onto a detector, whereas a separate path of light is passed through the reference (in green) and onto a detector.

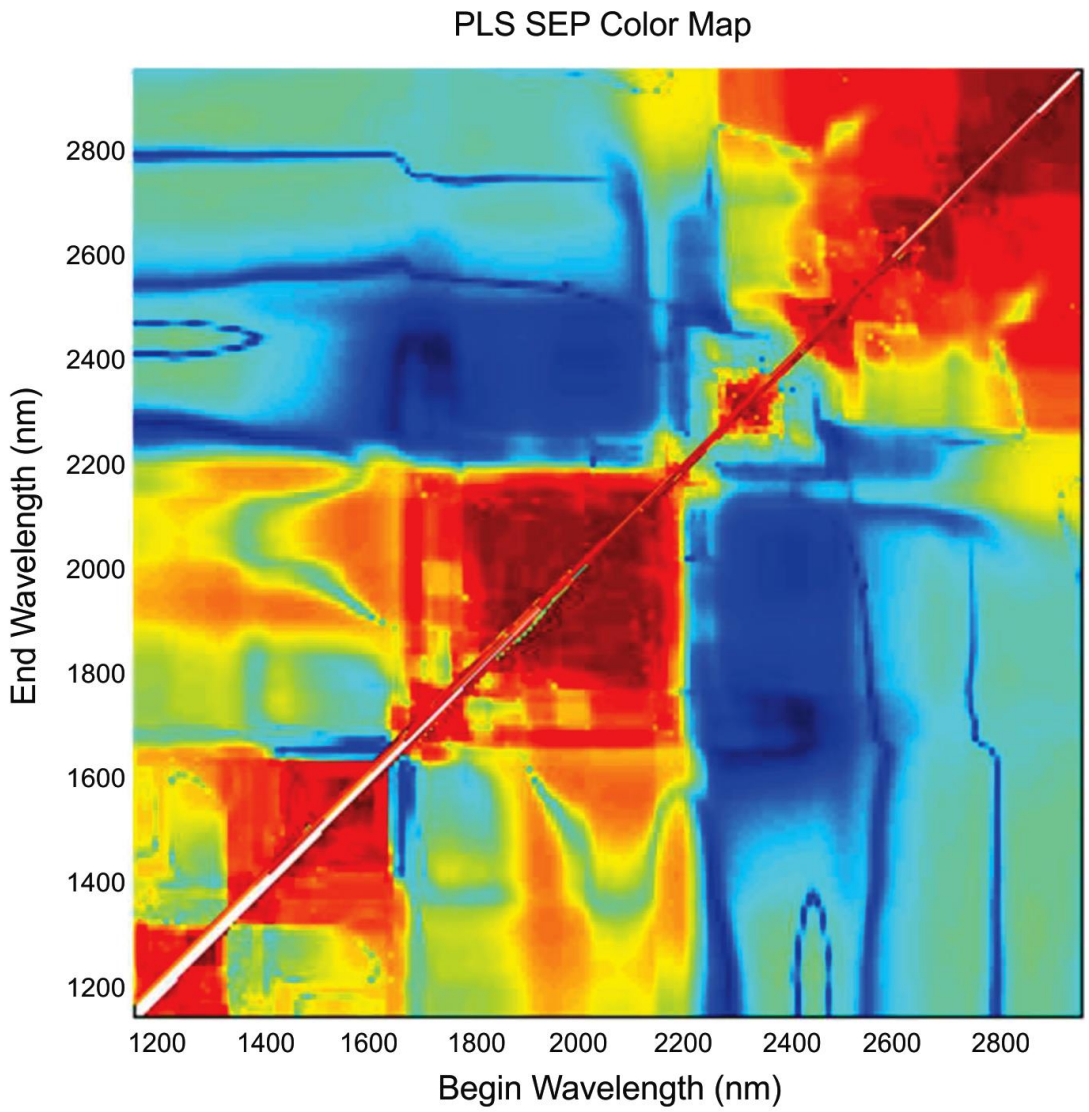

Figure 3.4: Color map of the PLS SEP for beginning wavelengths to ending wavelengths for methane. Dark blue is low SEP better than 5% relative to the methane calibration range, and dark red is higher than 30% SEP relative to the calibration range.

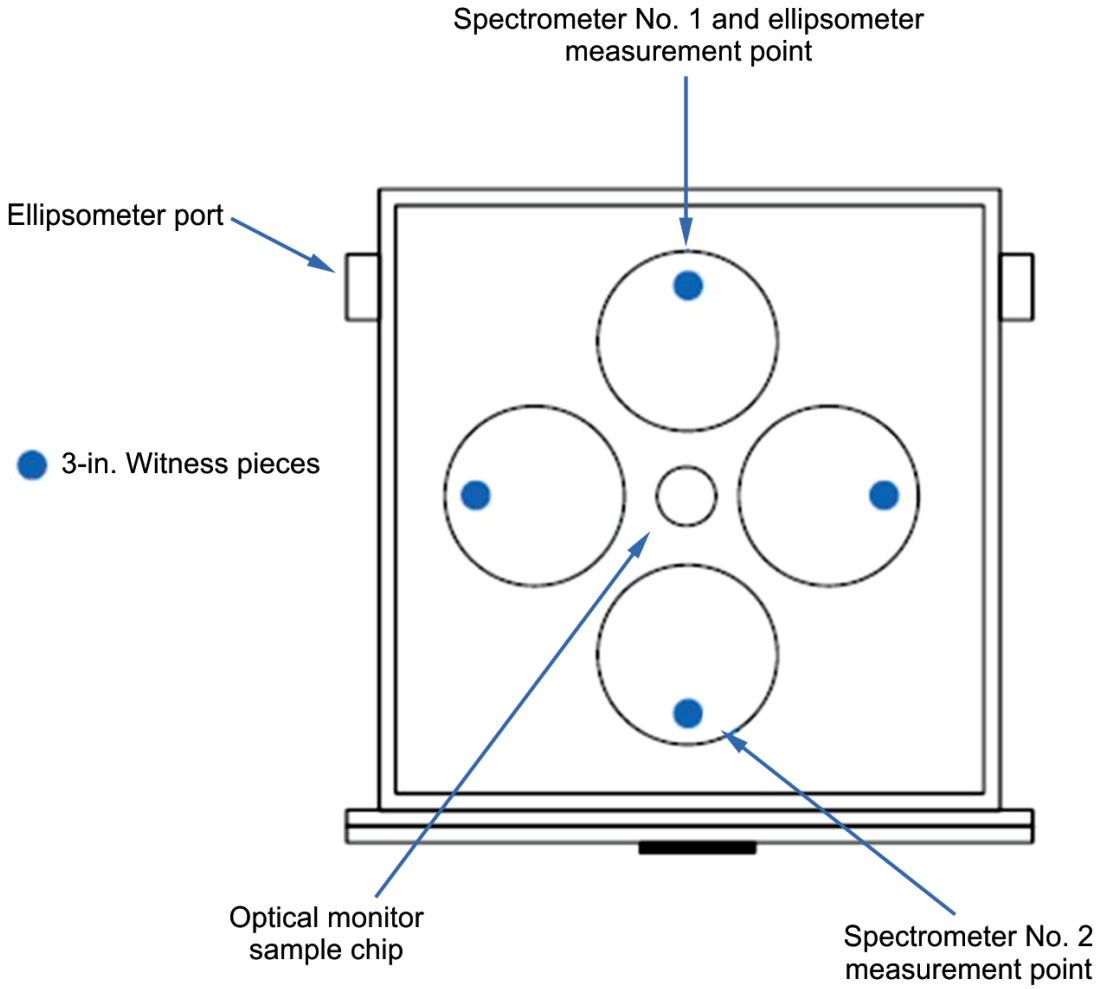

Figure 3.5: Top-down schematic of the ion-assisted e-beam deposition system.

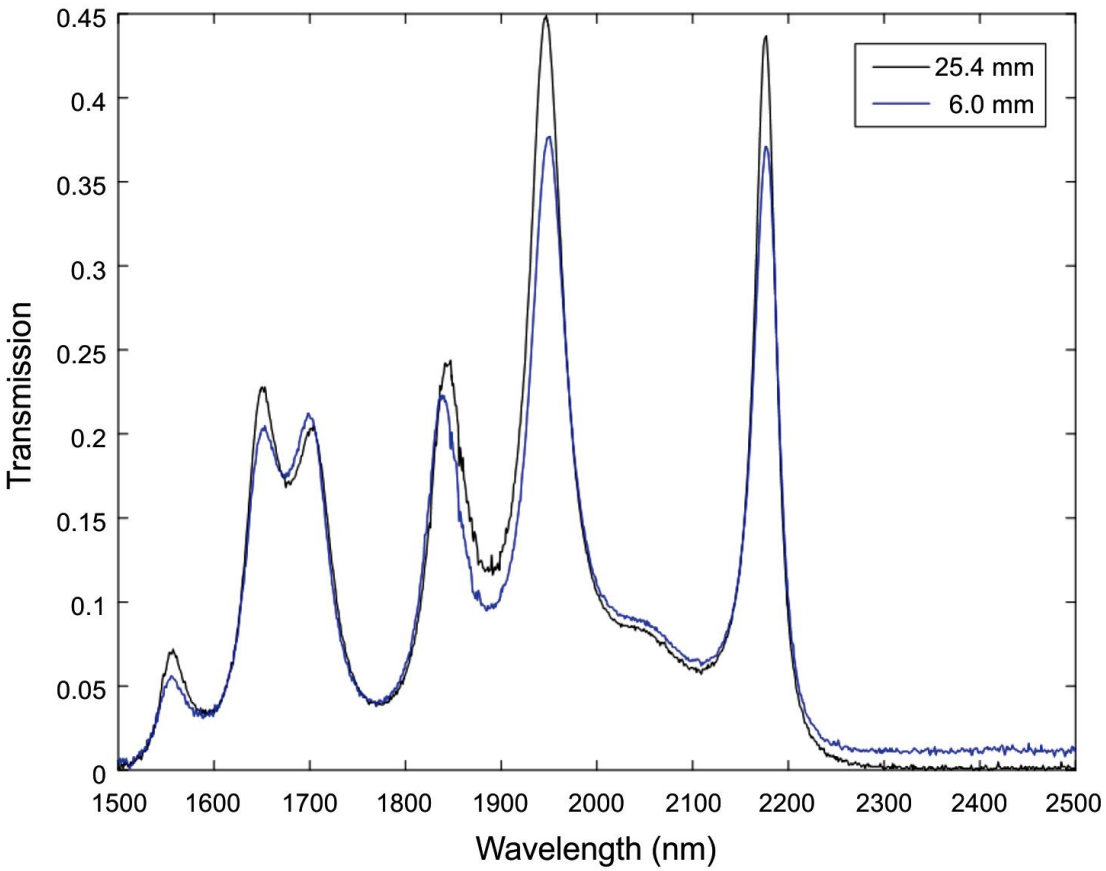

Figure 3.6: Middle MOE transmission of 20 optical elements for a 25.4 mm vs. 6.0 mm double-sided fabrication.

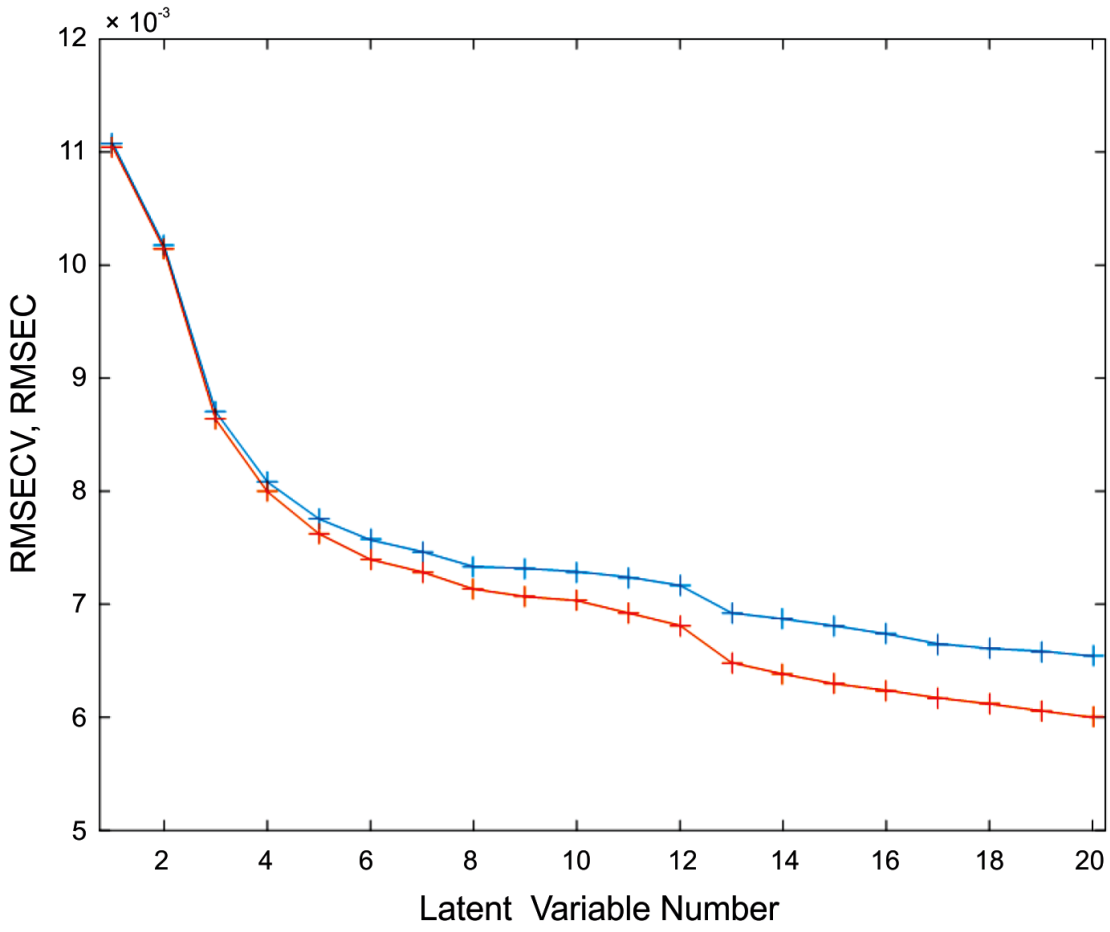

Figure 3.7: Knee-plot of model error vs. number of PLS model levels. The SEP by RMSECV is shown in blue and SEC by root mean square error of calibration (RMSEC) is shown in red.

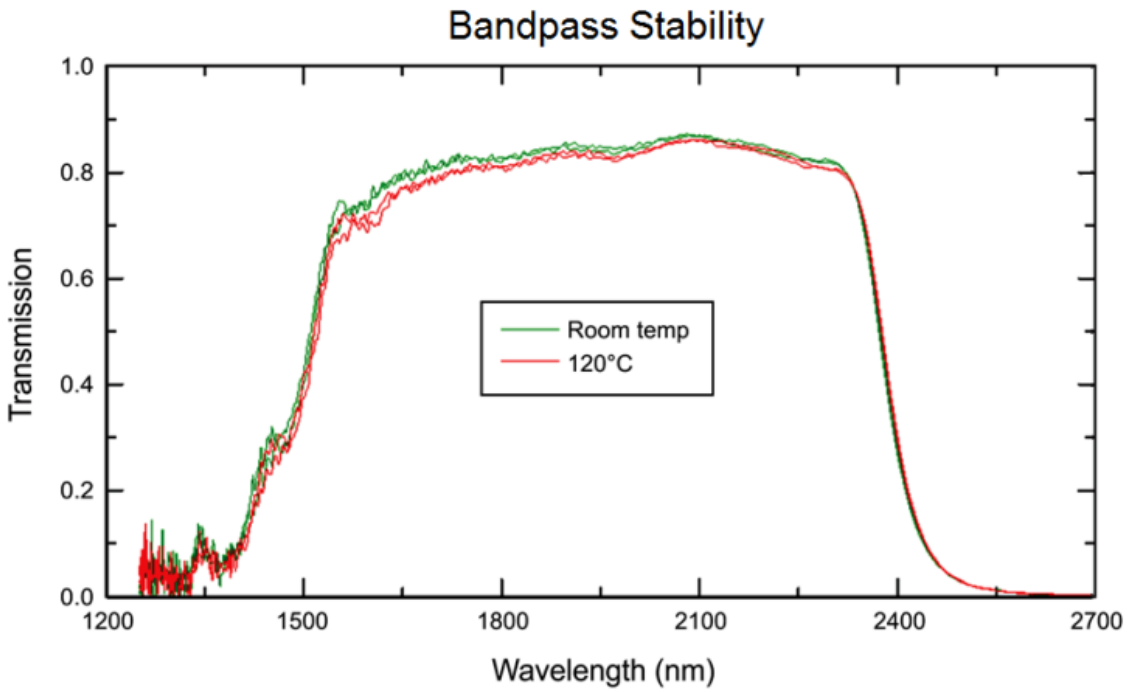

Figure 3.8: Temperature stability and repeatability of custom bandpass. The leading edge at 1502.6 nm has a temperature stability of 0.0495 +/- 0.0004 nm/°C and trailing edge at 2388.5 nm has a temperature stability of .0374 +/- 0.006 nm/°C. The repeatability of the leading edge is +/- 3.1 nm and trailing edge is +/- 1.4 nm for the batch at the 95% confidence interval.

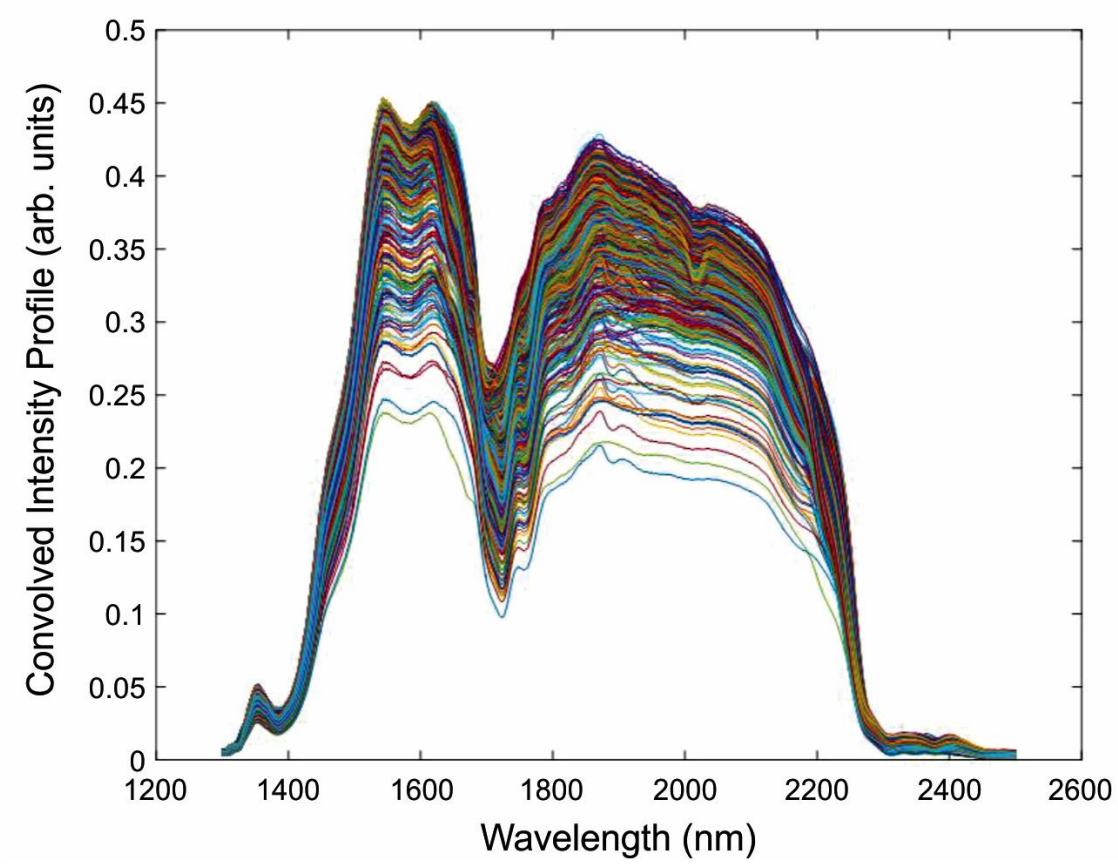

Figure 3.9: The virtual sensor spectra used for calibration are generated as the vector product of the transmission function for all optical components in the MOC sensor, thereby representing the spectra that the MOC detector would observe.

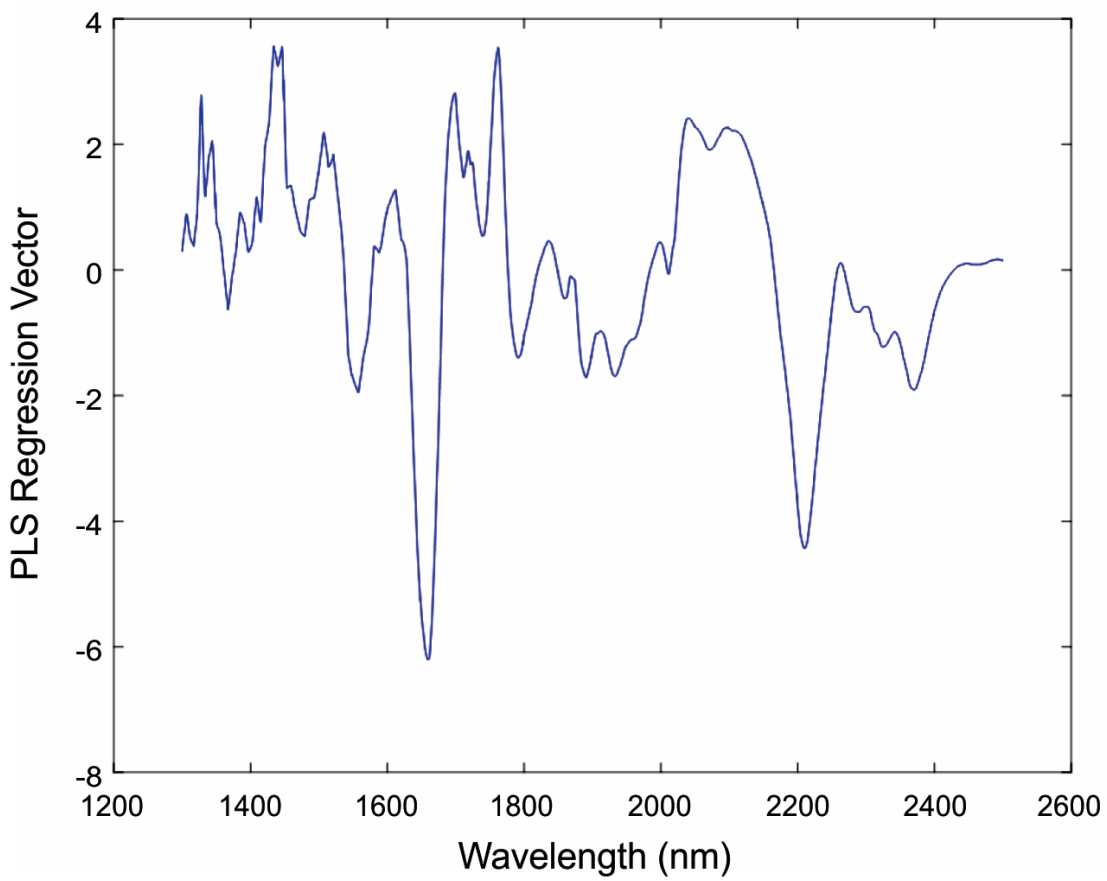

Figure 3.10: Methane 5 level PLS regression vector for FTIR virtual sensor single beam transmittance. The regression vector is designed to the virtual sensor single beam transmittance calibration set.

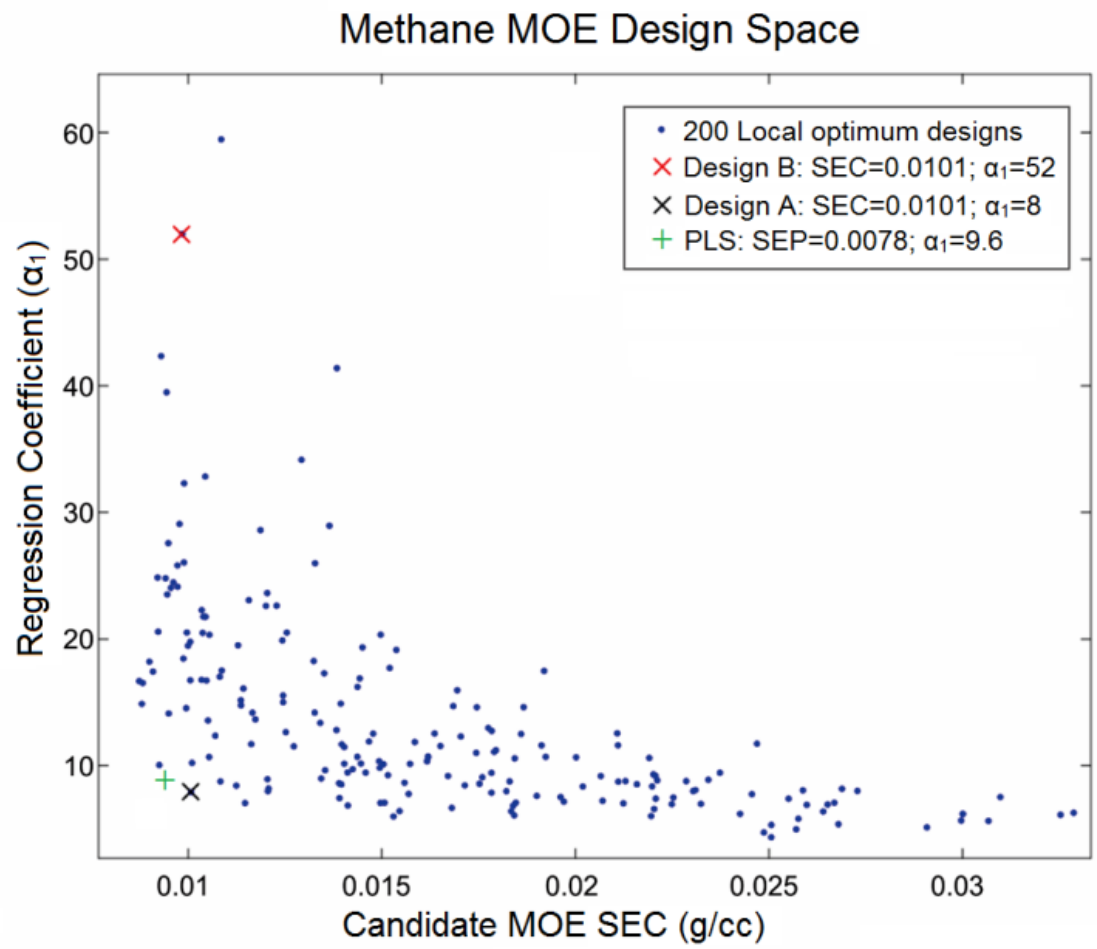

Figure 3.11: Methane design plotted against SEC and the sensitivity related regression coefficient α_1. The black X shows the optimal Design A, and the red X shows Design B, which has a similar SEC but substantially lower sensitivity. The green cross shows the hypothetical position of an ideally transferred PLS regression vector.

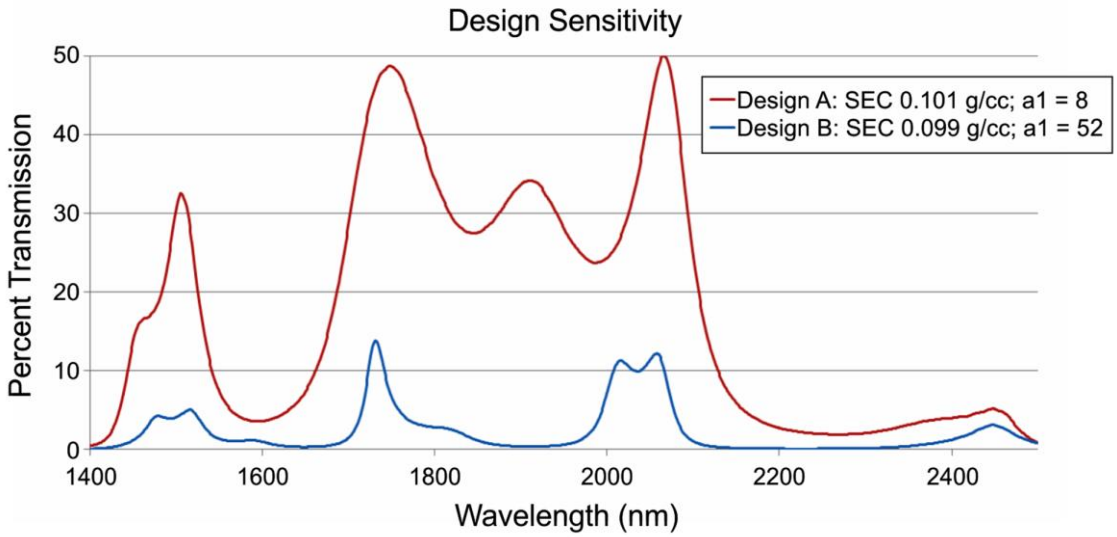

Figure 3.12: MOE transmission profile for a large (red curve) and small (black curve) regression coefficient design. Note this transmission profile is not convoluted with the custom band pass filter.

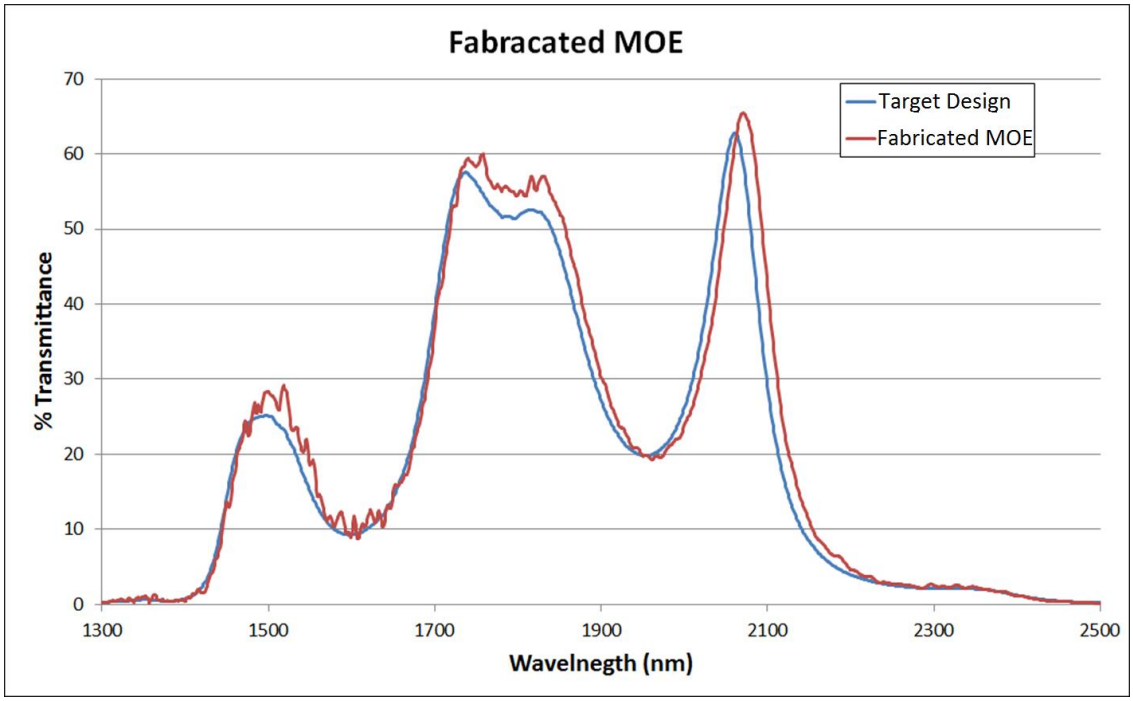

Figure 3.13: Fabricated MOE stack compared to the theoretical transmission based on the stack design. The differences in the target design vs the fabricated MOE are due to the re-optimization process. As little stack errors build layer upon layer during the fabrication process, the nonlinear optimization routine uses the in-situ measured optical constants and the transmission profile for the partially fabricated MOE to re-optimize the remaining layers in order to achieve the best SEC performance as opposed to retaining the original transmission shape.

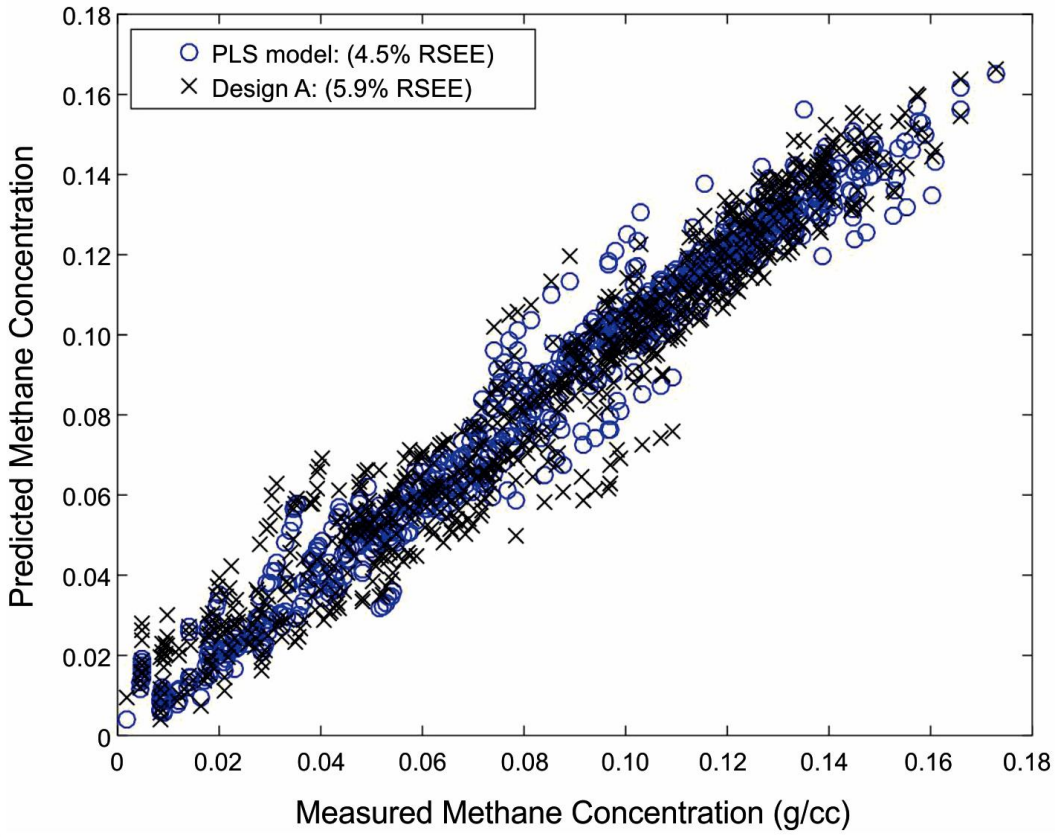

Figure 3.14: Measured vs. predicted methane concentration comparison between theoretical PLS model and MOE design.

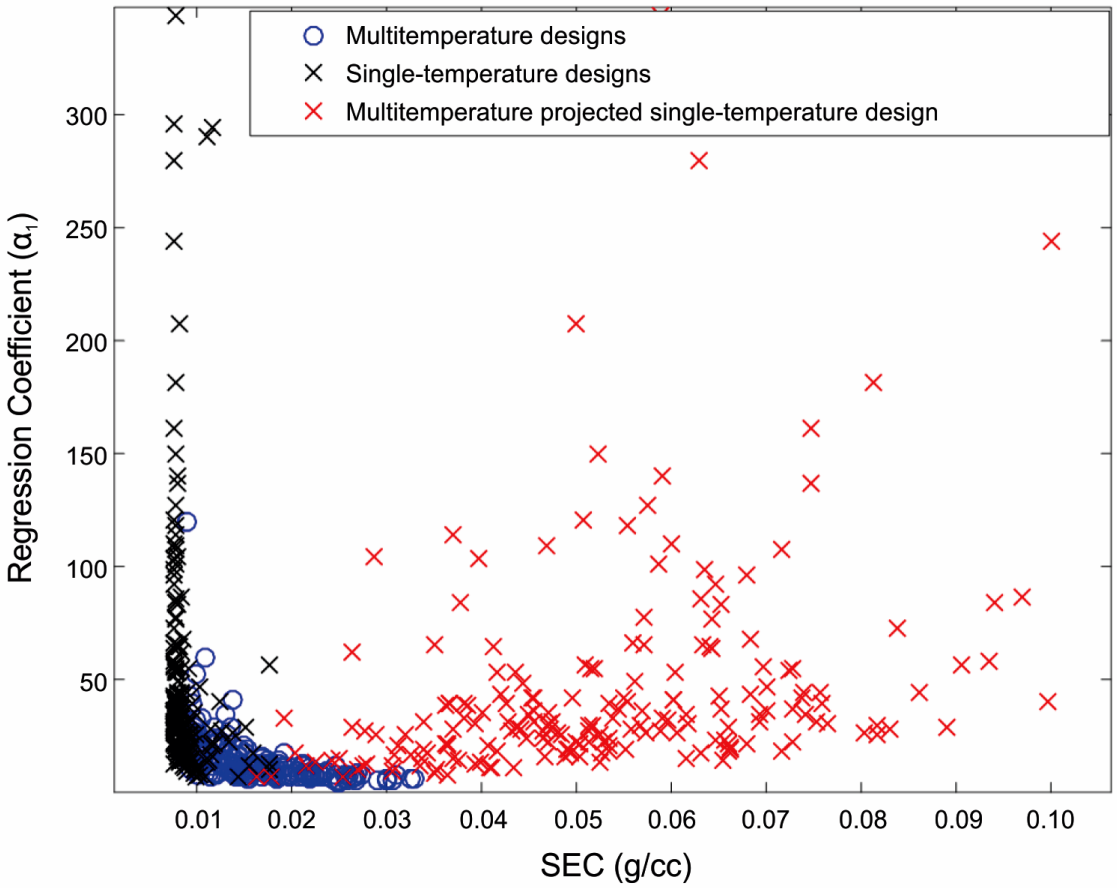

Figure 3.15: Temperature analysis results for 200 random seeded designs, using the same random seeds for the single- temperature vs. multitemperature optimizations.

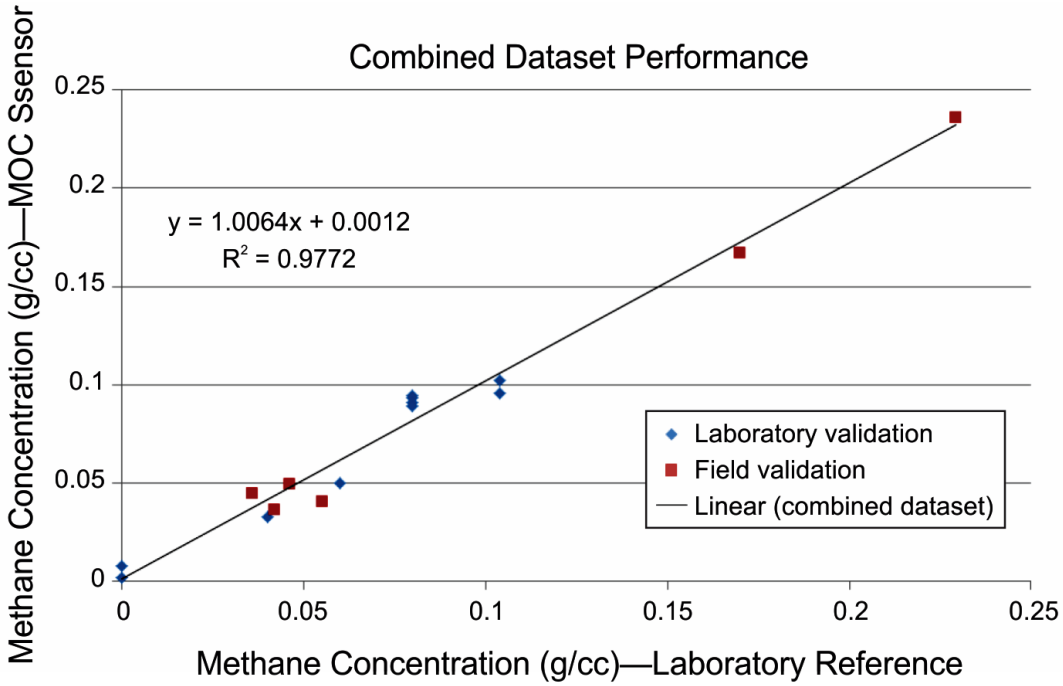

Figure 3.16: Performance for the combined validation study of methane by MOC sensor compared to laboratory gas chromatography analysis.

REFERENCES

1. Elshahawi, H.; Hashem, M. N.; McKinney, D.; Ardila, M.; Ayan, C. The Power of Real-Time Monitoring and Interpretation in Wireline Formation Testing–Case Studies. *SPE Reservoir Evaluation and Engineering* **2007,** *10* (3), 241–250.

2. Dong, C.; O'Keefe, M.; Elshahawi, H.; Hashem, M.; Williams, S.; Stensland, D.; Hegeman, P.; Vasques, R.; Terabayashi, T.; Mullins, O.; Donzier, E. New downhole-fluid-analysis tool for improved reservoir characterization. *SPE Reservoir Evaluation and Engineering* **2008,** *11* (6), 1107-1116.

3. Hashem, M.; McHardy, A.; Wynne, M.; Pool, W.; Viets, T.; Keuser, C.; Eriksen, K. O. Formation Pressure While Drilling, Wireline Formation Testing, And Fluid Sampling In a High Pressure/High Temperature Exploration Well Using Oil Based Mud: A Case History1. *Petrophysics* **2007,** *48* (4), 258-270.

4. American Petroleum Institute. *API Recommended Practice 44: Sampling Petroleum Reservoir Fluids, second edition;* Orginization; American Petroleum Institute: Washington, DC, 2003.

5. Ahmed, K.; Hassan, F.; Taqi, F.; Ahmad, F.; Pearl, M.; Jones, C.; Vasquez, R.; Zuilekom, A. v.; Pelletier, M. Real-Time Downhole Fluid Analysis and Sampling with a New Optical Composition Analysis Sensor: A Case Study from Kuwait Heavy Oil Formation. *SPE International Heavy Oil Conference and Exhibition*, Mangaf, Kuwait, 2016; pp SPE-184112-MS.

6. Achourov, V.; Gisolf, A.; Kansy, A.; Eriksen, K. O.; RWE-Dea; O'Keefe, M.; Pfeiffer, T. Applications of Accurate In-Situ Fluid Analysis in the North Sea. *Offshore Europe*, Aberdeen, UK, 2011; pp SPE-145643-MS.

7. Angeles, R.; Torres-Verdin, C.; Malik, M. PREDICTION OF FORMATION-TESTER FLUID-SAMPLE QUALITY IN HIGHLY-DEVIATED WELLS. *SPWLA 49th Annual Logging Symposium*, Austin, Texas, 2008; pp SPWLA-2008-SS.

8. Crombie, A.; Halford, F.; Hashem, M.; McNeil, R.; Thomas, E.; Melbourne, G.; Mullins, O. Innovations in Wireline Fluid Sampling. *Oilfield Review* **1998,** *10* (3), 26-41.

9. Elshahawi, H.; Venkataramanan, L.; McKinney, D.; Flannery, M.; Mullins, O. C.; Hashem, M. Combining Continuous Fluid Typing Wireline Formaion Testers, and Geochemical Measurments for an Improved Understanding of Reservoir Architecture. *SPE Reservoir Evaluation and Engineering* **2008,** *11* (1), 27 - 40.

10. Hammond, P. S. One- and two-phase flow during fluid sampling by a wireline tool. *Transport in Porous Media* **1991,** *6* (3), 299-330.

11. Hy-Billiot, J.; Bickert, J.; Montel, F.; Segalini, G. Getting the Best From Formation Tester Sampling. *SPE Annual Technical Conference and Exhibition*, San Antonio, TX, 2002; pp SPE-77771-MS.

12. Malik, M.; Torres-Verdín, C.; Sepehrnoori, K. Axially symmetric compositional simulation of formation tester measurements. *Journal of Petroleum Science and Engineering* **2007,** *59* (3), 333–349.

13. Malik, M.; Torres-Verdín, C.; Sepehrnoori, K.; Jackson, R.; Weinheber, P.; Mullins, O. C.; Elshahawi, H.; Dindoruk, B.; Hashem, M. Comparison of Wireline Formation-Tester Sampling with Focused and Conventional Probes in the Presence of Oil-Base Mud-Filtrate Invasion. *49th Annual Logging Symposium*, 2008; pp SPWLA-2008-LL.

14. Pedersen, K. . a. P. L. C. P. *Phase Behavior of Petroleum Reservoir Fluids;* CRC Press: Boca Raton, 2007.

15. Mullins, O. C.; Beck, G. F.; Cribbs, M. E.; Terabayashi, T.; Kegasawa, K. Downhole Determination Of Gor On Single-Phase Fluids By Optical Spectroscopy. *SPWLA 42nd Annual Logging Symposium*, Houston, Texas, 2001; pp SPWLA-2001-M.

16. Mullins, O.; Rodgers, R.; Weinheber, P.; Klein, G.; Venkataramanan, L.; Andrews, A.; Marshal, A. Oil Reservoir Characterization via Crude Oil Analysis by Downhole Fluid Analysis in Oil Wells with Visible−Near-Infrared Spectroscopy and by Laboratory Analysis with Electrospray Ionization Fourier Transform Ion Cyclotron Resonance Mass Spectrometry. *Energy and Fuels* **2006,** *20* (6), 2448-2456.

17. Ellis, D. V.; Singer, J. M. *Well logging for Earth Scientists, 2nd Ed.,* 2nd ed.; Springer: Dordrecht, 2008.

18. Andrews, A.; Schneider, M.; Canas, J.; Freitas, E.; Song, Y.; Mullins, O. Fluorescence Methods for Downhole Fluid Analysis of Heavy Oil Emulsions. *Journal of Dispersion Science and Technology* **2008,** *29* (2), 171-183.

19. Jones, C. M.; Freese, B.; Pelletier, M.; Perkins, D.; Chen, D.; Shen, J.; Atkinson, R. Laboratory Quality Optical Analysis in Harsh Environments. *Presented at the SPE Kuwait International Petroleum Conference and Exhibition*, Kuwait City, Kuwait, 2012; pp SPE-163289-MS.

20. Jones, C.; Gao, L.; Perkins, D.; Chen, D.; Gascook, D. Field Test of the Integrated Computational Elements: A New Optical Sensor for Downhole Fluid Analysis. *SPWLA 54th Annual Logging Symposium*, New Orleans, Louisiana, 2013; pp SPWLA-2013-YY.

21. Jones, C. M.; Freese, R.; Perkins, D. L.; Dai, B. Multivariate optical computing enables accurate harsh-environment sensing for the oil and gas industry. *Laser Focus World* **2014,** *50* (8), 27-31.

22. Jones, C.; Dai, B.; Chen, D.; He, T.; Pelletier, M.; Gascooke, D. Measurement and use of Formation Fluid, Saturate, and Aromatic Content, With Wireline Formation Testers. *SPWLA 56th Annual Symposium*, Long Beach, 2015; pp SPWLA-2015-EE.

23. Myrick, M. L.; Soyemi, O.; Karunamuni, J.; Eastwood, D.; Zhang, L.; Greera, A. E.; Gemperlineb, P. A single-element all-optical approach to chemometric prediction. *Vibrational Spectroscopy* **2002,** *28* (1), 73–81.

24. Soyemi, O.; Eastwood, D.; Zhang, L.; Li, H.; Karunamuni, J.; Gemperline, P.; Synowicki, R. A.; Myrick, M. L. Design and Testing of a Multivariate Optical Element: The First Demonstration of Multivariate Optical Computing for Predictive Spectroscopy. *Analytical Chemistry* **2001,** *73* (6), 1069–1079.

25. Soyemi, O.; Haibach, F.; Gemperline, P. J.; Myrick, M. L. Nonlinear Optimization Algorithm for Multivariate Optical Element Design. *Applied Spectroscopy* **2002,** *56* (4), 477-487.

26. Wold, S. Chemometrics; what do we mean with it, and what do we want? *Chemometrics and Intelligent Laboratory Systems* **1995,** *30* (1), 109-115.

27. Beebe, K. R.; Kowalski, B. R. An Introduction to Multivariate Calibration and Analysis. *Analytical Chemistry* **1987,** *59* (17), 1007-1017.

28. Thomas, E. V. A Primer on Multivariate Calibraiton. *Analytical Chemistry* **1994,** *66* (15), 795-804.

29. Massart, D. L.; Vandeginste, B. G.; Deming, S. N.; Michotte, Y.; Kaufmann, L. *Chemometrics: a textbook;* Elsevier Science Publishers: Amsterdam, 1988.

30. Martens, H.; Naes, T. *Multivariate Calibration;* Wiley: New York, 1992.

31. Nadler, B.; Coifman, R. R. Partial least squares, Beer's law and the net analyte: statistical modeling and analysis. *Journal of Chemometrics* **2005,** *19* (1), 45–54.

32. Deming, S.; Morgan, S. . *Experimental Design: A Chemometric Approach;* Elsevier Science Publishers: New York, 1987.

33. Malinowski , E.. *Factor Analysis in Chemistry, 3rd Edition;* Wiley-Interscience: New York, 1991.

34. Wold, S.; Sjostrom, M.; Eriksson, L. PLS-regression: a basic tool of chemometrics. *Chemometrics and Intelligent Laboratory Systems* **2001,** *58* (2), 109-130.

35. Aske, N.; Kallevik, H.; Sjöblom, J. Determination of Saturate, Aromatic, Resin, and Asphaltenic (SARA) Components in Crude Oils by Means of Infrared and Near-Infrared Spectroscopy. *Energy and Fuels* **2001,** *15* (5), 1304-1312.

36. Melendez, L. V.; Lache, A.; Orrego-Ruiz, J. A.; Pachon, Z.; Mejia-Ospino, E. Prediction of the SARA analysis of Colombian crude oils using ATR–FTIR spectroscopy and chemometric methods. *Journal of Petroleum Science and Engineering* **2012,** *90-91* (Supplement C), 56-60.

37. Laxalde, J.; Ruckebusch, C.; Devos, O.; Caillol, N.; Wahl, F.; Duponchel, L. Characterisation of heavy oils using near-infrared spectroscopy: optimisation of pre-processing methods and variable selection. *Analytica Chimica Acta* **2011,** *705* (1), 227-234.

38. Satya, S.; Roehner, R. M.; Deo, M. D.; Hanson, F. V. Estimation of properties of crude oil residual fractions using chemometrics. *Energy and Fuels* **2007,** *21* (2), 998-1005.

39. Riveros, L.; Jaimes, B.; Ranaudo, M. A.; Castillo, J.; Chirinos, J. Determination of Asphaltene and Resin Content in Venezuelan Crude Oils by Using Fluorescence Spectroscopy and Partial Least Squares Regression. *Energy and Fuels* **2006,** *20* (1), 227-230.

40. Long, Y.; Dabros, T.; Hamza; Hassan. Analysis of Solvent-Diluted Bitumen from Oil Sands Froth Treatment Using NIR Spectroscopy. *Canadian Journal of Chemical Engineering* **2004,** *82* (4), 776-781.

41. Macho, S.; Larrechi. Near-infrared spectroscopy and multivariate calibration for the quantitative determination of certain properties in the petrochemical industry. *TrAC Trends in Analytical Chemistry* **2002,** *21* (12), 799-806.

42. Honigs, D. E.; Hirschfeld, T. B.; Hieftje, G. M. Near-Infrared Determination of Several Physical Properties of Hydrocarbons. *Analytical Chemistry* **1985,** *57* (2), 443–445.

43. Abbas, O.; Dupuy, N.; Rebufa, C.; Vrielynck, L.; Kister, J.; Permanyer, A. Prediction of source rock origin by chemometric analysis of fourier transform infrared-attenuated total reflectance spectra of oil petroleum: evaluation of aliphatic and aromatic fractions by self-modeling mixture analysis. *Applied Spectrosctroscopy* **2006,** *60* (3), 304-314.

44. de Peinder, P.; Petrauskas, D. D.; Singelenberg, F.; Salvatori, F.; Visser, T.; Soulimani, . F.; Weckhuysen, B. M. Prediction of Long and Short Residue Properties of Crude Oils From Their Infrared and Near-Infrared Spectra. *Applied Spectroscopy* **2008,** *62* (4), 414-422.

45. Van Agthoven, M. A.; Fujisawa, G.; Rabbito, P.; Mullins, O. C. Near-Infrared Spectral Analysis of Gas Mixtures. *Applied Spectroscopy* **2002,** *56* (5), 593–598.

46. Fujisawa, G.; Van Agthoven, M. A.; Jenet, F.; Rabbito, P. A.; Mullins, O. C. Near-infrared compositional analysis of gas and condensate reservoir fluids at elevated

pressures and temperatures. *Applied Spectroscopy* **2002,** *56* (12).

47. Lorber, A.; Faber, K.; Kowalski, B. . R. Net Analyte Signal Calculation in Multivariate. *Analytical Chemistry* **1997,** *69* (8), 1620-1626.

48. Wold, S.; Martens, H.; Wold, H. The multivariate calibration problem in chemistry solved by the PLS method. *Matrix Pencils*, Pite Havsbad, Sweden, 1982; pp 286-293.

49. H. M. Hcise, D. Infrared spectra of gases. In *Infrared and Raman Spectroscopy: Methods and Applications;* Schrader, Bernhard, Eds.; VCH Verlagsgescllschaft: Weinheim, 1995; p 264.

50. Jackson, E. J. . *A user's guide to principal components;* John Wiley & Sons: New York, 2005.

51. Nelson, M. P.; Aust, J. F.; Dobrowolski, J. A.; Verly, P. G.; Myrick, M. L. Multivariate Optical Computation for Predictive Spectroscopy. *Analytical Chemistry* **1998,** *70* (1), 73–82.

52. Gemperline, P. J.; Long, J. R.; Gregoriou, V. G. Nonlinear multivariate calibration using principal components regression and artificial neural networks. *Analytical Chemistry* **1991,** *63* (20), 2313-2323.

53. Næs, T.; Isaksson, T. Locally Weighted Regression in Diffuse Near-Infrared Transmittance Spectroscopy. *Applied Spectroscopy* **1992,** *46* (1), 34-43.

54. Liu, F.; Jiang, Y.; He, Y. Variable selection in visible/near infrared spectra for linear and nonlinear calibrations: A case study to determine soluble solids content of beer. *Analytica Chimica Acta* **2009,** *635* (1), 45-52.

55. Centner, V.; Massart, D. L. Optimization in Locally Weighted Regression. *Analytical Chemistry* **1988,** *70* (19), 4206-4211.

56. Bro, R.; Anderson, C. M. Theory of net analyte signal vectors in inverse regression. *Journal of Chemometrics* **2003,** *17* (12), 646-652.

57. Faber, N. (. M. Efficient Computation of Net Analyte Signal in Inverse Multivariate Calibration Models. *Analytical Chemistry* **1998,** *70* (23), 5108-5110.

58. Soyemi, O. O.; Haibach, F. G.; Gemperline, P. J.; Myrick, M. L. Design of angle-tolerant multivariate optical elements for chemical imaging. *Applied Optics* **2002,** *10* (10), 1936-1941.

59. Simcock, M.; Myrick, M. Precision in imaging multivariate optical computing. *Applied Optics* **2007,** *46* (7), 1066-1080.

60. Blanco, M.; Coello, J.; Iturriaga, H.; Maspoch, S.; Pezuela, C. D. L. Effect of Data Preprocessing Methods in Near-Infrared Diffuse Reflectance Spectroscopy for the Determination of the Active Compound in a Pharmaceutical Preparation. *Applied Spectroscopy* **1997,** *51* (2), 240–246.

61. Candolfi, A.; De Maesschalck, R.; Jouan-Rimbaud, D.; Hailey, P. A.; Massart, D. L. The influence of data pre-processing in the pattern recognition of excipients near-infrared spectra. *Journal of Pharmaceutical and Biomedical Analysis* **1999,** *21* (1), 115-132.

62. Zeaiter, M.; Roger, J.-M.; Bellon-Maurel, V. Robustness of models developed by multivariate calibration. Part II: The influence of pre-processing methods. *TRAC Trends in Analytical Chemistry* **2005,** *24* (5), 437–445.

63. Jones, C. M.; Pelletier, M. T.; Atkinson, R.; Shen, J.; Moore, J.; Anders, J.; Perkins, D. L.; Myrick, M. L. A Small-Volume PVTX System for Broadband Spectroscopic Calibration of Downhole Optical Sensors. *Review of Scientific Instruments* **2017,** *88* (7).

64. Valderrama, P.; Braga, J. W. B.; Poppi, R. J. Variable Selection, Outlier Detection, and Figures of Merit Estimation in a Partial Least-Squares Regression Multivariate Calibration Model. A Case Study for the Determination of Quality Parameters in the Alcohol Industry by Near-Infrared Spectroscopy. *Journal of Agricultural Food Chemistry* **2007,** *55* (21), 8331–8338.

65. Born, M.; Wolf, E. *Principles of optics: electromagnetic theory of propagation, interference and diffraction of light (7th ed.);* Cambridge University Press: Cambridge, UK, 1999.

66. Nayak, A. B.; Price, J. M.; Dai, B.; Perkins, D.; Chen, D.; Jones, C. M. Characterization of Ion-Assisted Induced Absorption in A-Si Thin-Films Used for Multivariate Optical Computing. *Next-Generation Spectroscopic Technologies VIII*, Baltimore, Maryland, 2015; p 94820A.

67. Haibach, F.; Greer, A.; Schiza, M.; R., P.; Soyemi, O.; Myrick, M. On-Line reoptimization of filter designs for multivariate optical elements. *Applied Optics* **2003,** *42* (10), 1833-1838.

68. Eriksen, K. O.; Jones, C.; Freese, R.; van Zuilekom, A.; Gao, L.; Perkins, D.; Chen, D.; Gascooke, D.; Engelman, B. Field Tests of a New Optical Sensor Based on Integrated Computational Elements for Downhole Fluid Analysis. *SPE Annual Technical Conference and Exhibition*, New Orleans, Louisiana, 2013; pp SPE-166415-MS.

69. Jones, C. M.; van Zuilekom, T.; Iskander, F. How Accurate Is Enhanced Optical Fluid Analysis Compared to Lab PVT Measurements? *SPWLA 57th Annual Logging*

Symposium, Reykjavik, Iceland , 2016; pp SPWLA-2016-JJJ.

70. Hursan, G.; Ma, S. M.; Soleiman, W.; Eyuboglu, S.; Sethi, N.; Guergueb, N. New Wireline, In-situ, Downhole Fluid Compositional Analyses to Enhance Reservoir Characterization and Management. *SPE Annual Technical Conference and Exhibition*, Dubai, UAE, 2016; pp SPE-181526-MS.

CHAPTER 4

MEASUREMENT OF CARBON DIOXIDE AND METHANE IN PETROLEUM RESERVOIRS WITH DUAL-CORE MULTIVARIATE OPTICAL COMPUTING

4.1 INTRODUCTION

Accurate compositional measurements of reservoir petroleum fluid are necessary for various exploration and production activities, such as ensuring a well is safely drilled, identifying new discoveries, evaluating the production potential and value of such discoveries, optimizing the capital investment for production, and designing a field management system across multiple wells.(1-3) To determine the petroleum fluid composition in a newly drilled well, samples are typically acquired from within that well at high temperature and pressure using a wireline formation tester (WFT).(1-13) The WFT is lowered into the well using an electrical wireline cable and physically extracts fluid, by means of a mechanical pump, from the rock formation to capture that fluid in pressurized sample chambers. The pumping action reduces near-wellbore drilling fluid filtrate contamination, which invades the rock as a result of the drilling process. Sufficient pumping time is necessary to acquire a sufficiently clean formation fluid sample with little miscible filtrate contamination. It is important to ensure that those samples are of low contamination and represent the formation fluid from which they were collected; otherwise, a laboratory analysis will not provide the information necessary to

address the exploration and production activities. The dissolved methane gas concentration in the petroleum fluid is used to address these concerns.(1,3,14-15) Chemical fluid composition has been measured in-situ using filter spectrometers or a combination of filter and grating spectrometers.(2,8,15-16) The state-of-the-art measurement is achieved with the filter and grating spectrometer combination, providing an accuracy of 0.0139 g/cc.(2,6)

In-situ detection of carbon dioxide in petroleum-bearing formations is highly desirable. The presence of carbon dioxide in a petroleum asset negatively affects the value of that asset.(17-18) Carbon dioxide lowers the BTU value of natural gas, and it needs to be scrubbed from a fluid stream before pipeline shipping to prevent lowering the value of the commingled production.(19-22) Petroleum production operational costs can be higher as a result of carbon-dioxide-related scale, which chokes the production and requires remediation.(23-25) Additionally, the presence of carbon dioxide can corrode production systems, surface facilities, and pipelines not designed to handle corrosive concentrations of carbon dioxide. In fact, the capital asset investment to construct corrosion-resistant wells, corrosion-resistant production equipment, and surface scrubbing facilities is significantly higher compared to production without carbon dioxide.(17) Corrosion alone costs the oil and gas industry USD 1.4 billion, with approximately 60% of failures directly related to carbon dioxide.(17) Furthermore, lost production related to corrosion failures costs the oil and gas industry further tens of billions of dollars in lost revenue.(18) Concentrations greater than 2 bar partial pressure are considered highly corrosive and from 0.2 to 2 bar moderately corrosive.(26) Assuming a typical gas reservoir pressure of 200 to 1000 bar and gas molecular weight of

19 to 22 g/mol (27-28) the concentration at which carbon dioxide is highly corrosive corresponds to between 0.41 to 2.4 wt%. A system can be moderately corrosive from 0.041 to 2.4 wt%. In the liquid petroleum phase with the presence of organic acids, 0.1 to 1 mM can have the same corrosive power as that of 0.2 bar and 2 bar, respectively.(29)

However, carbon dioxide can be valuable for enhanced oil recovery when used as a sweeping fluid to push oil out of a reservoir, as long as the carbon dioxide does not break through to production and reduce the concentration of oil produced.(30-32) In addition, during enhanced oil recovery in silicate rock formations, the reservoir geochemistry acts as a permanent sink for carbon dioxide sequestration as long as the carbon dioxide does not break through.(33,34) With environmental concerns regarding carbon dioxide, it is desirable to prevent release while, at the same time, carbon dioxide sequestration represents an opportunity for the petroleum industry to offset its impact, particularly as carbon credits become more popular.(35-38) However, for carbon credits to become effective for enhanced oil recovery sequestration, monitoring and verification are necessary.(39-40)

Measurement of carbon dioxide content allows for better operational and financial management of petroleum assets.(25) Measurement of carbon dioxide in-situ has been accomplished with a 20-channel filter near-infrared (NIR) spectrometer attached to a retrievable WFT with a limit of detection for oils of 7 wt% and an absolute accuracy of 4 to 10 wt%.(41) The authors attribute the low accuracy and high limit of detection to a lack of sensitivity in the NIR for carbon dioxide relative to the spectroscopically interfering hydrocarbons present in petroleum or low net analyte signal (NAS).

MOC has been shown to match the sensitivity and accuracy of a partial least squares (PLS) regression using a Fourier transform infrared spectrometer.(42) MOC performs an analogue dot product regression in the optical domain with the use of a MOE. 43 The NIR (1952 to 2080 nm) region is still less sensitive for analyte carbon dioxide than the mid infrared (MIR) (2686 to 2835 nm) region, with a peak band intensity ratio of (43) between the two regions.(44) Therefore, a new dual MOE MOC sensor has been developed to access the MIR for carbon dioxide detection. The accuracy of the carbon dioxide and methane measurements with an MOC sensor is 0.0011 g/cc (+/-0.16 wt%) and +/-0.0063 g/cc (+/-1.0 wt%), respectively, at high pressure (62.05 Mpa) and high temperature (65.5 °C).

4.2 THEORY

For fractional transmittance, *T*, attenuation of an optical signal increases with concentration, such that the signal is negatively correlated to concentration, as shown in Equation 4.1.(45) Specifically, an initial light intensity *I0* impinges a sample and is attenuated exponentially as it passes through a length, *l*, of the sample by a material- and wavelength-specific attenuation constant, ε. The attenuation is also exponentially related to the concentration of the attenuating substances, and therefore spectroscopy can be used to derive the concentration of a substance by measuring the resultant optical intensity, *I*, for a characterized system. Used here, (decadic) absorbance, *A*, is the negative log10 of fractional transmittance and is linearly related to the concentration of a chemical species, as shown in Equation 4.2.(46) Chemical interference is an additive signal not caused by the analyte but rather a species that responds to the measurement technique.(47-48) This is in contrast to matrix interference (47-48) also known as matrix effects, which have a

multiplicative nature and will not be discussed here. With a Beer's law relationship for optical signals, all chemical species, including the analyte and chemical interference species, provide a unidirectional correlated signal with concentration (i.e., negative for transmittance and positive for absorbance). Beer's law can be defined in matrix form as shown in Equation 4.3, where $\vec{A}_i$ is the column vector of absorption as a function of wavelength for species i, at a given concentration and $\vec{\varepsilon}_i$ is the column vector multi-wavelength attenuation constant, known as the molecular fingerprint. Any spectrum of the set of spectra, *S*, is the sum of absorbance from all optically active species, *i*, and *X*, the response matrix, as a set of *S* as rows of *X*. The response matrix *X*, or spectral set *S*, can also be filled with pseudo linear transmittance data.(49-50) A calibration response matrix is obtained from samples of linearly independent concentrations of optically active species and a set of reference analyte properties, which are usually concentrations, the vector *y*. Using linear least squares, a regression vector *B* can be calculated by Equation 3.2 for a set of corresponding analyte reference values, the vector *y*, and then projected against a new spectral set to obtain a predicted analyte concentration estimate, the vector $\hat{y}$, using Equation 3.3.(48,51-52)

$$T = \frac{I}{I_0} 10^{\varepsilon l C} \qquad 4.1$$

$$A = -LOG_{10}(T) = \varepsilon l C \qquad 4.2$$

$$\vec{A}_i = (\vec{\varepsilon}_i l) C \qquad 4.3$$

$$B = (X^T X)^{-1} X^T y \qquad 4.4$$

$$B^T S = \hat{y} \qquad 4.5$$

For a large set of highly correlated channels, as is often the case with NIR data, the response matrix of Equation 3.2 can be poorly conditioned for inversion.(53) Rotation

of the correlated variables to a set of orthogonal latent variables by means such as principal component analysis (PCA) overcomes this difficulty.(51) A principal component (PC) scores matrix is constructed as a linear combination of the original response matrix by projecting the responses for each sample onto a new set of orthogonal axis dimensions (i.e., PCs). The PC axis is constructed such that each PC is orthogonal and captures the largest residual variation within the dataset not described by previous (lower-order) PCs.(54) The PC dimensions capture the internal correlation of the dataset, and the reduced dimensionality of new orthogonal variable scores is well-conditioned for inversion. A linear dot product regression vector in the original response variable space can be constructed from the PC scores coefficients and the PC eigenvectors as a principal component regression (PCR) to the analyte.(51) PLS is another eigenvector calibration technique of reduced dimensionality. PLS also designs a linear dot product regression vector, but each successive eigenvector is constrained to capture the maximum variation for the reference analyte concentration from the calibration matrix.(51) Although the PCR and PLS regression vectors are constructed from different rotations of the calibration matrix, the performance is often similar, even over a broad range of conditions, but PLS generally requires fewer eigenvector latent variable levels.(52) In fact, many algorithms, linear and nonlinear, can be used to construct a linear dot product regression vector of similar performance.(55)

MOC is a multivariate linear regression technique that performs an analog dot product calculation, in the optical domain, between a linear regression vector and the inherent optical intensity spectrum of light emanating from a sample. The regression vector shape is encoded as a transmission pattern for one or more optical elements. MOC

most typically uses an MOE, which is constructed as an interference filter. Laminated, thin film layers of two materials with different refractive indexes (R_i) are deposited onto a substrate. Here, R_i is used to denote the complex refractive index (index of refraction) as opposed to the real part n vs. the imaginary part ik for $R_i = n + ik$. The goal of calibration is to encode a regression vector as a transmission profile using a thin film stack design. A specifically designed thin layer stack can sufficiently match a regression vector shape. The MOE regression vector can either be predetermined—for instance, by PCR or PLS—or directly designed to a calibration set.(56) As spectral light passes through the MOE, the Hadamard vector product, an element-by-element multiplication, of the sample intensity spectrum with the MOE naturally occurs. The Hadamard vector product is followed by a summation of all light wavelengths by a detector, thereby completing the dot product. Therefore, the resultant detector signal is proportional to the analyte concentration for which the regression vector was designed plus a sample-dependent offset.(57) The sample-dependent offset can be subtracted either by use of light reflected from the element, a reference spectral signal, or a secondary optical element.(43,58) MOEs operate on the intensity spectrum emanating from a sample, as described in Equation 4.1, not the linear absorbance form of the Beer-Lambert law from Equation 4.2. Therefore, the MOE does not strictly operate on signals linear with the analyte concentration. However, it has been shown that higher-order linear models can model some nonlinearity.(49-50,58-60) As such, MOEs operating on single-beam intensity transmittance can still provide a reasonable measurement, as long as they can reproduce a higher-order regression vector.

A regression vector that corrects interference contains both positive and negative coefficients. For transmittance data, the negative coefficients sum the analyte signal, whereas the positive coefficients subtract the interference. Because light passing through the MOE can only supply a positive signal to the detector, giving rise to the sample-dependent offset, correction of that sample-dependent offset requires a second signal attained simultaneous to the MOE signal multiplexed in time or a combination therein. The second signal is subtracted from the first signal, either as complimentary positive and negative lobes to the regression vector, (58) as a beam splitter reflection of the MOE, (43,57,61) or as a bandpass reference to which the MOE is designed (62). The positive and negative lobe configuration places an awkward constraint on the design, such that the complimentary lobe MOEs need to have zero transmission where the other has a signal. In practice, it is difficult to encode all but the simplest complimentary transmission functions. The beams splitter configuration overcomes this difficulty because the light reflected from the MOE vs. light transmitted through the MOE naturally fix the regression vector lobes. Further, this method has the potential to have the greatest sensitivity because both the transmitted and reflected light have the potential to strike a detector. Unfortunately, this configuration has proved difficult to implement robustly, and instead the bandpass reference has been the basis for commercial applications.(63-68)

Traditionally, the design of an MOE is accomplished by a nonlinear optimization of a single randomly seeded thin layer film stack, such that the transmission spectrum matches a dot product regression vector.(56-57) The film stack layers are typically constrained to be alternating high- (e.g., silicon) and low- (silicon dioxide) index

materials on a BK7 substrate, respectively. This transmission spectrum is projected against an analyte property, such as concentration, to determine the predictive accuracy and sensitivity of the randomly chosen design. The merit-based regression analysis step follows by changing the layer thicknesses, and therefore the transmission spectra, until a local minimum can be achieved in the predictive performance. The traditional merit function for the search process for a single optimal filter is that of SEC^2 as the average of $\|y - \hat{y}\|^2$ for n samples, as shown in Equation 4.6.

$$SEC^2 = \frac{\|y - \hat{y}\|^2}{n} \quad 4.6$$

$$X_{1MOE} = [X \cdot T, X \cdot BP] \quad 4.7$$

$$[\alpha, \beta] = B_{MOE} \quad 4.8$$

For Equation 4.6, the vector of estimated concentrations, $\hat{y}$, is calculated from Equation 3.3 using X_{1MOE} as the spectral set, S. X_{1MOE} is a two-column matrix, where the first column is calculated as the dot product of the MOE transmission function, T, and the spectral calibration set X, and the second column is the sum of the spectral intensity over reference bandpass function BP. The MOE transmission function, T, is a column vector equal to the number of columns of X. The set of regression coefficients, B, is estimated from Equation 3.2 using the calibration matrix X_{1MOE}. The first and second coefficients of B for an MOE, B_{MOE}, of any two-channel design are herein referred to as α and β, as reflected by Equation 4.8. For a single MOE reference design, α coefficient represents the MOE magnitude and is inversely proportional to sensitivity. β represents the magnitude to which the reference bandpass is subtracted to mitigate the sample-dependent offset. The optimization finds a local optimum of T by iteratively changing the thickness of each layer of MOE thin-film structure, such that the squared error of

calibration $\|y - \hat{y}\|^2$ (SEC^2) (69) is minimized. As a result of the non-convex nature of this optimization problem, a global minimization solution might not be obtained with a single starting point. Because the solution is a local optimum, multiple initial seeds are used to increase the likelihood of determining a satisfactory utilitarian minimum or generate multiple near optimum solutions with different stack properties. The resulting designs are sorted by SEC and sensitivity and compared to the SEC and sensitivity of a reference calibration, such as PLS.(51)

The success of the single-core MOE with a reference bandpass depends on the complexity of the regression vector required for a given application. That is, the more complex the required regression vector shape, the more difficult it is to design and fabricate an MOE transmission pattern that matches a PLS regression vector performance Also, a more complex the transmission pattern shape requires more thin film layers, which decreases the composite transmission throughput. Because the sensitivity of an MOC sensor is related to the total optical throughput of the system, complex MOE shapes usually dictate a lower-sensitivity sensor. The theoretical limits for performance could be difficult to achieve because a single MOE core and neutral density linear combination does not yield the high-frequency structure representative of an optimized regression vector, such as a PLS regression vector. The carbon dioxide regression is sufficiently complex that a single MOE designed to a bandpass reference does not perform well. A new dual-core MOE configuration allows an MOC sensor for carbon dioxide to better approach PLS performance. Significantly more complex MOE regression vectors can be developed by utilizing two optical elements in two complimentary channels. Unlike the complimentary lobe technique, the dual core does

not constrain transmission to zero at any wavelength of either MOE, thereby removing the awkward constraint of the earlier method.

4.3 EXPERIMENTAL

4.3.1 MOE Design

A dead oil sample is a petroleum fluid which has lost components that are volatile at standard stock tank conditions (i.e., 14.7 psi and 68°F). The common volatile components that are lost include the hydrocarbon components of methane, ethane, propane, butanes, and pentanes, and the common volatile inorganic gases lost include carbon dioxide, nitrogen, hydrogen sulfide, argon, and helium.(27) A live oil is one that has been sampled from a petroleum reservoir and maintained in a compensated pressure chamber, above the bubble point, such that the gas remains dissolved as a single-phase fluid. Dead oil fluids can be reconstituted to live oil conditions, which is referred to as a reconstituted fluid. For this study, dead oil samples were used as a base fluid to be reconstituted using a small-volume pressure, volume, temperature, x-composition (PVTX) system outfitted with a Fourier transform infrared (FTIR) spectrometer, which has been previously described.(70) Two mutually exclusive datasets were used to design the methane dual-core MOE and carbon dioxide dual-core MOE. For this study, 721 spectra at a wavelength between 1300 to 2500 nm were used for the design of the methane MOEs, and 291 spectra at a wavelength between 2500 to 3300 nm were used for the design of the carbon dioxide MOEs. Outlier detection and resampling was used for this final selection of spectra in both calibration sets.(71) The base fluids used to construct the methane calibration set contained medium oils of <22.5 to 30 API weight; light oils of <30 to 40 API weight, which had a gas to oil ratio (GOR) less than 1700

scf/bbl; volatile oils of <30 to 45 API weight, which had a GOR between 1700 and 3500 scf/bbl; condensate fluids of 35 to 50 API weight, which had a GOR higher than 3500 scf/bbl; and gas samples containing no liquid oil portion. Heavy oils of API weight 22.5 and less were excluded from the calibration matrix. The reconstituted base oils used for the methane calibration set were designed to mimic the natural variation of reservoir petroleum as determined by a four-component factor analysis (54) of a large commercial petroleum composition dataset (GeoMark, Houston, Texas) containing more than 14,000 petroleum fluid analyses. A total of 161 base fluids was reconstituted with gas to form the calibration set for methane, along with six gas mixtures. For the methane calibration set, only the gas samples contained carbon dioxide. The carbon dioxide calibration set contained 31 medium oil samples as base fluids that were reconstituted to different live oil compositions. For the carbon dioxide calibration set, the methane and carbon dioxide reconstitution composition targeted the reservoir composition from which the base oils were sampled. Because there is little optical activity of methane, ethane, and propane relative to that of carbon dioxide in the 2500 to 3300 nm region, only methane was added as the dominate hydrocarbon gas component (27-28) to attain matrix conditions for the in-situ reservoir fluid. Table 4.1 shows the range of compositions for each of the calibration sets. The spectra for both sets were collected at 65.5, 93.3, and 121.1°C and at 20.684, 41.369, 62.053, and 82.727 MPa, which spans the pressure and temperature range for the intended MOC system use. The base fluid was then recombined with different concentrations of gas components, with subsequent spectral collection at the temperature-pressure combination points.

The dual-core MOE design process simultaneously optimizes the two MOE transmission patterns to operate as a single regression vector. This is in contrast to the single-core design, for which a single MOE transmission pattern is optimized to a static bandpass function. Several improvements can be realized with respect to the existing single MOE design method. Allowing a regression vector to be distributed between two transmission patterns provides a significantly larger degree of freedom to identify acceptable regression vectors. Accordingly, the design complexity of each of the two MOEs can be reduced, and the MOEs can be more easily manufactured with less susceptibility for error and variability. Finally, superior accuracy in the predictive performance is realized because a regression vector can be achieved that has a much higher frequency structure and greater complexity compared to a single MOE transmission profile, which is more Gaussian in nature.

Modifications to the design process are made for the dual-core MOE design to be used in petroleum wells. The dual-core MOE needs to be designed for use in broad temperature ranges. The transmission profiles T_a and T_b of the MOE pair are calculated as a function of temperature, *t*. To do so, the complex index of refraction constants are characterized as a function of temperature. At each temperature of each iteration step of the optimization routine, an in-house routine solves Abele's matrix formalism (72) for the propagation of electromagnetic waves through an alternating layer dielectric medium. (56) The formalism is used to calculate the total transmission and reflection profile for the evolving stack design as a function wavelength, angle, and ensemble of all layer complex indexes of refraction and thicknesses for every temperature of the characterized index of refraction. The transmission profiles, T_a and T_b, are temperature matched to the

same temperature for which the spectra X_t have been collected in Equation 4.9. The X_{2MOE} matrix is used with Equation 3.2 to calculate the regression vector B, yielding the coefficients α and β. In practice, three temperatures were selected for design: 65.6, 93.3, and 121°C. Additionally, the elements of the reference concentration vector y_t need to be temperature matched to the predicted concentration vector $\hat{y}_t$, as absolute concentration is also a function of temperature. If the temperature-dependent transmission functions are used with Equation 4.6, the SEC will now reflect an MOE SEC over the temperature-evaluated range. Ultimately, by accounting for the temperature behavior in the MOE transmission profiles, spectral signatures, and reference concentration vector, the MOE will be designed optimally across the intended temperature range of use.

A second design consideration for the MOE is the MOC sensor detector sensitivity. The merit function of Equation 4.6 optimizes an MOE to SEC without an explicate regard to sensitivity. Therefore, the MOE will be optimized to the inherent signal-to-noise ratio (SNR) of the data from which the MOE is designed. This can result in accurate regression vectors that fail in the presence of actual instrument drift and noise. Although detector noise is only one component of a system's noise characteristics, the MOC sensor, which uses a thermopile detector, does not have the SNR of the laboratory FTIR liquid-nitrogen-cooled mercury cadmium telluride (MCT) detector. The digital reference spectra X_t used in the optimization have a larger SNR than is inherent to the MOC sensor. The magnitude to which analyte prediction is degraded by noise-related error is inversely proportional to the sensitivity of the regression vector. The MOC sensitivity is also related to the quantity of light that reaches the detector. This quantity of light is influenced in part by the MOE design. To design an MOE regression vector for an

actual MOC sensor, a merit function needs to contain a penalty related to the evolution low-sensitive designs as well as the accuracy of the regression vector. Equation 4.10 calculates the error of an individual spectrum prediction $\hat{y}_i$ as the deviation from the reference value y_i. Equation 4.11 calculates a detector intensity of a spectral signal Xi through a transmission function equal to either $T_a(t)$ or $T_b(t)$. Because there is also an error associated with each detector signal, Equation 4.12 calculates this error for each spectral signal as the sum of squares of the error for Detector A, D_A, and Detector B, D_B. Equation 4.12 amplifies this noise by the inverse of each of the dual-core MOE's contribution to sensitivity, α and β, using the MOC characterized SNR. The final mean squared error is calculated as the sum of the squares for the noise and accuracy contributions of every design with Equation 4.13. Essentially, the mean square error (MSE) objective function is derived to optimize a pair of MOE cores such that the error associated with accuracy and sensitivity are both minimized. *MSE* scales linearly with SEC accuracy, and typically the minima for *MSE* will also be the most accurate design as well. The nonlinear optimization routine (56) needs no functional modification, as the layers of each dual-core MOE in the pair are modified as a composite in one iteration step but applied separately to the individual cores. For Equation 4.13, the number of calibration samples, n, is equal to 291 for the case of carbon dioxide and 791 for methane. The SNR is empirically determined as the lower 95% confidence limit, a value of 500 for the NIR and 200 for the MIR, as measured form 85 MOC sensors. The SNR is used to constrain the design solutions to meet acceptable real-world sensor sensitivity criteria. The binary scheme of weighting devised for Equations, 4.10, 4.12 and 4.13 could be more generally replaced with a sum of squares response for SEC accuracy and noise.

However, because crude oils are of significant optical density variation, this scheme was derived to provide weight to the source of errors as a winner-takes-all approach for a particular oil type. Designing an MOE with the consideration of noise allows easy identification of the most optimal design and potentially helps evolve designs that otherwise would not if noise was not considered during the evolutionary design process.

$$X_{2MOE} = [X_t \cdot T_a(t), X_t \cdot T_a(t)] \quad 4.9$$

$$\sigma_{iA} = |y_i - \hat{y}_i| \quad 4.10$$

$$D_i = X_i \cdot T \quad 4.11$$

$$\sigma_{iN} = \frac{1}{SNR}\sqrt{\alpha^2 * D_{iA}^2 + \beta^2 * D_{iB}^2} \quad 4.12$$

$$MSE = \sqrt{\frac{1}{n}\sum_{i=1}^{i=n}({\sigma_{iA}}^2 + {\sigma_{iN}}^2)} \quad 4.13$$

The third consideration in the design of an MOE is the ability to fabricate that MOE. The uniformity of the ion-assisted electron beam (e-beam) deposition system used to fabricate the MOE pairs has been determined as +/-1 nm thickness to one standard deviation. This corresponds to a standard deviation of approximately a +/-7 nm wavelength for features in a typical transmission function, although exact thickness effects are dependent on wavelength and transmission design. With a single core, it is customary to screen a batch of designs for fabrication effects; however, because two cores are expected to work in tandem, it was decided to include the uniformity tolerance as part of the design process. As the nonlinear optimization evolution process proceeds, designs are perturbed by +/- 1 nm thickness using a normal random distribution. In this manner, the design process only produces designs that are inherently able to be fabricated. The final design is returned and evaluated without perturbation.

Sensitivity is a crucial factor determining the robustness of a regression vector for a given instrument. The sensitivity of a generic multivariate regression vector to a calibration set can be assessed using NAS theory across multiple instruments and multiple wavelength ranges. (55,73-75) The sensitivity of a single MOE regression vector can be compared to a dual core or to that of a PLS regression vector shape. Therefore, a calibration of carbon dioxide in the NIR can be directly compared to a calibration of carbon dioxide in the MIR. NAS as proposed by Faber, (74) in the form of Bro, (75) will be used. Although the form of NAS calculation is the same, Faber argues that the analyte concentration to be used is the reference concentration as the best estimate of the true analyte concentration so that the best estimate of a true NAS can be calculated. Bro argues that the concentration that should be used is the model-predicted concentration, so that the figures of merit can be better calculated to specifically compare various models. This work follows Bro's recommendation. Specifically, this method allows estimation of a NAS directly from a regression vector *B*, as given in Equation 4.14, where $x^*_{k,i}$ is the net analyte vector for the kth analyte in the ith sample for the analyte concentration $\hat{y}_i$. The literature refers to the NAS as both the vector and the vector norm; however, here NAS will refer directly to the vector and NNAS to the norm of the vector. For calculation of the NAS sensitivity, the MOE single- and dual-core regression vectors can be calculated as B_{2MOE} and B_{2MOE}, respectively, using Equations 4.15 and 4.16.

$$x^*_{k,i} = B(B^TB)^{-1}\hat{y}_i \quad 4.14$$

$$B_{1MOE} = \alpha T + \beta BP \quad 4.15$$

$$B_{2MOE} = \alpha T_a(t) + \beta T_b(t) \quad 4.16$$

The NAS vector represents the signal space from the analyte in each sample that is orthogonal to interference.(73-74) Because various regression vectors can span a different cross-section of a fundamental NAS vector space, this method of calculation is specific to a regression vector. The norm of the NAS vector is the magnitude of a signal from which a univariate model can be used to construct model figures of merit that fully represent the multivariate model. NAS allows multiple MOE designs to be compared to one another and directly to a PLS or other dot product regression vector over multiple wavelengths, as long as the wavelength resolution and magnitude are appropriately scaled.

Carbon dioxide has predominant spectral features in both the NIR (1300 to 2500 nm) region as well as the MIR region (2500 to 3300 nm). The FTIR transmittance PLS regression for both the separate regions provides a similar prediction of 4.5% over the full range from 0 to 0.1060 g/cc, which is 0.6 wt% for an 0.8 g/cc oil. The MIR PLS calibration and regression vector are shown in

Figure 4.1. However, the NIR region regression vector is more complex and requires latent variables (seven) compared to the MIR regression vector, which requires four latent variables. This can be expected as a result of the larger amount of hydrocarbon interference in the NIR.(41) Because the regression vector in the NIR must be orthogonal to more interference, the effective signal is reduced. NAS was performed on both regions independently, and the results are illustrated in

Figure 4.2. The norm of the NNAS for each is plotted vs. the carbon dioxide concentration, with the slope being indicative of the overall sensitivity. From the Figure 1, the MIR region offers a 27× stronger signal response compared to the NIR region

despite the overall light throughput being weaker in the MIR region resulting from the black body lamp emission profile.

Using leave-one-out cross-validation, the PLS analysis identifies a root mean square error of cross-validation (RMSECV) of 0.0048 g/cc (or 4.5% of the range) using a four-level model. The good cross-validation result suggests the dataset is of sufficient rank for modeling. This helps establish a performance limit for the dual-core design process and will help evaluate the design results with reference to a global optima. Using the same dataset for a PLS and MOE deign, it would be difficult to obtain an MOE SEC larger than the PLS RMSECV, and if any designs are obtained with a numeric SEC larger than the PLS RMSECV, they might be suspect of overfitting the data. Therefore, certain designs, those with significantly greater SEC than the PLS SEC limit, are discarded as potentially overfit. Along with the performance limits, the PLS analysis also provides the four-level-based regression vector. The PLS regression vector can also be used to identify the spectral regions most important for the analyte of interest.

To design a set of MOE channels for an MOC sensor, the spectra are transformed to the single-beam spectra that the detector of the MOC sensor would observe. To accomplish this, the spectra are normalized to fractional transmittance and then convolved with the radiometric contributions of optical components along the optical path of the sensor, including the lamp, bandpass, windows, and detector. The spectra used for carbon dioxide calibration are shown in Figure 4.3. The activity from 2650 to 2900 nm is caused by the carbon dioxide combination ($\nu_1+\nu_3$) band.(44) Because there is significant baseline activity in the region resulting from the unassigned background of the

oil matrix, a wider region from 2500 to 3300 nm is selected for MOE design for multivariate background interference correction.

To ensure a design sufficiently close to a global optimum for carbon dioxide in the prediction error is identified, 500 initial MOE seed designs are generated with a random number of layers and random thicknesses. The total thickness is constrained to 6 micrometers and the number of layers for each of the MOE pairs to 16. The design is similar in fashion to the single-core design described previously.(56) However, because two transmission functions are generated simultaneously, both sets of layers are adjusted in response to the regression vector dot products (Equation 4.13) using the nonlinear optimization routine. That is, at each optimization iteration, the MOE transmission is projected vs. the spectral dataset as a dot product. This dot product between each MOE transmission profile and the convolved spectral dataset represents a virtual MOC sensor response. Next, a multiple linear regression (MLR) model is established consisting of the two virtual detector responses and the measured concentration values of the analyte of interest.(51) The result of this MLR model yields the two regression coefficients, α and β, which can be applied to each MOE transmission profile to define the optical regression vector. The optimization routine then continues this process by iteratively changing the layer thicknesses of each MOE to derive the next iteration of the MOE transmissions. The optimization routine is terminated when the resulting optimized optical regression vector produces a minimum in the mean square quantity (MSE) objective function defined by Equations 4.13.

Figure 4.4 compares a design optimization of carbon dioxide single- and dual-core MOE designs with an initial 500 randomly seeded designs. The initial 500 random-

seed designs all had an SEC greater than 18%. Note the performance improvements of a dual-core design compared to the single-core design solutions. This example is one way to illustrate the performance improvements offered by a dual-core design approach compared to a single-core solution. The best performing single MOE design has an SEC of approximately 8% with an MSE of 0.008 g/cc, whereas the dual-core design has an SEC equal to 5.4% and an MSE of 0.0064 g/cc. The results of the optimization plotted in

Figure 4.4 are also used to select the best candidate design. Another way to illustrate the performance improvements that a dual-core design offers is to evaluate the results with respect to NAS.

Figure 4.4b plots the same optimized design solutions vs. the NNAS. As a reference point, the PLS limits for both SEC and NNAS are provided by the green dashed line. The results shown in

Figure 4.4b suggest that the dual-core design solutions offer a significantly larger NAS compared to those of the single-core design solutions for SECs greater than 15%. To calculate the PLS NNAS, the regression vector was scaled from the maximum to minimum value of 2 as if it had been encoded as a dual-core MOE into a virtual MOC.

Figure 4.5a plots both MOE transmission profiles for the best performing dual-core design selected as the lowest MSE. The width and frequency of these transmission peaks and valleys are dictated by the thin film structure and have a limit to the fidelity of their features. These features change for different thin film structures of the MOEs, but they are typically larger than the spectral fidelity usually observed for a PLS regression vector in this spectral region. With the dual-core pair of MOE cores, an optical regression

vector can be computed using the weighted regression coefficients from the MLR model at a higher fidelity than that of the typical single-core MOE. Figure 4.5b shows the optical regression vector achieved by applying a first coefficient (α = -2.84) to MOE-A and a second coefficient (β = 5.96) to MOE-B. This dual-core MOE design optical regression vector is also compared to the best performing single-core design solution.

Figure 4.6 plots the close agreement between the predicted results achieved with the optimized dual-core design with that of the PLS analysis. The SEC for the dual-core regression vector is similar to that of the PLS regression vector, with a relative accuracy of 5.4% compared to 4.5%, respectively. In addition, the structure of the analyte residuals appears similar, with groups of sample concentration projected by both PLS and MOC in a similar fashion.

A review of the double methane core MOE results provides some insight into the additional complexity achievable with a double core vs. single core. The 721 spectra used as the methane calibration set were normalized to a virtual MOC sensor and then used to optimize both single- and dual-core MOE designs. A total of 2,500 initial random-seed designs were optimized for each dual-core MOE design and a single MOE design. A five-level PLS regression vector for methane, as assessed by a leave-one-out RMSECV, achieved 5.3% accuracy. A seven-level PLS regression vector for methane, as assessed by a leave-one-out RMSECV, achieved 4.3% accuracy. Figure 4.7 shows that some single cores do achieve the five-level PLS accuracy for both SEC and NNAS sensitivity (not shown); however, none reach the performance in either SEC accuracy or sensitivity of a seven-level model. Further, there is greater difficulty for the optimization routine to converge to a consistent minimum for a single core. With the dual-core MOE solution,

not only do cores achieve the PLS accuracy and sensitivity but most converge to that limit, suggesting that the dual core offers a significant additional degree of freedom.

Figure 4.8b shows the individual MOE-A and MOE-B transmission functions. The linear combination using an α and β as 6.51 and -4.53, respectively, is shown in Figure 4.8b superimposed on the PLS regression vector. Although every inflection is not mimicked, the individual MOE transmission functions of Figure 4.8a combined broadly resemble the features of the PLS regression vector. Figure 4.8a is representative of the Gaussian-esque regression vector shapes that can be achieved with a single MOE core solution. The linear combination of two cores, however, allows nuanced inflections, which can be crucial to a regression but are not possible with a single core.

4.3.2 MOE Fabrication

The selected MOE is fabricated using a custom ion-assisted e-beam vacuum deposition process described previously.(76) The ion-assisted e-beam vacuum deposition system was built by Denton Vacuum LLC (Moorestown, New Jersey). This tool uses electromagnetically focused high-energy electrons to evaporate a target's atomic species. The ion-assisted beams then help focus and densify the vapor atomic species onto the MOE substrates, which are borosilicate glass in the current study. Four substrate holders, 13 inches in diameter, are mounted in the chamber in a planetary configuration that rotates about the chamber azimuthal axis, which is 16 inches in diameter, as well as the substrate holder axis. This dual-rotation planetary configuration allows for highly reproducible, uniform film deposition for all MOE products. Each substrate holder accommodates 66 MOE substrates of 25.4 or 6 mm and a 3 inch glass witness sample for optical monitoring.

To monitor the deposition process in-situ, the chamber is also equipped with a suite of analytical tools. Rate control and physical thickness monitoring is supplied by an INFICON (Bad Ragaz, Switzerland) IC6 crystal sensor deposition controller slaved to the main control system for recipe downloads and active feedback. Each e-beam gun has its own crystal sensor head unit. A Newport (Irvine, California) single-wavelength optical monitor system is also employed for deposition rate control. Both of these in-situ tools are coupled with the e-beam gun to provide real-time feedback for endpoint detection. A visible (VIS)-NIR spectroscopic ellipsometer (J.A. Woollam, Lincoln, Nebraska) is mounted to the chamber windows with a fixed 70° angle of incidence and can be used to measure the film thicknesses and optical constants after the thin films are deposited. NIR and MIR transmission spectrometers (Newport, Irvine, California) are mounted to the chamber at normal incidence and can also be relied upon for measuring the transmission response of the fabricated MOE, as well as the individual film layer thicknesses.

The temperature of the deposition system can be changed from ambient to greater than 230°C. Typical silicon (Si)/silicon dioxide (SiO_2) fabrication occurs at 200°C, with optical monitoring at various temperature increments, usually of 27.8°C, from ambient to 176.7°C. This allows temperature-dependent characterization of both the transmission profile of MOEs under fabrication and the optical constants to be determined at increments throughout the deposition process. Characterization and re-optimization of remaining layers is crucial for MOE performance of the target shape.(3,43, 77) Because of the temperature dependency of the index of refraction and material thermal expansion, the transmission profile of the optical element changes with temperature. It is therefore important to re-optimize the remaining layers based on measurements and

characterization across the intended temperature range for MOC sensor use. As many as five materials can be located in one of five protected pockets within the deposition system, such that only a single material is exposed during e-beam vaporization. For the current study, Si and SiO_2 are loaded as the deposition materials, although aluminum dioxide and titanium dioxide were present.

The carbon dioxide and methane dual-core MOEs are fabricated according to the designs provided in Table 4.2. The Si and SiO_2 layers are deposited by means of ion-assisted e-beam evaporation at a pressure of 1E-4 Torr and temperature of 200°C onto a BK7 (Schott AG, Mainz, Germany) 6 mm substrate. A total of 30 substrates is loaded for each of the methane MOE-A and MOE-B cores. A total of 30 substrates is loaded for each of the carbon dioxide MOE-A and MOE-B cores. Optimization of the ion-assisted process variables allows for densely packed films that are invariant to moisture absorption and temperature-induced changes in the optical properties. This is evident after the deposition of each individual layer, where the process is paused so that in-situ transmission spectra and spectroscopic ellipsometry data can be acquired. Data analysis of the multiple spectra sets allows precise characterization of the materials' optical constants and deposited thickness. These data are then implemented back into the film stack design and held constant while the remaining layers are subsequently optimized to provide an in-situ re-optimization process that precisely accounts for any deviations in the fabrication process from the intended design.(77) As verification of the deposition process, the dual-core MOEs are each measured with the NIR and MIR spectrometer. A matching routine for MOE-A and MOE-B cores is created based on the measured transmission functions so that the best combination of pairing is achieved. Every

combination of possible core matches is projected vs. the design database to calculate the standard error estimate. This provides a possible 900 combinations for methane and a possible 121 combinations for carbon dioxide. The lowest SEC match is selected as the first pair, with the next lowest selected from the remaining pool until all matches have been made. The methane cores all verified between 4.90 and 5.07% relative standard error estimates, with an average of 4.98% +/- 0.048% to one standard deviation. The carbon dioxide cores all verified between 5.27 and 5.85% relative standard error estimates, with an average of 5.51% +/- 0.18% to one standard deviation.

4.3.3 Validation

For validation, the dual-core carbon dioxide and methane MOEs are placed into a MOC systems. The MOC sensor for which the MOE is designed has been described previously.(63-64,67,78-80) Briefly, a 5 watt tungsten halogen powered at 1.8 watts is focused by a gold-coated back parabolic reflector through a 1 mm sample gap. The high-pressure windows are 9.5 mm diameter sapphire with a 6 mm clear aperture and length of 12.7 mm. A 6 RPM rotating carousel carries an inner and outer circumference of 20 paired positions for MOE-A and corresponding MOE-B. The light emanating from the high-pressure sapphire sample cell is split and passed through the MOE and bandpass reference along separate paths and subsequently focused onto a pair of balanced dual-channel thermopile detectors by means of gold-coated off-axis parabolic mirrors. The total distance from filament to detector is less than 33 mm.

For laboratory validation, a set of MOC sensors containing the MOEs is placed into an oven and attached to a hydraulic pump to provide conditions similar to that of a fluid in a subterranean petroleum well at 65.5°C and 62.05 MPa. The validation setup is

similar to that described previously.(70) However, in the current validation, the optical cell and spectrometer described in (70) are removed from the system, with the MOC sensor instead plumbed into the validation system. A custom in-house built driver board supplies power to the light source, detector amplifier, and motor, and a custom data acquisition board acquires analog signals from the sensor to be stored in a computer. Four validation fluids were selected with the composition shown in Table 4.3. The compositions were selected to represent the distinctly different fluid types of a volatile oil, light oil, medium oil, and heavy oil to help ensure the MOC sensor would operate for a diverse range of oil types. Although a heavy oil was not included in the calibration matrix, the heavy oil chosen is on the borderline with medium oils, with the distinction between the two groups as 22.5 API weight base oil. The volatile oil, medium oil, and heavy oil were reconstituted live fluids, whereas the light oil was obtained as a live fluid from a petroleum reservoir.

The validation fluids are measured with the MOC sensor in the oven, which is operated at 65.5°C and 62.05 MPa to mimic the operational conditions of a petroleum reservoir. Measurements are calculated as a 15 minute average for a total of 90 measurements. Each measurement represents a 50 ms snapshot as the MOE pair rotates into position in full continuous view of the detector. Figure 4.9 shows the results for carbon dioxide. The predicted concentration was calculated from the theoretical α and β designed values derived from the virtual MOC sensor. The linearity of the reference concentration with the measured concentration is surprisingly high, with a squared correlation coefficient of 0.997, especially across the large diversity of validation fluids. The MOC sensor shows a small offset of -0.0009 g/cc but a rather large slope of 1.8293

and a standard error estimate of 0.0011 g/cc. The relative standard error estimate is 1.1% of the design range for carbon dioxide, or +/- 0.16 wt%. Methane is validated with a squared correlation coefficient of 0.988, slope of 1.8161, and intercept of -0.364, with a standard error estimate of 0.0063 g/cc. The relative standard error estimate is 3.62% of the design range for methane or +/-1.0 wt%. The measured response, slope, and offset for methane and carbon dioxide are used to calibrate the MOC sensor.

The MOC sensor is placed in a WFT, which is used to acquire reservoir samples during the process of formation pumpout.(1-13) The WFT was lowered to a location within the petroleum well having a pressure of 67.07 Mpa and temperature of 89.9°C. The calibration conditions for the MOC sensor in the laboratory differed slightly at 24.4°C (6.7% absolute temperature deviation) and 5.02 Mpa (7.5% absolute pressure deviation) from the field conditions. In principal, the MOC sensor is designed to be temperature robust, but it was intended to provide close conditions for calibration. Fluid is withdrawn from the formation through a hydraulically sealed probe using a mechanical pump in an effort to clean the near-wellbore fluid of drilling fluid filtrate contamination, a byproduct of the drilling process. Throughout the pumpout, the contamination is reduced and the concentration of drilling fluid filtrate increases. After 228 minutes, a sample of the formation fluid is captured. Figure 4.10 shows the measured methane, carbon dioxide, and GOR throughout the pumpout as determined by the MOC sensor without averaging. The captured sample was sent to a laboratory for analysis by gas chromatography and reference bulk properties, also shown in Figure 4.10. The final MOC sensor readings are presented as an average for the last 50 sensor measurement points acquired over 500 seconds. Pseudo normalization (58) is used to compensate any

drifting of the MOC system. The in-situ measured methane concentration matched the laboratory value within 2%, and the measured carbon dioxide value matched the laboratory value within 20%. The GOR is a measure of the total hydrocarbon and carbon dioxide gas divided by the amount of oil. The MOC sensor also contains a previously described (63,67,78) single-core hydrocarbon GOR MOE, which, although not the subject of this study, is useful for reference in the discussion. From the laboratory analysis, the total gas of the GOR is composed of 56.23% methane, 23.3% carbon dioxide, with the balance being hydrocarbon components of ethane through pentane. The sampled fluid contains residual drilling fluid filtrate equal to 3.22 wt%, based on a gas chromatograph analysis, as compared to that of a pure filtrate sample, (11) which was collected at the well site. Additionally, the pH of the acquired filtrate sample is measured as 8.9.

4.4 RESULTS AND DISCUSSION

The dual-core MOE offers a better sensitivity and accuracy combination than the single-core MOE for both carbon dioxide and methane, as designed for an MOC sensor with noise considerations. It is interesting that although the designed SEC performance of the methane and carbon dioxide dual cores never exceeded the SEC for the PLS regression vector, the laboratory validated dual-core MOE performance for both analytes exceeded that of the PLS leave-one-out validation. In fact, the validated performance was also better than the designed MOE accuracy. It is possible that the validation set was not representative; however, the validation set was specifically designed to span the range of compositional and matrix variation, as determined by the commercial database. The four oils chosen for validation fell into the standard categorical formation oil definitions of a

heavy oil, medium oil, light oil, and volatile oil. Anecdotally, this has been the observation for many MOE validations. A second possible explanation could be that FTIR spectra obtained contain both linear and nonlinear artifacts. When designing an MOE, either single or as a dual pair, it is evaluated against the FTIR spectra. Therefore, the evaluated performance might not be better than the quality of the spectra from which it was designed. However, on average, the primary features of the analyte are present within the spectral data, and therefore the MOE evolves to capture the variation of these features. Further, the MOE regression vector, as evidenced by Figure 4.8b, is smoother than the PLS regression vector. It is possible that the PLS regression vector itself is not entirely orthogonal to the artifacts within the calibrations set and therefore has a higher leave-one-out RMSECV validation accuracy than if the data contained no spectral artifacts. Because the MOE is inherently smoother than the PLS regression vector, a natural constraint of the interference-based transmission pattern, it is more difficult for the MOE to capture some of the higher-frequency artifacts. Perhaps the MOE was designed with some FTIR spectral data artifacts, potentially giving rise to the negative intercept observed for both the carbon dioxide and methane regression. However, because the spectral light emanating from the sample that strikes the MOE does not contain the FTIR spectral artifacts, the effect could simply be corrected with the calibration of actual fluids. This is not to say that the MOC device does not contain its own artifacts; rather, overall, the impact of the artifacts in the MOC sensor is smaller than that of the FTIR. A future simulation experiment could explore this concept further.

The sensitivity (i.e., slope) of the MOC sensor for methane and carbon dioxide (1.82 and 1.83, respectively) was significantly higher for the actual MOC sensor than that

expected from the virtual MOC sensor. The similarity of the methane and carbon dioxide slopes suggests that the deviation is caused by the MOC sensor itself and not deviations in the fabricated MOE relative to the designed MOE. This is not entirely surprising because both the estimates of optical throughput and noise are conservatively estimated for the virtual MOC sensor. This ensures that the MOEs are designed for a suite of actual sensors having natural performance variations and are field deployed. The sensitivity is related to the total amount of light reaching the detector as well as the level of interference correction. The greater the interference correction (i.e., more light that is subtracted from the signal resulting from the interfering species), the lower the NAS. For carbon dioxide, neither the dual- or single-core MOE designs achieve the NNAS sensitivity and SEC accuracy combination compared to the PLS regression vector for a virtual MOC sensor. Effectively, no combination of dual cores or any single core allowed as much light to strike the detector as a hypothetical PLS MOE. Some of this is a result of the individual MOE transmission limits of each MOE core. From Figure 4.8a, it can be observed that the MOE-A transmission range is approximately 60%, with a 65% peak minus a 5% baseline; for the MOE-B, it is 80% with a 80% peak minus a 0% baseline. The total intensity range then of the selected design is only 70% that of a hypothetical PLS MOE. In the evolutionary MOE design process, there are additional constraints for the MOE fabrication that require an MOE to be temperature robust and able to be fabricated. Designs that are not stable or able to be fabricated are of little practical use. No such constraint is applied to the PLS regression vector. Ina addition, the MOE is designed with respect to noise that is not inherent to the FTIR data. Therefore, comparison of the MOE regression vector to a PLS regression vector is primarily only

instructive for design selection, not a full estimation of atonable limits. In fact, the methane MOE did nearly reach the PLS limit of accuracy and far surpassed the limit of NNAS sensitivity. This can be rationalized from Figure 4.8b. Note the strong negative feature at 1610 to 1685 nm corresponding to the methane CH first overtone stretch ($2\nu_3$) and the negative feature from 2150 to 2250 nm corresponding to the combination band.(81) Whereas the PLS regression vector more strongly weights the 1610 to 1685 nm region, the MOE more strongly weights the 2150 to 2250 nm region. Likely, the greater transition strength intensity of the combination band region provides significantly greater sensitivity with similar albeit slightly less accuracy to that of the overtone region. However, the MOE evolution, which is designed with MOC noise considerations, optimizes to weight the combination region. In addition, note that the digital weights of the PLS regression vector are sharp, whereas the analog weights of the interference-based transmission pattern are broad. If the sharp features of the PLS regression vector are scaled to the maximum range for a dual MOE core arrangement of 2, less light than that of the broad arrangement actually strikes the MOC detector. Specifically, a PLS regression vector designed as a digital operation might not be the optimal transmission pattern to encode as an MOE for an MOC sensor.

Laboratory analysis of the final sampled fluid from the field test compares well to that of the real-time in-situ determination. Methane differed by 0.07% absolute (2% relative), and carbon dioxide differed by 1.8% absolute (20% relative). Both methane and carbon dioxide values, as determined by laboratory analysis, are within the range of each calibration. Real-time determination of methane and carbon dioxide is highly valuable. Carbon dioxide levels were determined to be significantly higher than that at which

carbon dioxide becomes a corrosion problem. For methane, the concentration determined is sufficient to provide sampling information. During the sampling pumpout process, drilling fluid filtrate, which is present in the near-wellbore region, is flushed through the WFT by mechanical pumping action and expelled into the wellbore. As the pumpout continues, the composition of the fluid in the WFT grades from drilling fluid filtrate to formation fluid. Drilling fluid filtrate contains no dissolved gas, whereas the formation fluid usually has some dissolved gas. In Figure 4.10, it can clearly be observed that the level of gas to oil increases throughout the pumpout asymptotically to a constant value of 1412 scf/bbl. Carbon dioxide accounts for 23.3% of the GOR, or 324 scf/bbl. Although the MOC measured value of carbon dioxide is low at 20% or 65 scf/bbl, this is only 4.6% of the total GOR and less than the measurement accuracy of GOR. Nearly 80% of the carbon dioxide increase occurs after 91 minutes of pumpout, a curious observation indeed. The GOR after 91 minutes increases from 1125 to 1412 scf/bbl, which is accounted for by the increase in carbon dioxide.

Drilling fluid filtrate is caustic, containing multiple oil- or water-soluble basic compounds designed to scavenge acidic compounds, such as hydrogen sulfide or carbon dioxide. Drilling fluid can contain water-soluble and/or oil-soluble acid scavenging compounds to help reduce corrosion and bind with acid species to protect against hydrogen sulfide. These reactions can be reversible with a reduction in pressure to recover carbon dioxide or hydrogen sulfide.(82-83) It might be the case that, before 91 minutes, the concentration of the drilling fluid filtrate was sufficient that carbon dioxide was largely bound in a complex. For caustic chemicals used to scavenge acidic species in drilling fluid filtrate, such as amines, the optical spectroscopy of bound carbon dioxide is

likely different from that of unbound carbon dioxide.(84-85) A spectroscopic signature for bound carbon dioxide therefore would likely not have registered as free carbon dioxide for an MOC sensor. The WFT contained a density sensor, (86-88) which recorded a 100% filtrate fluid as having a density of 0.8150 g/cc and a 3.22% filtrate fluid as 0.7016 g/cc. Using a linear mixing model for drilling fluid filtrate contamination in a formation fluid, (89-90) the contamination at 91 minutes, just before the carbon dioxide level increase, can be calculated as 14.28% by using the measured density of 0.71452 g/cc. If one assumes a filtrate component binding of carbon dioxide as a limiting reagent, then 14.28% binds with 100% of the carbon dioxide, and 3.22%, the measured contamination in the sample, would bind with 22.6% of the carbon dioxide, thereby accounting for the difference between the carbon dioxide measured by the MOC sensor vs. the laboratory. If corrected for this potential drilling fluid filtrate effect, the concentration of carbon dioxide in the reservoir fluid by measure of the MOC sensor would be estimated as 9.35 wt% compared to the laboratory measure of 9.04 wt%, a difference of only 0.31 wt%.

4.5 CONCLUSION

The MOC sensor and MOE regression vector provide many advantages compared to conventional spectroscopic equipment using typical PLS regression vectors. The MOC system is compact and robust for real-world applications. The MOC system can, in some circumstances, be at least as accurate, if not more so, than the conventional laboratory system. In fact, for this study, the MOC based on a dual-core MOE has been validated to better accuracy than that of an FTIR using a conventional PLS regression. However, this performance equivalence is likely dictated by the complexity of the regression vector

necessary and data preprocessing required. It is conceivable, and even probable, that various applications could require a more complicated MOE regression vector than that which is possible with a composite transmission function achievable by an interference pattern. Additionally, complex spectral preprocessing methods, such as but not limited to derivative spectroscopy, as is common with digital representations, have not been shown with MOC. With these limitations aside, in many cases, such as during well monitoring of carbon dioxide and methane, the performance equivalence of MOC with laboratory systems is more than sufficient, and the robustness of the MOC system enables applications not otherwise easily achievable.

The dual-core MOE has been shown to achieve more complicated regression p than pattern that of a single core. Consequently, the dual-core MOE configuration has been shown to allow both more accurate and/or more sensitive designs than that of a previous single-core MOE configuration. The MOC has also been field tested with results for methane that were well within the expected accuracy range, as was laboratory validated. However, the carbon dioxide field results differed substantially from those expected based on laboratory validation. The field results for carbon dioxide might, in fact, be correct, and it is possible that it is the first observation of a physical process not previously suspected that can occur during a formation sampling pumpout. Specifically, it is proposed that components associated with the mud filtrate can bind the carbon dioxide. The components would then release the carbon dioxide with a pressure reduction. The mechanism for such a phenomenon is currently the subject of a different laboratory study. The proposal of such a mechanism seems self-consistent with the observed behavior of the pumpout trend, and the observed behavior can be used to

correct the MOC measured carbon dioxide to a level far more consistent with the measured laboratory concentration of carbon dioxide. Nonetheless, the uncorrected MOC measured values of carbon dioxide and methane are highly useful for assessment of production issues associated with carbon dioxide or various exploration and production activities, including WFT sampling.

Table 4.1: The composition range of recombined components into petroleum fluid base oils. The GOR shows the relative concentration of recombined fluids to the petroleum base. The design sets for methane and carbon dioxide dual-MOE cores are mutually exclusive.

Property	Methane Range		Carbon Dioxide Range	
	Min	Max	Min	Max
Temp. (°C)	65.5	121.1	65.5	121.1
Pressure (MPa)	20.684	82.727	20.684	82.727
CO_2 (g/cc)	0	0.1211	0	0.1060
Methane (g/cc)	0.002	0.1729	0	0.1556
Ethane (g/cc)	0	0.0882	0	0
Propane (g/cc)	0	0.071	0	0
Saturates (g/cc)	0	0.654	0.2618	0.5963
Aromatics (g/cc)	0	0.3694	0.0833	0.2294
Resins (g/cc)	0	0.1149	0.0065	0.2919
Asphaltenes (g/cc)	0	0.125	0.003	0.0257
GOR (scf/bbl)	76	22851	0	2223

Table 4.2: Stack designs for MOE dual cores.

Layer	Methane MOE A (nm)	Methane MOE B (nm)	Carbon Dioxide MOE A	Carbon Dioxide MOE B	Material
1	803.7	56.9	1908.9	247.3	Si
2	491.8	274.2	1290.2	224.0	SiO_2
3	620.5	231.8	1918.8	214.6	Si
4	489.0	777.1	174.6	844.4	SiO_2
5	246.4	336.9	1461.0	552.7	Si
6	487.2	654.6	—	657.2	SiO_2
7	675.3	152.1	—	1562.1	Si
8	—	8.2	—	415.0	SiO_2
9	—	77.4	—	694.3	Si
10	—	167.6	—	—	SiO_2
11	—	640.0	—	—	Si
Total	3813.9	2483.6	6753.5	5411.6	—

Table 4.3: Composition of validation samples for carbon dioxide dual-core MOE.

Property	**Volatile Oil**	**Light Oil**	**Medium Oil**	**Heavy Oil**
GOR (scf/stb)	1734	1156	955	533
CO_2 (g/mL)	0.0059	0.00124	0.0102	0.0389
C1 (g/mL)	0.1009	0.06396	0.0381	0.0204
C2 (g/mL)	0.0033	0.03352	0.0212	0.0102
C3 (g/mL)	0.0154	0.01888	0.0225	0.0234
iC4 (g/mL)	0.0042	0.00712	0.0115	0.0024
nC4 (g/mL)	0.0142	0.01802	0.0268	0.0082
iC5 (g/mL)	0.0071	0.00989	0.0112	0.0027
nC5 (g/mL)	0.0067	0.01096	0.0138	0.0052
C6+ saturates fraction (g/mL)	0.3022	0.35036	0.1994	0.2995
C6+ aromatics fraction (g/mL)	0.1183	0.09270	0.2429	0.3736
C6+ resins fraction (g/mL)	0.0798	0.03767	0.0542	0.0566
C6+ asphaltenes fraction (g/mL)	0.0040	0.02748	0.0754	0.0001
Reservoir fluid density (g/mL)	0.6622	0.6718	0.7271	0.8411
Stock tank density (g/mL)	0.8651	0.8435	0.8765	0.9187
API	32.1	36.3	29.9	22.5

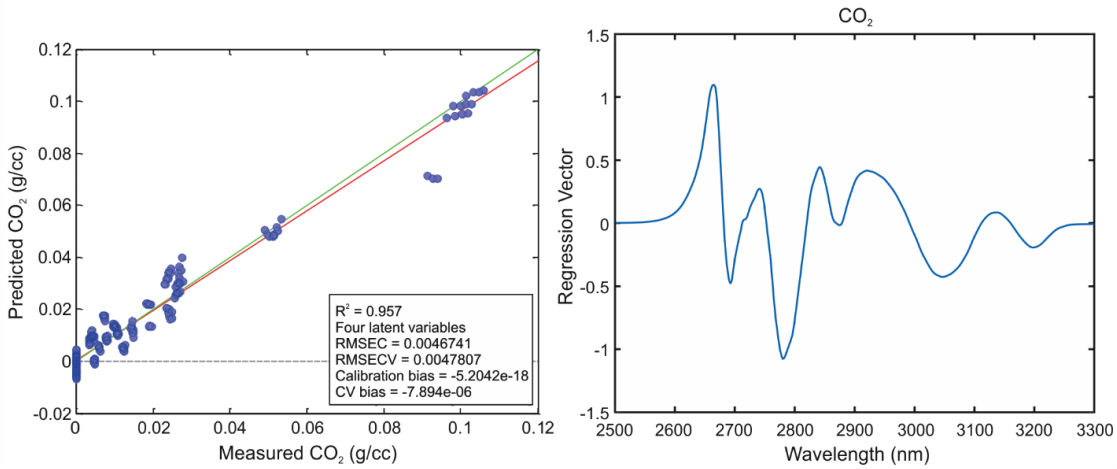

(a) **(b)**

Figure 4.1: PLS model prediction plot identifying a theoretical PLS calibration error of 0.00478 g/cc (a), and corresponding four-PC regression vector (b).

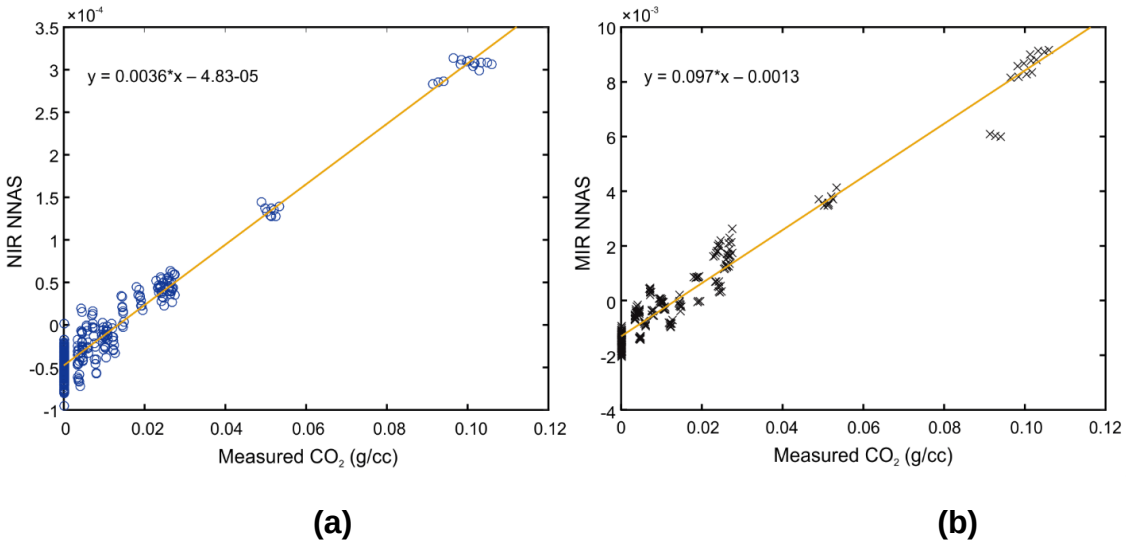

Figure 4.2: Figure, norm of NAS vs. measured carbon dioxide concentration for the NIR (a) and MIR (b) spectral regions. The range of the MIR NAS indicates ~27× stronger sensitivity compared to the NIR spectral region.

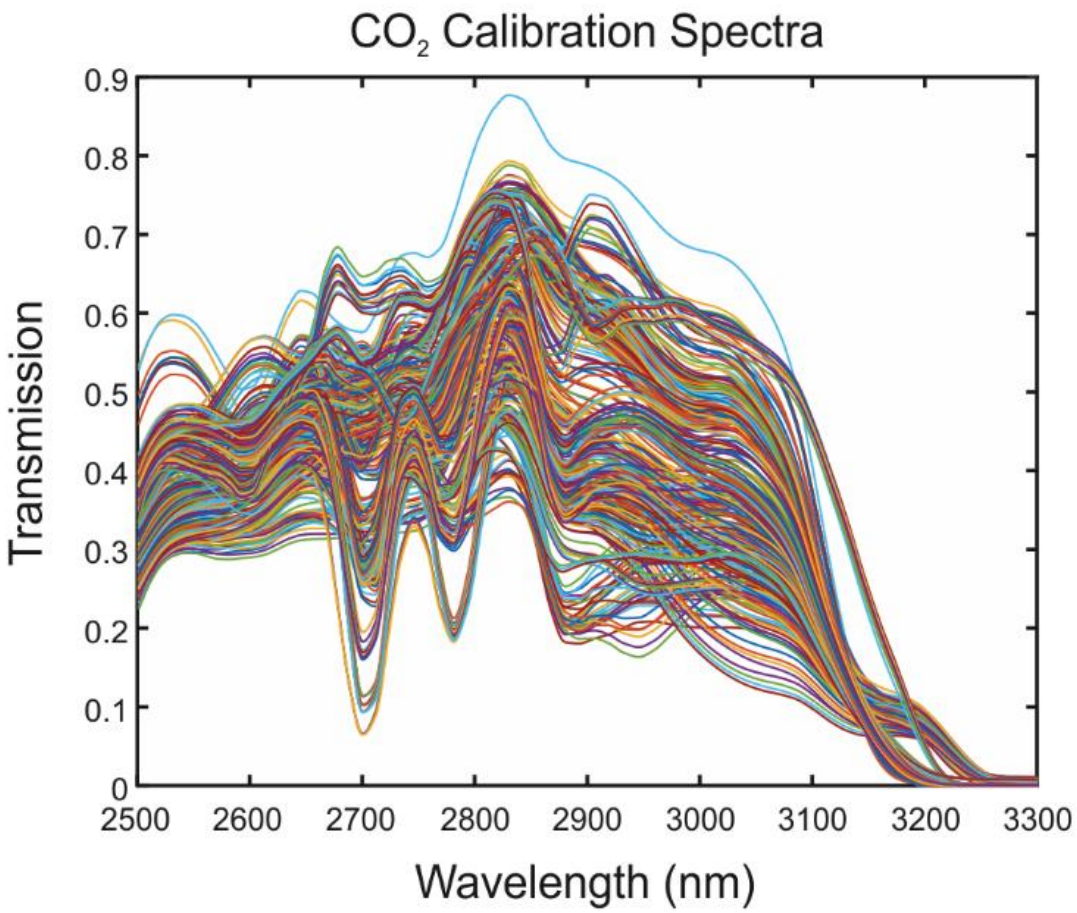

Figure 4.3: Transmission spectra of the pressure, volume, temperature (PVT) fluid spectra calibration dataset used for carbon dioxide.

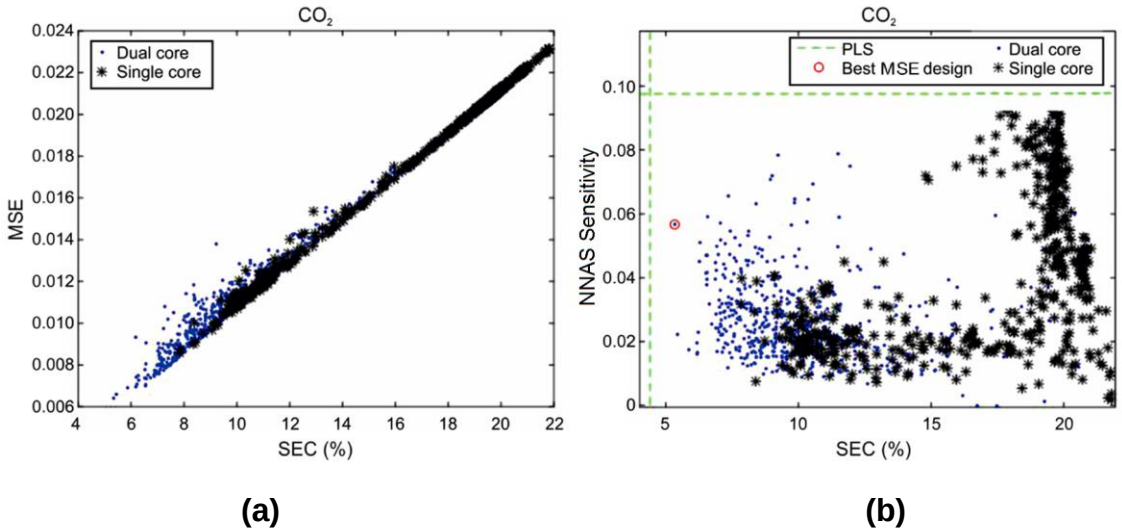

Figure 4.4: Carbon dioxide single- and dual-core MOE design results for 500 randomly seeded designs. To help identify viable candidates, MSE is plotted against SEC (a) and SEC against NNAS (b). The dashed green line plots the PLS limits to serve as a reference point.

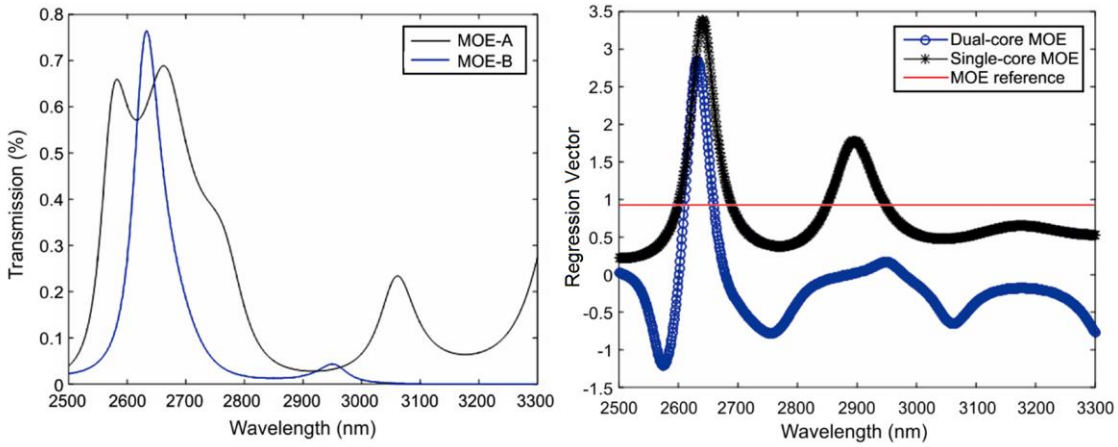

(a) (b)

Figure 4.5: Dual-core MOE transmission profiles for carbon dioxide (a); optical regression vector based on weighted regression coefficients and the spectra of the optical MOE core pairs (blue circles) and comparison with the single-core optical regression vector (b). The red line of (b) illustrates the reference offset level for positive vs. negative coefficients of the single core as determined by β for a single-core design.

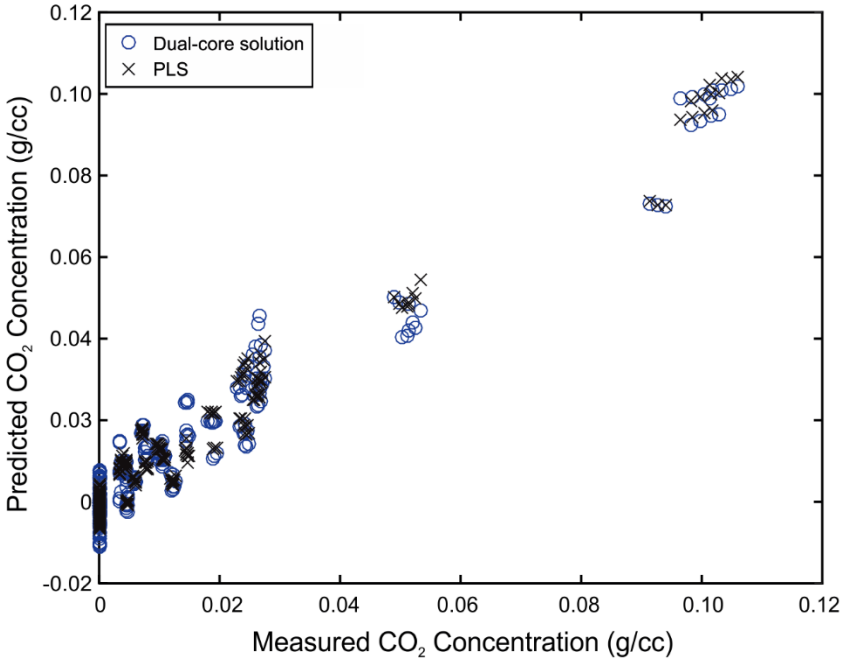

Figure 4.6: Comparison of predicted results between the dual-core optimized design and PLS.

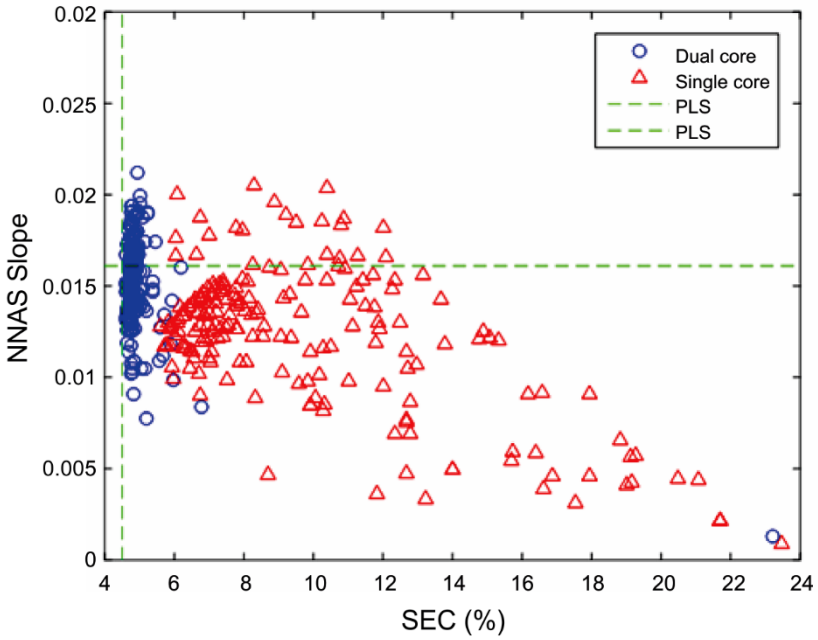

Figure 4.7: Methane single- (red triangles) and dual-core (blue circles) MOE design results for2,500 randomly seeded designs plotted vs. the norm of the NAS. The PLS limits (dashed green line) serve as a reference point.

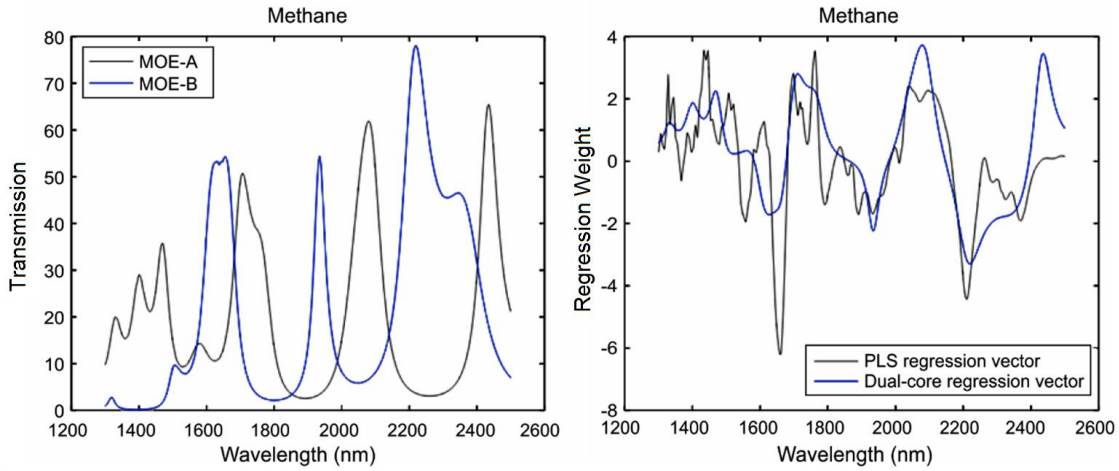

Figure 4.8: Dual MOE core design transmission functions (a) and dual MOE regression vector with PLS regression vector (b).

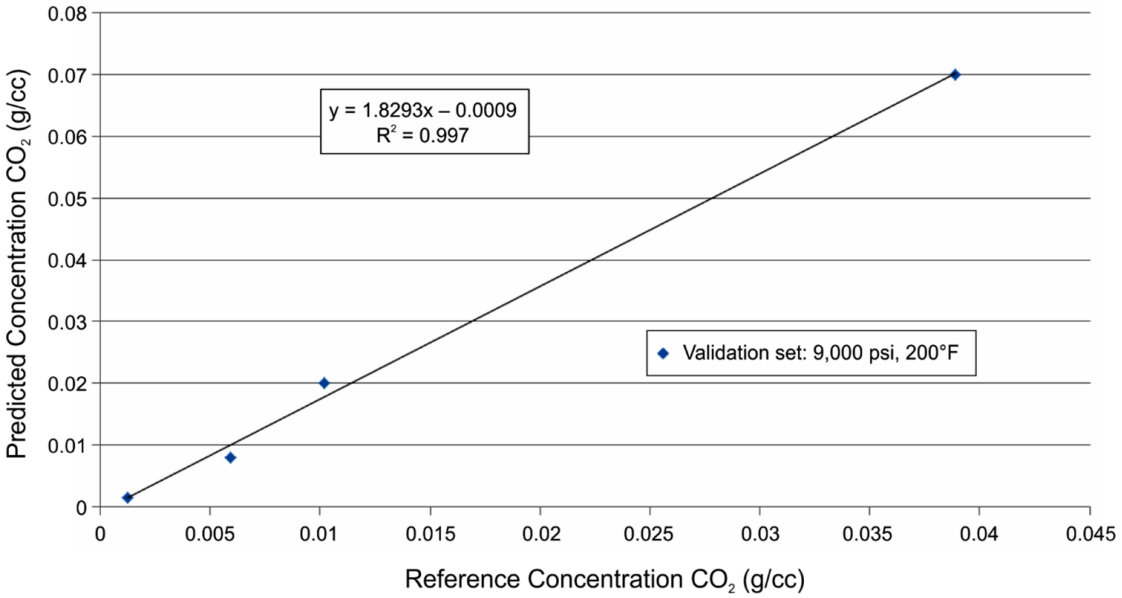

Figure 4.9: Predicted concentration of carbon dioxide for reference oils run at 62.05 Mpa and 65.5°C based on the theoretical MOC virtual master response.

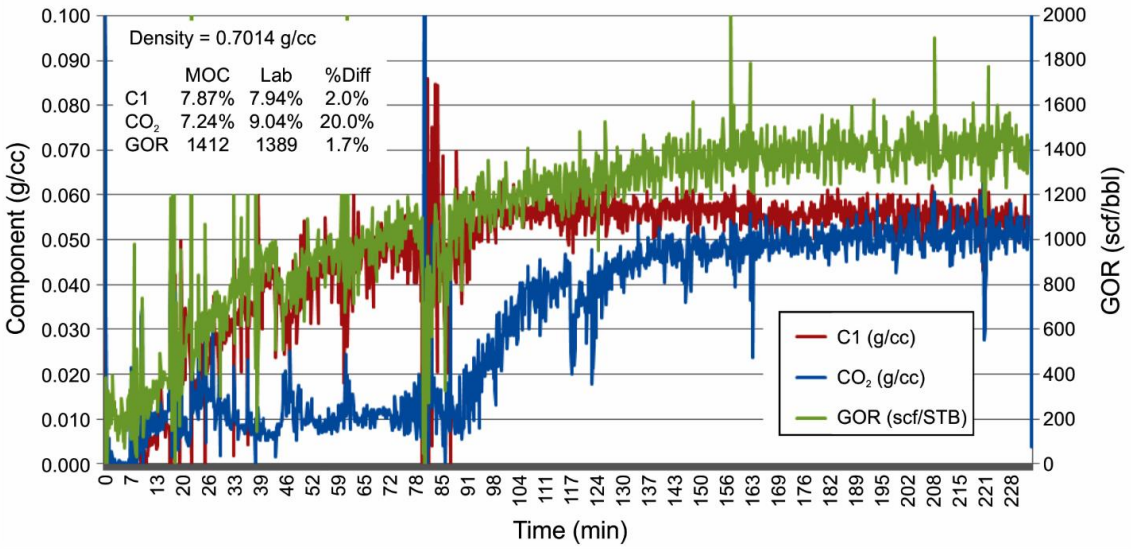

Figure 4.10: In-situ field test of the dual-core methane (C1) and carbon dioxide (CO_2) MOC sensor at 88.9°C and 67.07 Mpa. The left axis is carbon dioxide and methane components in g/cc, and the right axis is GOR in scf/bbl. The laboratory measured values for methane (C1), carbon dioxide (CO_2), the gas to oil ratio (GOR), and the reservoir fluid density are shown. The values were measured on a captured sample taken at time 228 minutes.

REFERENCES

1. Elshahawi, H.; Hashem, M. N.; McKinney, D.; Ardila, M.; Ayan, C. The Power of Real-Time Monitoring and Interpretation in Wireline Formation Testing–Case Studies. *SPE Reservoir Evaluation and Engineering* **2007,** *10* (3), 241–250.

2. Dong, C.; O'Keefe, M.; Elshahawi, H.; Hashem, M.; Williams, S.; Stensland, D.; Hegeman, P.; Vasques, R.; Terabayashi, T.; Mullins, O.; Donzier, E. New downhole-fluid-analysis tool for improved reservoir characterization. *SPE Reservoir Evaluation and Engineering* **2008,** *11* (6), 1107-1116.

3. Hashem, M.; McHardy, A.; Wynne, M.; Pool, W.; Viets, T.; Keuser, C.; Eriksen, K. O. Formation Pressure While Drilling, Wireline Formation Testing, And Fluid Sampling In a High Pressure/High Temperature Exploration Well Using Oil Based Mud: A Case History 1. *Petrophysics* **2007,** *48* (4), 258-270.

4. American Petroleum Institute. *API Recommended Practice 44: Sampling Petroleum Reservoir Fluids, second edition;* Orginization; American Petroleum Institute: Washington, DC, 2003.

5. Ahmed, K.; Hassan, F.; Taqi, F.; Ahmad, F.; Pearl, M.; Jones, C.; Vasquez, R.; Zuilekom, A. v.; Pelletier, M. Real-Time Downhole Fluid Analysis and Sampling with a New Optical Composition Analysis Sensor: A Case Study from Kuwait Heavy Oil Formation. *SPE International Heavy Oil Conference and Exhibition*, Mangaf, Kuwait, 2016; pp SPE-184112-MS.

6. Achourov, V.; Gisolf, A.; Kansy, A.; Eriksen, K. O.; O'Keefe, M.; Pfeiffer, T. Applications of Accurate In-Situ Fluid Analysis in the North Sea. *Offshore Europe*, Aberdeen, UK, 2011; pp SPE-145643-MS.

7. Angeles, R.; Torres-Verdin, C.; Malik, M. Prediction Of Formation-Tester Fluid-Sample Quality In Highly-Deviated Wells. *SPWLA 49th Annual Logging Symposium*, Austin, Texas, 2008; pp SPWLA-2008-SS.

8. Crombie, A.; Halford, F.; Hashem, M.; McNeil, R.; Thomas, E.; Melbourne, G.; Mullins, O. Innovations in Wireline Fluid Sampling. *Oilfield Review* **1998,** *10* (3), 26-41.

9. Elshahawi, H.; Venkataramanan, L.; McKinney, D.; Flannery, M.; Mullins, O. C.; Hashem, M. Combining Continuous Fluid Typing Wireline Formaion Testers, and Geochemical Measurments for an Improved Understanding of Reservoir Architecture. *SPE Reservoir Evaluation and Engineering* **2008,** *11* (1), 27 - 40.

10. Hammond, P. S. One- and two-phase flow during fluid sampling by a wireline tool. *Transport in Porous Media* **1991,** *6* (3), 299-330.

11. Hy-Billiot, J.; Bickert, J.; Montel, F.; Segalini, G. Getting the Best From Formation Tester Sampling. *SPE Annual Technical Conference and Exhibition*, San Antonio, TX, 2002; pp SPE-77771-MS.

12. Malik, M.; Torres-Verdín, C.; Sepehrnoori, K. Axially symmetric compositional simulation of formation tester measurements. *Journal of Petroleum Science and Engineering* **2007,** *59* (3), 333–349.

13. Malik, M.; Torres-Verdín, C.; Sepehrnoori, K.; Jackson, R.; Weinheber, P.; Mullins, O. C.; Elshahawi, H.; Dindoruk, B.; Hashem, M. Comparison of Wireline Formation-Tester Sampling with Focused and Conventional Probes in the Presence of Oil-Base Mud-Filtrate Invasion. *49th Annual Logging Symposium*, 2008; pp SPWLA-2008-LL.

14. Mullins, O. C.; Beck, G. F.; Cribbs, M. E.; Terabayashi, T.; Kegasawa, K. Downhole Determination Of Gor On Single-Phase Fluids By Optical Spectroscopy. *SPWLA 42nd Annual Logging Symposium*, Houston, Texas, 2001; pp SPWLA-2001-M.

15. Mullins, O.; Rodgers, R.; Weinheber, P.; Klein, G.; Venkataramanan, L.; Andrews, A.; Marshal, A. Oil Reservoir Characterization via Crude Oil Analysis by Downhole Fluid Analysis in Oil Wells with Visible−Near-Infrared Spectroscopy and by Laboratory Analysis with Electrospray Ionization Fourier Transform Ion Cyclotron Resonance Mass Spectrometry. *Energy and Fuels* **2006,** *20* (6), 2448-2456.

16. Andrews, A.; Schneider, M.; Canas, J.; Freitas, E.; Song, Y.; Mullins, O. Fluorescence Methods for Downhole Fluid Analysis of Heavy Oil Emulsions. *Journal of Dispersion Science and Technology* **2008,** *29* (2), 171-183.

17. Perez, T. E. Corrosion in the Oil and Gas Industry: An Increasing Challenge for Materials. *The Journal of The Minerals, Metals and Materials Society* **2013,** *65* (8).

18. Popoola, L. T.; Grema, S. A.; Latinwo, G. ; Gutti, B.; Balogun, S. A. Corrosion problems during oil and gas production and its mitigation. *International Journal of Industrial Chemistry* **2013,** *4* (35).

19. Goldstein, N.; Gersh, M.; Bien, F.; Richtsmeier, S.; Gruninger, J.; Adler-Golden, S.; Griffies, D.; Ronnenkamp, C.; Householder, D.; Krogue, J.; Gould, D. Real-Time Optical BTU Measurement of Natural Gas at Line Pressure. *4th International Symposium on Fluid Flow Measurement*, Denver, Colorado, 1999.

20. Ulbig, P.; Hoburg, D. Determination of the calorific value of natural gas by different methods. *Thermochimica Acta* **2002,** *382* (1-2), 27-35.

21. Udina, S.; Carmona, M.; Carles, G.; Santander, J.; Marco, L. A micromachined thermoelectric sensor for natural gas analysis: Thermal model and experimental results. *Sensors and Actuators B: Chemical* **2008,** *134* (2), 551-558.

22. Loubar, K.; Rahmouni, C.; Le Corre, O.; Tazerout, M. Combustion Properties Determination of Natural Gas Using Thermal Conductivity and CO2 Content. *SAE Technical Paper* **2005**.

23. Tjomsland, T.; Grotle, N. M.; Vikane, O. Scale Control Strategy and Economical Consequences of Scale at Veslefrikk. *International Symposium on Oilfield Scale*, Aberdeen, United Kingdom, 2001; pp SPE-68308-MS.

24. Abouie, A.; Korrani, A. K. N.; Shirdel, M.; Sepehrnoori, K. Comprehensive Modeling of Scale Deposition by Use of a Coupled Geochemical and Compositional Wellbore Simulator. Society of Petroleum Engineers. *SPE Journal* **2017,** *22* (4), 1225 - 1241.

25. Tjomsland, T.; Sæten, J. O.; Olav, V.; Michael, Z. Veslefrikk Scale Control Strategy and Economic Implications: Revisited 7 years later - did we improve? *SPE International Oilfield Scale Conference*, 2008; pp SPE-114086-MS.

26. NACE International. *Corrosion of Oil-and Gas-Well Equipment;* American Petroleum Institute: Dallas, TX, USA, 1958.

27. Pedersen, K. . a. P. L. C. P. *Phase Behavior of Petroleum Reservoir Fluids;* CRC Press: Boca Raton, 2007.

28. Dandekar, A. Y. *Petroleum Reservoir Rock and Fluid Properties;* Taylor & Francis Group, CRC Press : Boca Raton, 2006.

29. Bonis, M. R.; Crolet, J. L. Why So Low Free Acetic Acid Thresholds, in Sweet Corrosion at Low PCO2? *Corrosion*, Houston, 2005; pp NACE-05272.

30. Blunt, M.; Fayers, . F. J.; Orr, F. M. J. Carbon dioxide in enhanced oil recovery. *Energy Conversion and Management* **1993,** *34* (9-11), 1197-1204.

31. Kovscek, A. R.; Cakici, M.. Geologic storage of carbon dioxide and enhanced oil recovery. II. Cooptimization of storage and recovery. *Energy Conversion and Management* **2005,** *45* (11-12), 1941-1956.

32. Thomas., S. Enhanced Oil Recovery - An Overview. *Oil and Gas Science and Technology-Reveu de l Institut Francais du Petrole* **2008,** *63* (1), 9-19.

33. Shaw, J.; Bachu, S. Screening, Evaluation, and Ranking of Oil Reservoirs Suitable for CO2-Flood EOR and Carbon Dioxide Sequestration. *Journal of Canadian Petroleum Technology* **2002,** *41* (9), 51-61.

34. Cardoso, S. S. S.; Andres, J. J. T. Geochemistry of silicate-rich rocks can curtail spreading of carbon dioxide in subsurface aquifers. *Nature Communnication* **2014,** *5*.

35. Ravagnani , A. T. F. S.; Ligero, S. B.; Suslick, S. B. CO2 sequestration through enhanced oil recovery in a mature oil field. *Journal of Petroleum Science and Engineering* **2009,** *65* (3), 129-138.

36. Leach, A.; Mason, C.; van 't Veld , K. Co-optimization of enhanced oil recovery and carbon sequestration. *Resource and Energy Economics* **2001,** *33* (4), 893-912.

37. Jahangiri, H. R.; Zhang, D. Optimization of the Net Present Value of Carbon Dioxide Sequestration and Enhanced Oil Recovery. Houston, TX, 2011; pp OTC-21985-MS.

38. White, C. M.; Smith, D. H.; Jones, K. L.; Goodman, A. L.; Jikich, S. A.; LaCount, R. B.; DuBose, S. B.; Ozde, E.; Morsi, B. I.; Schroeder , K. T. Sequestration of Carbon Dioxide in Coal with Enhanced Coalbed Methane Recovery - A Review. *Energy and Fuels* **2005,** *19* (3), 659–724.

39. Lal, R. Carbon sequestration. *Philosophical Transactions of the Royal Society B* **2008,** *363* (1492), 815-830.

40. Benson, S.. Monitoring Carbon Dioxide Sequestration in Deep Geological Formations for Inventory Verification and Carbon Credits. *SPE Annual Technical Conference and Exhibition*, San Antonio, Texas, 2006; pp SPE-102833-MS.

41. Mueller, N.; Elshahaw, H.; Dong, C.; Mullins, O. C.; Flannery, M.; Ardila, M.; Weinheber, P. J.; McDade, E. M.; Mulins, O. C. Quantification of carbon dioxide using downhole Wireline formation tester measurements. *SPE Annual Technical Conference and Exhibition*, San Antonio, Texas, 2006; pp SPE-100739-MS.

42. Myrick, M. L.; Soyemi, O. O.; Schiza, M. V.; Farr, J. R.; Haibach, F. G.; Greer, A. E.; Priore, R. J. Application of multivariate optical computing to simple near-infrared point measuremnts. *Instrumentation for Air Polution and Global Atmospheric Monitering*, Boston, MA, 2002; p 208.

43. Myrick, M. L.; Soyemi, O.; Karunamuni, J.; Eastwood, D.; Zhang, L.; Greera, A. E.; Gemperlineb, P. A single-element all-optical approach to chemometric prediction. *Vibrational Spectroscopy* **2002,** *28* (1), 73–81.

44. Kiehl, J. T.; Bruhl, C.; Yamanouchi, T. A parameterization for the absorption due to the near infrared bands of CO2. *Tellus, Series B - Chemical and Physical Meteorology* **1985,** *37B* (4-5), 189-196.

45. H. M. Hcise, D. Infrared spectra of gases. In *Infrared and Raman Spectroscopy: Methods and Applications;* Schrader, Bernhard, Eds.; VCH Verlagsgescllschaft: Weinheim, 1995; p 264.

46. Chalmers, J. M., Griffiths, P. R., Eds. *Handbook of Vibrational Spectroscopy: Theory and instrumentation;* John Wiley & Sons Ltd: Chichester, 2002; Vol. V1.

47. Martens, H.; Naes, T. *Multivariate Calibration;* Wiley: New York, 1992.

48. Massart, D. L.; Vandeginste, B. G.; Deming, S. N.; Michotte, Y.; Kaufmann, L. *Chemometrics: a textbook;* Elsevier Science Publishers: Amsterdam, 1988.

49. Næs, T.; Isaksson, T. Locally Weighted Regression in Diffuse Near-Infrared Transmittance Spectroscopy. *Applied Spectroscopy* **1992,** *46* (1), 34-43.

50. Liu, F.; Jiang, Y.; He, Y. Variable selection in visible/near infrared spectra for linear and nonlinear calibrations: A case study to determine soluble solids content of beer. *Analytica Chimica Acta* **2009,** *635* (1), 45-52.

51. Beebe, K. R.; Kowalski, B. R. An Introduction to Multivariate Calibration and Analysis. *Analytical Chemistry* **1987,** *59* (17), 1007-1017.

52. Thomas, E. V. A Primer on Multivariate Calibraiton. *Analytical Chemistry* **1994,** *66* (15), 795-804.

53. Wold, S.; Sjostrom, M.; Eriksson, L. PLS-regression: a basic tool of chemometrics. *Chemometrics and Intelligent Laboratory Systems* **2001,** *58* (2), 109-130.

54. Jackson, E. J. . *A user's guide to principal components;* Wiley: New York, 2005.

55. Nadler, B.; Coifman, R. R. Partial least squares, Beer's law and the net analyte: statistical modeling and analysis. *Journal of Chemometrics* **2005,** *19* (1), 45–54.

56. Soyemi, O.; Haibach, F.; Gemperline, P. J.; Myrick, M. L. Nonlinear Optimization Algorithm for Multivariate Optical Element Design. *Applied Spectroscopy* **2002,** *56* (4), 477-487.

57. Soyemi, O.; Eastwood, D.; Zhang, L.; Li, H.; Karunamuni, J.; Gemperline, P.; Synowicki, R. A.; Myrick, M. L. Design and Testing of a Multivariate Optical Element: The First Demonstration of Multivariate Optical Computing for Predictive Spectroscopy. *Analytical Chemistry* **2001,** *73* (6), 1069–1079.

58. Nelson, M. P.; Aust, J. F.; Dobrowolski, J. A.; Verly, P. G.; Myrick, M. L. Multivariate Optical Computation for Predictive Spectroscopy. *Analytical Chemistry* **1998,** *70* (1), 73–82.

59. Gemperline, P. J.; Long, J. R.; Gregoriou, V. G. Nonlinear multivariate calibration using principal components regression and artificial neural networks. *Analytical Chemistry* **1991,** *63* (20), 2313-2323.

60. Centner, V.; Massart, D. L. Optimization in Locally Weighted Regression. *Analytical Chemistry* **1988,** *70* (19), 4206-4211.

61. Soyemi, O. O.; Haibach, F. G.; Gemperline, P. J.; Myrick, M. L. Design of angle-tolerant multivariate optical elements for chemical imaging. *Applied Optics* **2002,** *10* (10), 1936-1941.

62. Simcock, M.; Myrick, M. Precision in imaging multivariate optical computing. *Applied Optics* **2007,** *46* (7), 1066-1080.

63. Jones, C. M.; Freese, B.; Pelletier, M.; Perkins, D.; Chen, D.; Shen, J.; Atkinson, R. Laboratory Quality Optical Analysis in Harsh Environments. *Presented at the SPE Kuwait International Petroleum Conference and Exhibition*, Kuwait City, Kuwait, 2012; pp SPE-163289-MS.

64. Jones, C.; Gao, L.; Perkins, D.; Chen, D.; Gascook, D. Field Test of the Integrated Computational Elements: A New Optical Sensor for Downhole Fluid Analysis. *SPWLA 54th Annual Logging Symposium*, New Orleans, Louisiana, 2013; pp SPWLA-2013-YY.

65. Jones, C. M.; Freese, R.; Perkins, D. L.; Dai, B. Multivariate optical computing enables accurate harsh-environment sensing for the oil and gas industry. *Laser Focus World* **2014,** *50* (8), 27-31.

66. Jones, C.; Dai, B.; Chen, D.; He, T.; Pelletier, M.; Gascooke, D. Measurement and use of Formation Fluid, Saturate, and Aromatic Content, With Wireline Formation Testers. *SPWLA 56th Annual Symposium*, Long Beach, 2015; pp SPWLA-2015-EE.

67. Jones, C. M.; van Zuilekom, T.; Iskander, F. How Accurate Is Enhanced Optical Fluid Analysis Compared to Lab PVT Measurements? *SPWLA 57th Annual Logging Symposium*, Reykjavik, Iceland , 2016; pp SPWLA-2016-JJJ.

68. Hursan, G.; Ma, S. M.; Soleiman, W.; Eyuboglu, S.; Sethi, N.; Guergueb, N. New Wireline, In-situ, Downhole Fluid Compositional Analyses to Enhance Reservoir Characterization and Management. *SPE Annual Technical Conference and Exhibition*, Dubai, UAE, 2016; pp SPE-181526-MS.

69. Danzer, K.; Otto, M.; Currie, L. A. Guidelines for Calibration in Analytical Chemistry Part 2. Multispecies Calibration. *Pure and Applied Chemistry* **2004,** *76* (6), 1215–1225.

70. Jones, C. M.; Pelletier, M. T.; Atkinson, R.; Shen, J.; Moore, J.; Anders, J.; Perkins, D. L.; Myrick, M. L. A Small-Volume PVTX System for Broadband Spectroscopic Calibration of Downhole Optical Sensors. *Review of Scientific Instruments* **2017,** *88* (7).

71. Valderrama, P.; Braga, J. W. B.; Poppi, R. J. Variable Selection, Outlier Detection, and Figures of Merit Estimation in a Partial Least-Squares Regression Multivariate Calibration Model. A Case Study for the Determination of Quality Parameters in the Alcohol Industry by Near-Infrared Spectroscopy. *Journal of Agricultural Food*

Chemistry **2007,** *55* (21), 8331–8338.

72. Born, M.; Wolf, E. *Principles of optics: electromagnetic theory of propagation, interference and diffraction of light (7th ed.);* Cambridge University Press: Cambridge, UK, 1999.

73. Lorber, A.; Faber, K.; Kowalski, B. . R. Net Analyte Signal Calculation in Multivariate. *Analytical Chemistry* **1997,** *69* (8), 1620-1626.

74. Faber, N. (. M. Efficient Computation of Net Analyte Signal in Inverse Multivariate Calibration Models. *Analytical Chemistry* **1998,** *70* (23), 5108-5110.

75. Bro, R.; Anderson, C. M. Theory of net analyte signal vectors in inverse regression. *Journal of Chemometrics* **2003,** *17* (12), 646-652.

76. Nayak, A. B.; Price, J. M.; Dai, B.; Perkins, D.; Chen, D.; Jones, C. M. Characterization of Ion-Assisted Induced Absorption in A-Si Thin-Films Used for Multivariate Optical Computing. *Next-Generation Spectroscopic Technologies VIII*, Baltimore, Maryland, 2015; p 94820A.

77. Haibach, F.; Greer, A.; Schiza, M.; R., P.; Soyemi, O.; Myrick, M. On-Line reoptimization of filter designs for multivariate optical elements. *Applied Optics* **2003,** *42* (10), 1833-1838.

78. Ellis, D. V.; Singer, J. M. *Well logging for Earth Scientists, 2nd Ed.;* Springer: Dordrecht, 2008.

79. Jones, C. M.; Dai, B.; Chen, D. . H. T.; Pelletier, M.; Gascooke, D. Measurement and Use of Formation Fluid, Saturate, and Aromatic. *SPWLA 56th Annual Symposium*, Long Beach, 2015; pp SPWLA-2015-EE.

80. Eriksen, K. O.; Jones, C.; Freese, R.; van Zuilekom, A.; Gao, L.; Perkins, D.; Chen, D.; Gascooke, D.; Engelman, B. Field Tests of a New Optical Sensor Based on Integrated Computational Elements for Downhole Fluid Analysis. *SPE Annual Technical Conference and Exhibition*, New Orleans, Louisiana, 2013; pp SPE-166415-MS.

81. Nelson, R. C.; Plylerl, E. K.; Benedict, W. S. Absorption Spectra of Methane in the Near Infrared. *Journal of Research of the National Bureau of Standards* **1948,** *41,* 615-621.

82. Harrison, J. R.; Stansbury, M.; Patel, J.; Cross, A. T.; Kilburn, M. Novel Lime-Free Drilling Fluid System Applied Successfully in Gulf of Thailand. *SPE/IADC Drilling Conference*, Amsterdam, NE, 1999; pp SPE-52817-MS.

83. Garcia, J. M.; Lordo, S. A. Chemistry and Impacts of Chemistry And Impacts Of Commonly Used Amine-Based H2S Scavengers On Crude Unit Towers And

Overheads. *NACE International Conference and Expo: Corrosion*, Nashville, Tennessee, 2007; pp NACE-07571.

84. Vogta, M.; Pasel, B.; Bathena, D. Characterisation of CO2 absorption in various solvents for PCC applications by Raman spectroscopy. *Energy Procedia* **2011,** *4* (Supplement C), 1520-1525.

85. Idrisa, I.; Jensa, K.; Eimer, D. A. Speciation of MEA-CO2 Adducts at Equilibrium Using Raman Spectroscopy. *Energy Procedia* **2014,** *63* (Supplement C), 1424–1431.

86. Jones, C.; Alta, W.; Singh, J.; Proett, M. A.; Pedigo,. Collecting Single-Phase Retrograde Gas Samples at Near-Dewpoint Reservoir Pressure in Carbonates Using a Pump-Out Formation Tester With an Oval Pad. *SPE Annual Technical Conference and Exhibition*, Anaheim, California, 2007.

87. Palmer, R.; da Silva, A. S.; Al-Hajari, A. A.; Engelman , B.; van Zuilekom, T.; Proett, M. Advances In Fluid Identification Methods Using A High Resolution Densitometer In A Saudi Aramco Field. *49th Annual Logging Symposium*, Austin, Texas, 2008.

88. Gao, L.; Van Zuilekom, A. H. W.; Pelletier, M. T.; Proett, M. A.; Eyuboglu, A. S.; Engelman, R.; Elshahawi, H.; Hows, M. P. Sensitivity of a High-Resolution Fluid-Density Sensor in Multiphase Flow. *SPE Annual Technical Conference and Exhibition*, Florence, Italy, 2010.

89. Hsu, K.; Hegeman, P.; Dong, C.; Vasques, R. R.; O'Keefe, M.; Ardila, M. Multichannel Oil-Base Mud Contamination Monitoring Using Downhole Optical Spectrometer. *49th Annual Logging Symposium*, Austin, Texas , 2008.

90. Zuo, J. Y.; Gisolf, A.; Dumont, H.; Dubost, F.; Pfeiffer, T.; Wang, K.; Mishra, V. K.; Chen, L.; Mullins, C.; Gemelli, S. A Breakthrough in Accurate Downhole Fluid Sample Contamination Prediction in Real Time. *Petrophysics* **2015,** *56* (3), 251 - 265.

CHAPTER 5

CONCLUSION

Petroleum wells will continue to be be drilled for a long time into the future (1), and it is imperative to drill those wells as safely as possible, as to minimize health, safety, environment (HSE) impact, and as efficiently as possible, to minimize the total number of drilled wells. In situ measurement of methane, carbon dioxide, helps to accomplish these goals.(2-14) In fact, higher resolution, reliable, sensors able to monitor ever more properties, is respectively the number one, two, and three requirements for petroleum exploration and production technology development, together accounting for a majority of ranked priorities.(15) However, the harsh environment where even short term retrievable sensors must survive for up to two weeks (16), limits the capability of in situ sensors relative to a surface laboratory. Multivariate optical computing has been shown, herein, as an effective and viable means to measure the composition of petroleum in the harsh environments of petroleum wells with accuracy comparable to that of a laboratory FTNIR or FTIR spectrometer. Also, the dual core MOE configuration has been introduced a as a new implementation of MOC able to more easily match the performance of complex regression vectors, such that not only can laboratory spectrometer optical analysis accuracy be matched by MOC sensors, but for more complex analyte to matrix combinations. The measurement of carbon dioxide in the mid infrared is a new capability of in-situ petroleum measurement and is the first demonstration of any down hole mid infrared chemical measurement. Further, the

repeated in-situ measurements have shown the MOC sensor as durable for harsh environments thereby meeting the top three requirements of oilfield operators for exploration and production technology development.

The research conducted herein enabling harsh environment MOC sensors is a modest first step of MOC potential. Current and future research includes a more analytes such the dissolved gases of ethane, propane, butane, pentane and hydrogen sulfide, as well as the liquid C6+ fractions of saturates, aromatics, resins and asphaltenes, and water chemistry. Also future research may include extending in-situ monitoring to permanent emplacement monitoring for which sensors must survive for 5 to 20 years. Specifically it is of interest to monitor carbon dioxide in petroleum at the subsurface entrance from to the wellbore for effective management of enhanced oil recovery and carbon sequestration. It is also of interest to monitor the fluid in pipelines for flow assurance issues. Research to enable the monitoring of chemical feedstocks and blended products for refinery and petrochemical applications is also underway. Each of these challenges will require new MOC capability such as ultraviolet sensing, derivative spectroscopy MOC, calibration tunable MOC regression vectors, with even smaller size, even greater durability, and reduced cost. As harsh environment sensing for petroleum applications improves, it is possible that other industries and research fields leverage this capability.

REFERENCES

1. Conti, J.; Holtberg, P.; Diefenderfer, J.; LaRose, A.; Turnure, J. T.; Westfall, L. *International Energy Outlook 2016 With Projections to 2040;* United States Government; United States Department of Energy: Washington D. C., 2016.

2. Elshahawi, H.; Hashem, M. N.; McKinney, D.; Ardila, M.; Ayan, C. The Power of Real-Time Monitoring and Interpretation in Wireline Formation Testing–Case Studies. *SPE Reservoir Evaluation and Engineering* **2007,** *10* (3), 241–250.

3. Hashem, M.; McHardy, A.; Wynne, M.; Pool, W.; Viets, T.; Keuser, C.; Eriksen, K. O. Formation Pressure While Drilling, Wireline Formation Testing, And Fluid Sampling In a High Pressure/High Temperature Exploration Well Using Oil Based Mud: A Case History 1. *Petrophysics* **2007,** *48* (4), 258-270.

4. Mullins, O. C.; Beck, G. F.; Cribbs, M. E.; Terabayashi, T.; Kegasawa, K. Downhole Determination Of Gor On Single-Phase Fluids By Optical Spectroscopy. *SPWLA 42nd Annual Logging Symposium*, Houston, Texas, 2001; pp SPWLA-2001-M.

5. Mullins, O.; Rodgers, R.; Weinheber, P.; Klein, G.; Venkataramanan, L.; Andrews, A.; Marshal, A. Oil Reservoir Characterization via Crude Oil Analysis by Downhole Fluid Analysis in Oil Wells with Visible−Near-Infrared Spectroscopy and by Laboratory Analysis with Electrospray Ionization Fourier Transform Ion Cyclotron Resonance Mass Spectrometry. *Energy and Fuels* **2006,** *20* (6), 2448-2456.

6. Perez, T. E. Corrosion in the Oil and Gas Industry: An Increasing Challenge for Materials. *The Journal of The Minerals, Metals and Materials Society* **2013,** *65* (8).

7. Popoola, L. T.; Grema, S. A.; Latinwo, G. ; Gutti, B.; Balogun, S. A. Corrosion problems during oil and gas production and its mitigation. *International Journal of Industrial Chemistry* **2013,** *4* (35).

8. Goldstein, N.; Gersh, M.; Bien, F.; Richtsmeier, S.; Gruninger, J.; Adler-Golden, S.; Griffies, D.; Ronnenkamp, C.; Householder, D.; Krogue, J.; Gould, D. Real-Time Optical BTU Measurement of Natural Gas at Line Pressure. *4th International Symposium on Fluid Flow Measurement*, Denver, Colorado, 1999.

9. Ulbig, P.; Hoburg, D. Determination of the calorific value of natural gas by different methods. *Thermochimica Acta* **2002,** *382* (1-2), 27-35.

10. Udina, S.; Carmona, M.; Carles, G.; Santander, J.; Marco, L. A micromachined thermoelectric sensor for natural gas analysis: Thermal model and experimental results. *Sensors and Actuators B: Chemical* **2008,** *134* (2), 551-558.

11. Loubar, K.; Rahmouni, C.; Le Corre, O.; Tazerout, M. Combustion Properties Determination of Natural Gas Using Thermal Conductivity and CO2 Content. *SAE*

Technical Paper **2005**.

12. Tjomsland, T.; Grotle, N. M.; Vikane, O. Scale Control Strategy and Economical Consequences of Scale at Veslefrikk. *International Symposium on Oilfield Scale*, Aberdeen, United Kingdom, 2001; pp SPE-68308-MS.

13. Abouie, A.; Korrani, A. K. N.; Shirdel, M.; Sepehrnoori, K. Comprehensive Modeling of Scale Deposition by Use of a Coupled Geochemical and Compositional Wellbore Simulator. Society of Petroleum Engineers. *SPE Journal* **2017,** *22* (4), 1225 - 1241.

14. Tjomsland, T.; Sæten, J. O.; Olav, V.; Michael, Z. Veslefrikk Scale Control Strategy and Economic Implications: Revisited 7 years later - did we improve? *SPE International Oilfield Scale Conference*, 2008; pp SPE-114086-MS.

15. Kimberlite. *Formation Evaluation Supplier Performance & Competitive Positioning Report;* Kimberlite International Oilfield Research: Spring, TX , 2016.

16. Djefel, M.; Tigre Maia, C. R. S.; Proett, M. A.; Eyuboglu, A. S.; Naupari, C. E.; Beck, G. Potential Economic Value-Added Model Using Formation Sampling-While-Drilling in Development Fields. *SPE Latin American and Caribbean Petroleum Engineering* , Lima, Peru, 2010; pp SPE-138956-MS.